

University of Nottingham
UK | CHINA | MALAYSIA

Near-Infrared Semiconductor Photonic Switches for Quantum Sensors

Bruce Saleeb-Mousa

Thesis submitted to the University of Nottingham
for the degree of Doctor of Philosophy

October 2021

"The best that most of us can hope to achieve in physics is simply to misunderstand at a deeper level"
Wolfgang Pauli

Abstract

The promising performance of atom interferometry in determining precise values of fundamental constants, lends itself to applications in many areas of modern physics and engineering. In particular, the cold-atom gravimeter has proven itself to be a useful tool in determining the local acceleration due to gravity with a precision of $\delta g/g = 10^{-9}$, with long term stability and accuracy. In recent years, there has been a major incentive to develop these mainly laboratory-based experimental systems towards more compact, portable and eventually commercialised systems. Part of this development involves the design, fabrication and testing of bespoke underpinning technologies such as high performance, low power integrated active optical components which would help to reduce the size, weight and power of these sensors.

In this thesis, the design, fabrication and testing of a novel integrated optical switch on semi-insulating gallium arsenide substrates is detailed. A standard double heterostructure with highly doped capping layers for ohmic metal contacts is grown on these substrates to form a PIN diode structure, consisting of a core of high refractive index and cladding layers of lower refractive index. The refractive index of each layer is selected by growing $Al_xGa_{(1-x)}As$ $(0 \leq x \leq 1)$ with differing fractional aluminium concentrations, x. This structure provides both electrical confinement of injected carriers and optical confinement of a guided optical wave in the core. The switch structure is then fabricated on these wafers, consisting of a beam-steering section and a waveguiding section. An optical beam enters the steering section where it is guided into one of two single mode waveguides delineated at the end of the steering section. This action provides the beam switching effect. This switching mechanism is based on a previously reported phenomena of optical beam steering, whereby an injection of a sufficient density of carriers into the core of a planar waveguide produces regions of depressed refractive index due to the Moss-Burstein effect. This change forms a channel waveguide within the steering section, and the direction of the guided beam can be controlled by adjusting the amount of current injection either side of the guided optical wave. These optical switches are designed to be used in cold-atom gravimeter experiments, intended for both fast (μs) and high extinction ($\sim$80 dB) switching. These

devices could be used for switching of the trapping/cooling beams of the magneto-optical trap, used to form the gas of cold atoms, and for the precise switching of the beams used to perform the interferometery sequence. Three separate optical switching designs are presented and tested, which are intended to switch optical beams in wavelength ranges 890-920 nm, 750-780 nm and 745-775 nm, for use in caesium, rubidium and potassium based atom interferometers respectively.

Characterisation of the fabricated devices revealed observation of the beam steering effects at low current injections (<20 mA), but suppression of the mechanism at higher injection currents due to excessive heating. The heating is attributed to current crowding due to the mesa geometry of the switch design on semi-insulating substrates. The switching was observed to be strongly wavelength-dependent, as predicted by the theory, with a maximum extinction of 21.42±0.03 dB at 734 nm achieved for a single device. Devices can be cascaded in series on a single chip to provide an enhanced extinction. This was observed using the wafer designed for 767 nm. The extinction achieved at this wavelength for this wafer was measured to be 6.69±0.03 dB. The switches designed for operation at 904 nm and 780 nm achieved measured extinction ratios of 13.40±0.03 and 2.39±0.03 respectively. As a result of these observations, a new epitaxial design is proposed for switching at 780 nm. The fabricated devices were also characterised electrically. Current-voltage measurements revealed that the p-i-n structure devices behave as expected with low power requirements - sufficiently low to be able to be sourced by commercially available circuits for packaged optoelectronics. Optical propagation loss measurements showed that the fabricated devices can offer propagation losses as low as ∼1 dB for all epitaxial designs, due to their small dimensions of ∼1 mm in the optical propagation axis. Finally, the measured optical rise and fall times of one of the fabricated switches was measured to be 670±5 ns and 675±5 ns respectively, meeting the initial design requirements and confirming suitability of the speed of the switching mechanism for the intended application.

Acknowledgements

There are a number of people I would like to express sincere thanks to, without whom it would have been impossible to complete this PhD. First and foremost, I would like to say a huge thank you to my supervisors Dr Chris Mellor and Dr Jessica Maclean. Thank you both for the opportunity to work on this project and for all of your support throughout. Jessica, thank you for your continued encouragement and support, especially in preparing for conferences and communicating my research to the scientific community in a clear and concise way, and thank you for teaching me the importance of attention to detail in the world of microfabrication. Chris, thank you for your endless support and advice on all things scientific. Your breadth and depth of knowledge never ceases to impress me and you always made time to discuss every aspect of the project, for which I am very grateful. I am especially grateful for the extra support you provided to me during the restarting of research activities following the initial shutdown due to the pandemic. This was a challenging time for everyone and I am thankful for the support that you both provided to me throughout.

Thank you to my examiners for taking the time to read this thesis. I hope it has been stimulating and that we have some interesting discussions to follow!

Thank you to Mr Jasbinder Chauhan for taking the time to provide me with one-to-one clean room training sessions at the start of the PhD, and for always being around to offer fabrication advice and for always ensuring the clean rooms are operating smoothly. More recently, thanks to Dr Jake Greener for also providing help and technical support with all things clean room related and for always being up for a general chat during lunch. Thank you to all of the other technical staff, especially Mr Andrew Stuart for always having a solution to problems I had with electronics.

Thanks to all of my workplace friends, Dr James Moss, Dr Sarah Heywood, Dr Niall Holmes, Dr Ashley Tyler, Mr Nathan Cottam, Dr Richard Cousins, Dr Chris Corden and all of my office desk neighbours. James, you always showed huge enthusiasm for this project which always nice to see, especially on a Monday morning! Thank you for teaching me the basics and helping me get to grips with the project from the very start. Our discussions always helped me sanity check

my calculations and work and sometimes helped grow new ideas and ways of approaching problems. Sarah, thanks for all your help and advice with microfabrication techniques and for being around in the tea room for a chat and a cup of tea which kept me sane (pre-pandemic of course). Niall, Ashley and Nathan, we have known each other for the best part of 10 years and we have experienced the journey from fresh physics undergraduate to PhD together. Thanks for always being there to chat about anything and everything and for always keeping things light-hearted. Special thanks to Niall for encouraging me to return to do a PhD a year after finishing the undergraduate degree! Richard, thank you for always being there to provide me with help and support in the nmRC. Chris, thanks for always giving me advice on all things optics related, and for advising me on how to best repair my car! Thanks to my office desk neighbours George and Nathan for always listening to me complain about my code not working and subsequently pointing out my silly mistakes! Thanks to all of my other friends, in particular, Joe, Matt and Steve for all your support and encouragement and for helping me switch off at weekends and during holidays. I am a forgetful person so no doubt I have forgotten to thank some of you. If so, feel free to insert your name here: ...

Finally, thanks to my mum, dad and brother for always supporting me through everything I have done, and for your unconditional love. Last but certainly not least, I would like to give huge thanks and appreciation to my fiancée Amelia for supporting me over the past ten years. You have always been by my side through all of the good times and bad, and your support, patience, and love has been invaluable throughout. I could not have achieved what I have thus far without you and for that I am eternally grateful.

List of Publications & Conferences

1. Saleeb-Mousa, Bruce, et al. "Near infrared integrated photonic switches for portable quantum sensors." Journal of Physics: Conference Series. Vol. 1919. No. 1. IOP Publishing, 2021. https://doi.org/10.1088/1742-6596/1919/1/012007

2. Photon 2020: IOP Webinars for the Physics Community. 1^{st} - 4^{th} September 2020. Talk: Integrated Optical Switches based on Epitaxial Aluminium Gallium Arsenide for Portable Quantum Sensors.

3. UK Semiconductors conference 2019, 10th-11th July 2019, Sheffield Hallam University. Poster: Investigation into the Implementation of GaAs/$Al_xGa_{(1-x)}$As-based Optical Switches in Cold Atoms-based Quantum Sensors.

4. Semiconductor and Integrated Opto-Electronics (SIOE) Conference, Cardiff, 16-18$^{\text{th}}$ April 2019. Poster: Optical Switch using Beamsteering at 900nm wavelength in GaAs/$Al_xGa_{(1-x)}$As with High Extinction Ratio for Quantum Sensors. Presented by Dr James L. Moss.

Contents

Abstract i

Acknowledgements iii

List of Publications & Conferences v

List of Tables xi

List of Figures xiii

1 Introduction 1

1.0.1 Integrated Photonics for Quantum Sensing 3

1.1 Atom Interferometry for Quantum Sensing 4

1.1.1 Ultracold Quantum Gases 4

1.1.2 Atom Interferometry 5

1.1.3 Magneto-Optical Trap 6

1.1.4 The Interferometry Sequence 10

1.1.5 Experimental Realisation 12

1.2 Existing Switching Technologies 14

1.2.1 Performance Indicators 14

1.2.2 Acousto-optical Modulator 18

1.2.3 Electro-optical Switches 22

1.2.4 Electro-absorption Modulators 24

1.2.5 Mach-Zehnder Modulator 26

1.2.6 Microring Resonators 27

1.2.7 MEMS Switches 28

1.3 Summary 29

1.4 Statement of Contributions 30

2 Beam Steering Photonic Switches: Theory and Modelling 32

2.1 Introduction 32

2.1.1 Wafer Structure 32

2.2 Carrier-induced Refractive Index Change Effects 33

2.2.1 Moss-Burstein Effect 35

2.2.2 Bandgap Shrinkage Effect . . . 39
2.2.3 Free-carrier Absorption . . . 40
2.2.4 Combination of Refractive Index Change Effects . . . 42
2.3 Electrical Confinement . . . 45
2.3.1 Band Structure . . . 45
2.3.2 Carrier Leakage . . . 48
2.3.3 Carrier Spreading . . . 53
2.4 Optical Confinement . . . 57
2.4.1 Effective Index of the Slab Mode . . . 57
2.4.2 Strip-loaded Waveguides . . . 60
2.5 Optical Switch Design . . . 61
2.6 FFT-BPM Simulations . . . 66
2.6.1 Algorithm . . . 66
2.6.2 Beam Steering Simulations . . . 69
2.7 Summary . . . 72

3 Device Fabrication 73
3.1 Introduction . . . 73
3.2 Photolithography . . . 73
3.2.1 Photoresist Profile Optimisation . . . 75
3.3 Ohmic Contacts . . . 79
3.3.1 Metal Deposition . . . 81
3.3.2 Circular Transmission Line Measurements . . . 84
3.4 Dry Etching . . . 86
3.4.1 p-GaAs Removal . . . 89
3.4.2 Waveguide Etch . . . 90
3.4.3 Mesa Etch . . . 91
3.4.4 Micromasking . . . 93
3.5 Passivation . . . 97
3.5.1 BCB Coating . . . 97
3.5.2 Top-up Contact Pads . . . 100
3.5.3 BCB Swelling . . . 101
3.6 Dicing . . . 102
3.7 Bonding . . . 104
3.8 Summary . . . 109

4 Testing Instrumentation 111
4.1 Introduction . . . 111
4.2 Requirements of the Test System . . . 111
4.2.1 Electrical Control & Optical Detection Speed . . . 112

4.2.2 Optical Coupling . . . 114
4.3 Hardware Design . . . 115
4.3.1 Input Side . . . 116
4.3.2 Output Side . . . 122
4.3.3 Facet Illumination & Imaging . . . 127
4.3.4 Plan-view Inspection . . . 128
4.3.5 Electronics . . . 130
4.4 Software Design . . . 137
4.4.1 Hardware Communication . . . 138
4.4.2 Sub-Routines . . . 139
4.5 Limitations & Concluding Remarks . . . 143

5 Device Characterisation 145
5.1 Introduction . . . 145
5.2 Current-Voltage Characteristics . . . 145
5.2.1 Summary . . . 152
5.3 Luminescence Spectra . . . 153
5.3.1 Photoluminescence Measurements . . . 153
5.3.2 Electroluminescence Measurements . . . 162
5.3.3 Summary of Luminescence Data & Implications . . . 167
5.4 Passive Waveguide Testing . . . 171
5.4.1 Propagation Loss Measurements . . . 172
5.4.2 Discussion . . . 176
5.5 Switching Characteristics . . . 177
5.5.1 Extinction Ratio . . . 177
5.5.2 Current Crowding . . . 183
5.5.3 Switching Speed . . . 187
5.6 Heating Effects . . . 190
5.7 Discussion of Results . . . 193
5.8 Conclusion . . . 194

6 Conclusions and Outlook 195
6.1 Summary of Work . . . 195
6.2 Design Limitations and Future Work . . . 198
6.2.1 Carrier Spreading . . . 198
6.2.2 Metal Contacts . . . 201
6.2.3 Packaging . . . 203
6.2.4 780 nm Switch Redesign . . . 205
6.3 Recent Developments & Future Trends . . . 207
6.3.1 Silicon Nitride Technologies . . . 208

6.3.2 Final Remarks 209

Appendices **210**

A Device Fabrication Process Flow **210**

A.1 Wafer Dicing 210
A.1.1 Standard Solvent Clean 210
A.1.2 Tape & Wafer Mounting 211
A.1.3 Scribing & Breaking 212
A.2 p-Type Contacts 213
A.2.1 Patterning 213
A.2.2 Thermal Evaporation 214
A.2.3 Metal Lift-off 215
A.2.4 Metal Anneal 216
A.3 p-GaAs Etch 216
A.4 Waveguide Etch 217
A.4.1 Waveguide Patterning 217
A.4.2 Etching 218
A.5 n-GaAs Reveal Etch 218
A.5.1 Patterning 218
A.5.2 Etching 219
A.6 n-Type Contacts 219
A.6.1 Patterning 219
A.6.2 Thermal Evaporation 219
A.6.3 Metal Lift-off 220
A.6.4 Metal Anneal 220
A.7 BCB Encapsulation 221
A.7.1 Si_3N_4 Deposition 221
A.7.2 Adhesion Promoter 221
A.7.3 BCB Coating 222
A.8 BCB Etching 222
A.8.1 Patterning: Part 1 222
A.8.2 Etch 1 223
A.8.3 Patterning: Part 2 223
A.8.4 Etch 2 224
A.9 Top-up Metal Contacts 224
A.9.1 Ion Milling & Ti Sputter 224
A.9.2 Patterning 224
A.9.3 Thermal Evaporation 224
A.9.4 Lift-off 225

A.9.5 Isolation Etch 225
A.10 Dicing & PCB Mounting 226
A.10.1 Preparation 226
A.10.2 Dicing 226
A.10.3 PCB Mounting 228
A.11 Wire Bonding 229
A.11.1 Ball & Wedge Bonding 229
A.11.2 Bond Reworking 230

List of Tables

1.1 Typical key performance parameters for optical switches relevant for use in quantum sensors. 30

2.1 Layer compositions of semi-insulating (SI) GaAs epitaxial wafers, grown by Dr Richard Campion, for optical switching devices. The p-i-n region is highlighted in bold. 34

2.2 Calculated nominal band-gap energy values and their corresponding photon wavelengths for cladding and core regions of all wafers. 46

2.3 Calculated effective indices of the fundamental TE and TM modes for the slab mode of each epitaxial wafer. 60

2.4 Various theoretically calculated current injections for devices from each wafer to couple the maximum amount of light possible into either output waveguide (ON or OFF), demonstrating the range which is able to be coupled into each waveguide. Note that the percentages do not total 100% since some of the power falls outside the region of both waveguides. Device design and therefore current injection are symmetric so the values of current injection to couple into one waveguide are reversed to couple into the other. 72

3.1 Key recipe parameters for patterning of waveguides, mesa etch and metal contacts using the AZ5214E photoresist. 79

3.2 Summary of the electrical parameters obtained via cTLMs. 87

3.3 Summary of the dry etching processes used in defining the device structure. Etch depths were measured after the etching process using a KLA-Tencor Stylus Profiler. Measurements were taken at 7 points on the sample and an average calculated. The etch depth was not measured for the p-GaAs etch because this etch is self-passivating at the required depth. 93

4.1 Calculated beam diameters for each laser diode used for testing of the fabricated optical switches. 118

4.2 Calculated spot size diameters for each testing wavelength, using the Thorlabs C260TMD-B aspheric lens. 120
4.3 Calculated numerical apertures (to 3 significant figures) of devices from each epitaxial design at the relevant testing wavelengths. . . 124
4.4 Overview of the various packages and interfaces used to communicate with the test system hardware. 139

5.1 Summary of the ideality factors obtained from the p-i-n I/V measurements. Structure D did not display diode-like I/V behaviour so the ideality factor could not be calculated using the same method in this instance. p-i-n test structures were not patterned onto the RC187 die due to its smaller size after half of the sample was damaged early in the fabrication process. 149
5.2 Layer compositions of semi-insulating (SI) GaAs epitaxial wafers, grown by Dr Richard Campion, for optical switching devices. The p-i-n region is highlighted in bold. 154
5.3 Empirical effective phonon energies due to the GaAs and AlAs-like longitudinal optical (LO) and transverse optical (TO) phonon modes [134], compared with the measured phonon energies from fitting the phonon replica peaks to Gaussian functions. Uncertainties on the measured values have been determined by the 95% confidence bounds on the linear fit. 158
5.4 Summary of the measured propagation losses of the test waveguides. 175
5.5 Summary of the measured extinction ratios for optical switching devices from each wafer at various operating wavelengths. 178
5.6 Summary of the theoretically calculated current spreading lengths due to the mesa geometry, according to [144]. 185

6.1 Layer compositions for the new proposed epitaxial design, for optical switching devices at 780 nm. The p-i-n region is highlighted in bold. 205

List of Figures

1.1 Hyperfine structure of the ^{87}Rb D2 transition. 7
1.2 Principle of the magneto-optical trap [20]. 9
1.3 Configuration of a classical Mach-Zehnder Interferometer. Light is split along two paths by a beam splitter before being reflected by mirrors and recombined using another beamsplitter. Interference fringes are detected from the combined beam and the path difference between the two beams may be inferred from the phase shift. 10
1.4 Schematic diagram illustrating the process of a three pulse atom interferometer as detailed by Kasevich and Chu [29]. 12
1.5 Definition of the rise time, τ_r, of a signal is the time taken for the rising edge of a signal to transit from 10% to 90% of its final value. 17
1.6 Typical structure of a Bragg type acousto-optical modulator . . . 19
1.7 Interaction of an optical beam with the wave front of the acoustic signal in the AOM crystal. 21
1.8 Semiconductor band diagram illustrating the Franz-Keldysh effect in the presence of an electric field. The parameter x represents the distance from the surface of the semiconductor whilst E_C and E_v represent the energy of the conduction and valence bands respectively, and t is the thickness of the semiconductor sample. 25
1.9 Schematic illustration of a microring resonator with separte input and output bus waveguides. 28

2.1 Theoretical change in refractive index of undoped GaAs as a function on photon energy due to the Moss-Burstein effect, for three increasing values of carrier concentration, at T = 300 K. Charge neutrality is assumed so that $N = P$. 36
2.2 Theoretical change in refractive index for the core regions ($Al_xGa_{(1-x)}As$) of (a): RC184 and (b): RC187 due to the Moss-Burstein effect, as a function of photon energy, at T = 300 K. 37

2.3 Change in refractive index of the core region of RC101, RC184 and RC187 at T = 300 K, as a function of carrier concentration due to the Moss-Burstein effect, at photon wavelengths relevant to quantum sensing applications. In this situation, the magnitude of Δn is higher for GaAs as the simulated wavelengths than the other concentrations of $Al_xGa_{(1-x}As$ at their simulated wavelengths due to the proximity of these photon wavelengths to the corresponding wavelength of the nominal band gap. As discussed, the strength of the Moss-Burstein effect is increased the closer the wavelength of the absorbed photon is to this nominal band gap wavelength. . 38

2.4 Schematic illustration of a direct band-gap semiconductor (a): before and (b): after a significant injection of carriers, resulting in a reduction in the band-gap energy from E_g to $E_g^{'} = E_g - \Delta E_g$. . . 39

2.5 Change in band-gap energy due to the band-gap shrinkage effect for GaAs and $Al_xGa_{(1-x)}As$ with x = 0.221, 0.25, calculated using Equation 2.3. 41

2.6 Change in refractive index as a function of the carrier concentration due to free carrier absorption for the core region of RC101, RC184 and RC187, at photon wavelengths relevant to quantum sensing applications. The corresponding nominal band gap wavelengths are 873 nm, 730 nm and 715 nm respectively. 42

2.7 Change in refractive index as a function of photon energy for GaAs at a carrier concentration of $N = P = 1 \times 10^{18}$ cm^{-3}, due to the three aforementioned carrier effects, and their summation. The sharp peaks are a caveat of the model and would not be observed experimentally due to the Urbach absorption tail. 43

2.8 Change in refractive index as a function of carrier concentration due to combined band-gap shrinkage and Moss-Burstein effects, at photon wavelengths relevant to quantum sensing applications for the core region of each wafer. In (b) the point at which the band gap shrinkage effects become important is shown in more detail. . 44

2.9 Energy band diagram of the double heterostructure of RC101, with doped capping layers, at (a): equilibrium and (b): 1.2 V forward bias. 47

2.10 Schematic diagram of a cross section of the p-i-n device structure on a semi-insulating (SI) GaAs substrate, illustrating the direction of carrier injection and leakage processes into and out of the intrinsic core of the double heterostructure. The red arrows represent current injection and the blue arrows leakage. 48

2.11 Schematic diagram showing the different leakage processes in the device structure, detailed in the model described by [80]. The solid green arrows represent the injection currents whilst the hollow red arrows represent the leakage currents. 49
2.12 Carrier leakage as a function of the injected current densities for the three wafers, (a): RC101, (b): RC184, (c): RC187. 52
2.13 Schematic diagram depicting the model of current injection into the device and the spreading of carriers due to diffusion, as modelled by [88]. The carrier density is assumed to be uniform over the width of the stripe, which extends from $-S$ to $+S$. Outside the stripe region in the x-direction, the density of carriers decays exponentially. In the z-direction, there is no variation. 54
2.14 Distribution of current in the core in the region underneath the contact stripe (a): ignoring leakage effects and (b): including current leakage. The electrical parameters used in this calculation have been determined from experimental data. The injected current density was assumed to be $J_0 = 3000A/cm^2$. The green dashed lines indicate the positions of the edges of the contact stripe. 56
2.15 Illustration of the planar waveguide formed by epitaxial AlGaAs cladding and core layers, grown on a GaAs substrate, with differing aluminium concentrations, where $y > x$. The doped capping layers have been omitted here for clarity. 57
2.16 Calculation of the effective index of the planar waveguide of RC101 heterostructure layers at $\lambda = 894.5nm$ for the fundamental TE mode by solving the transcendental equation, Equation 2.23. The y-axis (labelled Y), represents the numerical value of the left hand side (red) or right-hand side (blue) of Equation 2.23. 59
2.17 Illustration of the cross section of a strip-loaded waveguide, where W is the width of the waveguide strip and t is the strip height. . . 60
2.18 Theoretical calculation of the normalised frequency for various waveguide widths, as a function of the top cladding etch depth for the RC184 wafer at 780.25 nm. The single mode cut-off value determines the maximum etch depth for single mode operation. . 62

2.19 Illustration of the proposed switch design showing the various epitaxial layers, mesa structure and single mode strip-loaded waveguides. In (a) an isometric representation of a single device is shown, consisting of a steering (active) section and a waveguiding (passive section). In (b), a cross section of the steering section is illustrated. In this section, a bias is applied across the device contacts on both sides, causing carriers to be injected into the core, where the highest density resides directly below the p-contacts. If an equal bias is applied across each side of the mesa (b), the density of carriers either side of the guided wave in the core is approximately equal, resulting in regions of depressed refractive index either side of the guided wave. The guided wave is then confined to the central region. When an unbalanced bias is applied (c), there will be a higher density of carriers on one side of the guided wave, causing the refractive index profile to become unbalanced, resulting in stronger confinement on the side with higher refractive index. The result is beam steering in the direction where the current injection is lowest. The guided beam can then be steered into either waveguide input port, located at the end of the steering region. This forms the switching action. 63

2.20 Illustration of the positioning of the input of the waveguides, delineated at the end of the steering region. The waveguides are offset from the centre of the propagation axis, so some steering is required to couple the beam into either waveguide. 64

2.21 Simulated refractive index profile of the steering region of RC101 due to injection of 50 mA at each p-contact, for the fundamental TE mode at 904 nm. 68

2.22 FFT-BPM simulation of propagation of a 767 nm fundamental TE mode beam through the steering region of a device from the RC187 wafer, due to a current injection of 96 mA and 250 mA at the left and right contacts respectively. (a) shows a plan view of the beam propagation and (b) shows a cross section of the output profile, where the peak is shown to have shifted by 6.2 μm from the centre of the propagation axis. 70

2.23 Calculation (a), and illustration (b) of the method for simulating the portion of optical power coupled into each output waveguide of the device. In (a), RC187 has been simulated for a guided optical wave at 780 nm with a current injection of 60 mA at the left hand-side contact (with respect to the propagation direction), and 160 mA at the right hand-side contact. The portion of the beam coupled into each waveguide has been calculated by integrating across the width of each waveguide and dividing this value by that obtained by integrating across the 24 μm width of the facet (the width of the portion of the facet from the edge of one p-contact to the other). Note that the width of the waveguides here are 6 μm as they are tapered out from the required 2 μm width to increase the coupling efficiency. 71

3.1 Experimentally measured film thicknesses for AZ5214E resist on 15 mm $\times$ 15 mm blank semi-insulating GaAs samples. Samples were spun at the given speed for 30 seconds and then cured on a hotplate at 110 ^{o}C for 90 seconds. Characteristic data provided by the manufacturer is also presented for comparison. The function fitted to both data sets is $f(x) = a/\sqrt{x}$, with R^2 values of 0.96 for the experimental data and 1 for the manufacturer data respectively. Uncertainties on the measured data come from the resolution of the instrument used. 75

3.2 Schematic illustration of the result of a differing UV dose on the final attained photoresist sidewall profile. With a low dose, the UV cannot penetrate through to the substrate-near resist, making these areas more soluble in the developer. When the dose is high, almost all of the polymer chains in the resist film are cross-linked, making the dissolution rate in developer very low, resulting in a less pronounced undercut profile. 76

3.3 Schematic illustration showing an overview of the patterning process using the AZ5214E image reversal resist. Main stages of the process are: Image exposure using a photomask, image reversal bake, flood exposure, and finally development. 77

3.4 Optical microscope images showing the resulting photoresist undercut profiles for (a): waveguide patterning and (b): metal contacts patterning for the lift-off process. Angle of the positive slope, α, is (a): 60^o and (b): 52^o. 79

3.5 Optical microscope images showing the feature resolution limit of (a): the patterning recipe for the metal contacts and (b): the patterning recipe for the waveguides. It is clear that the waveguide patterning recipe in (b) achieves a higher resolution of 2 μm compared to $> 5\mu$m with the contacts recipe. In (a), the aggressive undercut has caused smaller features to de-adhere from the substrate. In (b), only the 2 μm features are shown. 80
3.6 Schematic illustration of current transfer from semiconductor to metal, represented by the arrows. The current chooses the path of least resistance to the contact, resulting crowding near the contact edge. The transfer length, L_T, is defined as the distance at which the current density falls to $1/e$ of its value at the edge. 81
3.7 Schematic illustration of the thermal evaporation process. High purity metal samples are sonicated in isopropyl alcohol and subsequently placed in tungsten boats in the evaporator. The chamber is then pumped down to high vacuum (HV) and the boat is rotated into the contact position using the carousel. Low voltage, high current is then passed through the tungsten boat, heating it above the boiling point of the metal inside the boat, causing it to evaporate onto the sample. A film thickness monitor (FTM) is used to estimate the thickness of the evaporated film during the evaporation. 82
3.8 Schematic illustration of the sample susceptor, used to ensure uniform temperature distribution across the semiconductor sample during the RTA process. 84
3.9 P-type cTLM test structure patterned onto RC184 during the first process step. The cTLM structure consists of a series of circular contacts surrounded by outer metal, separated by various ring shaped gaps. The size of the centre contact remains constant, whilst the size of the gap changes size in each feature. This is a simple structure which can be patterned onto the semiconductor surface with one mask. Radius of the inner metal contact is 130μm. 85
3.10 Fitting of the p-type cTLM data from a sample of RC184. Calculated specific contact resistivity in this case was $\rho_c = 0.56 \pm 0.05 \times 10^{-6}$ Ωcm^2 86
3.11 Schematic illustration showing the configuration of the RIE process and the formation of the ion sheath, leading to anisotropic etching. 88

3.12 Summary of the dry etch processes required to form the device structure. 1) Using the p-contacts as a hard mask to reveal the p-cladding layer in the areas where the p-contacts do not exist. 2) Etching away part of the p-cladding in the waveguiding section to form the waveguides. 3) Etching away layers in the steering section to reveal the n-GaAs layer, onto which the n-contacts are deposited. 89
3.13 Simulated (a) and logged (b) EPD signals for the etching of the entire p-GaAs layer of a RC184 sample. The oscillation amplitudes for the recorded signals are much smaller than the simulated ones since the real EPD laser is attenuated due to absorption and scattering losses. 90
3.14 Simulated (a) and logged (b) EPD signals for the required waveguide etch depth for RC184 91
3.15 Optical microscope images showing (a): an overview of the etched waveguides of several devices from RC187 after the waveguide etch and (b): ×100 magnification showing the tapered outputs of the waveguides. The smooth edges of the waveguides can clearly be seen in (b). The measured width of the centre of the straight waveguide labelled in (a) is 2.0±0.1 μm. 92
3.16 Simulated (a) and logged (b) EPD signals of the mesa etch for RC184. The interfaces between the layers are clear in both cases. 92
3.17 Analysis of RC187-C which was damaged at the n-GaAs reveal etch by micromasking effects. (a): SEM image of a cleaved edge of a window intended for an n-cTLM pad showing the presence of dense micromasking (black regions). (b): Optical microscope image of RC187-C which experienced micromasking effects (black areas) at the n-GaAs reveal etch step. Rounding of the edges of the photoresist due to the physical nature of the etch can also be seen in (a). 94
3.18 Optical microscope image showing the micromasking effects on RC187-GP after the BCl_3 etch to reveal the n-GaAs layer. (a): 1.25x magnification, (b): 100x magnification at the edge of the p-type contacts. 95
3.19 EDX line scan across the etch window of RC184-MF-TRIAL. There is a clear increase in the concentration of Zn across the p-contact and into the etch window. 96
3.20 Optical microscope image showing RC184-AC after the n-GaAs reveal etch, following the HCl dip.(a): ×1.25 magnification, (b): ×100 magnification at the edge of the p-type contacts. 97

3.21 Schematic illustrating the steps required to passivate the device using BCB and for electrical access to the underlying contact pads. Steering region only shown here. 98
3.22 Analysis of the p-type contact window etch into the BCB layer by (a): EDX imaging analysis of the p-type contact window in BCB and (b): AFM imaging of the 3D profile of the p-type window into BCB. EDX was performed by checking the concentration of silicon and carbon across the window, which is only present in the BCB film. The roughness of the trench in the AFM image, coupled with the height data also confirms that the window has been fully opened to the p-type contact. 99
3.23 Optical microscope image at ×10 magnification showing the adhesion of the top-up metal contact pads on a BCB-coated, blank GaAs sample after the tape peel test. There is no visible peeling of the metal film indicating good quality adhesion between the metal and BCB layer. 101
3.24 Optical microscope images showing finished (a): RC184 and (b): RC187 die. The RC184 die is 15 mm × 15 mm and contains 24 complete devices. The RC187 sample is a 15×11 mm^2 die and contains 16 devices. 102
3.25 Optical microscope images showing a RC184 die after lift-off of the evaporated metal film for the top-up metla contacts, (a): before heating on the hotplate at 200^{o}C and (b): after. The bubbles due to possible swelling of the BCB film from the hot DMSO solvent during the lift-off process is clearly visible in (a). 103
3.26 (a): Schematic illustration of the dicing process used to extract a single device from the parent die. (b): Labelled optical microscope image of a finished single device from RC184. 105
3.27 Schematic illustration of the ball-wedge bonding process [114]. . . 106
3.28 Optical microscope image showing a gold wire bonded device. Bonds to the p-contacts have been reworked using silver epoxy to improve the reliability of the bond 108
3.29 Schematic diagram showing the main stages of the entire fabrication process for the optical switching devices. A single device is shown for clarity, however each die contains 24 devices and other various test features. BCB: Benzocyclobutene, ICP: Inductively Coupled Plasma, PCB: Printed Circuit Board. 110

4.1 Plan-view illustration of the assembled test system used to characterise the fabricated devices. The overhead inspection microscope assembly is not included in this illustration for clarity. M: Mirror, AL: Aspheric Lens, PH: Pinhole, PCL: Plano-convex Lens, BD: Beam Dump, TL: Tube Lens, P: Polariser, $\lambda/2$: Half Wave Plate, LED: Light Emitting Diode, CMOS: Complementary Metal Oxide Semiconductor Sensor, BS: Beamsplitter, PCB: Printed Circuit Board, DUT: Device Under Test, PD: Photodetector, MM: Multi-mode, TEC: Thermoelectric Controller. 117
4.2 Schematic illustration of the spatial filter system used to improve the beam quality before coupling into the DUT. 119
4.3 Geometry of the focusing and expansion of the beam within the spatial filter. 121
4.4 Numerical Aperture of DUT and imaging objective. 123
4.5 Picture of the main central optical assembly used to image the input and output facets of a DUT. 124
4.6 Normalised spectrum of the 780 nm laser diode (Thorlabs L780P010) used for testing fabricated devices from the RC184 wafer, electroluminescence spectrum of a RC184 device, and an overlay of the transmission spectrum for the filter (Semrock FF01-792/64-25) used to extinguish the device emissions near the nominal band gap of $\sim$ 730 nm. A pulsed current of 250 mA was passed through one side of the device mesa, with a pulse width of 100 ms to reduce heating effects. 126
4.7 (a): Picture showing the imaging of the facets of a mounted RC187 device. (b): Camera snapshots during imaging of the input (left) and output (right) facets of a RC187 device. The larger field of view on the input facet and the uniform illumination characteristics are apparent. 129
4.8 Illustration of the overhead microscope assembly consisting of an Optem Fusion Optical Vision System and a custom configuration of Thorlabs mechanical mounting hardware. 130
4.9 Overhead (plan view) image of a RC187 device taken with the overhead imaging system. 131

4.10 Diagram showing the interface between electronics components used in the test system. DAC: Digital to Analogue Convertor, DUT: Device Under Test, TEC: Thermoelectric Controller, PC: Personal Computer, LIA: Lock-in Amplifier, DSO: Digital Storage Oscilloscope. The red arrows show interfacing with the PC and green arrows with the Red Pitaya FPGA. 131
4.11 Custom designed analogue voltage level toggle circuit for controlling device current set points. (a): Image of the populated PCB and (b): Corresponding circuit diagram. Circuit designed and fabricated by Mr Andrew Stuart. 133
4.12 Measured signal from one of the two outputs of the custom analogue toggle circuit. In this instance, a 1kHz signal was used with 50% duty cycle. Set points were $V_{low} = 0V$, $V_{high} = 1V$ (a) shows 5ms of the signal and (b) a rising edge. The measured 10-90 rise time of the signal (time taken for the signal to transit from 10% to 90% of the final voltage) is 386.3±0.1 ns. 134
4.13 Schematic diagram showing the interfacing between the Red Pitaya and other electronics. PCB: Printed circuit board, SoC: System on chip, I/O: Input/Output, RF: Radiofrequency, ADC: Analogue to digital converter, TEC: Thermoelectric Controller, DUT: Device under test. 135
4.14 Dark power spectrum of the Thorlabs PDA100A2. 137
4.15 Screenshot showing the GUI of the custom Python program built for controlling the test system. 138
4.16 Example of the results from semi-automated optimisation of the input coupling of light into the DUT. The hot spot in the final scan appears to be at a different piezo voltage to the first. This is due to hysteresis in the position of piezo actuator. The colour map represents the intensity of the light output as measured from the magnitude of the lock-in detection signal in Volts. 141
4.17 Flow diagram showing the conditional steps of the 'smart' z-scan algorithm used to mitigate expansion of the DUT at higher injection currents. 142

5.1 Equivalent circuit of a forward-biased p-i-n diode, where L is the parasitic inductance, R_c is the contact resistance, and R_s the series resistance. 146
5.2 log(I)-V characteristics for a diode with series resistance [97]. . . . 147

5.3 Optical microscope image showing the on-die p-i-n test structures for RC184. 148
5.4 (a): I-V characteristics from RC184-A p-i-n test structure and (b): log(I)-V characteristics of all test devices from RC184 above the threshold voltage. p-i-n structures A-F refer to those shown in the optical microscope image of Figure 5.3. 149
5.5 Identifier labels for each p-i-n diode structure of fabricated devices for RC184 (left) and RC187 (right). 150
5.6 A summary of the calculated ideality factors for RC184 (left) and RC187 (right). 151
5.7 Measured $\log(I)$-V data for diodes from the RC184 die. 152
5.8 Illustration of the extra contact resistance involved with the fabricated devices due to the interface between a thin layer of the top-up metal and the underlying annealed contact metal. 152
5.9 Measured photoluminescence spectrum at two different excitation wavelengths for a sample of RC101 with the top p-GaAs cap removed. Measurements were carried out by Mr James Felton. . . . 155
5.10 Measured photoluminescence spectrum at two different excitation wavelengths for a sample of RC184 with the top p-GaAs cap removed. Measurements carried out by Mr James Felton. 156
5.11 Measured photoluminescence spectrum at two different excitation wavelengths for a sample of RC187 with the top p-GaAs cap removed. Measurements carried out by Mr James Felton. 157
5.12 Photoluminescence spectrum as a function of photon emission energy for 532 nm excitation of (a): RC184 and (b): RC187 wafers. Positions of the phonon replica peaks within the overall spectrum have been estimated by fitting a series of Gaussian functions with fixed width of 50 meV to the spectrum. The insets show the least squares linear fitting of the maximum energy of these peaks as a function of the peak number - $R^2 = 0.996$ and $R^2 = 0.997$ respectively. The extracted slope determines the phonon energy, $\hbar\omega_{LO}$. . 159
5.13 Graphs showing the dependence of the normalised peak intensities, $I(n)$, which make up the PL spectra, as a function of the vibrational level of the excited state, n, for (a): RC184 and (b): RC187 respectively. The Huang-Rhys factors have been determined by fitting Equation 5.3 to the data and determining the factor S. In this case $S = 3.6$ for (a) and $S = 3.9$ for (b) respectively. 161
5.14 Experimental arrangement for characterisation of the electroluminescence emitted from the top of the device. 163

5.15 Electroluminescence spectra from the top of an RC101 device, using square wave current pulses with a width of 1 ms and a repetition rate of 200 ms. 164
5.16 Optical microscope image showing a failed top-up p-contact due to excessive heating from current injection. 165
5.17 Electroluminescence peaks of (a): RC184 and (b): RC187 devices as a function of injection current. Emission peaks determined by curve fitting to spectra, and uncertainties associated with fitting. . 166
5.18 Optical microscope image of the facet of a RC101 device with waveguides removed. Electroluminescence can be seen exiting the facet. A square wave signal was applied to each p-i-n region with a current peak of 150 mA, at 2 kHz with 5% duty cycle. 166
5.19 EL spectrum for a device from the RC101 wafer with the waveguides removed, measured at the facet. Total current injection was 150 mA. 168
5.20 Change in refractive index due to the Moss-Burstein effect for GaAs and $Al_{0.02}Ga_{0.98}As$, at the design wavelength for RC101 of 894.5 nm. 169
5.21 Change in refractive index due to the Moss-Burstein effect for $Al_{0.20}Ga_{0.80}As$ and $Al_{0.22}Ga_{0.78}As$, at the design wavelength for RC184 of 780 nm. 170
5.22 Plan-view (a) and output facet (b) microscope images of light aligned to one of the waveguides during measurement of the propagation loss. 173
5.23 Measured normalised transmitted optical power at the output facet of the RC184 sample, as a function of time whilst radiatively heating the sample from above using a resistive heater. Optical power input into the device was $\sim$300 μW and the collected optical power was $\sim$100 nW. 175
5.24 (a): Schematic representation of the device and (b): Image of the facet of an RC184 device at the end of the taper for the straight waveguide, with 760 nm light coupled into the device and 10 mA through each p-i-n channel. 178

5.25 Interpolated map showing the output intensity at the output facet of the straight waveguide for a device from the RC184 wafer, as a function of the current through each p-i-n region. The wavelength of the light used was 755 nm. The calculated extinction ratio for this device was 18.71±0.03. The extinction ratio is calculated with respect to the measured data. The current through each p-i-n junction was scanned from 5 mA to 115 mA in steps of 5 mA. . . 179
5.26 Microscope image showing the tapered waveguide inputs delineated at the end of the steering region. Each waveguide input is offset by 6μm meaning that a slight current imbalance is required to steer the beam into either channel. The single mode behaviour of the waveguide is clearly apparent here. 180
5.27 Beam propagation simulation showing the effect of a current injection of 115 mA through both p-i-n channels for RC101 at 904 nm. 181
5.28 Images of the output facet of an RC101 device with the waveguides removed and 904 nm light coupled in, with (a): electrical signals off and (b): 10 mA, 2kHz square wave with 5% duty cycle through each p-i-n section. A band-pass filter (Semrock FF01-900/32-25) was used to remove electroluminescence produced by the device from the current injection. When light is coupled in and the device is off, i.e. no current through either p-i-n section, weakly guided light is observed at the output facet which has reflected off the sidewalls of the device, causing an interference pattern. When the device is off, there is very little confinement of the guided wave in the direction perpendicular to propagation, so the beam is free to spread out in the core until it reaches the sidewall. When the device is switched on with a small amount of current (10 mA passing through each p-i-n section) we immediately observe the brightness of the output increase due to the stronger confinement caused by carrier injection. 182
5.29 Schematic illustration of the model used by [144] for the calculation of the current crowding effects in a mesa geometry, double heterostructure (DH) device on a semi insulating substrate. The arrows show the direction of the current path. The thickness of the p-GaAs layer is given by t_p and the n-GaAs layer by t_n. The width of the simulated region is given by w. 184

5.30 Current density as a function of the lateral distance across the mesa for parameter from the RC101 wafer, with 10 mA applied though each p-contact. The point 0 μm marks the centre point of the mesa and the left and right hand edges are located at -20 μm and 20 μm respectively. 186
5.31 Updated beam propagation simulation of a 904 nm, fundamental TE mode through the steering section of an RC101 device, with 115 mA applied through each contact, as a result of current crowding due to the mesa geometry. 187
5.32 Graphs showing the measured (a): rise time of a switch on sequence, and (b): fall time of a switch off sequence, using 904 nm lgiht coupled into a fabricated device from RC101. The measured rise time is 670±5 ns, and the measured fall time is 675± 5 ns respectively. 189

6.1 Schematic illustration of the p-dopant diffusion in a n-i-n double heterostructure device. 200
6.2 Schematic illustration showing the proposed epitaxial design for inclusion of an oxide aperture to limit carrier spreading effects. . . 202
6.3 Schematic illustration demonstrating the original and new proposed design for larger p-contacts, which would facilitate direct ball bonding. 203
6.4 Schematic illustration of a proposed inner packaging design for the fabricated optical switches. AlN: aluminium nitride 204
6.5 Simulation of the effective indices of the slab of the steering region and the strip-loaded waveguides of the waveguiding section, as a function of the core thickness for an optical wavelength of 780 nm and parameters shown in Table 6.1 206
6.6 Simulation of the concentration of carriers in the core region of the new epitaxial design, as a function of the lateral distance across the layer, for a current injection of 100 mA through each contact. 207
6.7 Simulation of the change in refractive index as a function of carrier concentration for the new epitaxial design at 780 nm, and a comparison with the original RC184 design. 208

Chapter 1

Introduction

Wave-particle duality [1] underpins the behaviour of atomic matter displaying wave-like phenomena, opening up the possibility of performing atom interferometry experiments. Atom interferometry has proven to be a powerful method of precision inertial sensing [2]. In particular, the cold-atom gravimeter has demonstrated itself to be a useful tool in obtaining one of the most precise values of local gravity of $\delta g/g = 10^{-9}$ [3], boasting long-term stability, and high accuracy. These advantages stem from the ability to control the environment of the cooled and trapped atomic samples under vacuum. The promising performance of these atom interferometers offer themselves to applications in many areas of modern physics and engineering, such as tests for the equivalence principle [4], determination of fundamental constants such as the fine structure constant, α [5] and Newton's gravitational constant, G [6], geosurveys and proposals for gravitational wave detection [7].

In recent years, there has been an enhanced drive to push these mainly laboratory-based systems towards more compact, low power, and portable equivalents [8]. One example is the European iSense project [9] which used a cold atom gravimeter as a demonstrator and featured a micro-integrated laser system, fibre optical delivery system, compact vacuum system and atom chip assembly, all integrated in a transportable package weighing around 63 kg [10]. The motivation for pushing forward the compactness and portability of these gravimeter systems stems from

the fact that portable gravity measurements are of prime importance to many modern, real-world problem scenarios - from mapping gravity variations on the kilometre scale to observe ice sheet thickness, for monitoring the effect of global warming [11], to smaller scale, higher precision ground-based measurements for locating buried objects or voids. The current highest precision, commercially available system for non-relative gravity measurements, the Micro-G LaCoste FG5 Absolute Gravimeter, is based on the free-falling corner cube scheme [12], which uses a classical laser interferometer to monitor the motion of a freely falling corner-cube retroreflector in a vacuum. This system can achieve a precision of $\delta g/g = 10^{-9}$, however this requires stringent requirements on material and manufacturing tolerances due to vibration-induced inaccuracies, and mechanical wear and tear resulting in reduced long term stability [13]. Furthermore, the FG5 has a limited operating temperature of 20-30 ^{o}C and weighs 150 kg. These impracticalities of the classical system make them less useful for geophysical applications, where high repetition rate, continuous measurements are required. Conversely, atom gravimeters offer the possibility of performing continuous measurements over a prolonged period of time [14], without any drift in measurement accuracy due to mechanical wear, and furthermore match or better the sensitivity of their classical counterparts. These advantages, coupled with the current drive for miniaturisation of their enabling technologies, make these systems an attractive platform for current research and commercial investment. Since these sensors rely heavily on carefully tuned and timed laser pulses, reliable optical subsystems are required to deliver and manipulate such pulses. Further development of these sensors into a fully integrated package thus requires the optimisation of size, weight and power (SWaP), through miniaturisation of such optical subsystems into a single, compact and robust package.

1.0.1 Integrated Photonics for Quantum Sensing

Over the past few decades, integrated photonic devices have emerged as a major commercial nanotechnology as a result of the proliferation of high speed networks and their requirements of high performance, integrated optical transmission and manipulation components [15]. Photonic networks used in data communications cover a wide range of operating wavelengths in the mid and near infrared (NIR) spectrum as well as in the visible and ultraviolet (UV) region. Such components are thus perfectly suited to be adapted to replace bulk optical subsystems, such as optical waveguides and switching devices in emerging quantum technologies. Optical switches used for directing an optical signal into one channel or another in response to a electrical control signal are of paramount importance in optical communications, and indeed other technologies which constitute the manipulation of an optical signal [16]. In particular, optical switching devices based on refractive index (RI) change effects have been realised via manipulation of various mechanisms, such as acousto-optic, electro-optic, magneto-optic, thermo-optic and electro-absorption (EA) effects [17]. Those based on III-V semiconductor material systems offer an attractive platform for optical switches operating in the near-infrared/visible spectrum as they allow for integration with other optical components [18]. In particular, these materials enable alternative switching mechanisms such as that of the carrier-induced refractive index change effect, which allows enhanced signal channelling by tailoring the refractive index profile of the material to guide light into the desired position via control of a small electrical signal [19].

In this thesis, the design, fabrication and testing of semiconductor integrated optical switches for functionality in three near infrared wavelength ranges for use in quantum sensors is detailed. These switches make use of the aforementioned carrier-induced refractive index change effects in their operation. In this chapter, the intended application for the switches and their technical requirements are discussed, before reviewing the performance, reliability and convenience of current

off-the-shelf commercial technologies widely used for this application. In Chapter 2, the optical switch design is presented, along with a detailed discussion of the operating principles and the formation of a computational model used to simulate their intended operation. Chapter 3 details the fabrication steps and complexities involved in producing these devices. In Chapter 4, the design and construction of an optical test bench, software, and associated semi-automated testing routines used to characterise the devices are presented, followed by characterisation of the devices using this setup in Chapter 5. Finally, Chapter 6 summarises the project findings and their implications along with suggested future improvements, and an outlook on the recent and future trends for related work.

1.1 Atom Interferometry for Quantum Sensing

It is important to understand the specific use case of the optical switches, so that their role may be appreciated. Therefore, this section begins with a description of a quantum gas which subsequently leads onto the description of an atom interferometer and how one can be experimentally realised. Finally, a discussion is presented on how these switches may be incorporated into such an atom-interferometer type system.

1.1.1 Ultracold Quantum Gases

When a bosonic gas reaches a critical temperature, statistical mechanics determines that the system undergoes a phase transition and all particles avalanche into their ground states. This is known as Bose-Einstein condensation (BEC). The theoretical treatment of BECs apply almost exactly to dilute vapours of alkali atoms and thus is highly relevant to the description of a quantum sensor based on quantum gases of these alkali atoms. Quantum statistical effects become relevant when the occupation of quantum states approaches unity, which is true when the gas makes this phase transition. It can be shown [20] that quantum

effects arise when the number density, $n = N/V$ where N is the number density of atoms and V is the occupied volume, reaches the value,

$$n = \frac{2.6}{\lambda_{dB}^3}, \tag{1.1}$$

where λ_{dB} is the thermal de Broglie wavelength, defined as,

$$\lambda_{dB} = \frac{h}{\sqrt{2\pi m k_B T}}, \tag{1.2}$$

where m is the mass of the atoms and T the absolute temperature. The de Broglie wavelength gives a measure of the delocalisation of the gas. Quantum effects become important when λ_{dB} becomes equal to the spacing between the atoms, so that the individual particles can no longer be distinguished. Equations 1.1 and 1.2, along with consideration of the Bose-Einstein distribution function and integration over the density of states, predicts that the critical temperature at which the transition to a quantum gas occurs for trapped alkali vapours is typically on the order of a few micro Kelvin. A detailed description of this theory and the relevant calculations of the critical temperature can be found in [20].

Once the gas of trapped alkali atoms has been cooled below its critical temperature to form a BEC, some striking properties are observed, namely superfluidity and coherence. These phenomena are related to the mircroscopic description of the condensate of N atoms sharing the same quantum mechanical wavefunction. Coherence is the property of the BEC exploited in atom interferometry - the entire condensate can be treated as a single matter wave, enabling interference effects and subsequently opening up the possibility of performing experiments analogous to those performed with light waves.

1.1.2 Atom Interferometry

A common measurement scheme for an atom interferometer involves the interference of matter waves produced by ensembles of laser-cooled rubidium-87 atoms,

in a Mach-Zehnder interferometer configuration [21]. Since these measurements require light-atom interactions and evolutions which take place over hundreds of milliseconds, the sensitivity of these schemes dramatically increases with longer interaction times. Assuming a Maxwell-Boltzmann distribution, the 1D root-mean-square velocity of an individual atom in a gas, v_{rms} is related to its temperature, T,

$$v_{rms} = \sqrt{\frac{k_B T}{m}}, \tag{1.3}$$

where k_B is the Boltzmann constant and m is the mass of the atom. Lowering the temperature of the atoms thus reduces their velocity, subsequently facilitating longer interaction times. Furthermore, collisions between atoms are more frequent at higher temperatures. These collisions collapse the aforementioned quantum state necessary for the interferometry sequence, rendering the measurement impossible. Thus, for the atomic vapour to firstly exhibit quantum coherence effects and for the interaction times of light with the vapour to be sufficient, the first stage in this measurement process requires the trapping and cooling of the atoms, which is achieved using a magneto-optical trap (MOT) [22].

1.1.3 Magneto-Optical Trap

As per its name, the MOT has two components - optical molasses, consisting of counter-propagating laser beams, used to cool the atoms, and a quadropole magnetic field used to help capture atoms with a wider velocity range [23]. Laser cooling relies on the cycling transition of a two-level atom, i.e. an atom which has two energy levels that can be addressed by absorption and emission of a photon. For ^{87}Rb, the so-called D_2 transition is used ($5^2S_{1/2} \Rightarrow 5^2P_{3/2}$) at $\approx$ 780.24 nm, as illustrated in Figure 1.1. This will be used as the demonstrative example here, but the same principles apply to other alkali atoms used for quantum sensing, such as the caesium-133 D1 transition at 894.5 nm and the potassium-39 D1 transition at 766.7 nm.

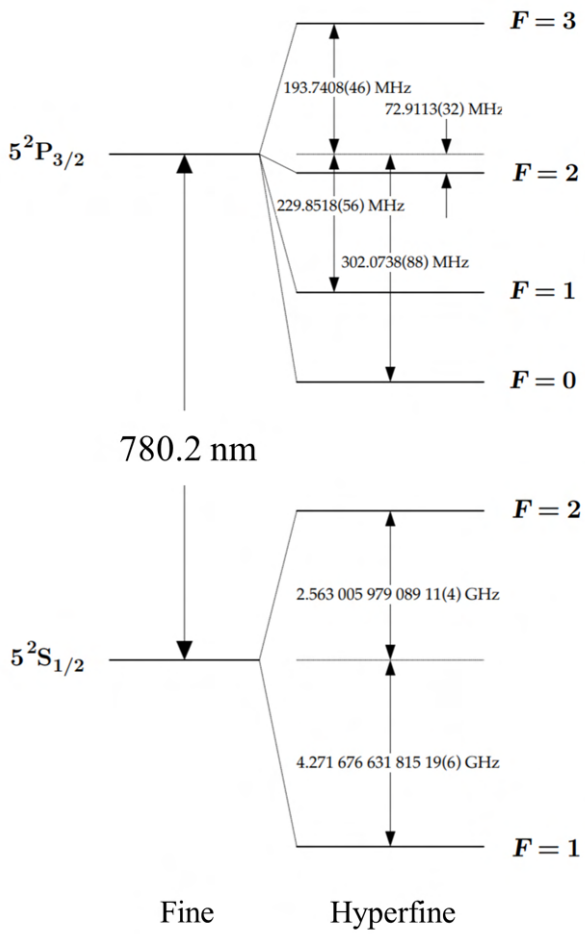


Figure 1.1: *Hyperfine structure of the ^{87}Rb D2 transition. Excited state frequencies from [24] and ground state frequencies from [25]. The quantum number, F, refers to the total atomic angular momentum.*

With each photon absorption, the atom recoils with an impulse equal to $\Delta\mathbf{p} = m\mathbf{v}_{\text{recoil}} = \hbar\mathbf{k}$, where m is the atomic mass, $\mathbf{v}_{\text{recoil}}$ is the recoil velocity and $\mathbf{k} = (2\pi/\lambda)\hat{\mathbf{k}}$, where λ is the photon wavelength and $\hat{\mathbf{k}}$ is the unit vector in the direction of propagation of the photon. The atom returns to the ground state by spontaneous emission of a photon. The time-averaged impulse due to this spontaneous emission is zero due to its random and symmetric nature [26]. The optical molasses exploit the Doppler effect in counter-propagating beams, in which the moving atoms experience a shifted frequency of light, depending on their velocity. These beams are set to a frequency lower than the frequency of transition (red-detuned). Subsequently, atoms travelling towards the beam experience a frequency shifted back up towards the transition frequency, and a

photon is absorbed, imparting its momentum to the atom. The cyclic nature of this transition causes the process to repeat, eventually leading to a significantly reduced velocity in the axis of the laser beam, and thus a reduced temperature of the gas. This scheme can be extended into three dimensions, with opposing light fields in three orthogonal axes [27]. Since the energy levels of the atom have a Lorentzian lineshape, rather than a δ-function, the frequency of the laser only needs to be near resonance to induce a transition. This relaxes the requirement on the linewidth of the laser. For example, for the cooling transition in ^{87}Rb, the linewidth is $\Gamma = 2\pi \times 6.066$ MHz. This highlights the need for optical sub systems which work efficiently at and around the centre of these aforementioned transition wavelengths.

The proportion of atoms cooled using the optical molasses is limited to those with low velocity and near resonance. Additionally, the molasses do not provide any spatial confinement of the atoms. To enhance cooling and ensure trapping of the atoms, a quadrupole magnetic field is used in addition to the optical field to form the MOT [28]. The quadropole field has a well defined magnetic flux zero point at its centre, with the flux increasing linearly in each axis. Due to the Zeeman effect, this spatially-dependent magnetic field consequently causes a position-dependent energy shift of the hyperfine sublevels, given by,

$$\Delta E_{|F,m_F\rangle} = \mu_B g_F m_F B_{x,y,z}, \tag{1.4}$$

where $\mu_B = e\hbar/2m_e$ is the Bohr magneton with e the electronic charge and m_e the electron rest mass, g_F is the Landé g-factor for the hyperfine transition, $B_{x,y,z}$ is the magnetic flux density in x, y, z and m_F, the magnetic quantum number which is the projection of the total atomic angular momentum, F, onto the axis of the magnetic field. The magnetic quantum number takes values $-F \leq m_F \leq F$ in integer steps.

The polarisation of light plays a significant role in the MOT. Conservation of angular momentum after emission and absorption processes leads to strict atomic

selection rules which determine the allowed spectroscopic transitions. These selection rules, along with the spatially-dependent magnetic field, are exploited in the MOT to produce spatial confinement of the atoms. In this situation, the counter-propagating beams are circularly polarised and are tuned just below the atomic resonance. The principle idea is based on the Zeeman shift causing an imbalance in the radiation force - an atom displaced from the centre of the trap in the positive z direction causes the $\Delta m_F = -1$ transition to move closer to resonance with the red-detuned laser. The selection rules lead to absorption of a photon which excited the σ^- transition[1] which in turn causes a scattering force, pushing the atom towards the centre of the trap. This is also true in the opposite case (for $z < 0$) [20]. These points are illustrated in Figure 1.2 for the simplified case of a $F = 0 \Rightarrow F' = 1$ transition.

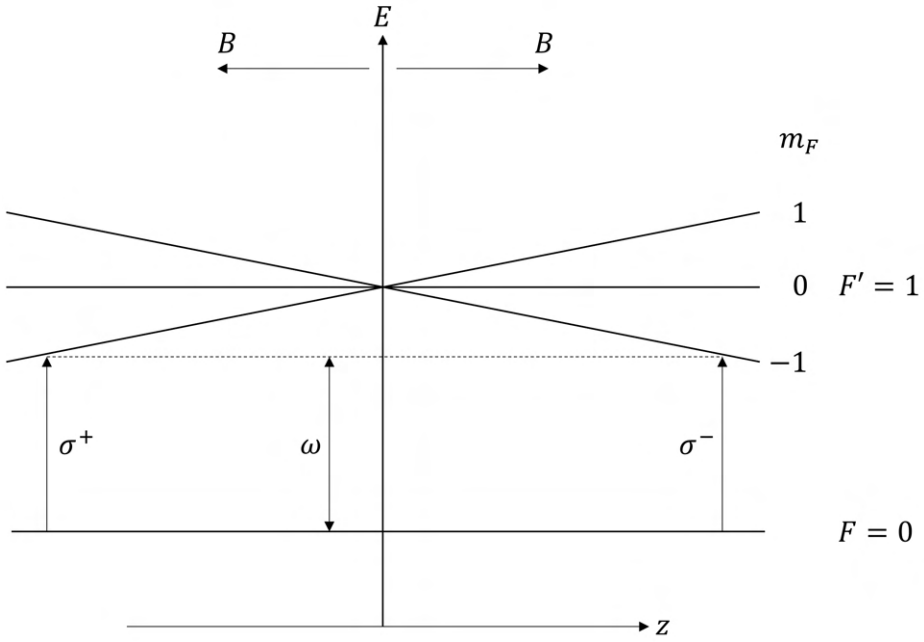


Figure 1.2: *Principle of the magneto-optical trap for the case of a $F = 0 \Rightarrow F' = 1$ transition [20]. Atomic selection rules for the absorption of circularly polarised light between magnetic sub-levels leads to an imbalance of radiative forces from the laser beams which acts to push the atoms towards the centre of the trap.*

[1] In this convention, the polarisation states are defined by considering the sense of the rotation of the electric field around the quantisation axis, rather than the direction of propagation of the laser beam

1.1.4 The Interferometry Sequence

Once the atoms have been sufficiently trapped and cooled using the MOT, it is then possible to form an atom interferometer by manipulating their wave-like nature. Common configurations of atom inteferometers resemble a classical Mach-Zehnder interferometer (MZI), in which light is split into two separate paths using a beamsplitter plate/cube, as depicted in Figure 1.3. After some propagation distance, the two beams are redirected towards each other using mirrors and recombined using another beamsplitter. By measuring the output power of this recombined beam, the phase shift between the two beams due to the path difference experienced during propagation may be measured.

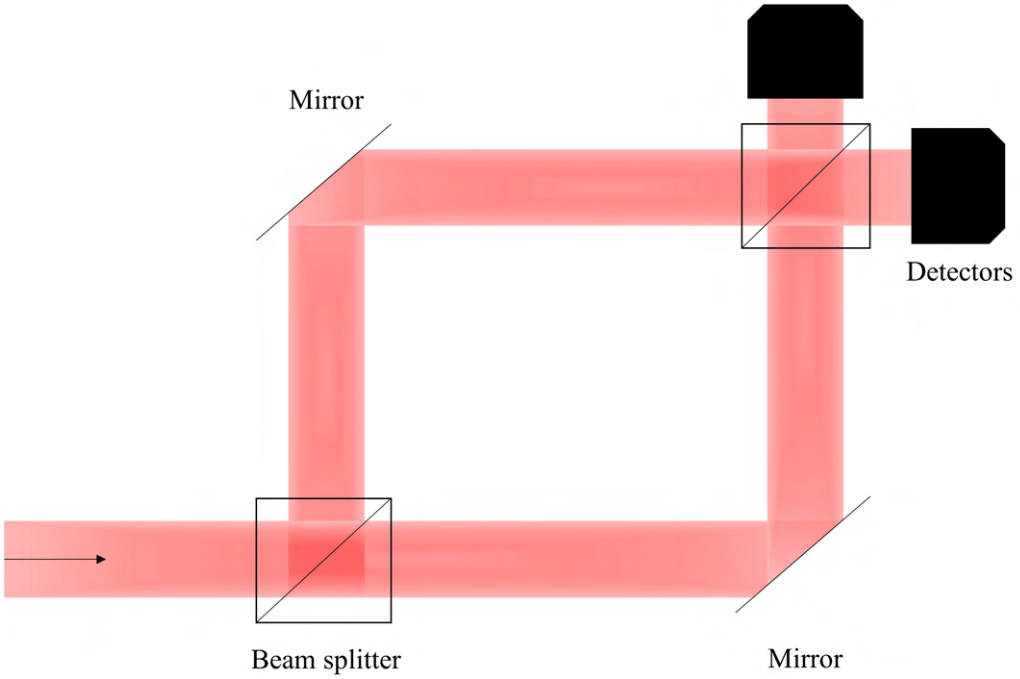


Figure 1.3: *Configuration of a classical Mach-Zehnder Interferometer. Light is split along two paths by a beam splitter before being reflected by mirrors and recombined using another beamsplitter. Interference fringes are detected from the combined beam and the path difference between the two beams may be inferred from the phase shift.*

Since atom interferometry is based around the probabilistic nature of atomic transitions, light is used to manipulate matter waves, akin to the mirror and beamsplitter in a classical MZI. The principle of conservation of momentum, upon interaction of the atoms with an electromagnetic field, is used to form an interferometry sequence. When this field interacts with an atom, the populations

in the ground and excited states are coherently driven in an oscillatory fashion, known as Rabi oscillations. Tuned laser pulses of specific time lengths are applied to the cooled atomic cloud. Starting with the undisturbed atoms in their ground states, the first pulse is applied and stopped after a $\pi/2$ evolution of the Rabi oscillation, causing the atoms to reside in an equal-probability superposition of the ground and excited states. This $\pi/2$-pulse is akin to a classical beam splitter. Due to conservation of momentum, this pulse also creates a superposition of momentum states, causing the excited state wavepacket to separate from the ground state. After some time τ, the two wavepackets will have separated by some distance $\hbar k\tau/m$, where $\hbar$ is the scaled Planck constant, k is the wavenumber and m is the mass of the cloud. Subsequently, a π-pulse is used to invert the populations and redirect the wavepackets towards each other, acing like a classical mirror. Finally, after some more time, τ another $\pi/2$-pulse is used to recombine the wavepackets causing them to interfere. This interference can be detected, for example, by measuring the population of the atoms in the excited state. At each stage in this sequence, a phase is imprinted on the atoms since they are moving with respect to the light field. If the z-axis of the system is aligned vertically to the surface of the Earth as illustrated in Figure 1.4, gravity causes the wavepackets to gain an additional phase which is different for each path, leading to a total phase accumulation due to both the laser pulses and gravity [10], given by,

$$\phi = k_{\text{eff}} g T^2 - \phi_L, \tag{1.5}$$

where k_{eff} is the effective wavenumber of the light field, g is the acceleration due to gravity, T is the total interferometer time and ϕ_L is the phase imprinted by the laser. By varying the phase of the final pulse due to the laser, the phase due to gravity can be exactly cancelled, at which point all atoms are in the ground state and $\phi_L = k_{\text{eff}} g T^2$, giving a very precise value for g.

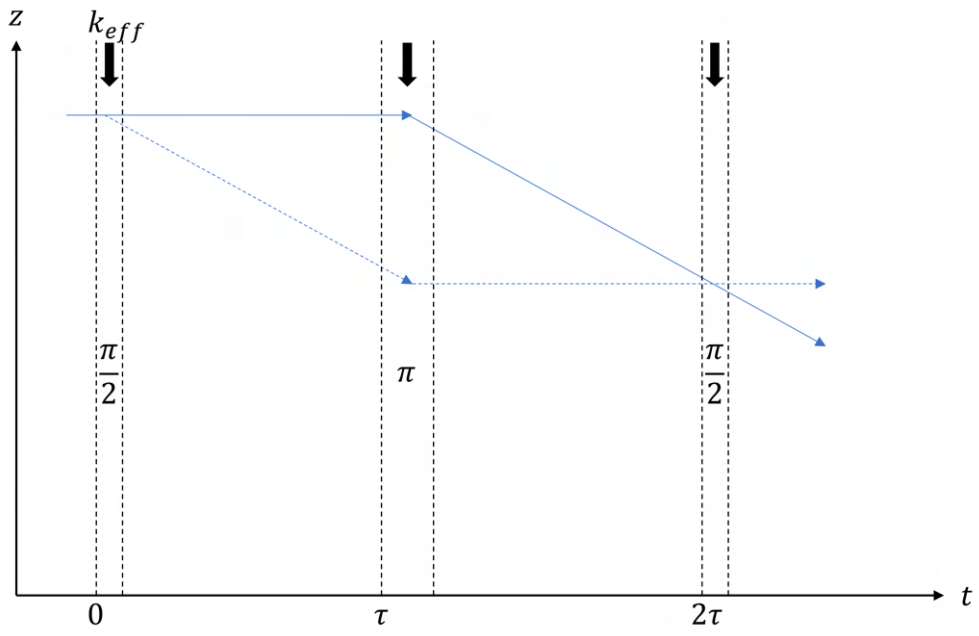


Figure 1.4: *Schematic diagram illustrating the process of a three pulse atom interferometer as detailed by Kasevich and Chu [29]. The first pulse induces a superposition of ground and excited states, giving a momentum kick to the excited state causing it to separate from the ground state. The second pulse inverts the population causing the wavepackets to move towards each other. The final pulse recombines the wavepackets causing them to interfere. In the presence of gravity, the depicted straight paths become parabolic. Diagram adapted from [10].*

1.1.5 Experimental Realisation

As we have seen, the properties of the interacting light beams in the context of a quantum sensing experiment involving the spectroscopy of alkali atoms are paramount for achieving precise measurements. Given the typical aforementioned measurement scheme for a quantum gravimeter, two different types of optical switching are required for experimental realisation - fast switching ($\sim \mu$s), which is used for state preparation and the interferometry sequence, and high extinction ratio switching, used to ensure that the light from the MOT is not present during the formation of the interferometer, which would degrade the final signal.

Typically, acousto-optical modulators (AOMs) are used for the fast switching and a combination of AOMs and mechanical beam shutters for the high extinction switching. AOMs can provide the fast switching speeds required, with most commercial devices capable of consistent switching speeds on the order of hundreds of nanoseconds or better. Typically, AOMs are used in a free-space configuration.

Application of a radio frequency (RF) signal to the AOM causes a beam travelling through the crystal to diffract into multiple orders. Use of the AOM as a switch then requires careful alignment of the beam and isolation of the first order mode. When the RF signal is switched off, the first order mode is consequently switched off. The speed of this switching depends on the transit time of the RF signal across the light beam (more detail given in Section 1.2.2). Although the free-space AOM can achieve very fast switching times, the tight alignment tolerances required in a free-space AOM setup mean that it is challenging to achieve high extinction between the 'ON' and 'OFF' state without significant spacing between the optical components. This issue can be overcome by using a fibre-coupled AOM, which adds more stability to the system and allows optical extinction of around 50 dB [10]. However, optical fibres are fragile components which need to be shielded from mechanical vibrations to ensure optical power stability and furthermore can suffer from large insertion and propagation losses when using polarisation maintaining, single mode fibres, as is common with cold-atom based experiments. Furthermore, these devices rely on high power, high frequency ($\sim$1 W, $\sim$100 MHz) signals to operate, requiring additional components adding to the bulk of the system.

Fibre-coupled mechanical shutters offer very high extinction and are available in the form of low power, integrated compact packages. Fibre-coupled mechanical switches usually consist of an internal prism or mirror which is physically moved during operation to direct light into an output fibre. This allows a very high extinction ratio between 'ON' and 'OFF' states of around 80 dB. However, due to their mechanical nature, they do not offer sufficient switching speeds for the interferometry sequences and furthermore can suffer from unwanted vibration-induced effects, such as switch 'bouncing', during the actuation of their mechanism [10]. A combination of fibre AOMs and mechanical switches is therefore required to achieve meet the sufficient requirements for the cold-atom gravimeter. The AOM is first used to extinguish most of the MOT beams in a short time, and the

mechanical switch is then used to enhance the extinction. Another AOM can then be used to perform the short microsecond pulses used for the interferometry phase.

These considerations enhance the requirement for reliable and robust integrated optical subsystems, which match or surpass the performance of the technologies currently in use. To be a feasible replacement for the AOM and fibre switches, the proposed optical switch therefore must be capable of switching the desired wavelength of light to the 'OFF' state on the order of microseconds, and holding it in this position. This must be achieved with an extinction between'ON' and 'OFF' states of at least 80 dB.

1.2 Existing Switching Technologies

Before describing the details of the switching devices developed in this research, it is important to consider some common existing commercial optical switching technologies and their corresponding relevance to their use in quantum sensing experiments. This will give a basis for the requirements and specification of the optical switches designed and fabricated in this study.

1.2.1 Performance Indicators

When designing or evaluating the performance of any photonic switching device, it is important to consider the requirements of the application and evaluate the performance of the device according to given operating characteristics. This section gives an overview of some of the most important indicators used to evaluate the performance of optical switching devices.

Extinction Ratio

A key performance parameter for both modulators and switches is the extinction ratio (ER). In the case of high-speed digital transceivers, the extinction ratio is

used to describe the optimal biasing conditions required for phase or amplitude modulation. For an optical switch, the extinction ratio describes how well the device can extinguish the light from an output port in the 'ON' state compared to the 'OFF' state. The extinction ratio can be quantitatively evaluated by simply considering the ratio of optical power in the 'ON' P_{ON} to the 'OFF' state P_{OFF},

$$ER(dB) = 10 \log_{10} \left(\frac{P_{ON}}{P_{OFF}} \right). \tag{1.6}$$

Switching & Modulation

It is of paramount importance to distinguish between modulating and switching structures. In some instances, such as in telecommunications, it is sufficient to simply reduce the intensity, or change the phase of a signal to transmit data. In such cases, the action of the modulation device is loosely said to be 'switching' the signal on/off however, strictly speaking, a modulator is not a switch. The function of an optical switch is to reroute or completely extinguish an incoming optical signal and thus can feature one or more input/output ports, whereas a modulator only ever has one input and one output. Figures of merit for modulators and switches, such as switching speed, insertion loss (IL) and cross talk (CT) often have some overlap, however these can help distinguish between the two as more emphasis is given on some parameters for switching structures. For a modulator, the speed is often an important parameter as this is what defines the data transmission rates, with modern commercial devices offering modulation rates in excess of 100 gigabauds per second (Gb/s) range. Typical extinction ratios for these high speed modulators are $\sim$20 dB. Conversely, in the case of integrated optical switching arrays, a slower switching speed may be acceptable, as the emphasis is on rerouting a signal and holding the switch in this state, rather than continuously switching the signal on/off. In such devices, extinction ratios are commonly $>$ 30 dB.

Insertion Loss

When light is coupled into a PIC, it will suffer attenuation introduced by various mechanisms such as reflection at the input facet and scattering/absorption during propagation. Insertion loss (IL) is a direct measure of this attenuation and is a particularly important parameter to consider when designing optical switching arrays or singlets as the desire is to retain as much of the original beam intensity as possible. Optical IL is usually stated in decibels (dB), and is defined by,

$$IL(dB) = 10\log_{10}\left(\frac{I_{\text{in}}}{I_{\text{out}}}\right), \tag{1.7}$$

where I_{in} is the intensity of the input beam and I_{out} is the intensity of the output beam. A lower insertion loss thus indicates a better designed PIC as this decreases the need for higher optical power sources at the input and/or amplifiers, and directly determines how many photonic components and optical paths the optical signal can support without the need for further amplification. An abundance of methods for reducing insertion loss exist. One such established method is that of the tapered waveguide, used to match optical modes, for example between an optical fibre and a GaAs/AlGaAs rib waveguide [30].

Rise Time

In electronics, the rise or fall time, τ_r or τ_f is often used to characterise the response of the rising or falling edge of a signal to change from some fraction $x\%$ to another fraction $y\%$ of a final value [31]. Ideally, this would happen instantaneously but in reality there are delays and aberrations associated with such a response which can be due to the intrinsic nature of a semiconductor component or circuit board layout. The intrinsic and parasitic resistance, R, and capacitance, C of the circuit results in a characteristic time constant, $\tau = RC$. Due to these aberrations which may occur at the extremities of the signal, such as overshoot or undershoot, the rise time is often defined as the time taken for the rising edge of a signal to transit from 10% to 90% of its final stabilised value,

and vice versa in the case of measuring the fall time of a negative slope. This is illustrated in Figure 1.5. In the case of an optical switch, this would ascertain to the time taken for the detected optical signal to transit from 10% to 90% of its final optical power level. In this case, the response of the equipment must be faster than the response of the optical switch to sufficiently measure the response limit of the switch.

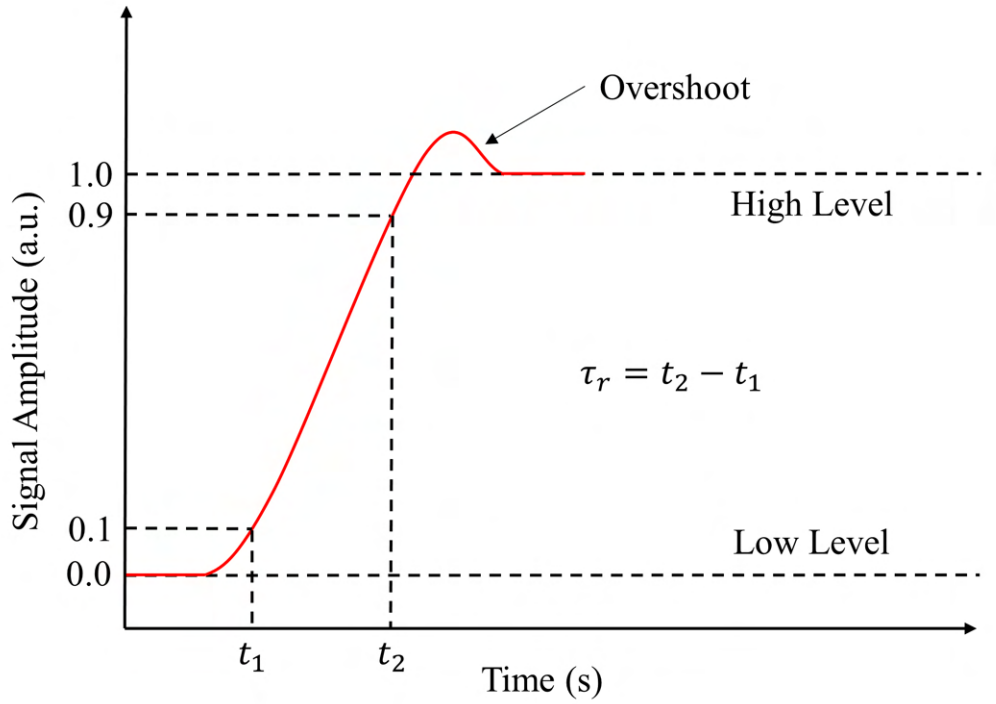


Figure 1.5: *Definition of the rise time, τ_r, of a signal is the time taken for the rising edge of a signal to transit from 10% to 90% of its final value.*

Crosstalk

Crosstalk, or channel interference, between adjacent optical waveguides describes the phenomena whereby guided optical signals in one waveguide structure leak into an adjacent by coupling of the evanescent tails of the optical mode. This becomes an issue in photonic integrated circuits (PICs) where the packing density of optical waveguides on a single chip is of paramount importance, and many methods have been devised to solve this issue, including the integration of non-uniform sub-wavelength strips on the PIC [32]. If the distance between adjacent waveguides is too small then optical crosstalk increases, degrading the signal to

noise ratio at a given waveguide output. The cross-talk between two waveguides can simply be evaluated by considering the ratio of the original intensity of light from a waveguide, I_1, to the intensity unintentionally coupled into the adjacent waveguide, I_2,

$$\text{Crosstalk}(dB) = 10\log_{10}\left(\frac{I_2}{I_1}\right). \tag{1.8}$$

1.2.2 Acousto-optical Modulator

Acousto-optical modulators (AOMs) have a wide range of uses in laser-based experiments. Primarily, they are used as optical switches, frequency shifters, and beam deflectors. All types of acousto-optical modulators are based on the same underlying physical principles, namely the use of the acousto-optical effect to produce a desired grating pattern in the refractive index profile of a given material. In the acousto-optical (AO) effect, a mechanical strain in a solid causes a change in the refractive index of the material which subsequently affects the phase of an optical wave travelling through the strained medium. This is known as the photo-elastic effect and is characterised by a fourth-rank tensor called the photoelastic tensor. The mechanical strain in the material is induced by passage of an acoustic wave, by application of a high power (∼1W) RF signal. It has been shown [33] that the change in refractive index is related to the power of the acoustic wave by,

$$\Delta n = \sqrt{\frac{n^6 p^2 (10^7) P_a}{2\rho v_a^3 A}}, \tag{1.9}$$

where n is the refractive index of the relaxed material, p is an element of the photoelastic tensor, P_a is the acoustic power, ρ is the mass density of the material, v_a is the acoustic velocity and A is the cross-sectional interaction area of the acoustic wave through the material. In the typical crystalline solid materials used for AOMs, such as quartz or tellurium dioxide (TeO_2), the refractive index change due to the stress caused by the travelling acoustic wave is on the order of

10^{-4}. Despite this small change, the diffraction effects experienced by an optical wave are significant, due to the accumulation of optical interactions resulting from the Δn produced by peaks in the acoustic wave, spread throughout the material. Figure 1.6 shows a schematic illustration of a Bragg type AOM, which are typically used in quantum sensing experiments.

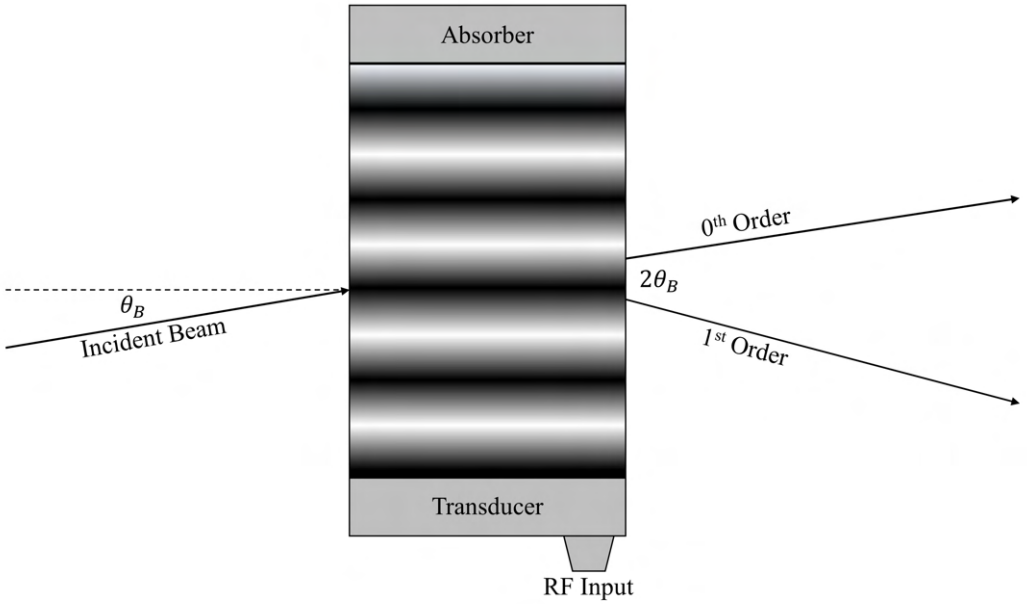


Figure 1.6: *Typical structure of a Bragg type modulator. The absorber is shaped to ensure secondary reflections of acoustic waves do not re-enter the crystal.*

In a Bragg-type device, an RF signal along with impedance matching electronics, is used to drive a piezo-electric transducer which in turn creates regions of compression and rarefaction within the material structure causing the aforementioned refractive index modulation. An optical wave then incident on the vibrating crystal diffracts into two orders. In this case, the interaction length between the optical and acoustic waves must be sufficiently long such that these multiple diffraction orders can occur [34]. Namely,

$$l \gg \frac{\Lambda^2}{\lambda_0}, \tag{1.10}$$

where l is the interaction length, Λ is the acoustic wavelength, and λ_0 is the optical wavelength. To ensure maximum diffraction efficiency the optical beam

input angle must be equal to the Bragg angle, θ_B,

$$\theta_B \approx \frac{\lambda_0 f}{2v_a}, \tag{1.11}$$

where f is the acoustic frequency and v_a is the acoustic velocity. The small angle approximation of $\sin(\theta)$ has been used here since the diffraction angles are on the order of milliradians (mrad). The diffracted beam then emerges from the device with an angle equal to $2\theta_B$ with respect to the undiffracted (0^{th} order) beam. Considering that the output beam of the AO device exists at a differing angle to the input beam, the AOM is thus inherently capable of acting as an optical switch. For example, if the frequency of the RF signal is held constant, the beam can be deflected through the angle $2\theta_B$ by supplying sufficient RF power i.e the 'on' state of the switch. To change the state of the switch to 'off', the RF power is simply reduced to zero. Using this scheme, by applying a digital (square wave) modulation to the RF signal, the AOM acts as a switch between the 0^{th} and 1^{st} orders of diffraction. Beam apertures can then be used to isolate the two beams.

The optical switching speed of an AOM is determined by the transit time of the acoustic wave across the waist of the optical beam in the crystal as depicted in Figure 1.7. The parameter of consideration here is the aforementioned optical rise time, determined by the transit time of the acoustic wave across the optical beam,

$$t = \frac{d}{v}, \tag{1.12}$$

where d is the $1/e^2$ Gaussian beam diameter and v is the acoustic velocity.
Since the optical rise time depends on $1/e^2$ diameter of the beam, reducing the beam size by increasing the focus of the beam will subsequently increase the switching speed. However, as the beam is focused to a tighter spot, the efficiency of the diffracted beam will begin to degrade due to Bragg angle errors - the angle of the outer rays of the input light cone begin to deviate from that of the rays at

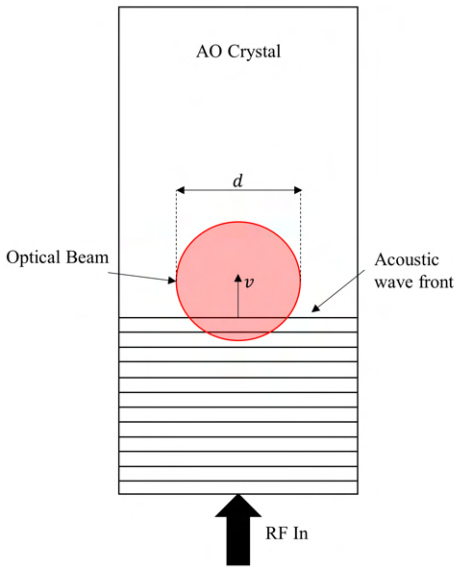


Figure 1.7: *Interaction of an optical beam with the wave front of the acoustic signal in the AOM crystal. Wavelength selectivity is usually tuned by applying an anti reflective coating to the AO crystal material which improves absorption at the design wavelength.*

the centre of the beam and so different parts of the beam experience a different diffraction efficiency resulting in a non-circular, degraded output beam.

Acousto-optical modulator structures can be employed in either waveguide or bulk modulators. The type is defined depending on the value of a/λ where a is the thickness of the active material and λ is the optical wavelength. If $a/\lambda \gg 1$ then the device is a bulk modulator. Bulk AOMs have been widely used for many years in both research and commercial applications and are still in use today. They are widely used in cold atoms-based experiments for beam switching. Waveguide-based AOMs can be used in optically-integrated circuits (OICs) and offer the same functionality as their bulk counterparts, but with the added benefit of lower RF power requirements due to their smaller size. The first waveguide AOM was reported in 1970 [35], and was based on a hybrid approach of quartz for the AO material and sputtered glass film for the waveguide. Other hybrid approaches with different materials have also been demonstrated, such as a tantalum pentoxide (TaO_5) waveguide on a quartz substrate [36], and an arsenic trisulphide (As_2S_3) film on a lithium niobate ($LiNbO_3$) substrate [37]. Monolithic approaches to waveguide AOMs have also been reported, where the

acoustic wave is fired directly into the waveguide. For example, a sputtered zinc oxide (ZnO) film on a fused-quartz substrate [38].

AOMs are thus very advanced and well-established devices in the field of integrated optics. They can easily achieve switching times on the order of tens of nanoseconds and are thus vital in the application space of an atom interferometer. AOMs can, however, suffer from a number of unwanted effects, such as the instability of beam alignment, fairly high power consumption, fragility, and most significantly a temperature dependence on the output diffraction angle. In a controlled environment, these problems can be dealt with accordingly. However, if these devices were to be implemented in fully portable quantum sensing devices, an alternative, compact and stable, switching scheme must be ideally found.

1.2.3 Electro-optical Switches

Electro-optical switches cover a wide range of applications and are key components of many commercial optical integrated circuits and standalone switching devices [17]. The term 'electro-optical switch' encompasses a wide range of optical switching schemes, however the majority are based around the operating principles of the first or second order electro-optical effects. Typically, electro-optic effects rely on the changes in the refractive index of an electro-optic material caused by the application of an external electric field. The applied field then causes a distortion of the electronic motion within the substance, or alternatively, distorts the crystal structure, causing changes in the optical properties. More specifically, electro-optic effects contain both first order and second order components. The linear (first-order) electro-optical effect is often referred to as the Pockels effect, whereas the non-linear phenomenon is known as the Kerr effect [39]. These two effects manifest themselves in a change in the refractive index,

$$\Delta n = \alpha E + \beta E^2 + ... \tag{1.13}$$

where the coefficients, α and β represent the linear and non-linear electro-optic

effects respectively. All materials exhibit the optical Kerr effect, however it can be shown [34] that the Pockels effect only occurs in crystalline materials which do not possess inversion symmetry. If a field E is applied in one direction across the material, followed by the reverse field, $-E$, then according to Equation 1.13, Δn should also change sign, i.e if the refractive index increases when E is applied, then it should show the corresponding decrease when $-E$ is applied and respond differently in the two cases. This means that the crystal structure must exhibit an asymmetry in order to exhibit this response. Crystalline materials which possess this asymmetry and exhibit the Pockels effect are said to be noncentrosymmetric. Semiconductors with the zincblende or wurzite (except diamond cubic) lattice symmetry may undergo the Pockels effect. Gallium arsenide and $Al_xGa_{(1-x)}As$ may undergo the Pockel's effect, however in silicon, which is a heavily used material in the photonics industry, the Pockel's effect is not observed unless its centro-symmentry is broken, for example by an inhomogeneous mechanical stress [40].

Even for those materials which possess noncentrosymmetry, the effect is highly dependent on the orientation of the crystal to the applied electric field, thus the design of switches exploiting this effect must be done with care [41]. Nevertheless, materials such as GaAs, gallium phosphide (GaP) and lithium niobate ($LiNbO_3$), which can be used to make integrated low-loss waveguides, also possess large Pockels coefficients for a given orientation. Thus, the Pockels effect is a widely exploited phenomenon in many integrated optics applications. Furthermore, the response time in solids for the electro-optic effect is very short and devices capable of GHz modulation frequencies and faster have been demonstrated [42], [43]. Many off-the-shelf optical switches are based on the first order electro-optic effect in the form of phase modulators, intensity modulators and polarisation modulators due to their low material cost and ease of implementation. In regards to quantum sensing experiments, electro-optic modulators (EOMs) are often used to add sidebands to a single master laser in order to address multiple transitions

during a interferometric sequence. However, these switches often have a strong polarisation-dependent performance and demand large operating voltages to acquire significant refractive index changes, resulting in the need for complex, and often bulky, driving electronics. Nonetheless these are one of the most widely implemented optical switches in commercial use due to their performance and relatively low cost.

The Kerr effect is observed in all materials, including glasses and liquids. This relaxes the aforementioned design constrains introduced with the Pockels effect. In the Kerr effect, the applied external electric field distorts the electron orbits of the material structure. Subsequently, an interacting electromagnetic wave experiences a different dispersion in the polarisation plane parallel to its propagation axis as compared to the perpendicular one. The result is an induced optical birefringence parallel to the propagation direction. The major drawback of implementing this scheme for optical switching is that the effect is very weak as compared to the Pockels effect in commonly used waveguide materials. Furthermore, the non-linear dependence on the electric field results in a significant distortion in the modulated signal. These caveats make the Kerr effect unsuitable for practical implementation in integrated optical switches

1.2.4 Electro-absorption Modulators

Another important class of optical switch/modulator is that of the electro-absorption modulator. Fundamentally, this device is classed as an electro-optic modulator as it relies on an external electric field to produce the intensity modulation. However, it does not exploit the electro-optic effect in its operation. Instead it is based on perturbation of the optical absorption coefficient by either the Franz-Keldysh effect for bulk semiconductors [44] or the Quantum-confined Stark effect (QCSE) for quantum wells [45].

In the Franz-Keldysh effect, the application of a strong external electric field causes the absorption edge of a semiconductor to shift to a longer wavelength.

By forming a Schottky barrier contact at the surface of the semiconductor, a reverse bias resulting in a strong electric field across the rectifying Schottky contact/semiconductor junction ($\sim 10^4$V/cm) can be applied through the sample. This causes a depletion layer to form, within which the electric field is non-uniform, taking a maximum value at the semiconductor surface resulting in band bending with a profile proportional to the electric field strength. Outside the depletion region, the bands are flat and a photon can only force an electron transition to the conduction band (CB) if it has sufficient energy. This is in contrast to the surface, where photons can promote electrons to the CB even if their energy is below the bandgap energy. This scheme is illustrated in Figure 1.8.

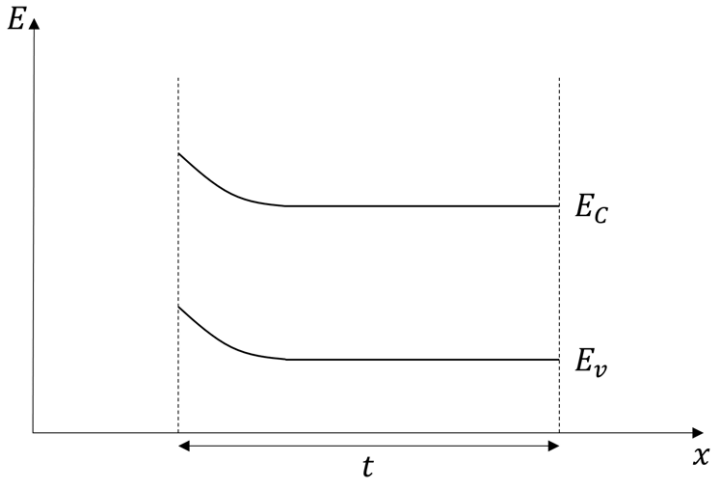


Figure 1.8: *Semiconductor band diagram illustrating the Franz-Keldysh effect in the presence of an electric field. The parameter x represents the distance from the surface of the semiconductor whilst E_C and E_v represent the energy of the conduction and valence bands respectively, and t is the thickness of the semiconductor sample.*

In designing an electro-absorption modulator/switch, parameters such as the length of the device and applied voltage are chosen by considering the absorption curves of the relevant materials. This ensures the device is capable of achieving the minimum desired insertion loss and maximum modulation depth for a given design wavelength. Common materials for such devices include the Al_x $Ga_{(1-x)}As/Al_y$ $Ga_{(1-y)}As$ heterostructure. The advantage of using this scheme is that the aluminium content in the waveguiding layer can be adjusted to provide optimum performance for a given wavelength. Such devices have been demon-

strated for 900nm wavelength [46] which show changes of transmission by a factor of 100 for an applied bias of −8V, and others for use at the telecommunications wavelengths of 1350nm and 1550nm [47]. These structures offer very efficient modulation, i.e. the electrical power required to produce a significant change in the absorption coefficient of up to 100cm^{-1} is fairly low, however they are strongly polarisation dependent, with the absorption for TM and TE modes differing significantly.

1.2.5 Mach-Zehnder Modulator

Amongst the plethora of different configurations for optical switches/modulators, perhaps the most successful scheme is that of the Mach-Zender interferometer (MZI) switch. In this scheme, an interference is produced between phase coherent light waves which have travelled over different path lengths. Coherent light is coupled into the device using a single-mode waveguide. Using a 3 dB coupler as a beam splitter, the light is equally divided into two waveguides [48]. The effective path lengths of these waveguides can be altered by applying a small voltage to electrodes placed either side of the waveguides. If the structure is well designed, without any electrical signal the beams from each waveguide should recombine to produce the same single mode beam at the output. Conversely, if the electric field is tuned to produce a phase change of π radians along the path length of one of the arms of the interferometer then the resulting output beam will have a null intensity at the centre of the output waveguide. The output beam can therefore be switched from the 'on' to 'off' state by the application of a small voltage. MZI type switches have been employed in many different platforms including silicon-on-insulator [49], indium phosphide [50], lithium niobate [51] and gallium arsenide [52]. The main issue with MZI switches is the constraints on the fabrication tolerances - even minute variations in fabrication parameters can result in unwanted deviations of the output field, manifesting themselves for example in a non-zero optical field in the 'OFF' state of the switch. This has an

adverse effect on the measured extinction ratio of the device. Furthermore, to achieve a significant path difference between the arms of the two beams, a longer propagation distance must be employed compared to other schemes. This can lead to higher insertion losses as more optical power is lost through a longer device. MZI switches are ideal for implementation in photonic integrated circuits (PICs), however due to their use of optical interference, like the AOM they can be sensitive to operating conditions making it challenging to achieve high extinction ratio switching. Typical extinction ratios achievable are around 30 dB for operating voltages in the region 5-10 V [53].

1.2.6 Microring Resonators

First proposed by Marcatili in 1969 [54], but advancing rapidly in more recent years due to advances in microfabrication technologies, an optical microring resonator is an integrated optical resonator constructed using a closed loop optical waveguide in a circular shape [55]. When light is coupled into the ring, it propagates around and interferes with itself after every round trip. When the roundtrip length is equal to an integer number of wavelengths of the guided wave, constructive interference occurs leading to a build up of the intensity of light in the form of sharp resonances. The optical microring resonator confines light in all spatial directions: transversely by the refractive index contrast of the material layers used, and longitudinally by the periodic boundary conditions imposed by the microring. Light is coupled out of the microring using evanescent field coupling between the microring and an external straight waveguide called a bus waveguide. Figure 1.9 schematically demonstrates these principles.

Microring resonators benefit from high wavelength selectivity, strong dispersion and large field enhancement of the guided wave making them highly versatile and suitable for a wide range of applications such as optical communication [56], signal processing [57] and sensing [58] to name just a few. Multiple microrings can be combined to produce an optical filter [59]. Microrings can be fabricated using

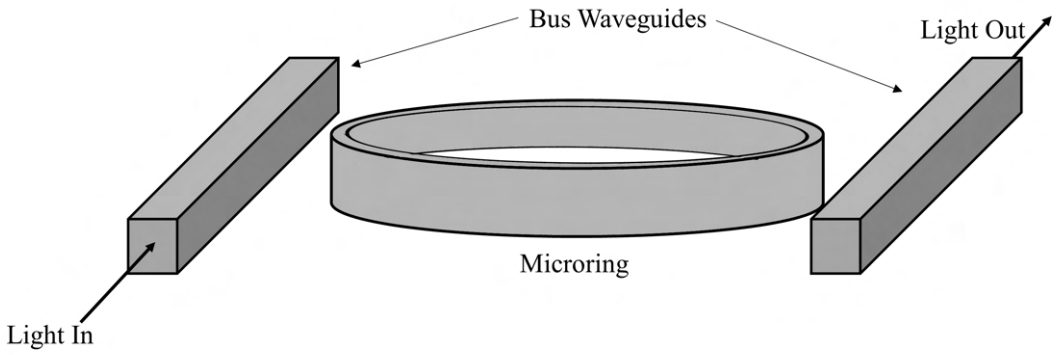


Figure 1.9: *Schematic illustration of a microring resonator with separte input and output bus waveguides.*

any integrated optical platform which can form waveguiding structures, making them highly suitable for integration onto PICs with various uses such as filtering, mode-locking and all optical switching. Once again however, the functionality of microring based devices suffer from susceptibility to thermal fluctuations [60] meaning that the operating environment must be thermally controlled. This may be achieved by incorporating thermoelectric controllers (TECs) within the photonics packaging, or by incorporating micro heaters on the PIC to control the substrate temperature. These subtleties increase the fabrication complexity of these devices making them less appealing than other integrated devices which are less sensitive to thermal fluctuations and work over a wider optical wavelength region. Nonetheless, very recently, silicon nitride microrings have proven themselves to be promising integrated optical components for laser locking applications for quantum sensors. More details will be discussed regarding current and future trends in silicon nitride technologies in Chapter 6.

1.2.7 MEMS Switches

Microelectromechanical systems (MEMS) are microscopic devices with optical, electrical and mechanical functionalities. MEMS technology is characterised by long lifetime, reliability, durability, and insensitivity to polarisation and wavelength, and is widely implemented in commercially available optical switching

devices [61]. Earlier in this chapter, the use of fibre-interfaced mechanical switches used in quantum sensing experiments after an AOM to achieve the extremely combined high extinction ratios (> 100 dB) required was discussed. These commercially available switches often employ a MEMS approach to couple or de-couple an optical beam from an output port by actuation of a mechanism which physically moves an optical component in and out of the optical path, via the application of a small electrical signal. These switches can achieve very high extinction ratio switching but are inherently mechanical and thus suffer from the disadvantages associated with mechanical actuation, such as a comparatively slow switching speed and switch 'bouncing' as previously discussed. Nonetheless, MEMS optical switches are important components of quantum sensing experiments and can be easily integrated on-chip, readily available for integration in future PICs. They may indeed prove important components for portable quantum sensors, in cases where fast switching is not of paramount importance.

1.3 Summary

In this introductory chapter we have discussed how the next generation of quantum sensors are making the move from lab-based systems to portable, commercial devices, and the complexities involved with this transition in technology by considering the operating principles of a quantum gravimeter.The development of enabling technologies from standard off-the-shelf bulk components to more bespoke integrated, on-chip components is a fundamental aspect of this transition. In particular, optoelectronic components play a major role in these sensors, so the importance of considering current and future trends for these devices is vital. The switching technologies discussed in this Chapter each offer unique advantages and disadvantages for specific applications. Table gives a summary of the typical performance indicators for the discussed existing technologies.

Knowledge of the key operating principles of these common switching mechanisms and schemes will further enable the design and development of new in-

Switch Type	**Extinction Ratio**	**Insertion Loss**	**Switching Speed**
Acousto-optical [10]	$\sim$ 30 dB	$\sim$ 5 dB	$\leq$ 50 ns
Electro-optical [61]	$\sim$ 30 dB	$\sim$ 1-4 dB	$\leq$ 10 ns
Electro-Absorption [62]	$<$ 10 dB	$\sim$ 2-5 dB	$\leq$ 1 ns
Microring [63]	$\sim$ 30 dB	$\sim$ 2 dB	$\geq$ 0.3 ms
Optical MEMS [61, 10]	$\sim$ 80 dB	$\sim$ 1-3 dB	$\sim$ 1 ms

Table 1.1: Typical key performance parameters for optical switches relevant for use in quantum sensors.

tegrated switching devices, optimised to enable the future development of fully portable quantum sensing devices. Therefore, in this thesis, a novel design for an integrated semiconductor optical switch will be presented as a possible future component for a portable quantum gravimeter. In the following chapter, the physical principles exploited in this optical switch will be discussed, and the proposed optical switch design presented. Towards the end of the chapter, simulations will be presented based on this theory, illustrating the intended operating characteristics of the device.

1.4 Statement of Contributions

The research work discussed in this thesis involved contributions from various others. This statement clarifies the work carried out by the author in relation to all the information and data presented in this thesis.

Epitaxial design of the semi-insulating GaAs wafers was carried out by Dr James Moss, Dr Chris Mellor and Dr Jessica Maclean and the wafers were grown using molecular beam epitaxy by Dr Richard Campion. The first iteration of devices for use at 904 nm were fabricated by Dr James Moss. All other devices were fabricated by the author, including the optimisation of the various processing steps. All fabrication steps, except for the dry etching which was completed

by Dr Chris Mellor, were carried out by the author. All of the simulations presented in this thesis were designed and coded by the author using MATLAB and Python. The design and construction of the optical test equipment and associated software are also the work of the author. Finally, the characterisation of all devices using this test equipment are the work of the author, except for the photoluminescence measurements which were carried out by Mr James Felton. A statement confirming those cases where information in this thesis is presented which was not carried out by the author is given alongside the data in each instance.

Chapter 2

Beam Steering Photonic Switches: Theory and Modelling

2.1 Introduction

In the previous chapter, the requirements for developing photonic components for quantum sensing devices were discussed by investigating the current off-the-shelf technologies and their associated advantages and disadvantages in the context of reducing the SWaP of these sensors. In this chapter, a proposed integrated photonic switch design for use in quantum sensing devices which rely on the spectroscopy of caesium, rubidium, and potassium is presented. The theoretical background which governs the operating principles of the device are first discussed, followed by a description of the device design and intended mode of operation. Towards the end of the chapter, results from a computational model, developed to demonstrate the intended switching effects, are presented giving insights into the ideal operating scenarios.

2.1.1 Wafer Structure

Three separate epitaxial structures were originally designed by Dr James Moss [64] for switching light in three separate wavelength windows: 890-920 nm, 750-

780 nm and 730-770 nm. These designs are intended for optical switching of lasing wavelengths suitable for quantum sensors involving spectroscopy of caesium-133 (D1 transition at 894.59 nm), rubidium-87 (D2 transition at 780.25 nm) and potassium-39 (D1 transition at 766.7 nm) respectively. A summary of the epitaxial structures including layer thicknesses and doping concentrations are given in Table 2.1. The wafer IDs presented in this Table will be used to refer to devices made from each of these structures throughout the thesis. A standard double heterostructure (a p-i-n diode structure on a semi insulating GaAs substrate) is employed for passive waveguiding and active switching of a guided optical wave. This design allows electrical injection of carriers to control the switching mechanism. In the following section, the underlying physical principles of this switching mechanism and the reasons for the epitaxial design will be discussed in more detail.

2.2 Carrier-induced Refractive Index Change Effects

Injection of carriers into a semiconductor, by optical or electrical means, can change the absorption spectrum of the material. For the devices designed in this study, wave-guided switching can be achieved by altering the optical absorption coefficient and consequently the refractive index profile (through the Kramers-Krönig relations [65]) by means of electrical carrier injection. This change can occur as a result of three main phenomena: free carrier absorption (plasma effect), band filling (Moss-Burstein effect), and band-gap shrinkage (band-gap renormalisation) effects. The first demonstration of carrier induced optical switching exploiting band-filling effects was using the indium gallium arsenide phosphide/indium phosphide (InGaAsP/InP) material system designed for switching at 1.2 μm optical wavelength, demonstrating a power isolation of 20.5 dB in a 1mm long multi-mode device [66]. Application of the effect to the GaAs/AlGaAs

Wafer ID	**Layer**	**Thickness (μm)**	**Doping (cm^{-3})**
RC101	SI GaAs	625	-
	Buffer layers	~ 0.3	-
	n-GaAs	1	2.5×10^{18}
	n-$Al_{0.2}Ga_{0.8}As$	**1**	$\mathbf{2 \times 10^{18}}$
	GaAs	**0.2**	-
	p-$Al_{0.2}Ga_{0.8}As$	**1**	$\mathbf{2 \times 10^{18}}$
	p-GaAs	1	2.5×10^{18}
	p-GaAs	0.2	2×10^{19}
RC184	SI GaAs Substrate	625	-
	Buffer layers	~ 0.3	-
	n-GaAs	1.2	4×10^{18}
	n-$Al_{0.45}Ga_{0.55}As$	**0.1**	$\mathbf{4 \times 10^{18}}$
	$Al_{0.22}Ga_{0.78}As$	**0.39**	-
	p-$Al_{0.45}Ga_{0.55}As$	**1**	$\mathbf{4 \times 10^{18}}$
	p-GaAs	0.4	2×10^{19}
RC187	SI GaAs Substrate	625	-
	Buffer layers	~ 0.2	-
	n-GaAs	1	4×10^{18}
	n-$Al_{0.55}Ga_{0.45}As$	**0.8**	$\mathbf{4 \times 10^{18}}$
	$Al_{0.25}Ga_{0.75}As$	**0.3**	-
	p-$Al_{0.55}Ga_{0.45}As$	**0.85**	$\mathbf{4 \times 10^{18}}$
	p-GaAs	0.4	2×10^{19}

Table 2.1: Layer compositions of semi-insulating (SI) GaAs epitaxial wafers, grown by Dr Richard Campion, for optical switching devices. The p-i-n region is highlighted in bold.

material system, designed for 900 nm wavelength was subsequently demonstrated and featured continuously controlled motion of the output beam [67]. Subsequently, a device featuring $In_{(1-x)}Ga_xAs_yP_{(1-y)}$ multiple quantum wells (MQWs) for 1.5 μm wavelength was established, which required a much lower injection current for operation due to an area-selective zinc in-diffusion used to channel charge carriers into the MQW [68].

In this section, the physics explaining these three effects contributing to carrier-induced refractive index change will be described, along with calculations giving an estimate of the combined effect they have on the change in refractive index, Δn, for the GaAs and $Al_xGa_{(1-x)}As$ layers relevant to the switching devices investigated in this study. These calculations form the basis for the custom beam propagation simulations presented at the end of this chapter.

2.2.1 Moss-Burstein Effect

Electrically injecting carriers into a semiconductor causes the lowest conduction band states to become occupied with electrons and the highest valence band states to be occupied with holes. As the conduction band begins to fill, electrons present in the valence band subsequently require an energy higher than the nominal band gap to be excited to the conduction band resulting in a decrease in absorption coefficient for photons with energies close to the band gap, and thus a blue shift in the absorption spectrum. This effect is also observed with doped semiconductors, known as the Moss-Burstein Effect [69, 70], and is most pronounced in semiconductor materials with small effective masses and energy band gaps. The Moss-Burstein effect does not alter the energy of emission and is only apparent in the absorption properties of the material. Since this bandfilling effect results from the movement of free carriers, electrical injection should give equivalent effects as doping, except for the fact that injection results in effects from both electrons and holes. The aforementioned shift in the absorption spectrum also results in a change in the refractive index via the Kramers-Kronig relations.

The change in absorption due to the Moss-Burstein effect as a function of energy (E), electron (N) and hole (P) concentration, is found to be [71],

$$\begin{aligned}\Delta\alpha(N,P,E) = &\frac{C_{hh}}{E}\sqrt{E-E_g}[f_v(E_{ahh}) - f_c(E_{bhh}) - 1] \\ &+\frac{C_{lh}}{E}\sqrt{E-E_g}[f_v(E_{alh}) - f_c(E_{blh)} - 1],\end{aligned} \tag{2.1}$$

where C_{hh}, C_{lh} are the fitting constants due to heavy and light holes respectively, $E = \hbar\omega$ is the photon energy, E_g is the band-gap energy and $f_{c,v}(E_{ahh,bhh,alh,blh})$ are the probabilities of carrier occupation of the conduction/valence band at energy E_a/E_b of heavy/light holes. A full description of this model can be found in the literature [71]. Figure 2.1 shows the change in refractive index due the the Moss-Burstein effect as a function of photon energy for GaAs, calculated from the change in absorption in Equation 2.1 using the Hilbert transform [72].

The maximum change in refractive index occurs just above the band gap energy. Close to and below the nominal bandgap the refractive index decreases whilst Δn becomes positive for energies within a few tens of meV above E_g. The sharp peaks shown are a result of the assumption that the unperturbed absorption follows a square root dependence on energy. In reality, the material would still exhibit some absorption just below the nominal band gap due to phonons, impurities, excitons and external electric field effects. This is known as the Urbach absorption tail [73]. The largest values of Δn are within a few meV of the bandgap, but the high absorption losses in the Urbach tail mean that waveguides and switches are impractical in this region.

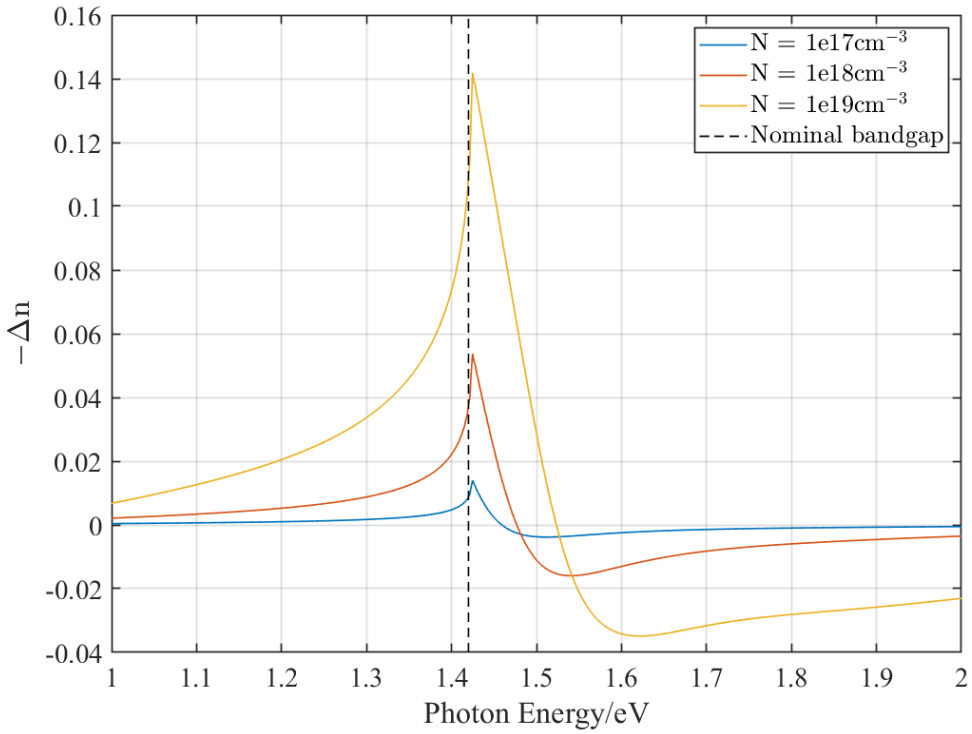
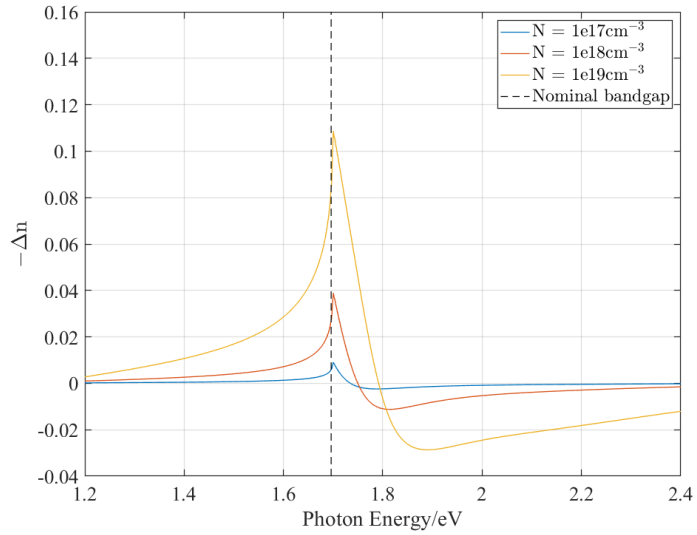


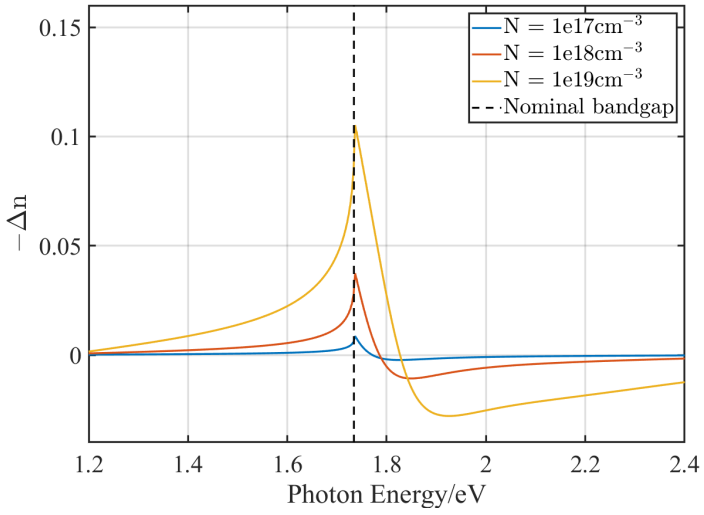
Figure 2.1: *Theoretical change in refractive index of undoped GaAs as a function on photon energy due to the Moss-Burstein effect, for three increasing values of carrier concentration, at $T = 300$ K. Charge neutrality is assumed so that $N = P$.*

The model detailed in [71] has been extended here to simulate the change in refractive index due to the Moss Burstein effect in $Al_xGa_{(1-x)}As$. The change in refractive index as a function of photon energy for the undoped core regions of RC184 and RC187 have been numerically calculated and are presented in Figure

2.2. The effect is slightly stronger for lower concentrations of aluminium since the effective masses of carriers and the magnitude of the nominal band gap increase with increasing aluminium content. The change in refractive index due to the Moss-Burstein effect is always negative for photon energies below the nominal band gap.



(a)



(b)

Figure 2.2: *Theoretical change in refractive index for the core regions ($Al_xGa_{(1-x)}As$) of (a): RC184 and (b): RC187 due to the Moss-Burstein effect, as a function of photon energy, at $T = 300$ K.*

The change in refractive index has also been calculated as a function of the carrier concentration for the core region of RC101, RC184 and RC187, at photon wavelengths below each of their nominal bandgap energies, and relevant to the application in a quantum sensor. This was achieved by computing the change in absorption for a given photon energy and numerically integrating this absorption data over a range of carrier concentrations. The results are illustrated in Figure 2.3. This simulation confirms that the magnitude of Δn increases with increasing carrier concentration.

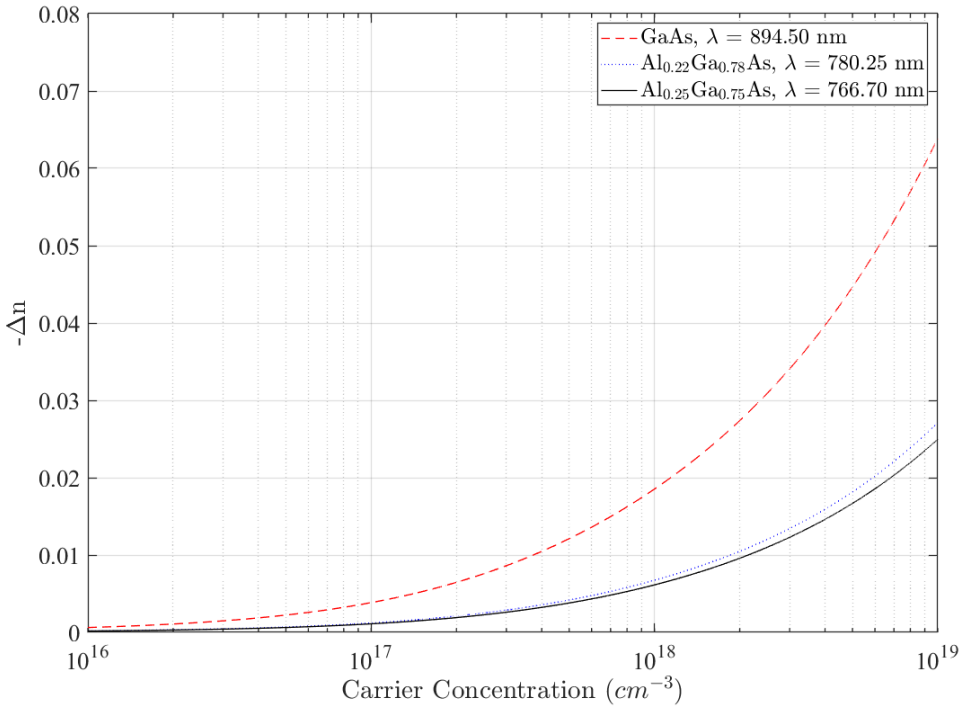


Figure 2.3: *Change in refractive index of the core region of RC101, RC184 and RC187 at $T = 300$ K, as a function of carrier concentration due to the Moss-Burstein effect, at photon wavelengths relevant to quantum sensing applications. In this situation, the magnitude of Δn is higher for GaAs as the simulated wavelengths than the other concentrations of $Al_x Ga_{(1-x}As$ at their simulated wavelengths due to the proximity of these photon wavelengths to the corresponding wavelength of the nominal band gap. As discussed, the strength of the Moss-Burstein effect is increased the closer the wavelength of the absorbed photon is to this nominal band gap wavelength.*

2.2.2 Bandgap Shrinkage Effect

In the case of very high free carrier concentrations, the wavefunctions of electrons will begin to overlap, thus forming a gas of interacting particles. Coulombic forces then cause electrons to repel each other along with statistical effects causing those with the same spin to avoid one another. The result is an electron screening effect which lowers their energy and consequently lowers the energy of the conduction band edge, as illustrated in Figure 2.4. A similar argument for holes leads to an increase in the valence band edge. The net result of these two phenomena is a shrinkage of the overall band gap. It was originally shown [74] that an expression for the band-gap shrinkage is given by,

$$\Delta E_g = -\left(\frac{e}{2\pi\epsilon_0\epsilon_r}\right)\left(\frac{3}{\pi}\right)^{1/3}\chi^{1/3}, \tag{2.2}$$

where ϵ_r is the relative dielectric constant of the material, and χ is the concentration of free electrons/holes.

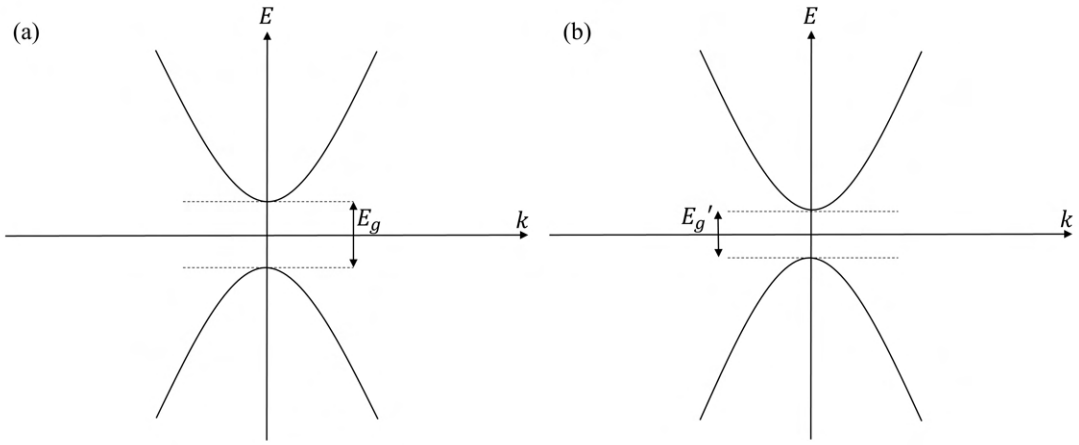


Figure 2.4: *Schematic illustration of a direct band-gap semiconductor (a): before and (b): after a significant injection of carriers, resulting in a reduction in the band-gap energy from* E_g *to* $E_g^{'} = E_g - \Delta E_g$.

Wavefunction correlation effects begin to become significant when the spacing of electrons (holes) approaches the Bohr radius ($\sim$ 100Å). Thus, Equation 2.2 does not hold for low carrier concentrations since the carrier spacing will be too large

to produce significant wavefunction overlapping. Another model which takes this caveat into account, adopted by [71] results in the following:

$$E_g(\chi) = \begin{cases} \frac{\kappa}{\epsilon_s}\left(1 - \frac{\chi}{\chi_{cr}}\right) & \chi \geq \chi_{cr}, \\ 0 & \chi < \chi_{cr}, \end{cases} \tag{2.3}$$

where κ is a constant parameter used for fitting, and χ_{cr} is the critical carrier concentration at which band shrinkage effects start to become significant. Based on experimental evidence, the value of χ_{cr} is related to the Mott critical density [75],

$$\chi_{cr} = 1.6 \times 10^{24} \left(\frac{m_e}{1.4\epsilon_s}\right)^3 cm^{-3}, \tag{2.4}$$

where m_e is used rather than m_{hh}, or m_{lh} since electronic correlation effects occur at lower carrier concentrations than for holes. For GaAs, $\chi_{cr} \approx 7.4 \times 10^{16} cm^{-3}$. The change in band gap energy due to the band-gap shrinkage effect has been calculated for GaAs and the relevant concentrations of Al in $Al_xGa_{(1-x)}As$ and shown in Figure 2.5.

2.2.3 Free-carrier Absorption

The absorption of light in a semiconductor is always related to the changing state of free carriers. A free carrier within an already excited state may absorb a photon of energy $E = \hbar\omega$, where ω is the angular frequency of light, and move from state E_1 to a state E_2 which has a higher energy within the same band. This momentum change may also occur via optical or acoustic phonons, or by impurity scattering. In the Drude model, it can be shown [76] that this intraband free carrier absorption, known as the plasma effect, results in a refractive index change given by,

$$\Delta n = -\left(\frac{e^2\lambda^2}{8\pi^2 c^2 \epsilon n}\right)\left(\frac{N}{m_e} + \frac{P}{m_h}\right), \tag{2.5}$$

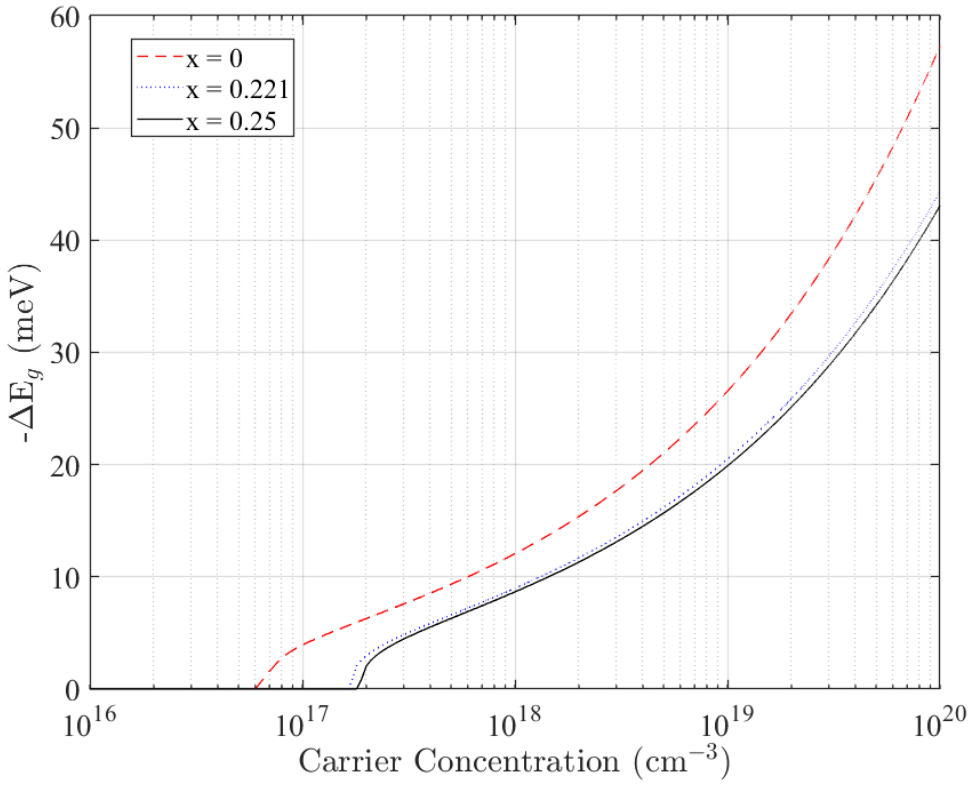


Figure 2.5: *Change in band-gap energy due to the band-gap shrinkage effect for GaAs and $Al_xGa_{(1-x)}As$ with $x = 0.221, 0.25$, calculated using Equation 2.3.*

where λ is the free space optical wavelength, e is the electronic charge, c is the speed of light in a vacuum, n is the intrinsic semiconductor refractive index, $\epsilon = \epsilon_0\epsilon_r$ is the permittivity, m_e is the effective electronic mass, m_h is the effective hole mass, and N and P are the electron and hole carrier densities respectively.

The change in refractive index due to free carrier absorption as a function of carrier concentration has been calculated for the aluminium concentrations present in the core region of RC101, RC184 and RC187, at the specified wavelengths and is illustrated in Figure 2.6. We observe that the change in refractive index due to free carrier absorption is negative and small ($\sim 10^{-3}$) even at high carrier concentrations ($\sim 10^{19}\text{cm}^{-3}$), and the effect is weaker for higher concentrations of aluminium. This is because the effective masses of electrons and holes increase with increasing aluminium content, subsequently leading to a smaller Δn. Due to the dependence on λ^2, the strength of the plasma effect increases as the photon wavelength increases above the nominal band gap value.

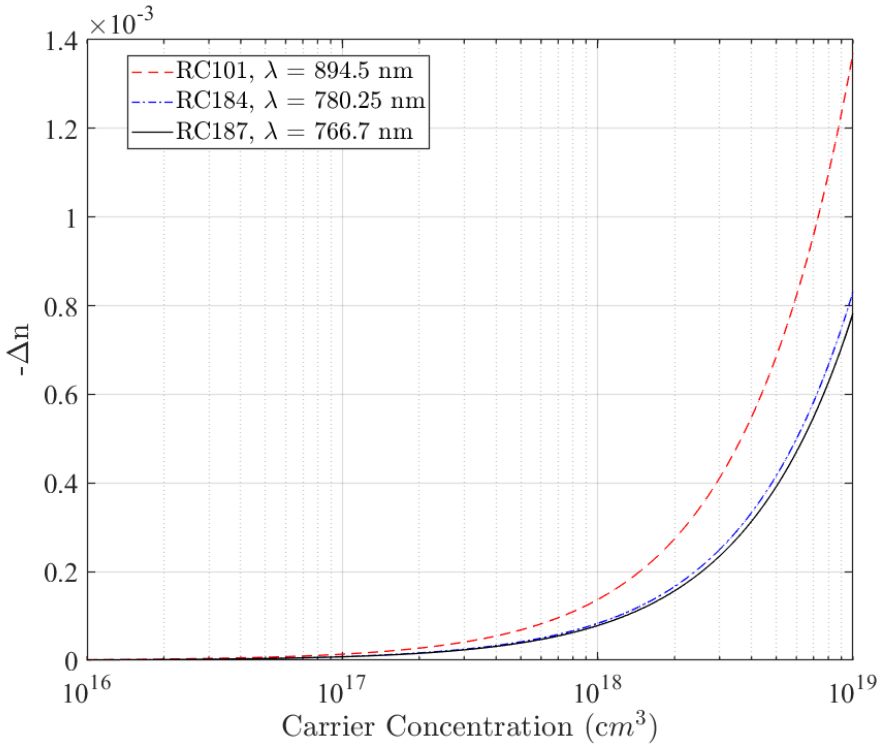


Figure 2.6: *Change in refractive index as a function of the carrier concentration due to free carrier absorption for the core region of RC101, RC184 and RC187, at photon wavelengths relevant to quantum sensing applications. The corresponding nominal band gap wavelengths are 873 nm, 730 nm and 715 nm respectively.*

2.2.4 Combination of Refractive Index Change Effects

The total change in refractive index due to the aforementioned carrier-induced effects is calculated in this model by simply summing their individual contributions. However, since we have shown that the contribution due to free-carrier absorption is small compared to the Moss-Burstein effect and the band gap shrinkage effect, this effect can be ignored in the final calculation. The change in refractive index for GaAs as a function of photon energy, at a carrier concentration of 1×10^{18} cm^{-3} due to the three individual effects and their sum has been calculated and is shown in Figure 2.7. This clearly shows that the free carrier absorption effects are negligible. The final change in refractive index is thus calculated by first considering the injection of carriers to cause a shrinkage of the band gap, followed by bandfilling of the new structure. This approach is supported by experimental absorption data for GaAs [77].

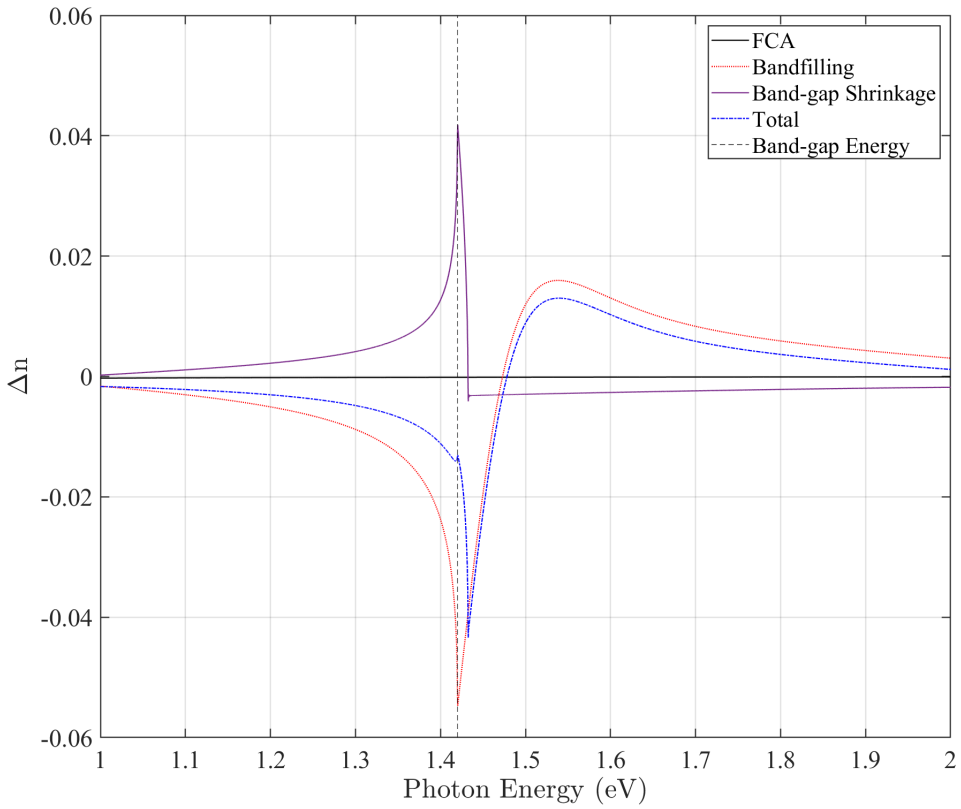
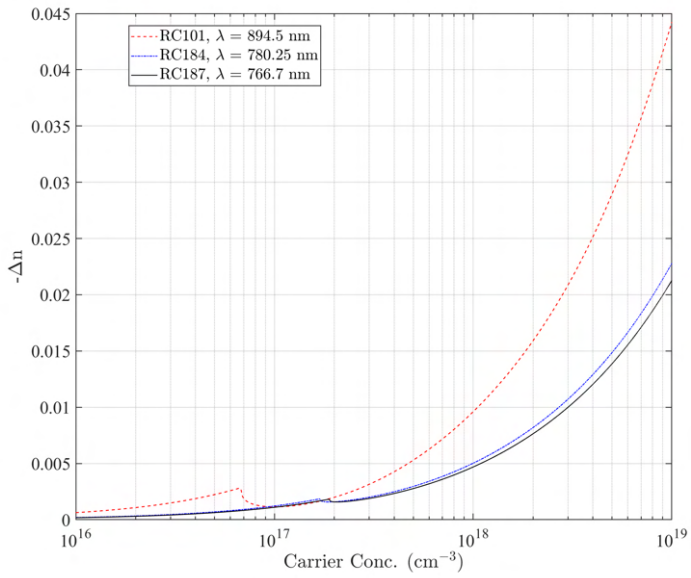


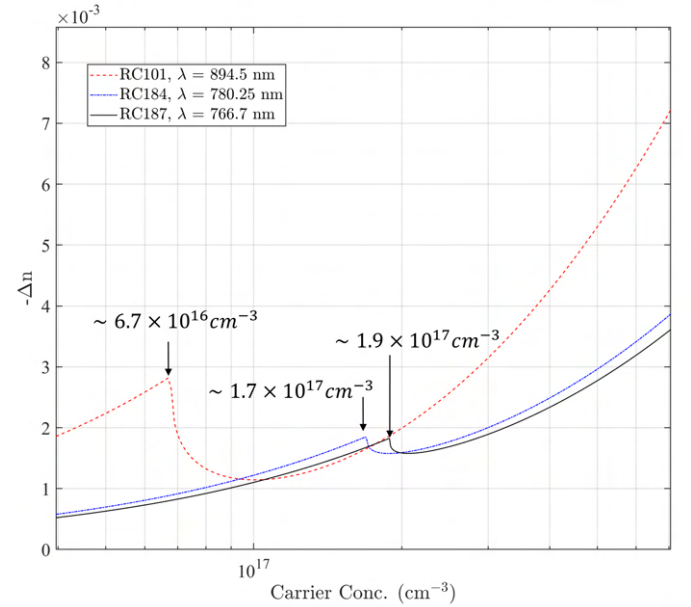
Figure 2.7: *Change in refractive index as a function of photon energy for GaAs at a carrier concentration of* $N = P = 1 \times 10^{18}$ cm^{-3}*, due to the three aforementioned carrier effects, and their summation. The sharp peaks are a caveat of the model and would not be observed experimentally due to the Urbach absorption tail.*

Using this approach, the change in refractive index has been calculated, as a function of carrier concentration, for the core region of each wafer, once again at photon wavelengths relevant to quantum sensing applications, and is shown in Figure 2.8. It can be seen that the band gap shrinkage effect has reduced the magnitude of the change in refractive index caused by the Moss-Burstein effect by approximately 34% for GaAs, 17% for $Al_{0.22}Ga_{0.78}As$ and 14% for $Al_{0.25}Ga_{0.75}As$. The point at which the band gap shrinkage effects become important can clearly be seen for each material, as there is a kink in the -Δn curve when the inter-particle spacing becomes sufficient enough to cause shrinkage effects. The effect that band-gap shrinkage has on decreasing the magnitude of $-\Delta$n is observed to decrease with increasing aluminium concentration in $Al_xGa_{(1-x)}As$ due to the higher effective masses. However, the magnitude of $-\Delta$n induced by bandfilling

effects also decreases with increasing aluminium concentration, thus the chosen aluminium concentration for the core of these double heterostructure devices must strike a balance between obtaining a reasonable $-\Delta$n induced by the two major contributing effects, along with consideration of the absorption losses associated with operating the devices at photon energies too close to the nominal band gap.



(a)



(b)

Figure 2.8: *Change in refractive index as a function of carrier concentration due to combined band-gap shrinkage and Moss-Burstein effects, at photon wavelengths relevant to quantum sensing applications for the core region of each wafer. In (b) the point at which the band gap shrinkage effects become important is shown in more detail.*

2.3 Electrical Confinement

As has been shown in the previous section, injection of a significant density of carriers into direct band gap $Al_xGa_{(1-x)}As$ (i.e. for $0 \leq x \leq 0.45$) can cause a decrease in the local refractive index profile of the material. Dynamic injection of a significant concentration of carriers into the material opens up the possibility of being able to dynamically control the optical confinement in a direction perpendicular to the flow of free carriers. There are two ways to achieve carrier injection in semiconductor materials: optical pumping, where electron-hole pairs are created by absorption of photons; and electrical injection through a p-i-n junction where electrons and holes are injected directly into the intrinsic material. As was discussed at the start of the chapter, the wafer structure of the devices studied in this project implement a standard p-i-n double heterostructure. This allows carriers to be electrically injected into the intrinsic region of the device, but also allows the formation of strip-loaded waveguides for the passive section of the device, due to the nominal refractive index contrast between the core (intrinsic) and cladding (doped) regions of the material. To accurately simulate the carrier-induced refractive index profile within these devices requires spatial knowledge of how carriers are trapped and diffuse through the structure. This section describes the mathematical models used to simulate these effects along with a discussion on their implications.

2.3.1 Band Structure

Heteroepitaxial layer growth of $Al_xGa_{(1-x)}As$ allows the design and construction of integrated waveguides and lasing structures, by varying the aluminium concentration in multi-layer configurations. The band-gap energy of $Al_xGa_{(1-x)}As$ may be calculated using the following expressions (in eV) [78],

Table 2.2: Calculated nominal band-gap energy values and their corresponding photon wavelengths for cladding and core regions of all wafers.

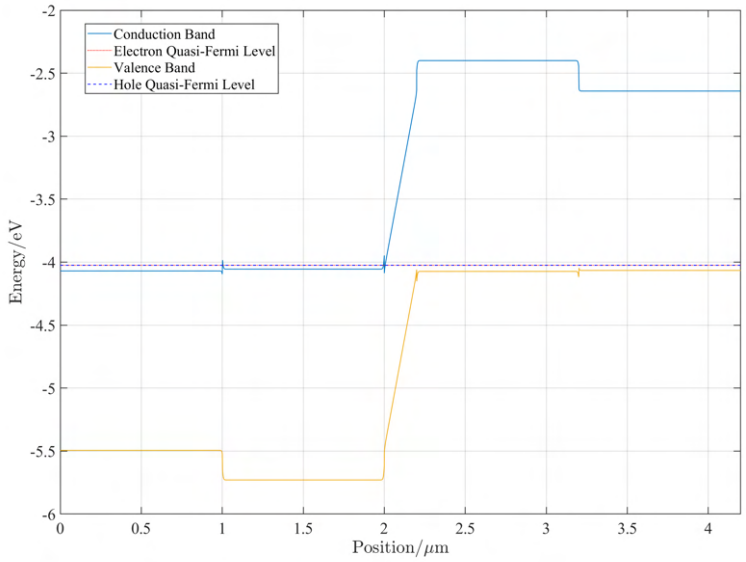
Layer	**Composition**	E_g **(eV)**	λ_g **(nm)**
RC101 Core	GaAs	1.424	871.9
RC101 Cladding	$Al_{0.20}Ga_{0.80}As$	1.672	741.5
RC184 Core	$Al_{0.22}Ga_{0.78}As$	1.698	730.2
RC184 Cladding	$Al_{0.45}Ga_{0.55}As$	1.983	625.2
RC187 Core	$Al_{0.25}Ga_{0.75}As$	1.734	715.0
RC187 Cladding	$Al_{0.55}Ga_{0.45}As$	2.012	616.2

$$E_g(x) = \begin{cases} 1.424 + 1.247x & x < 0.45, \\ 1.9 + 0.125x + 0.143x^2 & 0.45 \leq x \leq 1, \end{cases} \tag{2.6}$$

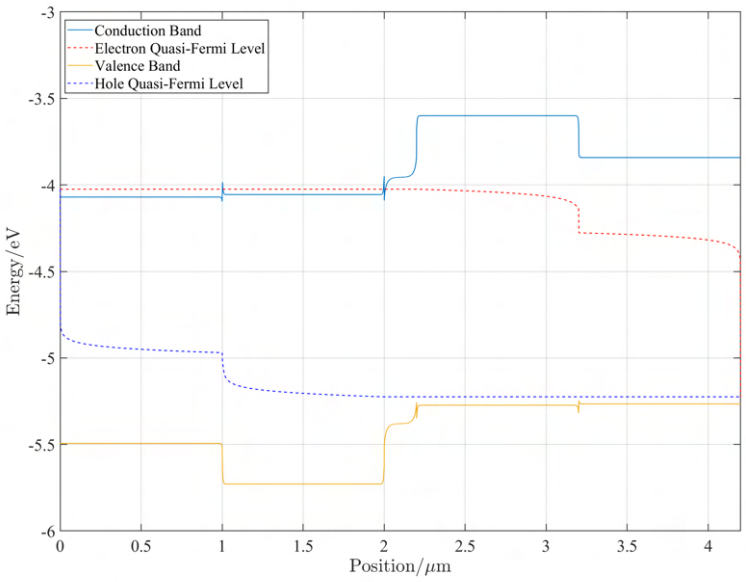
at $T = 300K$, where x is the aluminium mole fraction. The standard double heterojunction used in the proposed devices make use of this property of $Al_xGa_{(1-x)}As$ to provide electrical confinement: a lower band gap, undoped layer is surrounded, in the growth direction, in between two highly-doped, wider band-gap layers to provide electrical confinement of carriers. Using Equation 2.6, the nominal band-gaps of the core and cladding layers for each wafer have been calculated, and are summarised in Table 2.2.

To better understand how the magnitude of the barriers at the interface confine electrons and holes to the core, the energy band diagrams have been simulated using the SimWindows 1D optoelectronic semiconductor device simulator [79]. The energy band diagrams for RC101 at equilibrium and under 1.2V applied forward bias have been calculated and are illustrated in Figure 2.9. The depletion regions associated with the band bending effects are shown as notches at the clad/core interface and at the interface between the doped capping layers and cladding. In this condition, we observe that the quasi Fermi levels for electrons and holes coincide since the system is in thermal equilibrium. The built-in potential, $V_b = 1.428V$. Under forward bias ($V_a = 1.2V$), the quasi-Fermi levels separate (except at the contacts) and electrons and holes are injected from the doped cladding layers to populate the undoped core. Since the barriers at the

interface of the core and cladding are significantly larger than the thermal energy (k_BT) at room temperature, carriers are efficiently confined to the core region. As the forward bias increases, the barrier heights are reduced, leading to poorer confinement and subsequently higher leakage of carriers from the core region. The potential difference across the device is $V_b - V_a$. The leakage of carriers in these conditions will now be discussed in more detail (Section 2.3.2).



(a)



(b)

Figure 2.9: *Energy band diagram of the double heterostructure of RC101, with doped capping layers, at (a): equilibrium and (b): 1.2 V forward bias.*

2.3.2 Carrier Leakage

As discussed at the start of Chapter 2, the injection of charge carriers into the intrinsic region of the device causes an increase in the carrier density and subsequently a change in the refractive index due to the three carrier-induced effects, free carrier absorption, bandgap shrinkage and the Moss-Burstein effect. However, as we have seen, due to the finite barrier height at the heterojunction interface between the cladding and core regions, electrons and holes cannot be totally confined to the core and instead leak into the adjacent passive cladding. Thus the relationship between the refractive index of the core and the injected current must include these leakage effects. Figure 2.10 schematically shows a cross section of the device structure and the associated current injection and leakage routes. Further detail on the full device structure will be presented in Section 2.5.

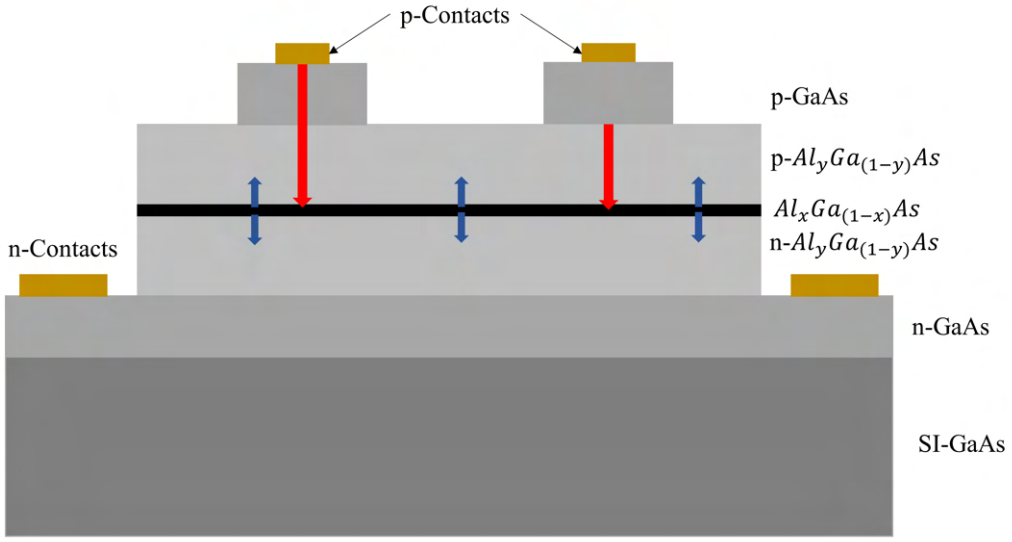


Figure 2.10: *Schematic diagram of a cross section of the p-i-n device structure on a semi-insulating (SI) GaAs substrate, illustrating the direction of carrier injection and leakage processes into and out of the intrinsic core of the double heterostructure. The red arrows represent current injection and the blue arrows leakage.*

The leakage has been modelled according to [80], which defines the carrier leakage to be a result of three separate processes: (i) - normal (Γ) electron leakage into the p-passive layer, (ii) - heavy (X) electron leakage into the p-passive layer and (iii) - hole leakage into the n-passive layer. These processes are illustrated in Figure 2.11. Thermionic emission can also play a role in carrier leakage, however

it has been shown [81], that diffusion currents dominate except in the case where the confinement barrier or carrier mobilities are very high. The leakage current is limited by the rate at which the carriers, with enough thermal energy to overcome the heterojunction barrier, can drift and diffuse into the cladding region. As we have seen in the previous section, under significant forward bias, the energy bands flatten and so a diffusion-limited current is assumed.

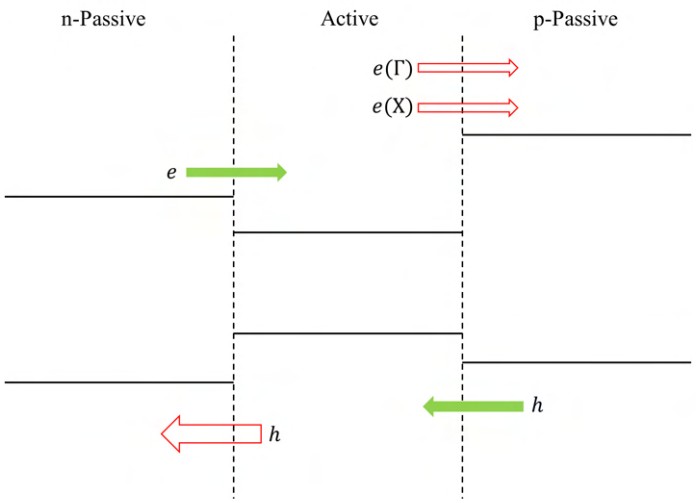


Figure 2.11: *Schematic diagram showing the different leakage processes in the device structure, detailed in the model described by [80]. The solid green arrows represent the injection currents whilst the hollow red arrows represent the leakage currents.*

Normal electron leakage

Electrons injected into the core are excited from this region into the conduction band of the p-passive region in the cladding before diffusing away. In this case, the resulting current can be described by,

$$J_\Gamma = \left(\frac{D_\Gamma}{L_\Gamma}\right) e n_\Gamma, \tag{2.7}$$

where L_Γ is the effective electron diffusion length, e is the electronic charge, D_Γ is the electron diffusion coefficient, given by $D_\Gamma = \mu_\Gamma k_B T/e$, where μ_Γ is the electron mobility, T is the absolute temperature, n_Γ is the density of excited carriers in the conduction band of the p-passive layer, given by,

$$n_\Gamma = N_c \left[\frac{p_{\text{active}} + N}{p_{\text{passive}}}\right] \exp\left(\frac{E_1 + \Delta E}{k_B T}\right), \tag{2.8}$$

where N_c is the effective density of states in the conduction band of the p-passive layer, p_{active} is the density of p-doping in the active region, N is the density of injected carriers, p_{passive} is the density of p-doping in the passive layer, E_1 is the quasi-Fermi level measured from the minimum of the conduction band, and ΔE is the heterojunction step energy. N_c takes the form,

$$N_c = \begin{cases} 2.5 \times 10^{19}(0.063 + 0.083x)^{3/2} & x < 0.41, \\ 2.5 \times 10^{19}(0.85 - 0.14x)^{3/2} & 0.45 \leq x \leq 1. \end{cases} \tag{2.9}$$

The quasi-Fermi level E_1 can be estimated by the empirical Nilsson approximation [82]. Typical values for the electron diffusion length, L_Γ, are 3-5μm, calculated by $L_\Gamma = \sqrt{D_\Gamma \tau_\Gamma}$, where τ_Γ is the carrier lifetime. However, given that the p-passive layer in all three of our wafers are significantly smaller than this value, an electron excited into this layer will diffuse the total thickness of the layer before recombining, thus L_Γ is taken to be the thickness of the p-passive layer, as per the model. Finally, the injected carrier density in the active region can be estimated from the injected current density, J, via,

$$N = \sqrt{\frac{J}{B_0 e d}}, \tag{2.10}$$

where d is the thickness of the active region and B_0 is the bimolecular radiative recombination coefficient, which has a value of $\sim 2 \times 10^{-10}$ cm$^3 s^{-1}$ for most III-V compound semiconductors [83, 84, 85]. Since this expression only considers the effect of bimolecular recombination, it is only valid for direct band-gap semiconductors, i.e. $Al_xGa_{(1-x)}As$, with $x \leq 0.45$. Given that the devices considered in this study have active regions with $x \leq 0.25$, it is valid to use this expression for the current density in the active region.

Heavy electron leakage: Along with normal electron leakage into the p-passive

region of the cladding, there will also be a current of electrons diffusing into the X conduction band of the p-passive layer. This leakage current can be written in terms of the Γ leakage as,

$$J_X = J_\Gamma ab \exp\left(-\frac{\Delta}{k_B T}\right), \tag{2.11}$$

where a and b are the ratios of the heavy to light electron mobilities and density of states respectively and Δ is the difference in energy between the Γ and X bands [86], given as,

$$\Delta = 0.38 - 0.892 x_{\text{passive}} - 0.365 x_{\text{passive}}. \tag{2.12}$$

Hole leakage

The calculation of hole leakage is analogous to that of normal electron leakage, except the hole quasi-Fermi level and valence band are substituted in place of the electron quasi-Fermi level and valence band. Due to the slower diffusion rates of holes, hole leakage is expected to be generally much smaller in magnitude than electron leakage effects. The estimated leakage effects have been simulated for the double heterostructures of each wafer and are shown in Figures 2.12a, 2.12b, and 2.12c.

As has been seen in the previous section, carrier leakage is more pronounced in the case of large carrier injection. In this scenario, the barrier heights are reduced and the Fermi energy level increases leading to an increased probability that carriers can overcome the heterostructure barrier and diffuse into the cladding layers. For RC101, we observe that normal (Γ) electron leakage dominates, whereas heavy (X) electron leakage dominates for the other two wafers. This is due to the increased aluminium concentration in the core regions - when the aluminium concentration of the core exceeds 15%, a larger portion of electrons tend to lie in the X minima owing to an increase in the density of states [81]. Current leakage in RC184 is calculated to be significantly lower than in the

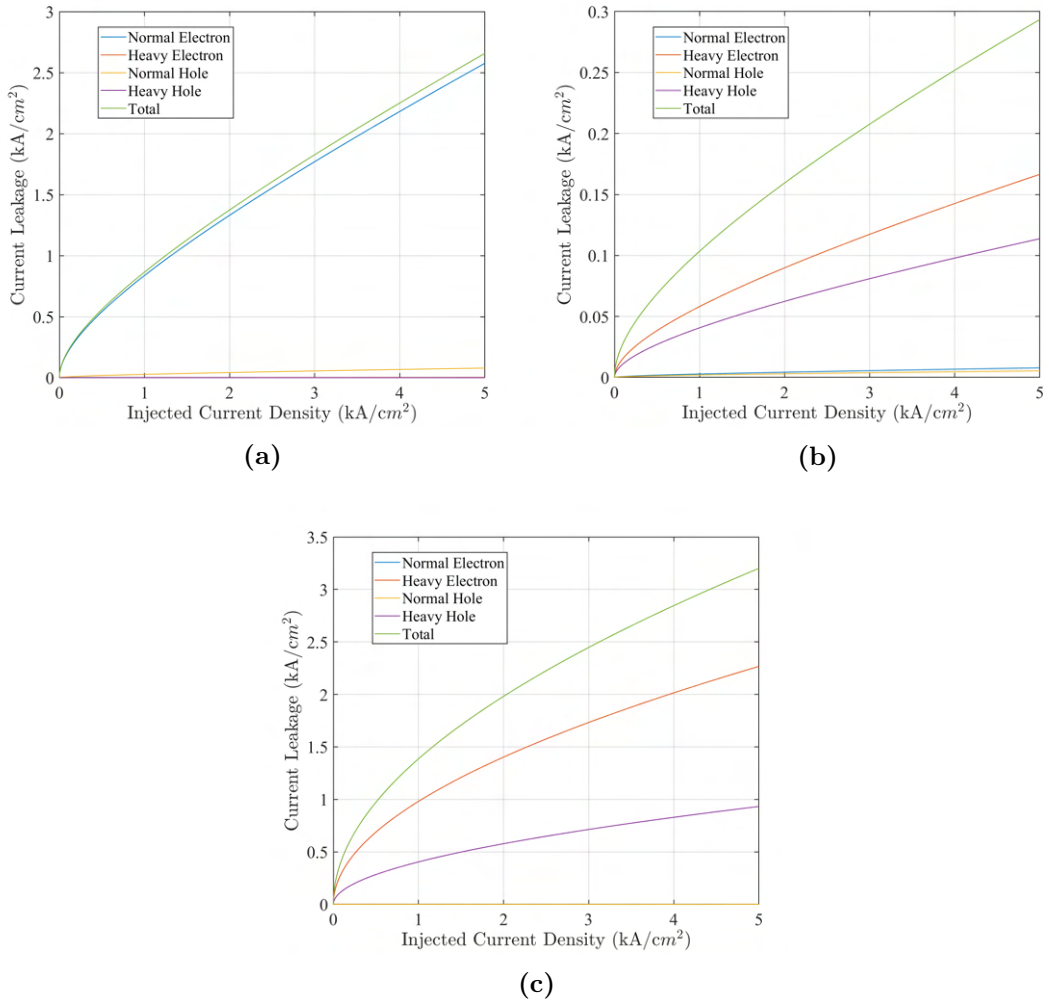


Figure 2.12: *Carrier leakage as a function of the injected current densities for the three wafers, (a): RC101, (b): RC184, (c): RC187.*

other wafers. This is most likely due to a combination of thick cladding layers and an increased aluminium concentration in the core. Thinner cladding layers ($\sim 20\%$ thinner), in RC187 lead to a higher overall leakage current.

The p-injection and n-confinement regions of devices fabricated from the RC184 and RC187 wafers in this study both have indirect band-gaps. This introduces another leakage path via the L-minima. However, hydrostatic pressure measurements of GaAsP/AlGaAs quantum well lasers, with indirect AlGaAs cladding, have shown that the electron transport through the X-minima governs the leakage process and that the Γ-minima leakage is insignificant [87]. This therefore validates the exclusion of the L-minima leakage path in this model for RC184

and RC187 devices.

2.3.3 Carrier Spreading

Due to the sheet resistance of the semiconductor material, carriers cannot spread freely after injection at the contact stripe. Therefore, to consider the spatial effects of the refractive index profile, we must incorporate the diffusion of carriers into the model. The carrier diffusion is modelled according to [88], Figure 2.13. This model assumes a direct current path to the n-type layer and knowledge of the sheet resistance of the semiconductor material under the contact. Sheet resistances for each wafer were calculated using the circular transmission line method during the fabrication process, further detail of which is given in Chapter 3. The carrier spreading model is modified later in the thesis in light of observations of the switch testing in Chapter 5 to include crowding effects due to the geometry of the mesa. The model in this section therefore ignores these crowding effects and better describes the simplified case of an optical switch with a backside contact. Nevertheless, these simulations are useful for demonstrating the fundamental operating principles of the switch design in a best-case scenario.

Within the stripe region $-S \leq x \leq S$, considering only spontaneous recombination, the linear diffusion of carriers is governed by,

$$\frac{d^2n(x)}{dx^2} = \frac{n(x)}{L^2} - R, \tag{2.13}$$

where $n(x)$ is the concentration of carriers, and R is the rate of carrier injection, given by,

$$R = \frac{J_0}{qDd}, \tag{2.14}$$

where D is the diffusion constant within the stripe region, and q is the electronic charge. Carriers diffuse symmetrically from the centre of the stripe, in which case the spatial variation of carriers for $-S \leq x \leq S$ is given by,

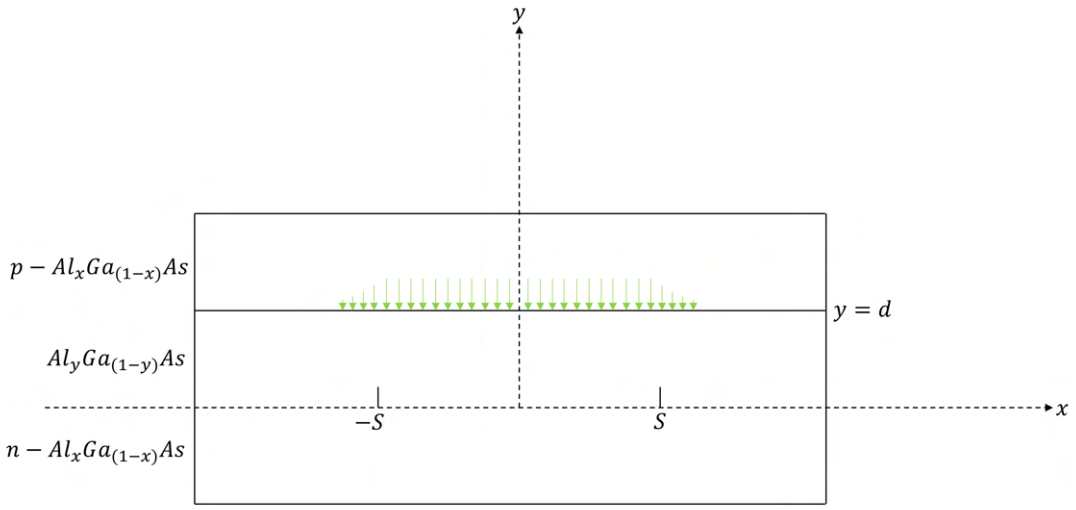


Figure 2.13: *Schematic diagram depicting the model of current injection into the device and the spreading of carriers due to diffusion, as modelled by [88]. The carrier density is assumed to be uniform over the width of the stripe, which extends from $-S$ to $+S$. Outside the stripe region in the x-direction, the density of carriers decays exponentially. In the z-direction, there is no variation.*

$$n(x) = RL^2 + [n(0) - RL^2] \cosh\left(\frac{x}{L}\right), \tag{2.15}$$

where $n(0)$ is the concentration of carriers at the point of injection.

Outside the stripe region, $|x| > S$, the current profile is given by,

$$J = J_0 \exp\left(-\alpha|x - S|\right), \tag{2.16}$$

where $\alpha = 2.2\sqrt{J_0 K/2\sigma}$, $K = q/n_f k_B T$, where n_f is the diode ideality factor (see Chapter 5 for more detail), and σ is the semiconductor sheet resistance. The diffusion equation in this case is then given by,

$$\frac{d^2 n(x)}{dx^2} = \frac{n(x)}{L'^2} - R_0 \exp\left(-\alpha|x - S|\right), \tag{2.17}$$

where L' is the diffusion length outside the stripe region. The general solution of 2.17 calculated by [88] is,

$$n(x) = A_1 \exp\left(\frac{-x}{L'}\right) + A_2 \exp\left(\frac{x}{L'}\right) + B \exp\left(-\alpha|x|\right), \tag{2.18}$$

where

$$A_1 = \frac{\left(\left(R_0 L - \frac{B}{L}\right)\sinh\frac{S}{L} - \alpha B\cosh\frac{S}{L}\right)e^{S/L'}}{\frac{1}{L}\sinh\frac{S}{L} + \frac{1}{L'}\cosh\frac{S}{L}}, \tag{2.19}$$

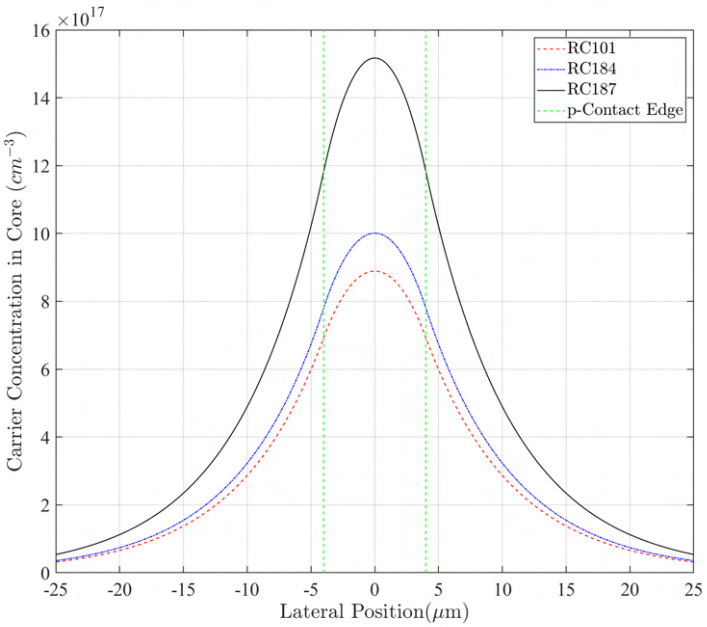
and

$$B = \left(\frac{J_0 L'}{qdD}\right)\left(\frac{L'^2}{1-(\alpha L')^2}\right). \tag{2.20}$$

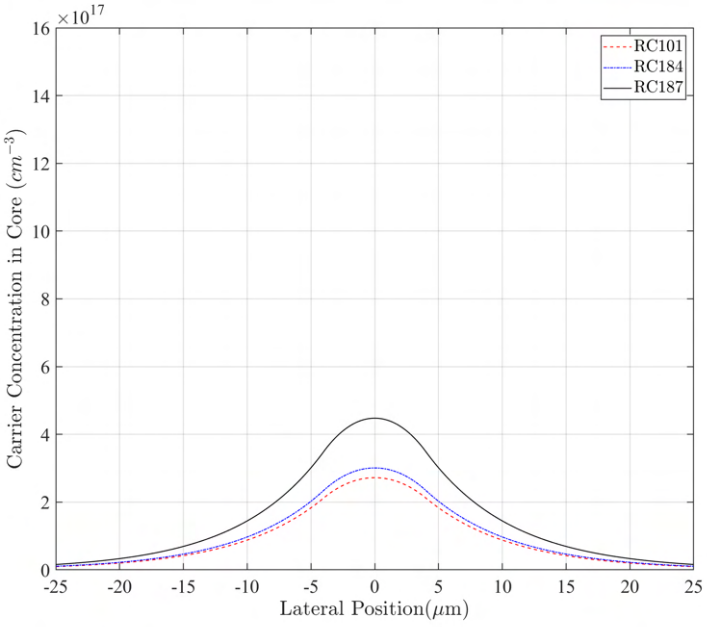
Continuity of the carrier concentration and diffusion current at $x = S$ gives $n(0)$ as,

$$n(0) = \frac{\left(\frac{B}{L'} - \alpha B - \frac{R_0 L^2}{L'}\right)}{\left(\frac{1}{L}\sinh\frac{S}{L} + \frac{1}{L'}\cosh\frac{S}{L}\right)} + RL^2. \tag{2.21}$$

Finally, the symmetric distribution of carriers at the point of injection means the solution may be simplified by only considering the region $S > L$, which results in $A_2 = 0$. The carrier concentration as a function of the lateral position around the stripe has been calculated for RC101, RC184 and RC187 with and without current leakage, and plotted in Figure 2.14. It is evident from these calculations that the diffusion effects are lower for higher aluminium concentrations as a result of the lower carrier mobilities, leading to a higher carrier concentration in the core.



(a)



(b)

Figure 2.14: *Distribution of current in the core in the region underneath the contact stripe (a): ignoring leakage effects and (b): including current leakage. The electrical parameters used in this calculation have been determined from experimental data. The injected current density was assumed to be* $J_0 = 3000A/cm^2$. *The green dashed lines indicate the positions of the edges of the contact stripe.*

2.4 Optical Confinement

In addition to the electrical confinement properties of the double heterostructure design, the nominal refractive index contrast between the cladding and core epitaxial layers gives rise to optical confinement in the form of a basic three-layer planar waveguide. This structure can also be modified to form waveguides which can provide stronger optical confinement in a given direction. In this section, the mathematical details concerning the calculation of the appropriate dimensions for strip-loaded waveguides are presented to ensure propagation of only the fundamental mode of a guided optical wave.

2.4.1 Effective Index of the Slab Mode

The fundamental geometry of the planar waveguide, illustrated in Figure 2.15, forms the basis for other more sophisticated wave-guiding structures used in optical integrated circuits, [17]. The refractive index contrast between the cladding (n_1, n_3) and core (n_2) layers provide optical confinement in the x direction, with propagation in z.

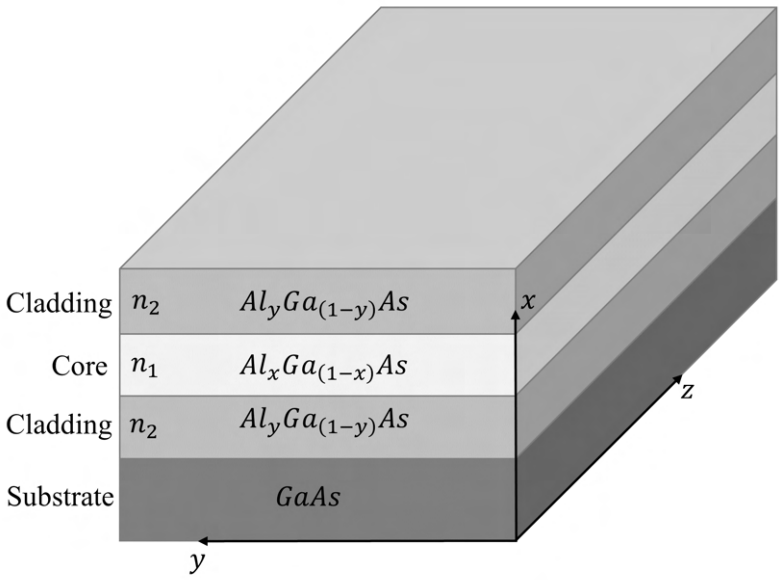


Figure 2.15: *Illustration of the planar waveguide formed by epitaxial AlGaAs cladding and core layers, grown on a GaAs substrate, with differing aluminium concentrations, where $y > x$. The doped capping layers have been omitted here for clarity.*

To simulate propagation of a plane wave within the wave-guiding structure, the phase change per unit length caused by propagation in the medium must be known. The effective refractive index, n_{eff} is the quantity used to determine this phase change, and is related to the frequency-dependent propagation constant β by,

$$\beta = n_{eff}\frac{2\pi}{\lambda_0} = n_{eff}k \tag{2.22}$$

where λ_0 is the free-space wavelength of the guided wave and k is the wavenumber. For a given mode and wavelength, the propagation constant of the waveguide may be calculated and subsequently the effective refractive index through Equation 2.22. For transverse electric (TE) modes, the propagation constant of a three-layer planar waveguide is calculated by solving the following transcendental equation (i.e. plotting both sides as a function of β and noting the intersection point),

$$\tan(ht_g) = \frac{p+q}{h(1-pq/h^2)}, \tag{2.23}$$

where

$$\begin{aligned} q &= \sqrt{(\beta^2 - n_1^2k^2)}, \\ h &= \sqrt{(n_2^2k^2 - \beta^2)}, \\ p &= \sqrt{(\beta^2 - n_3^2)}, \\ k &= \omega/c = 2\pi/\lambda_0. \end{aligned} \tag{2.24}$$

where t_g is the thickness of the core layer. The result is a set of discrete allowed values for β for a given mode and wavelength. For guiding of a given mode, the refractive index contrast between core and cladding,(Δn), where $\mathrm{n_{core}} > \mathrm{n_{cladding}}$, must obey,

$$\Delta n > \frac{m^2 \lambda_0}{4t_g^2(n_2 + n1)}, \tag{2.25}$$

where $m = 0, 1, 2, ...$ is the mode number. Figure 2.16 shows the calculation of the effective index for the fundamental TE mode of the RC101 material at 894.5 nm. This calculation was repeated for the layers of the other wafers at their relevant quantum sensing wavelengths for both TE and TM fundamental modes, and the results are summarised in Table 2.3. The relevant equations for TM modes are,

$$tan(ht_g) = \frac{h(\bar{p} + \bar{q})}{h^2 - \bar{p}\bar{q}}, \tag{2.26}$$

with

$$\bar{q} = \frac{n_2^2}{n_1^2} q, \tag{2.27}$$

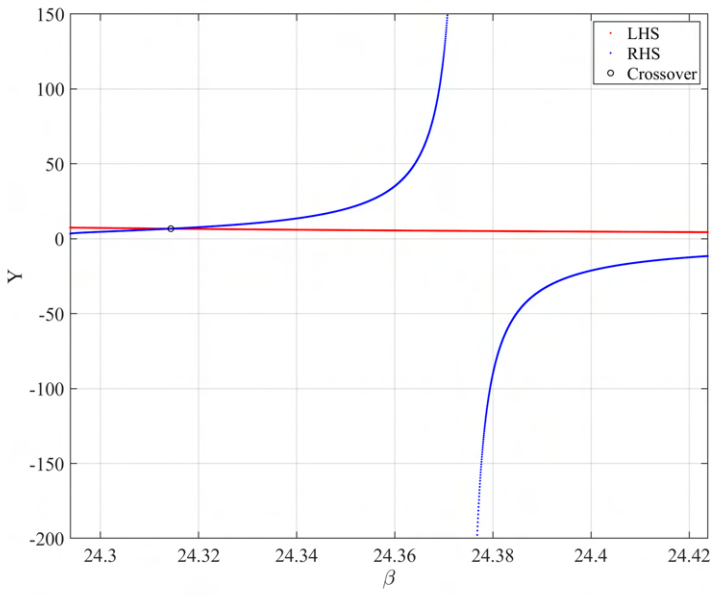


Figure 2.16: *Calculation of the effective index of the planar waveguide of RC101 heterostructure layers at $\lambda = 894.5nm$ for the fundamental TE mode by solving the transcendental equation, Equation 2.23. The y-axis (labelled Y), represents the numerical value of the left hand side (red) or right-hand side (blue) of Equation 2.23.*

Table 2.3: Calculated effective indices of the fundamental TE and TM modes for the slab mode of each epitaxial wafer.

Wafer	**Mode**	**Wavelength (nm)**	**Index Contrast Δn**	**Effective Index n_{eff}**
RC101	TE_{00}	894.50	0.14807	3.4615
RC101	TM_{00}	894.50	0.14807	3.4605
RC184	TE_{00}	780.25	0.18538	3.4917
RC184	TM_{00}	780.25	0.18538	3.4884
RC187	TE_{00}	766.7	0.22387	3.4519
RC187	TM_{00}	766.7	0.22387	3.4456

2.4.2 Strip-loaded Waveguides

Strip-loaded waveguides can be used to provide confinement in both x and y (propagation in z), by partially etching away the top cladding layer [89]. Figure 2.17 illustrates the principle of the strip loaded waveguide.

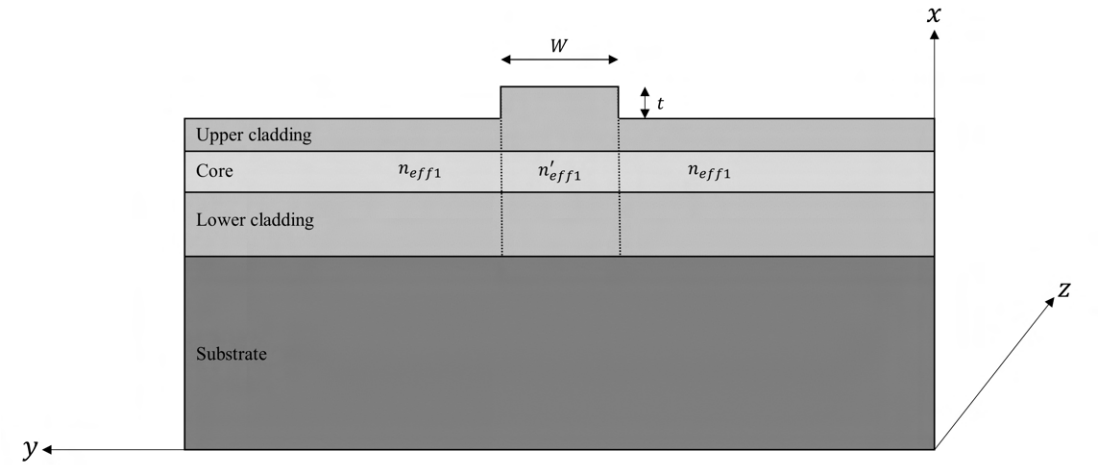


Figure 2.17: *Illustration of the cross section of a strip-loaded waveguide, where W is the width of the waveguide strip and t is the strip height.*

The formation of the 'loading strip' above the guiding layer causes the effective index in the region below the strip to be larger than the effective index in the adjacent regions, providing lateral confinement for the guided wave. This can be achieved by etching away a portion of the top cladding layer of a planar slab waveguide to form the strip. Of course, the height of the strip determines the extent of the confinement as well as the number of optical modes supported by the waveguide. To ensure propagation of only the fundamental mode, the effective

index method [90, 91] along with the normalised frequency,

$$V = \frac{W}{2} k \sqrt{{n'_{eff1}}^2 - n_{eff1}^2}, \tag{2.28}$$

where W is the waveguide width, n'_{eff_1} is the effective index below the loading strip and n_{eff_1} is the effective index in the adjacent region as illustrated in Figure 2.17, can be used to calculate the required etch depth of the loading strip according to the initial layer thicknesses, lateral dimensions of the waveguide, and requirements for single mode. The normalised frequency determines the fraction of the optical power in a certain mode which is confined to the waveguide core. It is assumed from the effective index method that waveguides with $V < \pi/2$ support only the fundamental mode, whereas waveguides with $\pi/2 \leq V \leq \pi$ and $\pi < V \leq 3\pi/2$ support two and three modes respectively [92]. As an example, Figure 2.18 shows the theoretically calculated normalised frequencies for various waveguide widths as a function of the top cladding etch depth for the RC184 wafer. The height of the strip can be adjusted in the fabrication process, whilst the width is fixed by the pattern on the photomask. Taller loading strips (deeper etches) result in stronger confinement and hence lower propagation losses, however this increases the probability of creating a multimode waveguide [17]. Therefore, there is a trade-off between confinement and reliable single-mode operation. Thus, etch depths must be chosen resulting in normalised frequencies just below the single mode cut-off values.

2.5 Optical Switch Design

The optical switch design exploits all of the aforementioned physical principles in its intended operation. The design is based on a semiconductor double heterostructure grown on semi-insulating (SI) GaAs (100) 76mm diameter substrates, using in-house molecular beam epitaxy (MBE) - see Table 2.1 for the epitaxial structure. Growth of the epitaxial structures was carried out by Dr

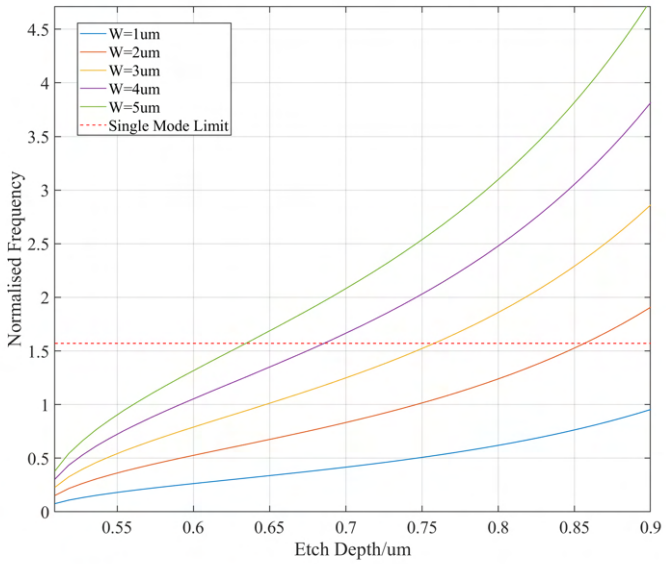


Figure 2.18: *Theoretical calculation of the normalised frequency for various waveguide widths, as a function of the top cladding etch depth for the RC184 wafer at 780.25 nm. The single mode cut-off value determines the maximum etch depth for single mode operation.*

Richard Campion at The University of Nottingham, using a Veeco Gen II MBE reactor equipped with reflection High Energy Electron Diffraction (RHEED) in-situ surface reconstruction monitoring, and BandIT temperature control systems.

A three-dimensional representation of the optical switch design is illustrated in Figure 2.19. The operation of the switch may be described as follows: at the cleaved facet light is coupled into the active steering region. A small voltage is applied across each set of contacts on either side of the mesa, causing an injection of carriers into the core layer, where they begin to diffuse. A portion of these carriers are lost by leakage effects. Those that are confined to the core cause a carrier density-dependent reduction in the band gap due to renormalisation effects, followed by band-filling effects causing an apparent expansion of the band gap. The result is an overall decrease in the local refractive index profile of the core under the contacts due to electrical carrier injection, forming a channel waveguide with a reduced effective index of refraction, n_{eff}, in this region.

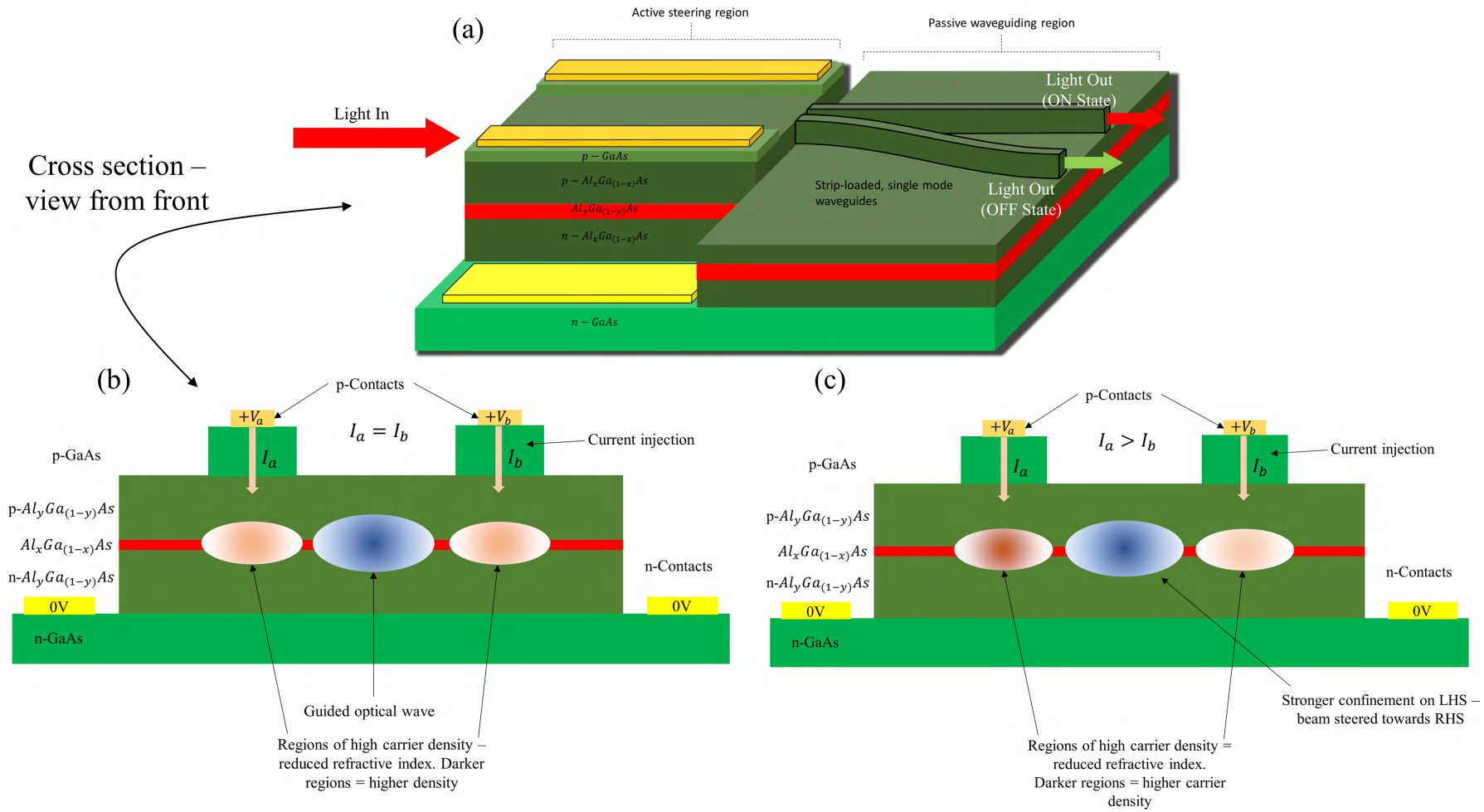


Figure 2.19: *Illustration of the proposed switch design showing the various epitaxial layers, mesa structure and single mode strip-loaded waveguides. In (a) an isometric representation of a single device is shown, consisting of a steering (active) section and a waveguiding (passive section). In (b), a cross section of the steering section is illustrated. In this section, a bias is applied across the device contacts on both sides, causing carriers to be injected into the core, where the highest density resides directly below the p-contacts. If an equal bias is applied across each side of the mesa (b), the density of carriers either side of the guided wave in the core is approximately equal, resulting in regions of depressed refractive index either side of the guided wave. The guided wave is then confined to the central region. When an unbalanced bias is applied (c), there will be a higher density of carriers on one side of the guided wave, causing the refractive index profile to become unbalanced, resulting in stronger confinement on the side with higher refractive index. The result is beam steering in the direction where the current injection is lowest. The guided beam can then be steered into either waveguide input port, located at the end of the steering region. This forms the switching action.*

By changing the balance of the voltages between the contacts, the carrier profile in the core can be altered and consequently the refractive index profile, allowing the guided beam to be steered into one of the two output, single-mode, strip-loaded waveguides at the end of the steering region. These waveguides are terminated using tapered outputs to allow for efficient coupling into a single mode fibre when packaged. With balanced currents, light enters the input facet in between the two regions of depressed refractive index and subsequently propagates through the steering region by total internal reflection (TIR), akin to propagation through a graded index waveguide. Using this configuration, the beam may be switched on or off by steering the beam into the straight or curved waveguide respectively. The inputs of the waveguides, delineated at the end of the steering region, are also tapered and offset from the centre of the propagation axis. This means that slightly unbalanced currents are required to steer the beam into either waveguide input, as shown in Figure 2.20.

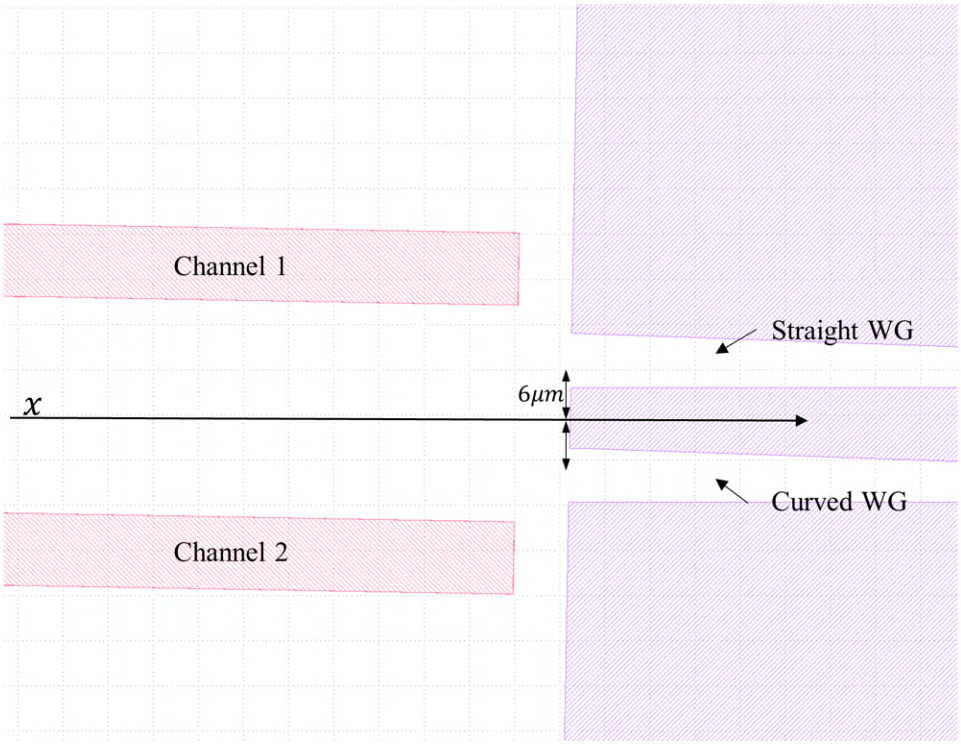


Figure 2.20: *Illustration of the positioning of the input of the waveguides, delineated at the end of the steering region. The waveguides are offset from the centre of the propagation axis, so some steering is required to couple the beam into either waveguide.*

The electrically-controllable beam steering capabilities of the proposed design allow flexibility in the configuration of the output waveguides. In its simplest form the device may be configured as a single module as illustrated, where the straight waveguide is used as the 'ON' channel and the curved waveguide used as the 'OFF' channel. When the beam is steered into the 'OFF' channel it may be coupled to an output fibre for optical power monitoring or simply dispersed in the bulk material, for cases where the optical beam power is low ($\leq$50 mW). For an enhanced extinction ratio, the output of the waveguides from the first device may be terminated by another device, thus becoming the input for a second active region. In the proposed design, switching devices which are intended to consist of multiple single switching modules have their curved 'OFF' waveguides terminated at a different position to the final module. This allows the 'OFF' channel at each stage to be monitored, whilst still maintaining the optoelectronic packaging standard 250 μm separation of the final waveguides for coupling into output fibres. As mentioned in Chapter 1, suitability for the intended application demands that the switching device has the capability of extinguishing the beam by $\sim$80 dB within a couple of microseconds. For the proposed design, this introduces a requirement of around 20 dB per switching module. Four devices cascaded in series on a single die would then form a entire optical switching device, with an extinction of $\sim$80 dB. The switching speed of the devices is dominated by the charge storage delay time of the device which is related to the capacitance of the p-i-n structure. The depletion-layer capacitance (transition capacitance) and diffusion-capacitance dominate the junction capacitance of the diode [93], although the diffusion capacitance is much larger in a forward biased p-in diode. These quantities are determined by the width of the intrinsic region and the dielectric properties of the material. Since the intrinsic layer as a much larger resistance than the surrounding cladding layers, the capacitance of the p-i-n structure is analogous to that of a parallel plate capacitor with capacitance, $C = \epsilon_r \epsilon_0 A/d$, where A is the plate (cladding layer) area and d is the

plate separation (core thickness). A further discussion on the estimated switching characteristics due to these effects will be presented in Chapter 4.

2.6 FFT-BPM Simulations

Introduced by Feit and Fleck in 1978 [94], the beam propagation method (BPM) is an approximate mathematical method for solving problems of light propagation in dielectric optical waveguides of arbitrary shape. BPM is a powerful tool for simulating the propagation of guided waves in optical circuits for situations where refractive index differences are small and reflections can be legitimately ignored. BPM can be implemented using the fast Fourier transform (FFT) algorithm to produce efficient simulations of guided optical waves through photonic devices. In this project, a custom FFT-BPM simulation has been designed to simulate the propagation of a guided wave through the active steering region of the proposed optical switch, taking into account the refractive index change effects due to carrier injection and also the aforementioned carrier leakage and spreading effects due to the double heterostructure design. These simulations firstly give a demonstration of the ideal intended operating characteristics of the device and also some insights into how different geometry considerations affect the performance. The model is adjusted in Chapter 5 as a result of observations from testing the devices to include carrier spreading effects due to the geometry of the mesa on semi-insulating GaAs substrates.

2.6.1 Algorithm

As a result of the assumption that the change in refractive index of the guiding medium is small, a guided wave (in z) is assumed to be travelling in a slightly inhomogenous medium and experiences diffraction and a given amount of phase shift depending on its x and y positions. Provided that the space along the propagation direction is divided into short segments of length Δz, these effects can be

applied separately in time and the continuous medium can be replaced by a series of thin lenses, with the regions in between the lenses having a constant refractive index, $\bar{n}$, given by the average of the refractive index distribution in the region between adjacent lenses. A more thorough explanation of the BPM algorithm can be found in [95], this section focuses on the description of the algorithm used to simulate the effect of the refractive index changes on the propagation of a guided wave through the steering section of the devices.

The devised algorithm for simulating beam propagation through the active steering region of the proposed devices begins with the calculation of the effective index of the planar slab, using the effective index method described in Section 2.4.1, according to the properties of the chosen wafer to be simulated. Once the injection current for each p-contact has been defined, the corresponding carrier concentration is calculated followed by the carrier leakage from the core region below each of the p-contacts. The distribution of these carriers due to diffusion effects and the specific contact resistivity of the underlying semiconductor layer is then calculated giving a one dimensional profile, as shown in the example calculated in Section 2.3.3, Figure 2.14. This results in a 1D vector of size N, representing the carrier density at each point in y (direction perpendicular to propagation). Since the p-contacts are homogeneous in the propagation direction, this 1D vector is repeated N times to give a $N \times N$, 2D mesh of the carrier density in the simulation region. Subsequently, the refractive index change effects for each value of the carrier density in the mesh is calculated according to the three effects discussed earlier in this Chapter, resulting in another 2D mesh with values of Δn for each point. The effective index of the slab mode of the steering region is than applied to the mesh, resulting in a refractive index profile for the steering region for the given injection currents at each p-contact. Figure 2.21 shows an example of the refractive index profile of the core of the steering region for an injection current of 50 mA at each p-contact for the RC101 wafer for the fundamental TE mode at 904 nm. The depressed refractive index profile at the positions of the

p-contact is clear here.

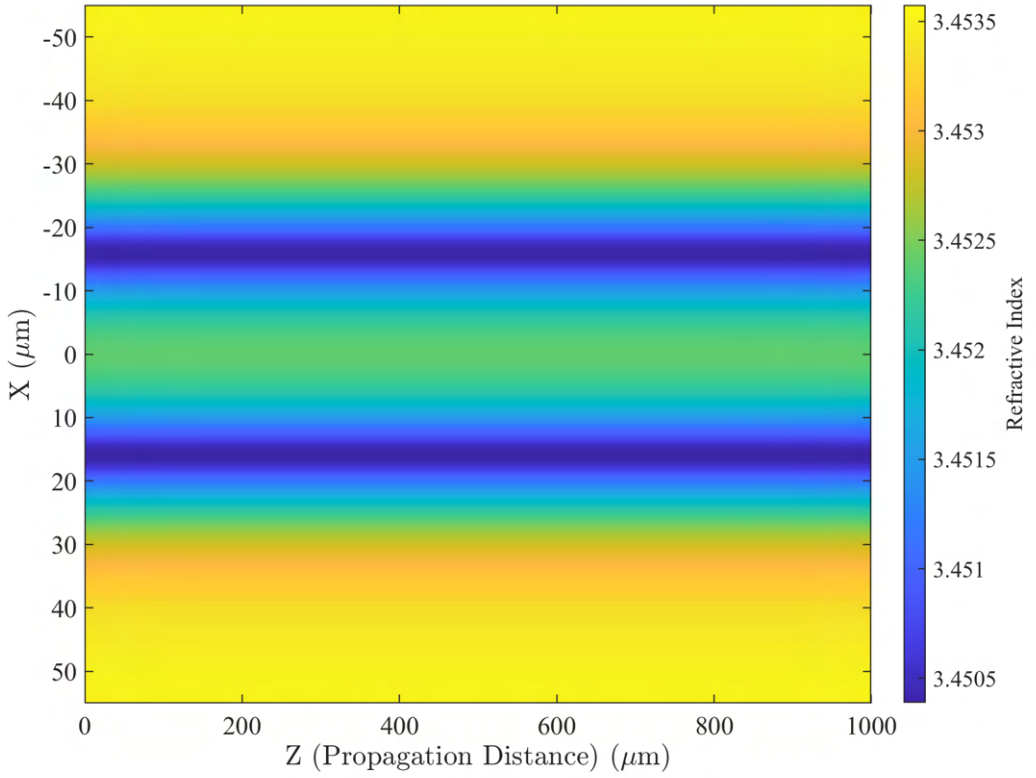


Figure 2.21: *Simulated refractive index profile of the steering region of RC101 due to injection of 50 mA at each p-contact, for the fundamental TE mode at 904 nm.*

Following calculation of the refractive index profile, a Gaussian pulse representing the input beam is set to propagate through the mesh at $x = 0$ with profile,

$$I = I_0 \exp\left(-\frac{(x - x_0)^2}{w_0^2}\right), \tag{2.29}$$

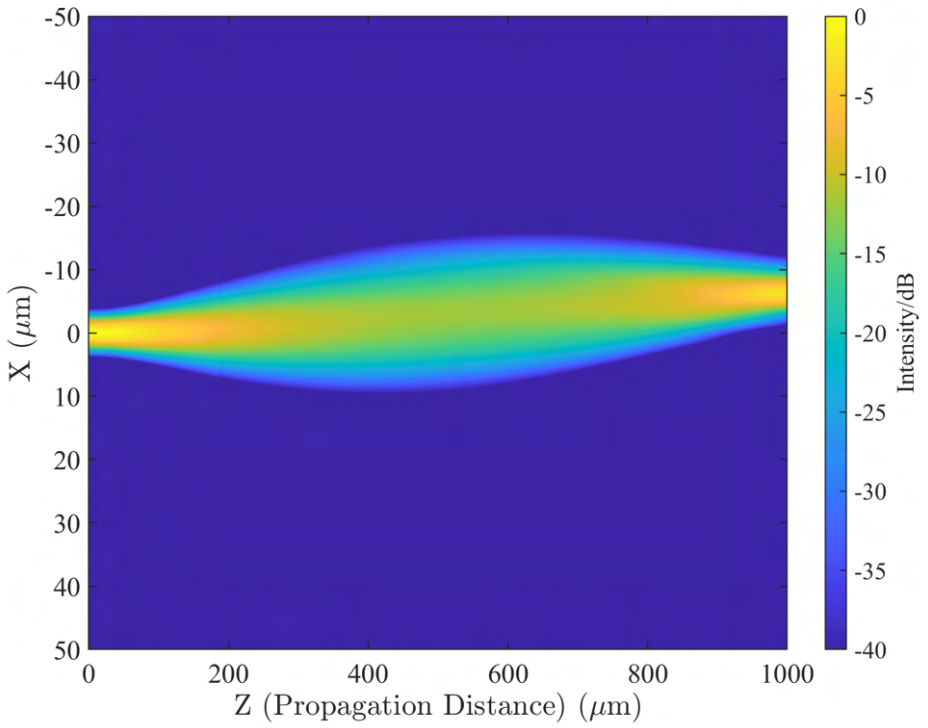
where I_0 is the peak intensity, x_0 is the position of the centre of the beam, and w_0 is the beam radius, defined as the distance at which $I = I_0$ to the point at which the beam intensity falls to $1/e^2$ of I_0. Propagation of this beam through the mesh is then computed by calculating the 'free space' step of wave propagation in a homogeneous medium and 'lens' step to correct for the phase change imposed by the inhomogeneous medium. A buffer region around the edge of the mesh is included to attenuate the beam to prevent back reflections of the wave into

the guiding region. The result is a new 2D mesh representing the magnitude of the beam intensity at each point in x and z as it propagates through the medium. These intensity values are converted to a decibel scale and plotted on an image map with a colour scale. The simulation is checked for completeness by numerically integrating the profile of the beam at the input in x and at the output. If the difference between these two values is less than a pre-defined tolerance level then the simulation is considered stable and is marked complete.

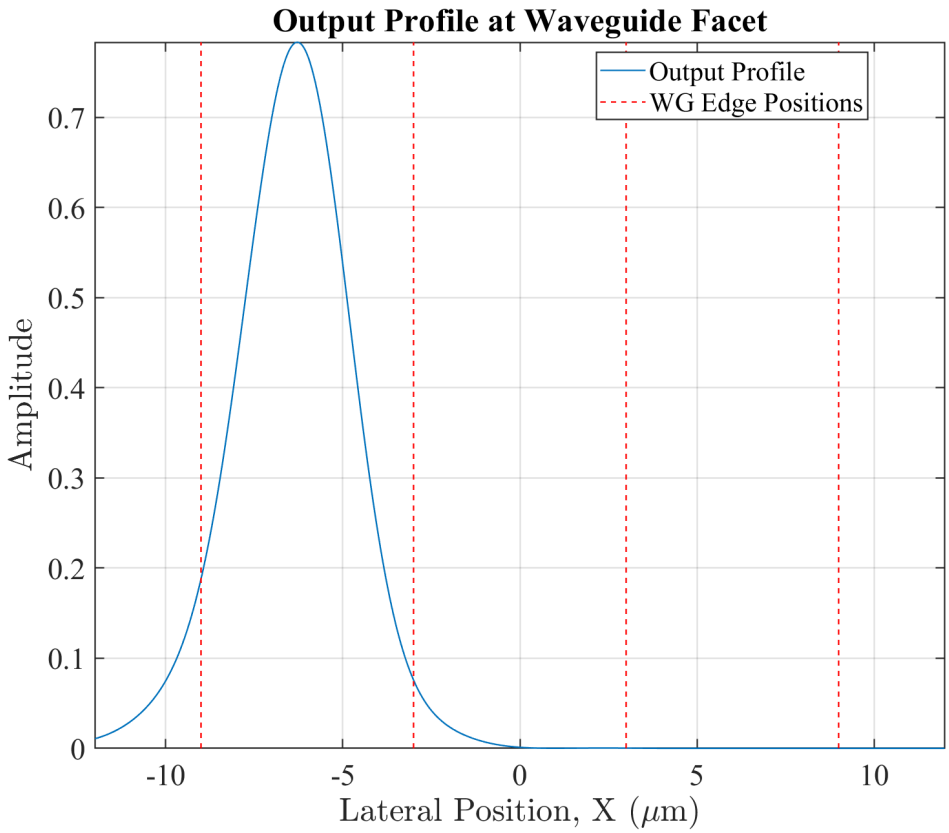
2.6.2 Beam Steering Simulations

Simulations using the FFT-BPM algorithm can give some insights into the strength of the intended beam steering effects for each epitaxy, and provide some quantitative analysis regarding the ideal parameters required to steer the beam into the output waveguides. Figure 2.22 shows the simulation of beam steering effects for the RC184 wafer at 780 nm (fundamental TE mode), for unbalanced current injections of 5 mA through the left contact (in the direction of propagation), and 50 mA through the right contact. Also shown is the output profile of the beam at the end of the steering region, which is shown to peak 2.9 μm from the centre of the propagation axis, indicating the strength of the beam steering for this set of input currents.

The BPM simulations were used to investigate the beam steering strengths for devices from each epitaxy, at their relevant design wavelengths to determine the ideal current injections required to steer the beam into each output waveguide, i.e. to steer the beam laterally by 6 μm in each direction. To do this, the portion of the guided optical beam at the entrance to the tapered waveguides was calculated by integrating across the width of each waveguide. This value was then divided by the total portion of the guided beam across the 24 μm width of the waveguide facet. Figure 2.23 shows an example of one of these calculations for RC184, and an accompanying schematic to illustrate the portion of the device concerned. The full results are summarised in Table 2.4.



(a)



(b)

Figure 2.22: *FFT-BPM simulation of propagation of a 767 nm fundamental TE mode beam through the steering region of a device from the RC187 wafer, due to a current injection of 96 mA and 250 mA at the left and right contacts respectively. (a) shows a plan view of the beam propagation and (b) shows a cross section of the output profile, where the peak is shown to have shifted by 6.2 μm from the centre of the propagation axis.*

We find that there are limitations on the beam steering capabilities with increasing current, which is more pronounced with RC101 than RC184 and RC187, and with RC184 than with RC187. This is due to the previously discussed phenomena which are contributing to, or working against the beam steering. The RC187 epitaxy has the strongest refractive index changes for a given current injection compared to the other two wafers, at its design wavelength. With RC184 and RC187, it is possible to squeeze the beam into the desired position by increasing the current through each side of the mesa. For RC101, the limitation is reached at a lower current injection as the band gap shrinkage effect takes over and further increasing the current acts to increase the refractive index, working against the Moss-Burstein effect and the result is weaker manipulation of the guided beam. The results is less power coupled into each waveguide.

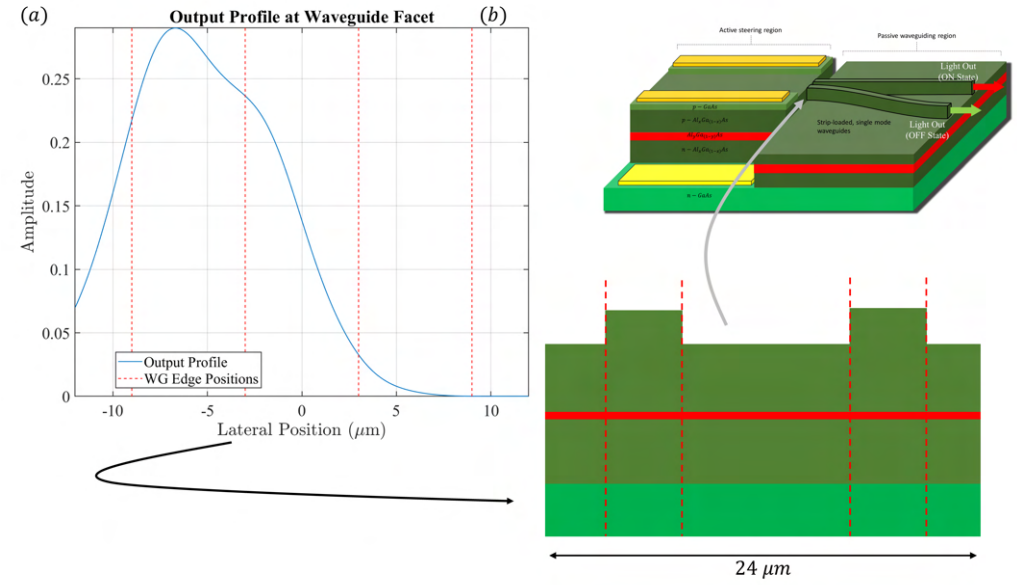


Figure 2.23: *Calculation (a), and illustration (b) of the method for simulating the portion of optical power coupled into each output waveguide of the device. In (a), RC187 has been simulated for a guided optical wave at 780 nm with a current injection of 60 mA at the left hand-side contact (with respect to the propagation direction), and 160 mA at the right hand-side contact. The portion of the beam coupled into each waveguide has been calculated by integrating across the width of each waveguide and dividing this value by that obtained by integrating across the 24 μm width of the facet (the width of the portion of the facet from the edge of one p-contact to the other). Note that the width of the waveguides here are 6 μm as they are tapered out from the required 2 μm width to increase the coupling efficiency.*

Table 2.4: Various theoretically calculated current injections for devices from each wafer to couple the maximum amount of light possible into either output waveguide (ON or OFF), demonstrating the range which is able to be coupled into each waveguide. Note that the percentages do not total 100% since some of the power falls outside the region of both waveguides. Device design and therefore current injection are symmetric so the values of current injection to couple into one waveguide are reversed to couple into the other.

Wafer	**Vacuum Wavelength (nm)**	**Current injection - LHS, RHS (mA)**	**Coupled Power - ON (%)**	**Coupled Power - OFF (%)**
RC101	904	40, 160	55.9	1.7
RC184	780	80, 250	73.4	0.17
RC187	767	96, 250	91.7	0.0007

2.7 Summary

In this chapter an optical switch design, based on carrier-induced refractive index change effects, has been presented. A theoretical model was developed, based on relevant literature, to estimate the strength of these effects for the designed epitaxial structures. Finally, a FFT-BPM simulation was used to simulate the propagation of fundamental TE modes through these structures, at their design wavelengths. From these considerations, the ideal operating conditions have been determined through the FFT-BPM simulations which will give a basis for the testing of the fabricated devices, discussed in Chapter 5. In the following chapter, the fabrication of these devices from the RC184 and RC187 wafers will be detailed, carried out at the clean rooms of The University of Nottingham.

Chapter 3

Device Fabrication

3.1 Introduction

The fabrication of semiconductor optoelectronic devices is a complex, multi-stage process, involving the optimisation and characterisation of individual steps to achieve consistent and reliable results. The fabrication of optical switching devices studied in this project are no exception, involving twenty major processing stages. In this chapter, the relevant characterisation and fabrication steps carried out at the clean rooms of The University of Nottingham to fabricate these devices will be presented. A step-by-step guide to fabricating the devices from start to finish is reserved for Appendix A.

3.2 Photolithography

To build up the structures on a semiconductor wafer forming an photonic integrated circuit (PIC), the wafer material must be first patterned. Optical photolithography using a photosensitive polymer was implemented as the patterning process of choice in the fabrication of the optical switching devices for this project. The photoresist used was the Clariant AZ5214E image reversal resist, which allowed the patterning of features as small as 2 microns for the waveguiding structures, as well as the flexibility of adapting the process to produce undercut

sidewalls for lifting off evaporated metal films when forming metal contacts.

To form the structural features of the PIC, various patterns are transferred from a chromium-plated photomask onto the photoresist-coated wafer by UV-exposure. These masks, designed by Dr James Moss, Dr Chris Mellor, and Dr Jessica Maclean, contain the patterns for each layer of the fabrication process. The first step in transferring a pattern from a mask to the wafer sample is thus to evenly coat the sample in the photoresist. This was achieved using a Laurell WS-650 Series Spin Processor. A 15 mm $\times$ 15 mm die was cleaved from the initial 3-inch wafer using a JFP Microtechnic S100 Scriber Breaker and mounted onto the spin processor using the vacuum clamp. The mounted sample was then flood coated with AZ5214E photoresist, dispensed using a pipette. The spin processor rotates the coated sample at high speed to draw out the polymer across the sample such that it distributes evenly into a thin film. The final thickness of the film is determined by the spin speed and the spin duration. The manufacturer provides data as a guideline for the final film thickness, but this can vary slightly according to age of the resist batch as well as specific spin coater settings. Knowledge of the resist film thickness is required for later fabrication steps, therefore to confirm the relationship between the spin speed and final film thickness for this batch, spin curve measurements were carried out on 15$\times$15 mm^2 blank semi-insulating GaAs samples. This was achieved by spin coating the samples at various speeds for 30 seconds, curing the resist on a hotplate for 90 seconds at 110 ^{o}C, followed by removing a small amount of the cured film with the tip of a pair of tweezers in three areas of the sample. The film thickness was then measured in these three areas using a KLA-Tencor Sylus Profiler, and an average value taken. The data obtained is presented in Figure 3.1, and shows that the target 4000 RPM for 30 seconds achieves a film thickness of around 1.55 μm.

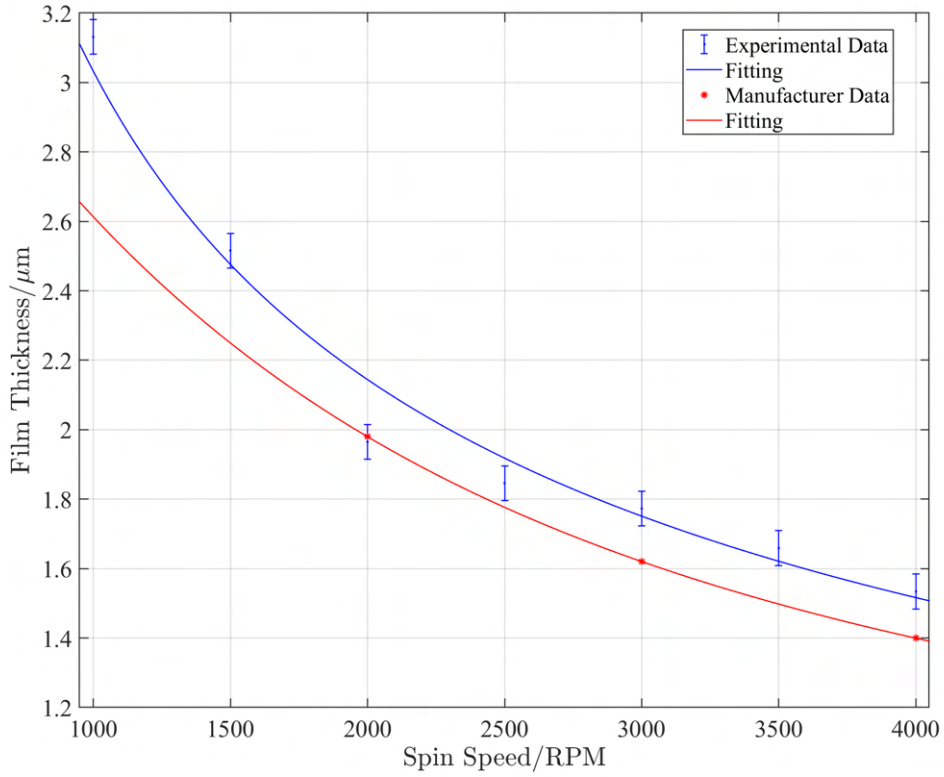


Figure 3.1: *Experimentally measured film thicknesses for AZ5214E resist on 15 mm × 15 mm blank semi-insulating GaAs samples. Samples were spun at the given speed for 30 seconds and then cured on a hotplate at 110 °C for 90 seconds. Characteristic data provided by the manufacturer is also presented for comparison. The function fitted to both data sets is* $f(x) = a/\sqrt{x}$*, with* R^2 *values of 0.96 for the experimental data and 1 for the manufacturer data respectively. Uncertainties on the measured data come from the resolution of the instrument used.*

3.2.1 Photoresist Profile Optimisation

The flexibility of the AZ5214E image reversal resist allows it to be used as both a lift-off resist as well as a mask for dry etching. Process parameters must therefore be optimised for the desired application. When optimising the processing parameters for use as a lift-off resist, the sidewall profile of the resist must show a negative slope of $< 85^o$ in order for the film to lift away cleanly [96] (refer to Section 3.3 for more details on the metal deposition and lift-off process).

The AZ5214E resist may be used in either positive or negative tone, depending on the application. All patterning steps in the fabrication of the optical switches in the project use the resist in the negative tone, by inclusion of a second 'image

reversal bake'. After spin coating and curing, the photoresist is exposed to UV light through the photo-mask using a Süss MA6 Gen3 mask aligner. The mask aligner ensures each patterned layer is aligned to the previous layer, and allows control of the doses of UV received by the sample. The areas of photoresist exposed to UV light in this first step define the structures of the pattern to be transferred from the mask. The exposure dose in this step strongly impacts the final attained resist profile - low exposure doses cause the resist near the substrate to be only partially exposed, thus maintaining a high dissolution rate in the developer and achieving a strong undercut profile, as illustrated in Figure 3.2.

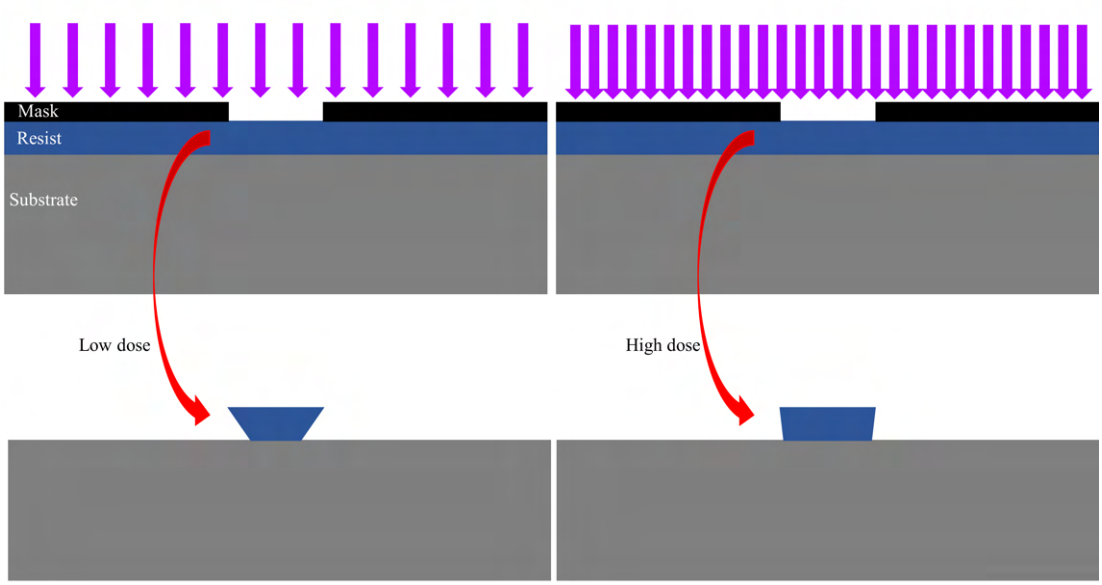


Figure 3.2: *Schematic illustration of the result of a differing UV dose on the final attained photoresist sidewall profile. With a low dose, the UV cannot penetrate through to the substrate-near resist, making these areas more soluble in the developer. When the dose is high, almost all of the polymer chains in the resist film are cross-linked, making the dissolution rate in developer very low, resulting in a less pronounced undercut profile.*

The image reversal bake takes place after the first exposure and cross-links the photo-active compound (PAC) exposed in the first step, causing it to become insoluble in developer. The reversal bake temperature and/or times have strong effects on the final obtained resist profile - low bake temperatures and/or times can only convert the strongly exposed areas of the PAC near the surface, resulting in a pronounced undercut profile. Conversely, high bake temperatures and/or

times convert the majority of the exposed PAC, resulting in a less pronounced undercut profile. The final stages of the patterning process involve a final 'flood' exposure, followed by development of the resist in a manufacturer-specified developing solution (Microchem AZ726 MIF). Figure 3.3 gives an overview of the entire patterning process using an image reversal resist

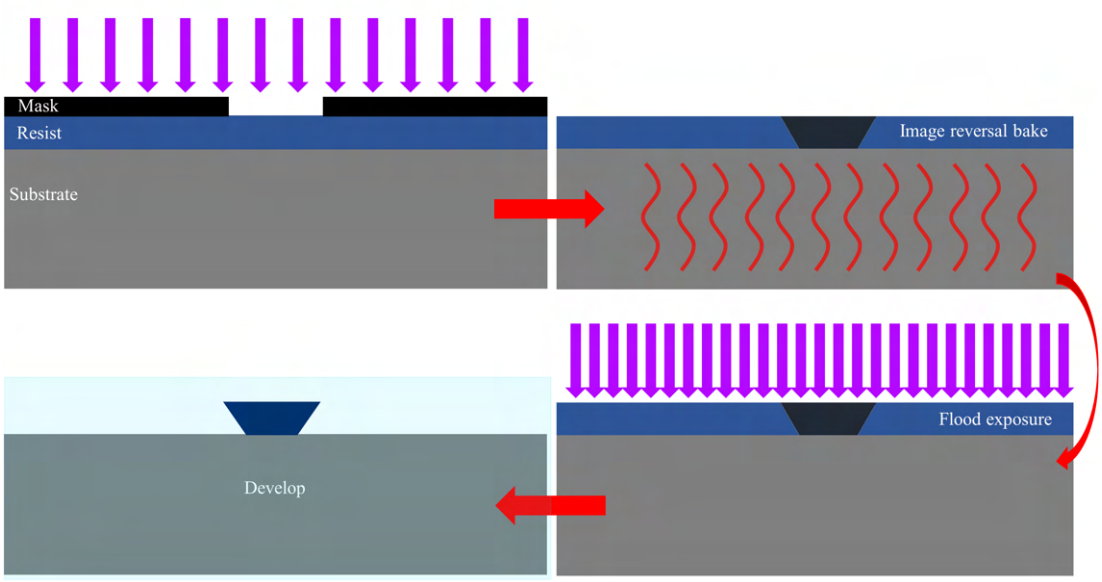


Figure 3.3: *Schematic illustration showing an overview of the patterning process using the AZ5214E image reversal resist. Main stages of the process are: Image exposure using a photomask, image reversal bake, flood exposure, and finally development.*

There are two separate patterning recipes required for fabrication of the optical switch devices. The first process for patterning the metal contacts has less stringent requirements on the desired resolution due to large feature sizes, but must show a pronounced undercut profile to allow lift-off of the photoresist after metal deposition. The second process for patterning the waveguides, the 'waveguide recipe' requires a higher resolution due to the desired 2 μm waveguide widths and furthermore the undercut has to be less pronounced so that the resulting etched waveguides have vertical sidewalls. This waveguide recipe features a longer post exposure bake to reduce the solubility of the resist in the developer. The process for plasma etching the mesa uses the same waveguide recipe due to requirements of smooth sidewalls which reduce optical propagation losses. Process parameters were initially developed by Dr James Moss [64] for

the fabrication of optical switch devices using the RC101 wafer, thus only small changes needed to be made to optimise the process for RC184 and RC187 wafers. To optimise the resist sidewall profile, the film thickness, first exposure dose, and reversal bake temperature were held constant according to original recipes, and the develop time was altered for various trial samples.

For the lift-off process, samples were firstly solvent cleaned and dehydration baked to remove any residual water vapour.. After cooling, samples were then individually mounted onto the Laurell WS650 Spin Coater and spin coated with AZ5214E photoresist, which was then cured on a hotplate. Samples were then mounted into the Süss MA6 Gen3 mask aligner with chosen mask plate and exposed with UV. The image reversal bake was then carried out, and the samples subsequently returned to the mask aligner for the flood exposure. To develop the pattern, samples were agitated in concentrated AZ726 MIF developer, followed by a rinse in de-ionised (DI) water and finally blow dried with a nitrogen gun. Samples were finally cleaved through a given feature using the JFP Microtechnic S100, and the resist sidewall imaged using a microscope. Figure 3.4 shows the optimised sidewall profile for the lift-off and waveguide patterning processes. Comparison of the resolution of small features for each recipe is illustrated in Figure 3.5. The process for defining the waveguides followed the same steps as outlined above but with differing bake times, exposure doses, temperatures and furthermore employing the hard-contact alignment mode whereby the mask is pressed into contact with the substrate. This allows for a higher resolution patterning process but also requires the additional step of removing the build-up of an edge bead of photoresist after the spin coating step. This was simply achieved by running an acetone-soaked cotton bud around the edges of the substrate after spin coating. The process for patterning the mask for dry-etching of the mesa used the same recipe parameters as for the waveguides to ensure the etched sidewalls were as vertical as possible. Process parameters for all recipes are summarised in Table 3.1.

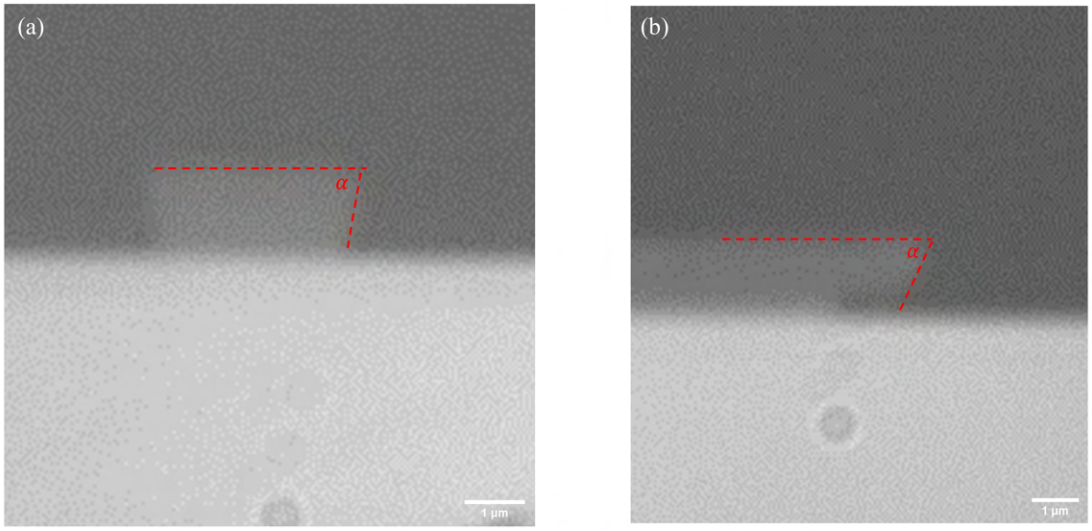


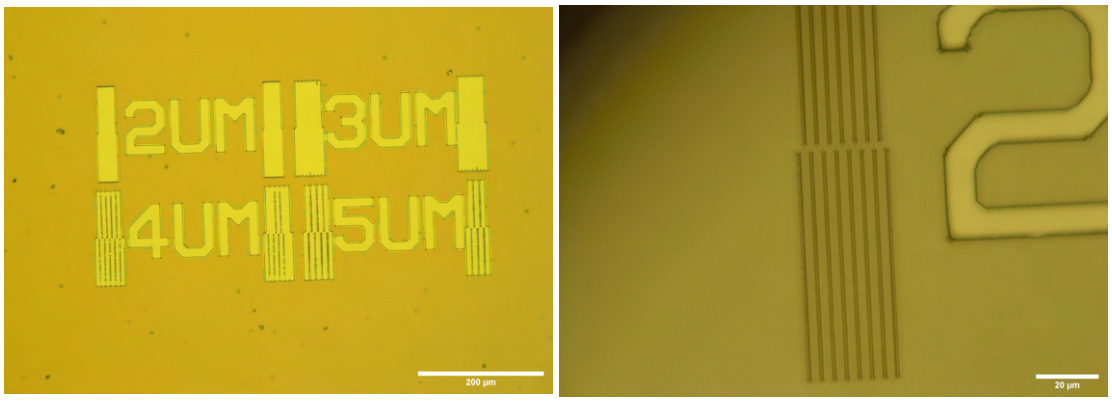
Figure 3.4: *Optical microscope images showing the resulting photoresist undercut profiles for (a): waveguide patterning and (b): metal contacts patterning for the lift-off process. Angle of the positive slope, α, is (a): 60º and (b): 52º.*

Table 3.1: Key recipe parameters for patterning of waveguides, mesa etch and metal contacts using the AZ5214E photoresist.

Recipe	**Cure**	**Image Exposure**	**Image Reversal Bake**	**Flood Exposure**	**Develop**
Waveguide	50s at 115^{o}C	10 mJ/cm^2 i-line	3 mins at 115^{o}C	250mJ/cm^2 i-line	100% AZ 726 MIF for 22s
Mesa Etch	50s at 115^{o}C	10 mJ/cm^2 i-line	3 mins at 115^{o}C	250mJ/cm^2 i-line	100% AZ 726 MIF for 22s
Metal Contacts	90s at 110^{o}C	22 mJ/cm^2 i-line	2 mins at 120^{o}C	250mJ/cm^2 i-line	100% AZ 726 MIF for 45s

3.3 Ohmic Contacts

Ohmic type contacts are paramount in the fabrication of the optical switches. Ohmic contacts have a low energy barrier to the conduction of current at the metal/semiconductor interface. The key to developing good quality ohmic contacts to the underlying doped GaAs layer is to design these barriers to be as low as possible so that charge carriers can cross the interface by thermionic or field emission. High doping in the GaAs layer beneath the contact metal helps to lower this energy barrier. The resistance to the flow of charge carriers through the final



(a) **(b)**

Figure 3.5: *Optical microscope images showing the feature resolution limit of (a): the patterning recipe for the metal contacts and (b): the patterning recipe for the waveguides. It is clear that the waveguide patterning recipe in (b) achieves a higher resolution of 2 µm compared to > 5µm with the contacts recipe. In (a), the aggressive undercut has caused smaller features to de-adhere from the substrate. In (b), only the 2 µm features are shown.*

device should be minimised and the contribution of the ohmic contacts should be negligible compared to the total device resistance. The total device resistance, R_T is comprised of the contact resistances R_c and the semiconductor resistance in between the contacts $R_s = \rho_s L/A$, where ρ_s is the semiconductor resistivity. The total device resistance is then given as $R_T = R_s + 2R_c$, where the factor of two is introduced due to contributions from both contacts. Since the contact resistance depends on the size of the contact, it is not the most useful parameter for comparison. Instead, the specific contact resistivity is used, which is defined as the resistance presented to uniform current flow across an interface of unit area between the metallisation and semiconducting layer, with units Ωcm^2.

Current flow in the semiconductor material between the contacts is uniform, however, this is not the case for the current flow into the contacts. As current passes through the semiconductor to the metal contact at the surface, it finds the path of least resistance to the contact, resulting in a larger current flow into the edge of the contact. This is known as current crowding [97] and is illustrated in Figure 3.6. The amount of current flowing into the contact therefore decreases with the distance from the edge of the contact and it is therefore useful to define another quantity, the transfer length L_T, which is defined as the distance at which

the current density falls to $1/e$ of the initial value at the edge of the contact.

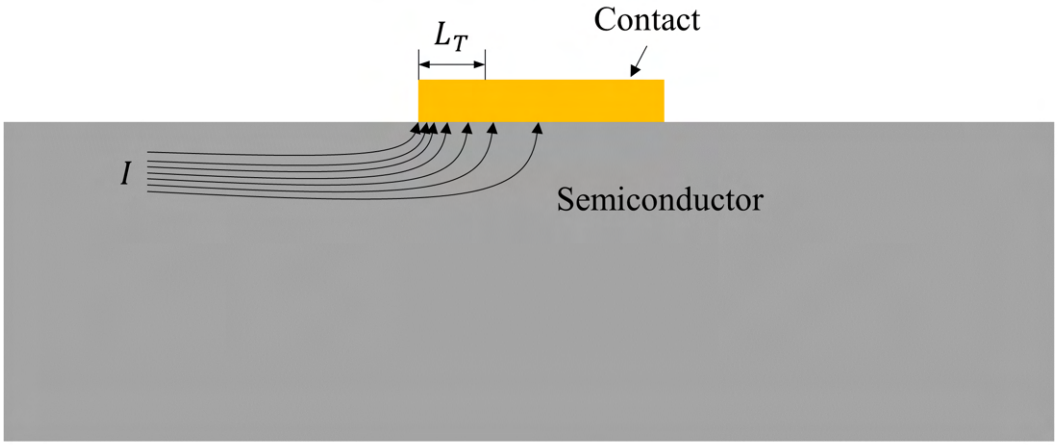


Figure 3.6: *Schematic illustration of current transfer from semiconductor to metal, represented by the arrows. The current chooses the path of least resistance to the contact, resulting crowding near the contact edge. The transfer length, L_T, is defined as the distance at which the current density falls to $1/e$ of its value at the edge.*

All three of the wafers used to fabricate the optical switch devices have highly doped n-type and p-type contact layers, around 10^{18}cm^{-3} and 10^{19}cm^{-3} respectively. We opted to use the Au/Zn/Au (5nm/20nm/200nm) recipe for the p-type contacts as detailed by [98], and the Ge/Au/Ni/Au (5nm/20nm/15nm/200nm) recipe for the n-type contact as detailed in [99]. The following section discusses the formation and characterisation of these metal contacts.

3.3.1 Metal Deposition

The first step in the fabrication of the optical switches is the formation of the p-contact electrodes on the top p-GaAs cap layer. This was achieved by first patterning the sample with lift-off photoresist, as described earlier. This pattern features narrow openings in the developed photoresist film in the desired p-contact positions. Prior to evaporation, samples were dipped in diluted hydrochloric acid solution (1 part HCl to 1 part H_2O by volume) for 30 seconds to remove any oxide layer. The relevant metals were prepared by sonicating in isopropyl alcohol (IPA) for 5 minutes, drying with a nitrogen gun and subsequently loaded into the metal boats of the evaporator. The photoresist-coated semiconductor samples were

then loaded into the Edwards Auto 306 thermal evaporator using the sample holder, and the vacuum pumped down to $\sim 10^{-7}$ mbar. The metal film was then thermally evaporated onto the sample, one layer at a time, by heating the relevant metal boat using a high current source, as illustrated in Figure 3.7. This resulted in a conformal thin film of metal covering the entirety of the patterned sample.

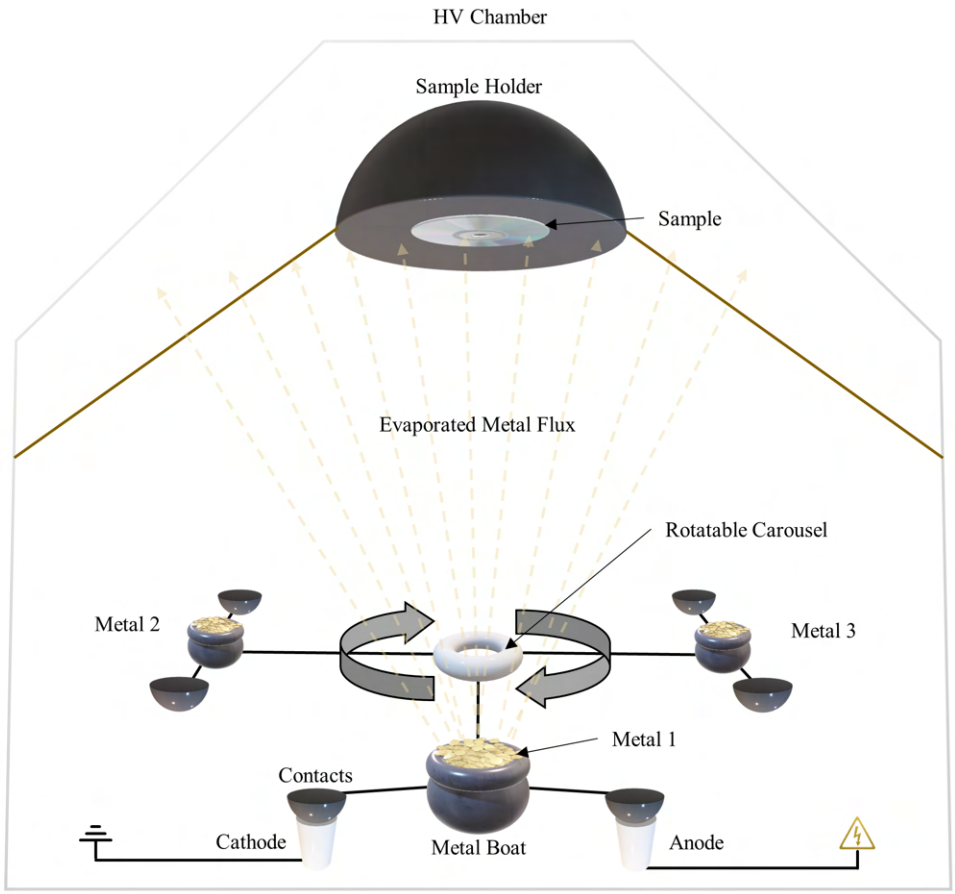


Figure 3.7: *Schematic illustration of the thermal evaporation process. High purity metal samples are sonicated in isopropyl alcohol and subsequently placed in tungsten boats in the evaporator. The chamber is then pumped down to high vacuum (HV) and the boat is rotated into the contact position using the carousel. Low voltage, high current is then passed through the tungsten boat, heating it above the boiling point of the metal inside the boat, causing it to evaporate onto the sample. A film thickness monitor (FTM) is used to estimate the thickness of the evaporated film during the evaporation.*

To isolate the contact pads from the rest of the film, the underlying photoresist layer has to be removed. This was achieved using a multi-stage lift-off process: the sample with the evaporated metal film was first placed in dimethylsulfoxide

(DMSO) solvent, heated to 80 ^{o}C, and left to rest for 45 minutes. This step is used to lift away the majority of the large areas of metal with underlying resist film. The sample was then rinsed with room temperature DMSO using a wash bottle and placed in a fresh beaker of DMSO. This beaker was then placed on an orbital stirrer and agitated for 15 minutes. This step helps to remove smaller areas of metal film. The sample was then rinsed with de-ionised water and placed in a beaker of de-ionised water for 10 minutes. Finally, the sample was rinsed thoroughly with IPA and blow dried with nitrogen to remove any residual contaminants and moisture. Throughout this process, it is paramount to ensure the sample does not dry in between steps as this can cause the liberated film to redeposit onto the sample and adhere. This process is repeated for the n-type contacts after the mesa etch.

The final step in defining the metal contacts is to diffuse the evaporated metal film into the underlying semiconductor layer, using a rapid thermal anneal (RTA) process. The RTA process uses an infrared heat source to ramp the temperature of the substrate from ambient to $\sim 350 - 450^{o}$C, followed by a short dwell at this temperature before finally cooling back to ambient. This is done under an inert atmosphere of nitrogen to avoid oxidation. The annealing process alloys the metal layers with the underlying GaAs layer by migration of Ga and As towards the metal surface. The specific recipe parameters depend on the mixture of metals as well as the doping of the semiconductor layer. Extensive studies have been carried out to find ideal ohmic contact recipes to p-GaAs and n-GaAs with contact resistivities as low as 10^{-6} Ωcm^2 [99]. Annealing of the p-type and n-type contacts was carried out using an AnnealSys AS-One RTA. Since the recipes called for a higher anneal temperature for the p-type contacts than the n-types, this was carried out first. The samples were loaded into the RTA by placing them face down on a graphite-coated, silicon carbide (SiC) susceptor plate. The sample was then covered using a second susceptor plate with a matching diameter to the first, as illustrated in Figure 3.8. This configuration ensures optimal absorption

of the infrared radiation during the annealing process, resulting in a more uniform temperature distribution across the sample.

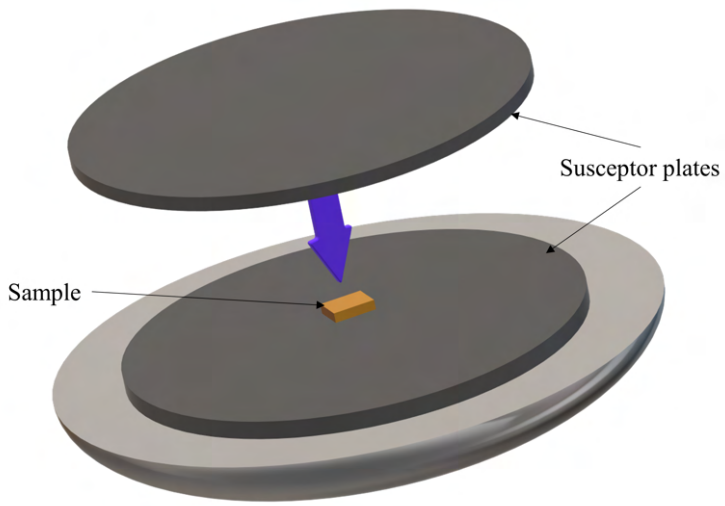


Figure 3.8: *Schematic illustration of the sample susceptor, used to ensure uniform temperature distribution across the semiconductor sample during the RTA process.*

3.3.2 Circular Transmission Line Measurements

The performance of the alloyed ohmic contacts can be evaluated by calculating the specific contact resistivity, ρ_c, and additionally the properties of electrical transport in the underlying semiconductor material via evaluation of the sheet resistance, σ and transfer length, L_T. This can be achieved via the so-called circular transmission line measurements (cTLM). cTLMs are a powerful tool for accurately determining the quality and performance of ohmic contacts [100], as illustrated in Figure 3.9.

cTLM structures on the die were characterised using a Keysight Technologies B2900A Series Precision Source/Measure Unit (SMU), via a four-point probe method. Contacts to the device were made using a probe station. A constant current was applied across each circular structure and the voltage drop induced across the two metal contacts measured. This measurement was repeated for a range of current values for each size annulus, resulting in an average total resistance R_{Tot} for each structure, which when plotted as a function of the gap

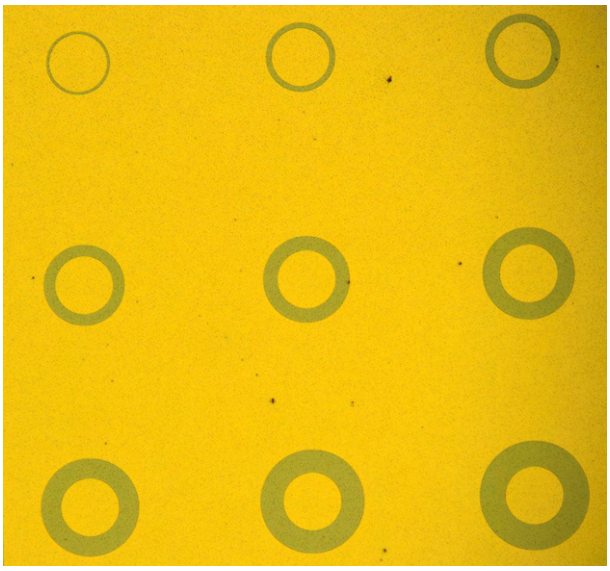


Figure 3.9: *P-type cTLM test structure patterned onto RC184 during the first process step. The cTLM structure consists of a series of circular contacts surrounded by outer metal, separated by various ring shaped gaps. The size of the centre contact remains constant, whilst the size of the gap changes size in each feature. This is a simple structure which can be patterned onto the semiconductor surface with one mask. Radius of the inner metal contact is 130μm.*

spacing, yields a curve as illustrated by the red data points in Figure 3.10.

The resistance between the contacts takes the form,

$$R = \frac{\sigma}{2\pi R_1}\left(s + 2L_T\right)c, \tag{3.1}$$

where σ is the sheet resistance, R_1 is the constant radius of the inner contact, s is the gap size, L_T is the transfer length and c is a correction factor used to convert the non-linear measured curve into a linear relationship [101], given by,

$$c = \frac{R_1}{s}\ln\left(\frac{R_1 + s}{R_1}\right). \tag{3.2}$$

The correction factors were calculated for each data point and the resulting total resistance plotted, as shown by the blue data points in Figure 3.10. The calculated electrical parameters for samples from RC184 and RC187 are summarised in Table 3.2. These results show excellent quality ohmic contacts which compare well with the relevant literature. It is important to note however, limitations of this model in the calculation of the specific contact resistivity. The sheet resistance

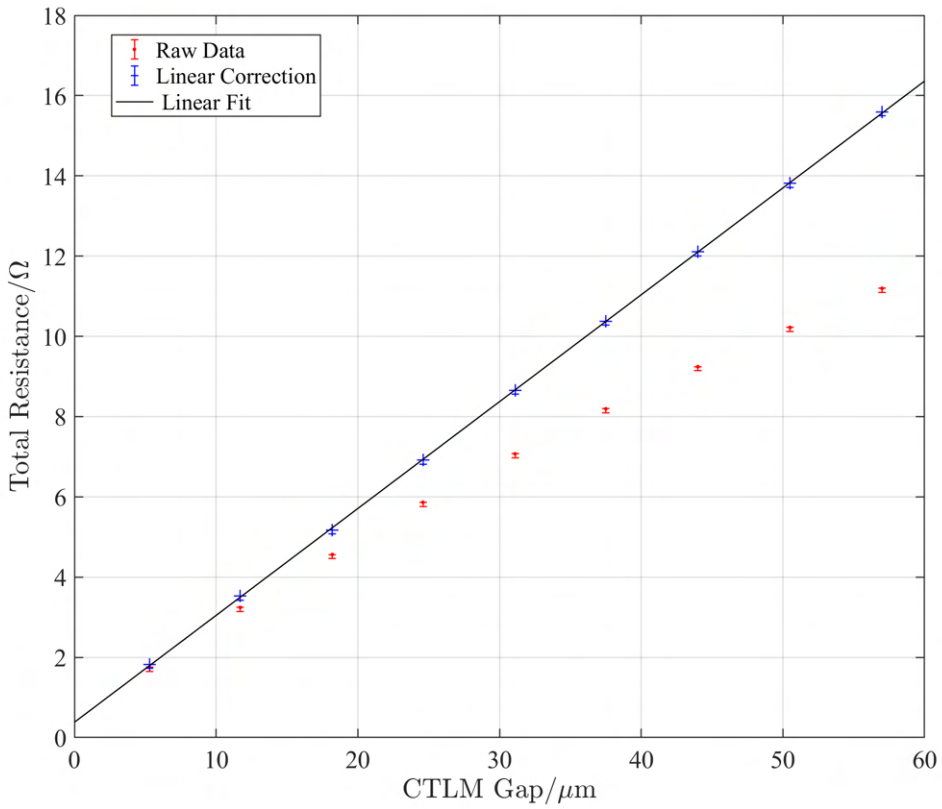


Figure 3.10: *Fitting of the p-type cTLM data from a sample of RC184. Calculated specific contact resistivity in this case was* $\rho_c = 0.56 \pm 0.05 \times 10^{-6}\ \Omega cm^2$

in Equation 3.1 is defined as the sheet resistance under the metal contact which can differ from the measured sheet resistance of the semiconductor between the metal annuli. The measured sheet resistance can be lower due to spiking of the metal below the contact into the semiconductor. One must therefore be sceptical of specific contact resistances less than $10^{-6}\ \Omega\ \text{cm}^2$. Nevertheless, nearing this limit is a sign of a good quality ohmic contacts which are more than sufficient for the needs of the optical switching devices fabricated in this project, and compare very well with measured values from the relevant literature [102].

3.4 Dry Etching

The fundamental technologies underpinning the fine geometric structures of modern electronics and photonics are mainly comprised of dry etching technologies,

Die Reference	**Contact Type**	**Contact Resistance R_c (mΩ)**	**Sheet Resistance σ (Ω/sq)**	**Transfer Length L_T (μm)**	**Specific Contact Resistivity ρ_c ($\mu\Omega cm^2$)**
RC184-AC	p-type	191.1 ± 25.6	108.8 ± 0.5	0.72 ± 0.02	0.56 ± 0.05
"	n-type	138.2 ± 19.8	9.48 ± 0.45	5.95 ± 0.55	3.36 ± 0.83
RC184-MF-TRIAL	p-type	420.4 ± 61.8	103.6 ± 1.4	1.67 ± 0.20	2.84 ± 0.85
"	n-type	116.0 ± 44.4	10.4 ± 1.0	4.56 ± 1.18	2.16 ± 1.60
RC187-GP	p-type	305.4 ± 60.4	152.3 ± 1.4	0.82 ± 0.15	1.02 ± 0.43
"	n-type	167.2 ± 27.9	11.53 ± 0.63	5.92 ± 0.63	4.04 ± 1.17

Table 3.2: Summary of the electrical parameters obtained via cTLMs.

combined with the previously discussed photolithography processes [103]. Dry etching is used to transfer the desired patterns for the IC or PIC from the patterned photoresist onto the underlying wafer.

All of the structure-defining etches used in the fabrication of the optical switching devices implement a reactive ion etch (RIE) process. In this situation, the chamber is first pumped down to high vacuum and the etching gases introduced into the chamber. Etching of GaAs/$Al_xGa_{(1-x)}As$ usually employs silicon tetrachloride ($SiCl_4$) or boron trichloride (BCl_3) as the etchants [104, 105]. A 13.56 MHz radiofrequency (RF) electromagnetic wave is then applied between a set of parallel plates which generates a plasma. The etching gases become dissociated in this plasma, forming free electrons, radicals, ions, and monomers. The free electrons collide with the etching gases ionising them further in a process known as electron impact ionisation, creating more ions and free radicals. Furthermore, ions and free electrons recombine in the gas phase to produce excited neutral species which themselves recombine to form ground state neutral molecules. This process results in a so-called plasma glow due to the change in energy states of

the molecules [103].

Since the free electrons have a smaller mass than the ions, they are able to follow the oscillation of the electric field. This leaves the plasma with a net positive charge, and the plate with a negative charge, leading to the formation of an ion 'sheath' with a direct current bias, as shown in Figure 3.11. This bias gives the ion-drift continuous directionality towards the sample. When these ions strike the sample they cause damage to the surface molecules, forming volatile reaction products which etch away the material. The RIE process is predominantly a chemical etch, assisted by physical modification of the surface by impacting ions. Since these ions are directional, so is the resulting etch. Only the exposed surfaces are etched which means that the profile of the photoresist defines the etched structure. This makes the RIE perfectly suited for forming the structure of a PIC, where the quality of etched sidewalls has a direct impact on the optical propagation losses of the device. This is in contrast to a wet chemical etch which proceeds isotropically, etching sidewalls at the same rate as the surface.

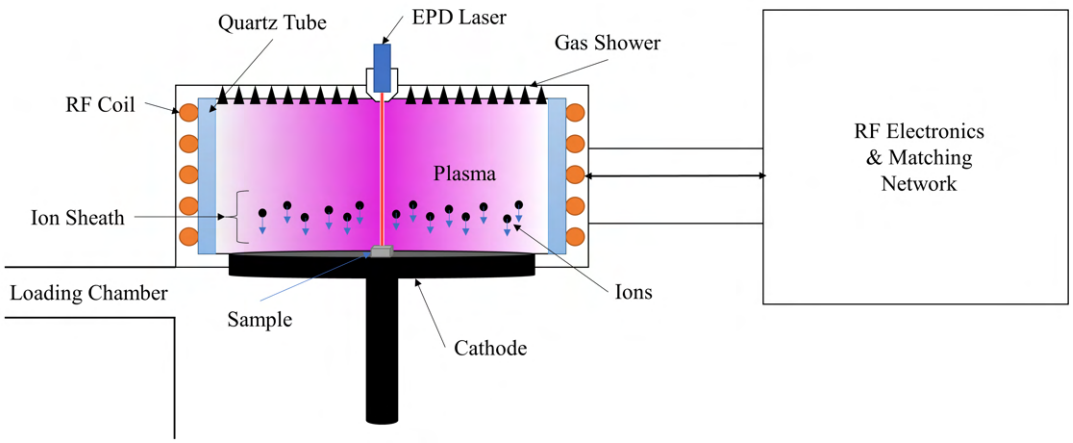


Figure 3.11: *Schematic illustration showing the configuration of the RIE process and the formation of the ion sheath, leading to anisotropic etching.*

The partly physical nature of the etch means that material is inevitably lost from the photoresist, despite the lack of chemical reactions at its surface. This can round off the edges of the photoresist causing undesirable imperfections in the etched sidewalls of the waveguides for example. It was therefore important to ensure that the profile of the patterned resist was as close to vertical as possible.

There are a number of etch steps required in the structure-defining fabrication process, illustrated schematically in Figure 3.12. All etch recipes were developed and carried out by Dr Chris Mellor using a Corial 200IL RIE/ICP etcher.

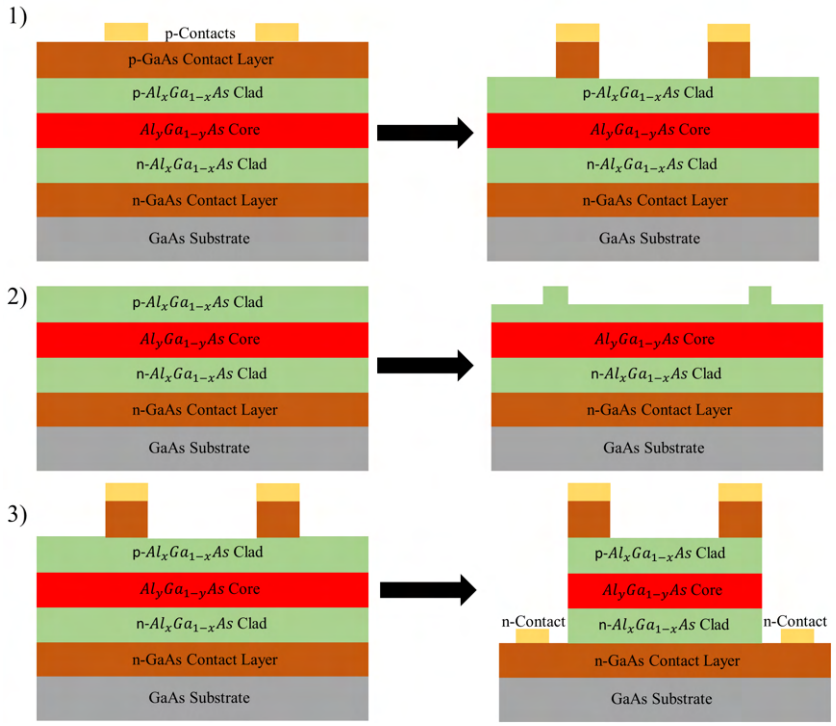


Figure 3.12: *Summary of the dry etch processes required to form the device structure. 1) Using the p-contacts as a hard mask to reveal the p-cladding layer in the areas where the p-contacts do not exist. 2) Etching away part of the p-cladding in the waveguiding section to form the waveguides. 3) Etching away layers in the steering section to reveal the n-GaAs layer, onto which the n-contacts are deposited.*

3.4.1 p-GaAs Removal

The first etch required in the fabrication process is the removal of the top p-GaAs cap layer which isolates the p-contacts and reveals the p-$Al_xGa_{(1-x)}As$ layer. The etching gases used in this case were a $SiCl_4/SF_6$ mixture. By varying the ratio of these two gases, a high selectivity of etching GaAs over $Al_xGa_{(1-x)}As$ can be obtained (up to 10^3), to the point where the etch essentially terminates at the p-$Al_xGa_{(1-x)}As$ layer [106]. The reason for this is due to a layer of AlF_3 forming on the $Al_xGa_{(1-x)}As$ layer, passivating the surface and subsequently inhibiting the etch. The presence of SF_6 also helps to remove silicon formed on the GaAs surface, increasing the etch rate of GaAs.

To monitor the etch depth, an end-point detection (EPD) signal was recorded in-situ. This consists of a 670 nm laser incident normal to the surface of the sample. This beam is reflected at the interface between the first and second epitaxial layers, and interferes with the incident beam. The EPD is then simply the recorded intensity of this reflected beam. As the thickness of the top layer changes, the reflected beam interferes with the incident beam by differing amounts, creating an oscillating pattern in the recorded EPD signal. Since the energy of the 670 nm photons are above the band-gap energy of the etching material, the EPD signal is attenuated from the epitaxial layers more than a micron or so from the surface. The transfer matrix method (TMM) has been used to simulate these EPD signals for each etch, and compared with the recorded EPD signal from the Corial 200IL RIE/ICP etcher. The simulated and recorded EPD signals for the p-GaAs etch of a RC184 sample are shown in Figure 3.13. Etch depths were confirmed using a KLA-Tencor Stylus profiler.

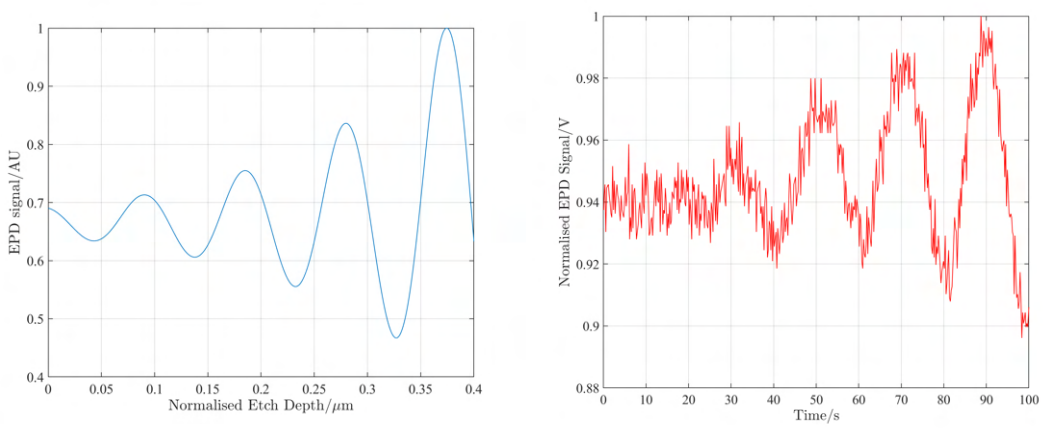
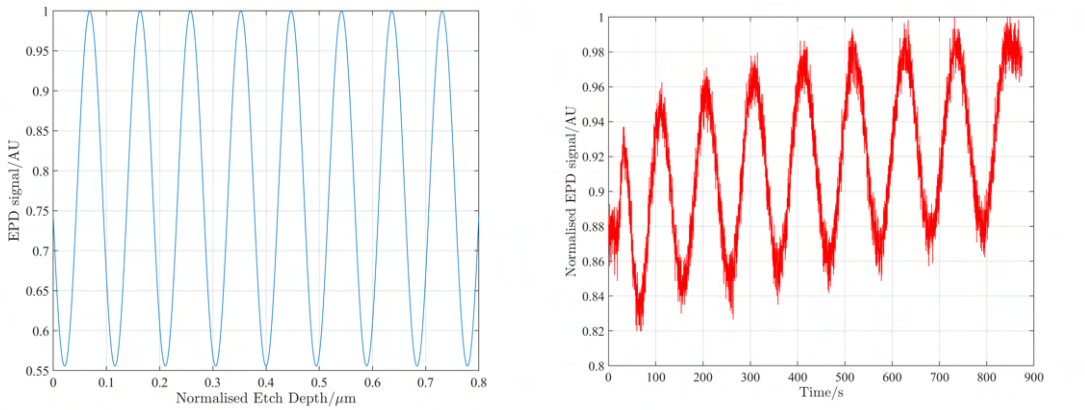


Figure 3.13: *Simulated (a) and logged (b) EPD signals for the etching of the entire p-GaAs layer of a RC184 sample. The oscillation amplitudes for the recorded signals are much smaller than the simulated ones since the real EPD laser is attenuated due to absorption and scattering losses.*

3.4.2 Waveguide Etch

The waveguide etch follows the p-GaAs etch and has the most stringent requirements on the etch depth tolerance and sidewall roughness. As mentioned in

Section 2.4.2, the height of the waveguide rib defined by the etch has a direct effect on the number of supported optical modes and the confinement of a guided wave. If the etch depth is too shallow, the confinement will be weak resulting in large propagation losses. On the other hand, if the etch is too deep, higher order modes will begin propagate through the waveguide, meaning the design requirements of the optical switch will not be met. The required waveguide etch depths for each epitaxial design were calculated according to the effective index method, as discussed in Chapter 2. The etching gas used for this process was BCl_3. The simulated and recorded EPD signals for this etch for RC184 are shown in Figure 3.14 and an example of the etched waveguides for RC187 is shown in Figure 3.15. The smooth edges of the etched waveguides are shown here and the measured waveguide width at the centre of the straight waveguide was 2.0 ± 0.1 μm for the labelled device in Figure 3.15.

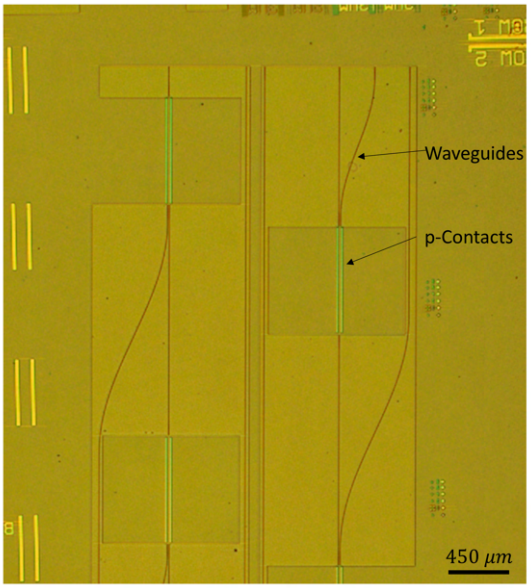


(a) **(b)**

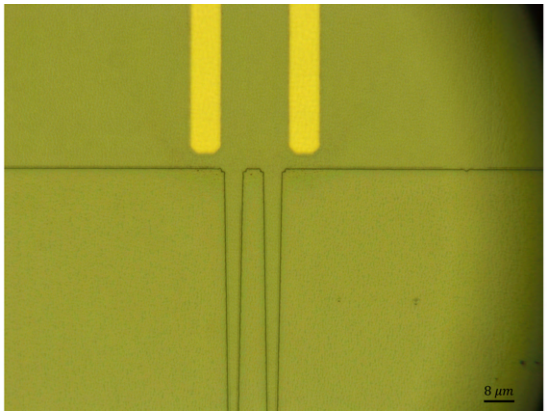
Figure 3.14: *Simulated (a) and logged (b) EPD signals for the required waveguide etch depth for RC184*

3.4.3 Mesa Etch

The final structure-defining etch in the fabrication process is the mesa etch, revealing the n-GaAs layer for deposition of the n-type contacts. This etch must proceed through several layers: p-$Al_xGa_{(1-x)}As$ cladding, $Al_xGa_{(1-x)}As$ core, n-$Al_xGa_{(1-x)}As$, and finally a small amount of the n-GaAs. The exact etch depth is



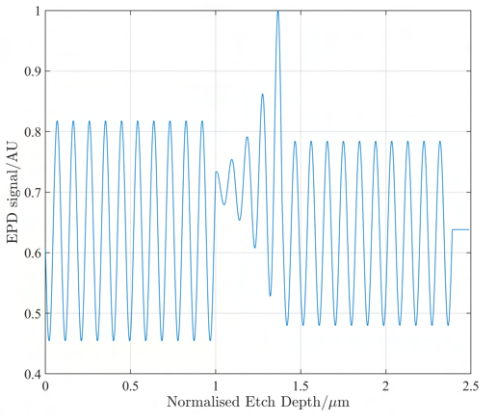
(a)



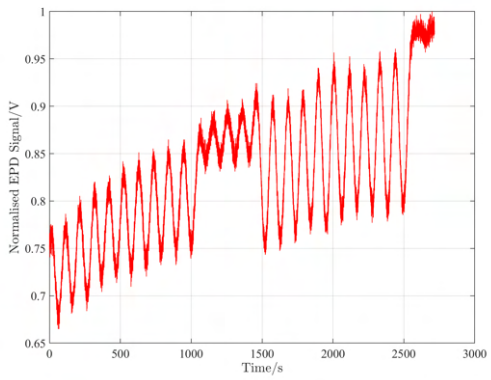
(b)

Figure 3.15: *Optical microscope images showing (a): an overview of the etched waveguides of several devices from RC187 after the waveguide etch and (b): ×100 magnification showing the tapered outputs of the waveguides. The smooth edges of the waveguides can clearly be seen in (b). The measured width of the centre of the straight waveguide labelled in (a) is 2.0±0.1 μm.*

not so important in this case, as long as it reaches the n-GaAs layer. Therefore, the etch is not stopped immediately after the n-$Al_xGa_{(1-x)}As$/n-GaAs interface, but rather allowed to proceed for a short while into the n-GaAs layer. Figure 3.16 shows the simulated and recorded EPD signals for this etch.



(a)



(b)

Figure 3.16: *Simulated (a) and logged (b) EPD signals of the mesa etch for RC184. The interfaces between the layers are clear in both cases.*

Unfortunately, this process was the most troublesome of the three etches as

a result of significant micromasking effects, which will be described in more detail in the following section. Nonetheless, these issues were solved and the final recommendation is to use a BCl_3 etchant for the whole process. This is a slow etch, with a rate of ∼55 nm/min, however this ensures a clean etch and significantly reduces the probability of micromasking effects. A summary of the etching processes is given in Table 3.3.

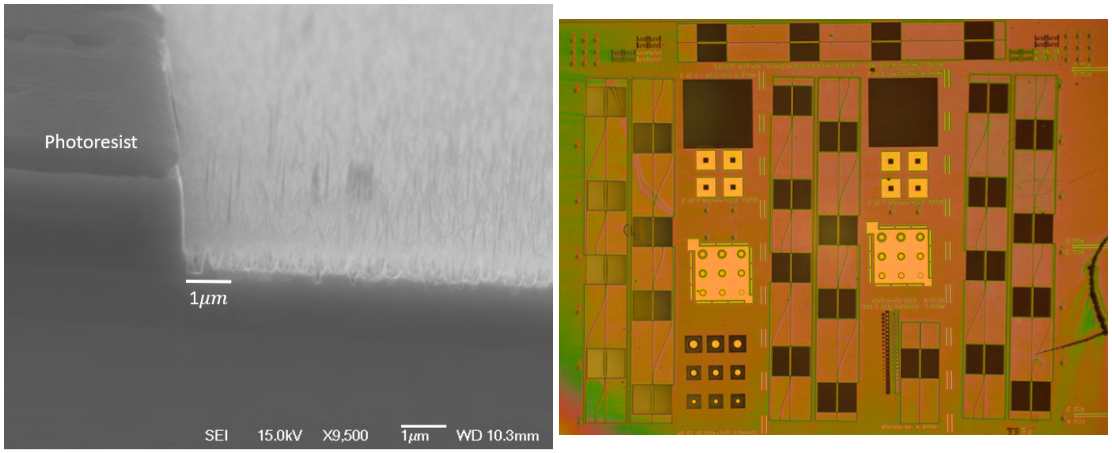
Etch Label	**Recipe Name**	**Etchants (sccm)**	**Required Depth (μm)**	**Measured Depth (μm)**
p-GaAs Etch	`'GaAs Etch'`	$SiCl_4$ (25)/SF_6 (2)	0.4	N/A
Waveguide Etch (RC184)	`'CJMBCL3_RIE_NOV_2018'`	BCl_3 (25)	0.65	0.64±0.01
Waveguide Etch (RC187)	`'CJMBCL3_RIE_NOV_2018'`	BCl_3 (25)	0.67	0.69±0.01
Mesa Etch (RC184)	`'CJMBCL3_RIE_NOV_2018'`	BCl_3 (25)	2.49	2.55±0.01
Mesa Etch (RC187)	`'CJMBCL3_RIE_NOV_2018'`	BCl_3 (25)	2.05	2.10±0.01

Table 3.3: Summary of the dry etching processes used in defining the device structure. Etch depths were measured after the etching process using a KLA-Tencor Stylus Profiler. Measurements were taken at 7 points on the sample and an average calculated. The etch depth was not measured for the p-GaAs etch because this etch is self-passivating at the required depth.

3.4.4 Micromasking

RIE of GaAs/AlGaAs films requires the optimisation of the chosen etch chemistry and the careful preparation of the sample to achieve consistent results. If the incorrect mixture of gases is used or the sample is not adequately prepared before etching, unwanted effects can occur such as micromasking. Micromasking results in the formation of micron or sub-micron sized grass-like pillars of unetched material. There are two main types of micromasking: micromasking due to surface residues and self-polluted micromasking. Self-pollution is caused by an

issue with the etch chemistry, whereas surface residues can be solved by paying more attention to sample surface preparation beforehand [107].



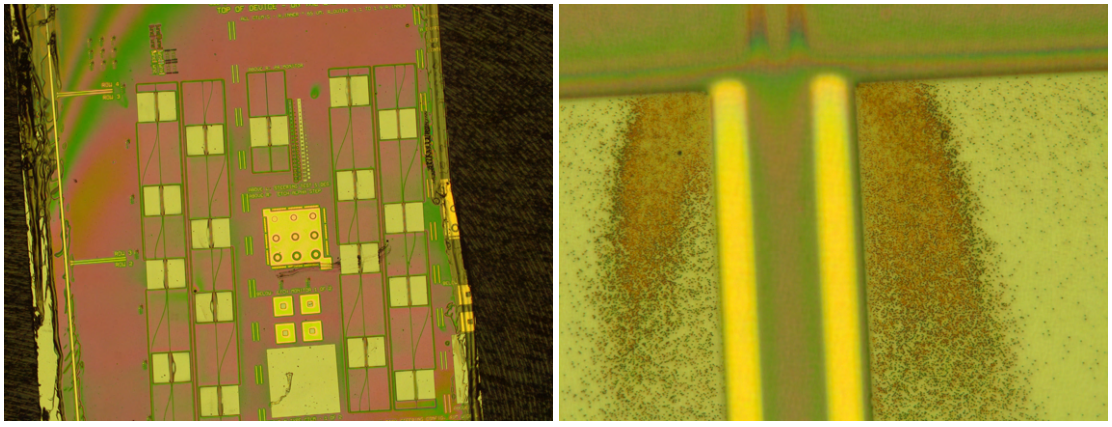
(a) **(b)**

Figure 3.17: *Analysis of RC187-C which was damaged at the n-GaAs reveal etch by micromasking effects. (a): SEM image of a cleaved edge of a window intended for an n-cTLM pad showing the presence of dense micromasking (black regions). (b): Optical microscope image of RC187-C which experienced micromasking effects (black areas) at the n-GaAs reveal etch step. Rounding of the edges of the photoresist due to the physical nature of the etch can also be seen in (a).*

During the fabrication of RC184 and RC187, there was a significant issue with micromasking during the etch used to reveal the n-GaAs layer, as shown in Figure 3.17. The unwanted micromasking resulted in the formation of very dense pillars in the etched region. The same etch chemistry and recipe was used for this etch as was successfully used in the fabrication of RC101, however this recipe was modified from an initial recipe which had caused micromasking with a RC101 sample. This original recipe was based on a $SiCl_4$ etch for the entire process but was modified to a $SiCl_4/BCl_3$ etch to reduce the micromasking effects caused by redeposition of the etch products.

One hypothesis was that the higher aluminium content was contributing to the micromasking effects since this etch involved removing AlGaAs films with up to 55% aluminium, possibly contributing to the formation of an unetchable alumina (Al_2O_3) residue redepositing on the surface. Therefore, the etch was changed to a BCl_3-based etch for the entire process of the n-GaAs reveal, since BCl_3 can etch Al_2O_3. This etch was tested on various samples with and without a photoresist

mask, with no apparent micromasking occurring. Subsequently, this recipe was used to etch a sample of RC187 (RC187-GP), resulting in an improvement on the previous etch, but still presented some micromasking effects, shown in Figure 3.18. This was most likely due to re-deposition of metal particles on the sample surface surrounding the metal contacts during the first etching step. In this etch, the p-contact metals were used as a hard mask whilst the surrounding p-GaAs layer was etched away. This caused the metal to thin by approximately 65 nm. It is therefore recommended to add an additional patterning step to this first etch. If the first mask is re-patterned onto the sample using the AZ5214E resist in positive tone, this will protect the deposited metal during the etch step. The photoresist can then be removed after the etch using solvents and/or a low power oxygen plasma.



(a) **(b)**

Figure 3.18: *Optical microscope image showing the micromasking effects on RC187-GP after the BCl_3 etch to reveal the n-GaAs layer. (a): 1.25x magnification, (b): 100x magnification at the edge of the p-type contacts.*

Further evidence that the micromasking was caused by surface contaminants of metal was observed by analysis of unetched samples by energy-dispersive x-rays (EDX). Since the p-type contacts contained zinc, which does not etch in the dry etch chemistry, it was possible that small amounts of zinc had been liberated during the p-GaAs etch as previously mentioned and/or the lift-off/alloying process and subsequently redeposited on the surface. Readings were taken to determine the elemental composition of various surfaces on the sample. One of the scans is

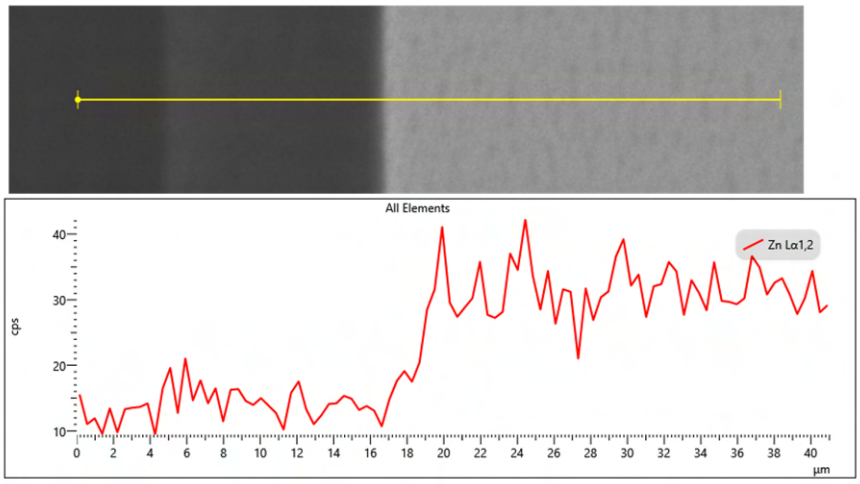
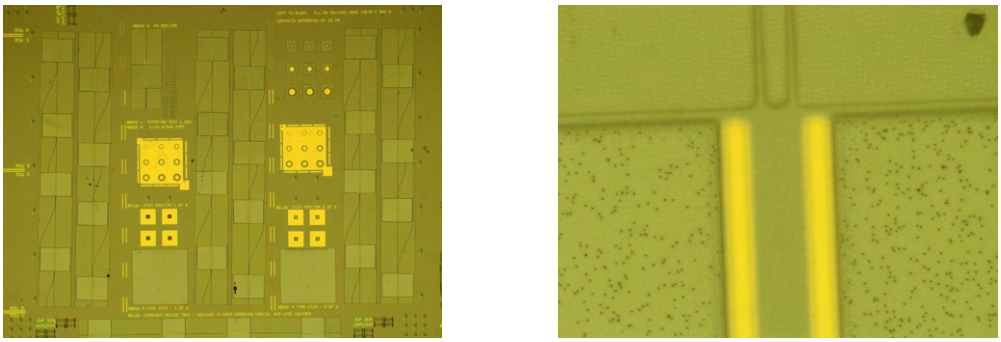


Figure 3.19: *EDX line scan across the etch window of RC184-MF-TRIAL. There is a clear increase in the concentration of Zn across the p-contact and into the etch window.*

shown in Figure 3.19. Here it can be seen how the composition of Zn increases across the etch window in the region where the micromasking was observed.

A fix to remove the zinc film had to have a minimal effect on the rest of the device structure. Hydrochloric acid (HCl) is often used before metal deposition on semiconductor samples of GaAs and Si to remove thin films of oxide. This method could also be used to remove very thin layers of Zn. HCl is also used for the selective wet etching of high aluminium content AlGaAs ($x > 0.7$) [108]. Given that the highest concentration of aluminium present in our samples is $x = 0.5$, a sample of RC187 was etched in concentrated HCl and the rate measured to be approximately 2nm/min. This is significantly lower than the $\sim$ 500nm/min etch rate detailed for $Al_{0.7}Ga_{0.3}As$, and would take a significant amount of time to adversely affect the samples. Given this information, the samples were dipped in dilute HCl:H_2O (1:1) for 1 minute to remove Zn residues followed by a 5 minute rinse in ultra-high purity (UHP) water. The subsequent dry etching process was largely successful with minimal micromasking - Figure 3.20. There was still a small amount of micromasking, however the density of pillars was significantly lower than in the first instance.



(a) (b)

Figure 3.20: *Optical microscope image showing RC184-AC after the n-GaAs reveal etch, following the HCl dip.(a): ×1.25 magnification, (b): ×100 magnification at the edge of the p-type contacts.*

3.5 Passivation

Passivation and packaging of microelectronics and photonics components is essential for the useful application of any fabricated device. Benzocyclobutenes (BCBs) are used commercially for microchip passivation [109]. Since the fabricated devices required larger contact pads which would enable wire bonding and subsequently electrical testing, the use of BCB as a planarisation and passivation layer was implemented. In this scheme, a BCB film is spun onto the semiconductor die and cured. During the curing process, the BCB film planarises the surface. Windows can then be opened in the BCB film above the contact pads using a dry etch process, and top-up metal subsequently deposited forming larger contact pads which can be used for bonding, as summarised in Figure 3.21.

3.5.1 BCB Coating

The first step involves coating the sample in a layer of silicon nitride (Si_3N_4). This is because the adhesion of BCB to III-V semiconductors is poor, so an intermediate layer must be introduced. The thickness of this Si_3N_4 is not paramount, but it must not be too thick such that stresses are induced between the Si_3N_4 and underlying semiconductor, which can lead to dislocation and lifting off of the layer. The Si_3N_4 coating was achieved using a Corial D250 PECVD tool and the layer thickness confirmed using a J. A. Woollam M-2000 Ellipsometer, by Dr

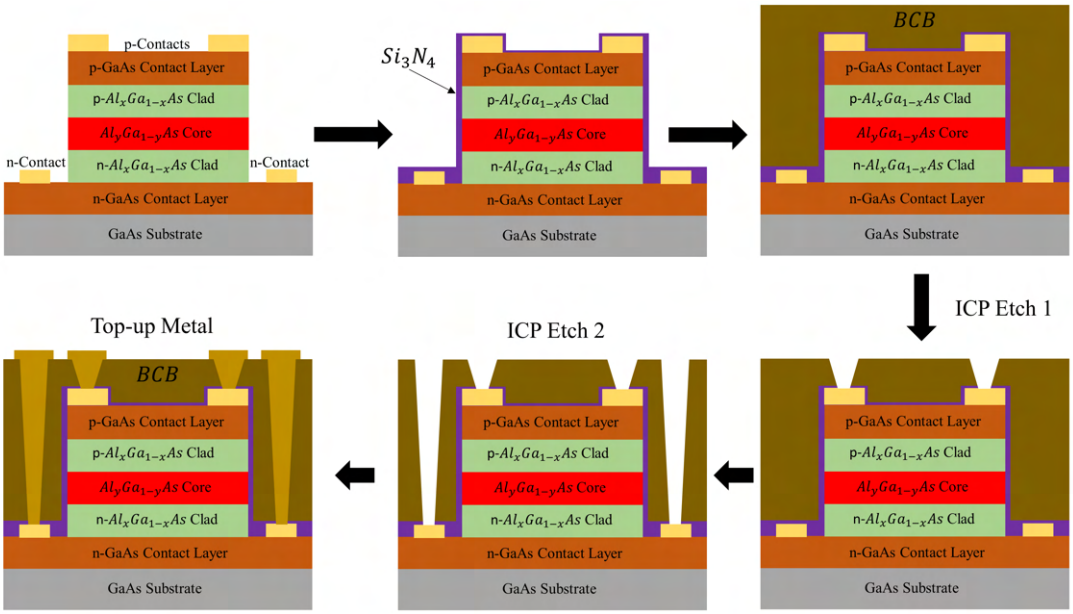


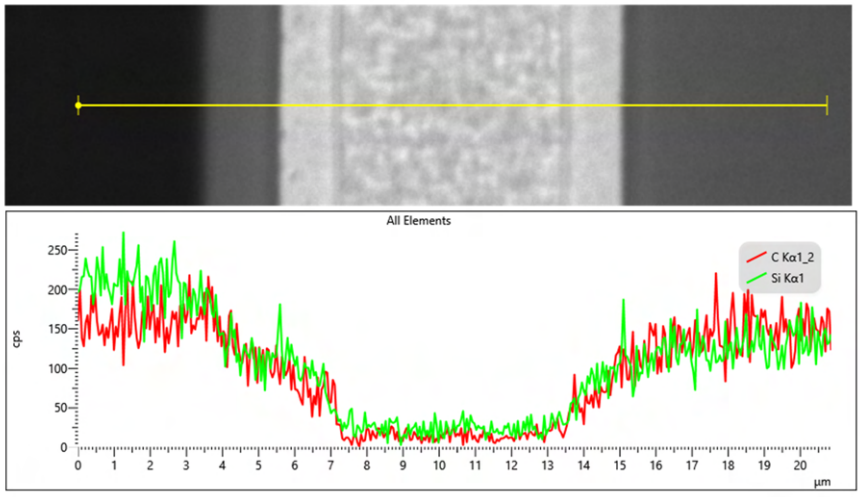
Figure 3.21: *Schematic illustrating the steps required to passivate the device using BCB and for electrical access to the underlying contact pads. Steering region only shown here.*

Chris Mellor. The deposition process was run for 50 seconds on RC187 resulting in a measured thickness of 47.7±0.7 nm. This process was repeated for the other samples. The subsequent step required a spin coat and soft bake of an adhesion promoter (Dow Chemicals AP3000) to the surface of the Si_3N_4. Subsequently, BCB (Dow Chemicals Cyclotene 3022-46) was coated on the surface, again using the spin coater, soft baked on a hotplate and finally multi-stage cured in a plane-levelled hotplate for a few hours which was purged with nitrogen to avoid oxidation of the BCB.

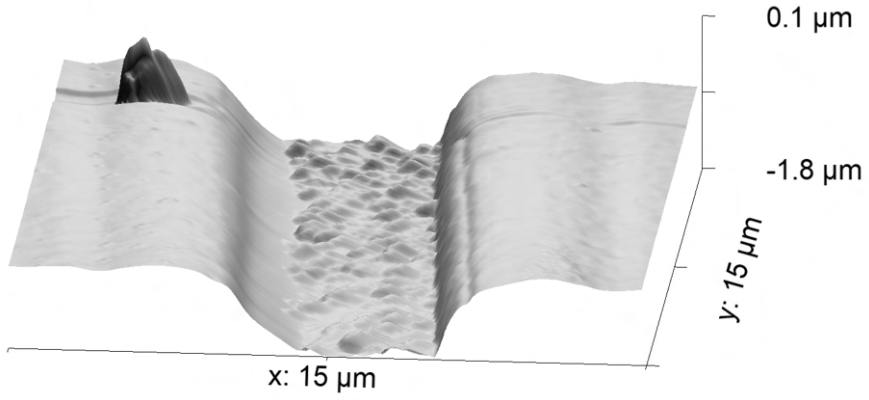
Once the BCB was cured, windows needed to be etched into the BCB to allow access to the underlying contact pads. This was achieved using an inductively coupled plasma (ICP) dry etching process after patterning the windows using AZ5214E photoresist on top of the planarised BCB layer. Since the p-type and n-type contacts exist at different heights, the challenge with the etch is to ensure the windows in the BCB are fully opened. Therefore, the etch was carried out in two stages. Samples were individually mounted on a carrier silicon wafer using wax (CIRE BLOC Wax) before loading into the etcher. The carrier wafer and wax help to dissipate the heat from the high-powered ICP etching process. This

particular wax is used for sample mounting as it does not react with the etchant gases, and has a low vapour pressure.

Both EDX imaging and atomic force microscopy (AFM) were used to check the status of the etches to ensure they had fully opened the windows to the contact pads, as shown in Figure 3.22. EDX analysis was used to measure the concentration of silicon and carbon across the contact window. Silicon and carbon are the main constituents in the BCB polymer so a lack of these elements in the window indicated that most of the BCB has been removed.



(a)



(b)

Figure 3.22: *Analysis of the p-type contact window etch into the BCB layer by (a): EDX imaging analysis of the p-type contact window in BCB and (b): AFM imaging of the 3D profile of the p-type window into BCB. EDX was performed by checking the concentration of silicon and carbon across the window, which is only present in the BCB film. The roughness of the trench in the AFM image, coupled with the height data also confirms that the window has been fully opened to the p-type contact.*

3.5.2 Top-up Contact Pads

The final step in the passivation process is to form electrical access to the metal contacts through the windows etch into the BCB film. Processing guidelines [110] indicate that a sputter etch and titanium seed layer are required before depositing metals onto BCB films. Thus, to test the adhesion of the metal top-up pads on the BCB film, blank semi-insulating GaAs samples were coated with BCB and cured. The samples were then argon ion milled and a blanket 10nm seed layer of Ti deposited by Dr Andrew Rushforth using a Mantis Deposition ion milling and nanoparticle system. Top-up contact pads were then patterned onto the samples using AZ5214E photoresist. Using the Edwards 306 Auto thermal evaporator, 20 nm of Ti followed by 500 nm of Au was subsequently deposited onto the samples and the contact pads isolated using the lift-off technique. The adhesion of the metal pads to the BCB were then tested by a simplified tape peel test (based on the ASTM D3359-17 standard). The rating is a semi-quantitative description of the damage after attachment and removal of the tape. Ratings range from 0B - large portions of the film delaminated, to 5B - no film loss or film damage. These tests indicated 5B results for both trial samples. Figure 3.23 shows a microscope image of a top-up metal contact pad on a BCB-coated trial sample after the tape peel test.

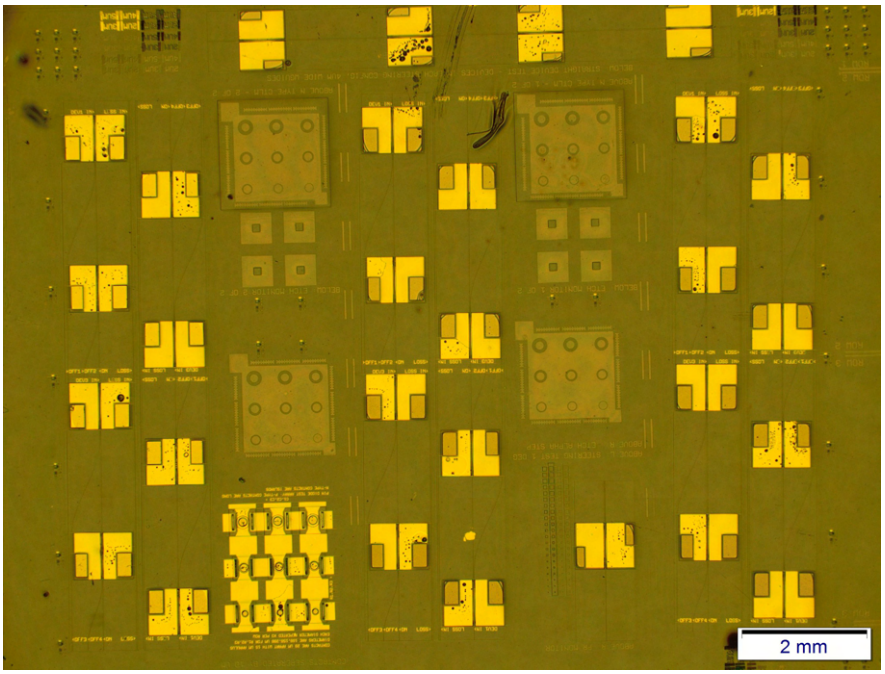
Following these trials, the same recipe was used to form the top-up contact pads on the device samples. A short RIE etch was then used to remove the 10 nm blanket Ti layer, deposited during the ion milling step. At this point fabrication of the on-die devices was completed and the current-voltage (I/V) characteristics were subsequently measured using a Keysight B9202A source-measure unit (SMU). Details of this testing are given in Chapter 5. Figure 3.24 shows an optical microscope image of the completed RC184 and RC187 die.



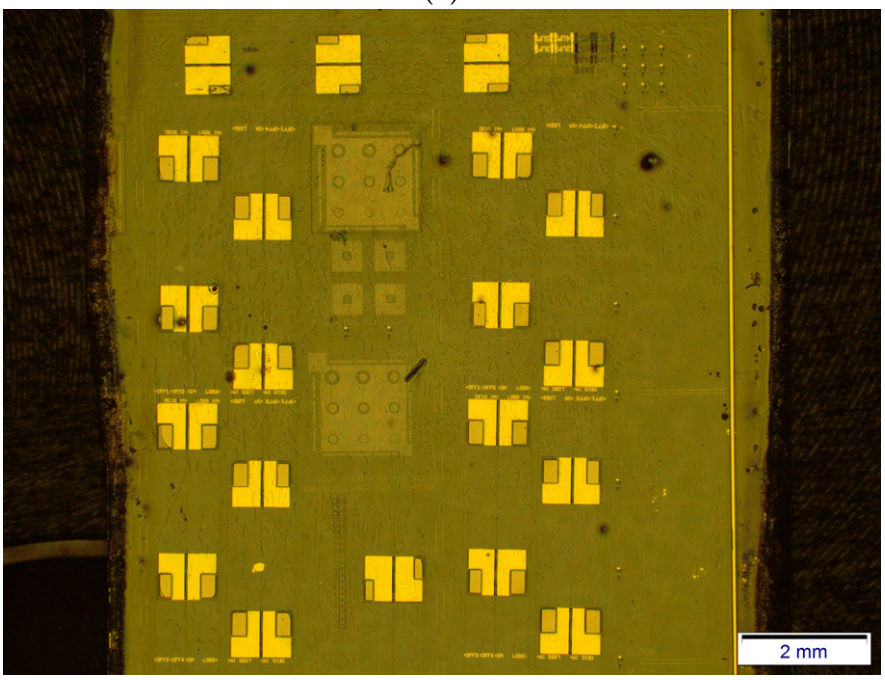
Figure 3.23: *Optical microscope image at ×10 magnification showing the adhesion of the top-up metal contact pads on a BCB-coated, blank GaAs sample after the tape peel test. There is no visible peeling of the metal film indicating good quality adhesion between the metal and BCB layer.*

3.5.3 BCB Swelling

One of the processing steps involved with formation of the top-up contact pads is to soak the sample in a bath of dimethyl sulfoxide (DMSO) at 80^{o}C to lift away the evaporated metal film in the unwanted areas. This step was reliable for removing the metal film, however it resulted in the formation of bubbles on the surface of the sample, as shown in Figure 3.25a. Analysis of these bubbles revealed that they seemed to be forming below the surface of the BCB. The manufacturer reports that BCB resins can be removed using their T1100 Rinse Solvent, which acts to severely swell the BCB film so it can be removed by a high pressure rinse [111]. We suspect that the heated DMSO was causing the BCB to swell in areas near the edges of raised features as it attacked the BCB sidewalls in exposed areas. By heating the sample on a hotplate at 200^{o}C for 10 minutes, a large portion of the bubbles were removed, giving evidence that the initial bubbles were due to swelling and indicating that the heating had relaxed the BCB film. This can be seen in Figure 3.25b.



(a)

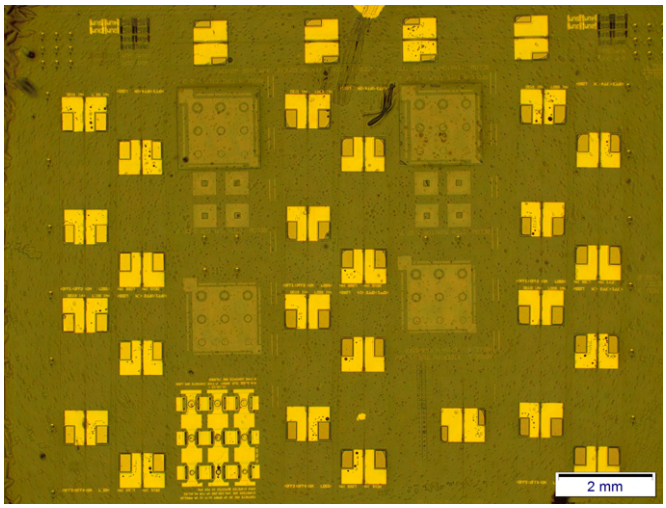


(b)

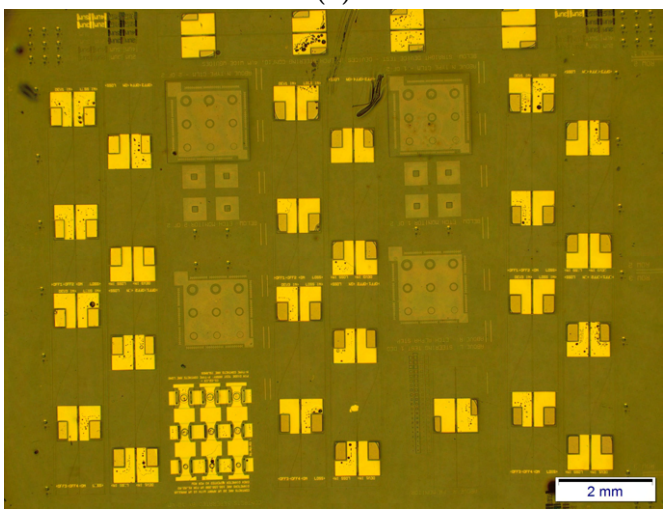
Figure 3.24: *Optical microscope images showing finished (a): RC184 and (b): RC187 die. The RC184 die is 15 mm × 15 mm and contains 24 complete devices. The RC187 sample is a 15×11 mm^2 die and contains 16 devices.*

3.6 Dicing

To enable optical access to an individual device, they must be diced from the parent die. As has been shown, a single 15 mm × 15 mm die contains 24 individual



(a)



(b)

Figure 3.25: *Optical microscope images showing a RC184 die after lift-off of the evaporated metal film for the top-up metla contacts, (a): before heating on the hotplate at 200°C and (b): after. The bubbles due to possible swelling of the BCB film from the hot DMSO solvent during the lift-off process is clearly visible in (a).*

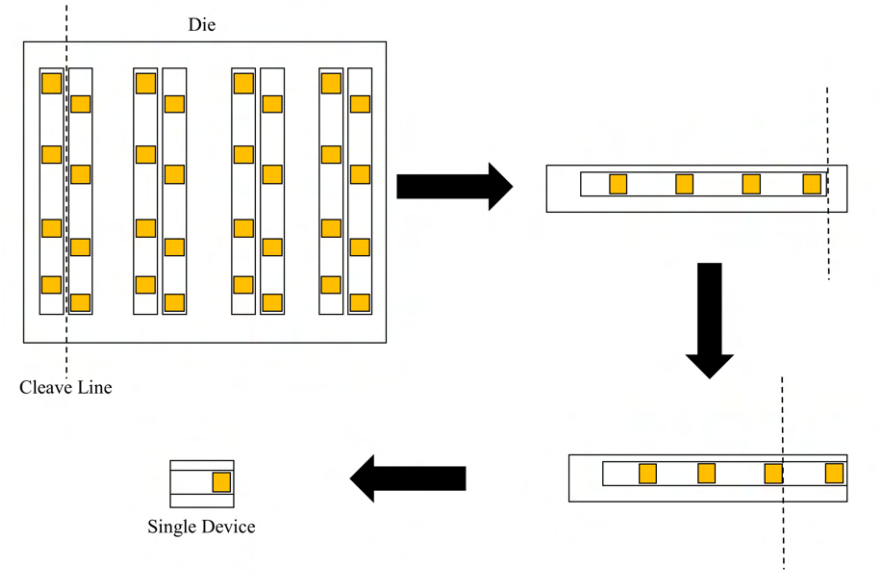
devices, in sets of four. This means there is the option of extracting an optical switch from the die, consisting of up to four separate devices, with the premise of an enhanced extinction ratio and lower coupling losses as compared to the situation of four separately optically coupled devices.

To ensure minimal coupling losses, devices must be extracted from the die by cleaving along the crystallographic axis forming smooth optical facets, free of imperfections and contaminants. This was achieved using a JFP Microtechnic S100. Wafer dicing tape was mounted to a ring frame and stretched using a Loadpoint Presspoint tape ring applicator. Samples were mounted to the adhesive

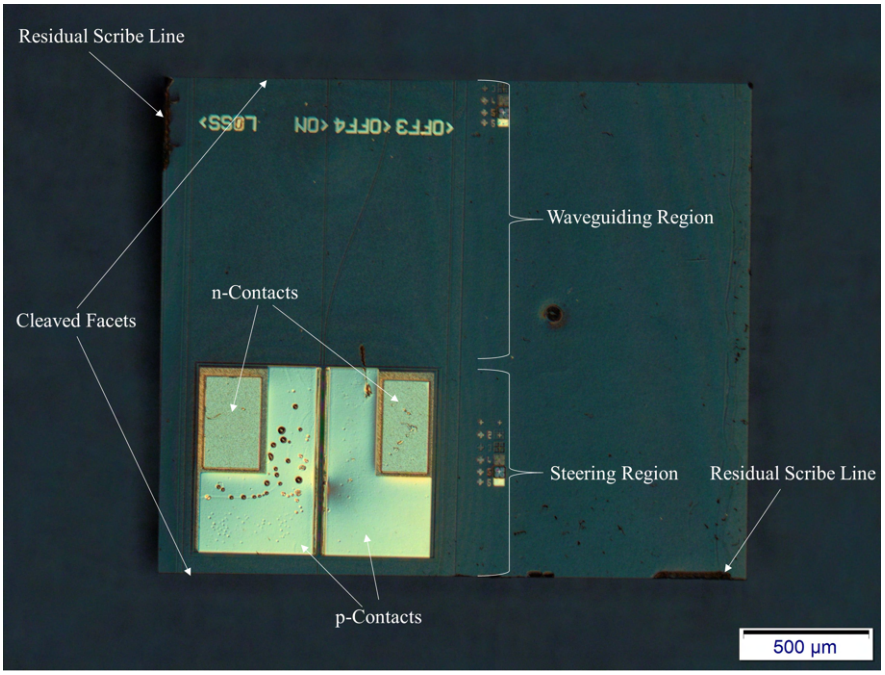
side of the tape and subsequently loaded into the JFP Microtechnic S100. After aligning the sample, the device was scribed by 1 mm along the required cleave axis, using the diamond tipped scriber. The device was then realigned to the scribe line and a break along the required axis formed by pressing the backside of the sample against a metal blade. The tape ring was then unloaded from the S100 and stretched further using the Loadpoint Presspoint to separate the cleaved section from the die. This ensures the cleaved facet does not come into contact with the die, which may cause damage. Using a pair of fine tipped tweezers, the cleaved section was separated from the ring and rinsed with deionised water, before being dried using a nitrogen gun. The cleaved section was then mounted onto a new tape ring and reloaded into the JFP for the next scribe and break, perpendicular to the first. This process was then repeated twice (with shorter scribe lines) to extract a single device from the row. The extraction and cleaning process was then repeated, with the end result being a single device with optically smooth facets. This process is summarised schematically in Figure 3.26a and a labelled optical microscope image of a finished cleaved device from the RC184 wafer is shown in Figure 3.26b.

3.7 Bonding

The final step in the fabrication process is the electrical wire bonding of the device to a custom designed printed circuit board (PCB). The wire bonding process typically connects an active semiconductor device to a package, using a gold wire [112]. In our case, the fabricated devices are prototypes so packaging at this stage is not necessary due to the time and costs required to develop a suitable custom packaging format. Instead, the devices are wire bonded to a gold-plated, copper PCB, which serves as an interface between the device and the control electronics. PCBs were designed and fabricated by Mr Ian Taylor and Mr Andrew Stuart. Gold plating of the PCBs was carried out by Dr Chris Mellor. Wire bonding was chosen to form the interconnects between the device and the PCB due to



(a)



(b)

Figure 3.26: *(a): Schematic illustration of the dicing process used to extract a single device from the parent die. (b): Labelled optical microscope image of a finished single device from RC184.*

its advantages of high reliability, electrical performance, and corrosion resistance [113].

There are two major wire bonding techniques used in the fabrication of semiconductor devices: ball-wedge bonding and wedge-wedge bonding. The ball-wedge bonding technique was used here, as it was found that the shape of the wire

loop formed by this process was more reliable due to the geometry of the device mounted onto the PCB. A summary of the ball-wedge bonding process is shown in Figure 3.27. In this process, a ball is first formed by an electric flame-off. The ball is then pressed against the required bond site and heat and ultrasonic energy is applied to form a cold-weld between the ball and the bond pad. These parameters must be optimised individually to form a reliable bond. A loop is then formed from this bond and the wire terminated by a wedge bond at the second site, again by applying pressure, heat and ultrasonic energy.

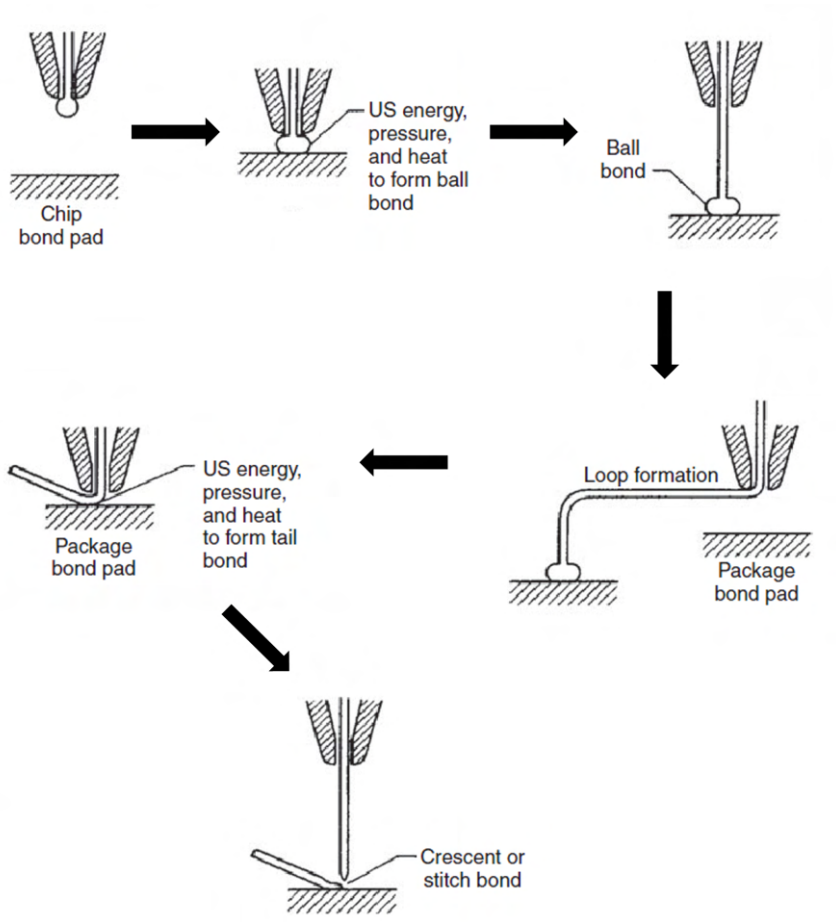


Figure 3.27: *Schematic illustration of the ball-wedge bonding process [114].*

Wire bonding of the fabricated devices was carried out using a TPT HB10 Wire Bonder, equipped with 25 μm diameter gold wire. Trials were carried out using the BCB-coated blank GaAs samples which were used to test the adhesion of gold pads onto BCB, as explained in Section 3.5. Samples were first manually transferred to the custom PCBs using fine-tipped tweezers and secured to the

PCBs using EPO-TEK H20E silver epoxy. This silver epoxy features a high thermal conductivity which enables some dissipation of heat generated by the device. The epoxy was cured by placing the PCB on a preheated hotplate at 150 ^{o}C for one hour.

After cooling, the PCB was mounted to the heated stage of the TPT bonder and the temperature allowed to stabilise at 80 ^{o}C. A series of bonds were then applied from the gold tracks on the PCB to the gold pads on the devices (ball to wedge) and the parameters adjusted individually to find the optimum bonding conditions. This was then repeated with dummy blank GaAs devices concurrently fabricated with the real devices. These dummy devices had the same structure as the real devices but without any epitaxial layers. It was found that bonding to the p-contact pads on the trial samples was unreliable, whereas bonds were formed to the device n-contacts with relative ease. This is due to the fact that the p-contact pads sit on the surface of the BCB, whereas the n-contacts are annealed to the semiconductor. Although the adhesion of these pads to the BCB was good in the context of the lift-off process and tape peel test, the wire bonding process is much more violent and thus the pads tear away from the BCB with relative ease, in most cases. To overcome this issue, a wire-bond rework method [115] using silver epoxy was implemented to secure the bonds to the p-contacts in the instances where the initial bond failed. Figure 3.28 shows an optical microscope image of a wire bonded device where the bonds to the p-contacts have been reworked with silver epoxy. The rework method was achieved by first wetting a probe needle with mixed silver epoxy, which was left for a few hours to slightly harden. This short cure at room temperature makes the epoxy slightly more viscous and easier to manipulate. The wetted probe was then moved into position above the sample using a micropositioner and lowered onto the contact pad. This process wets the contact pad and failed wedge bond with silver epoxy. If the wedge bond was not in the required position, a micropositioner and probe was used to manipulate the wire into place, and a second micropositioner and probe used to dispense

the required amount of silver epoxy. The sample can then be cured as before on a hotplate. Continuity between the bond and contact pad was then confirmed using a multimeter (Keysight Truevolt 34460A). This procedure was repeated if the bond was still weak or had a poor electrical connection.

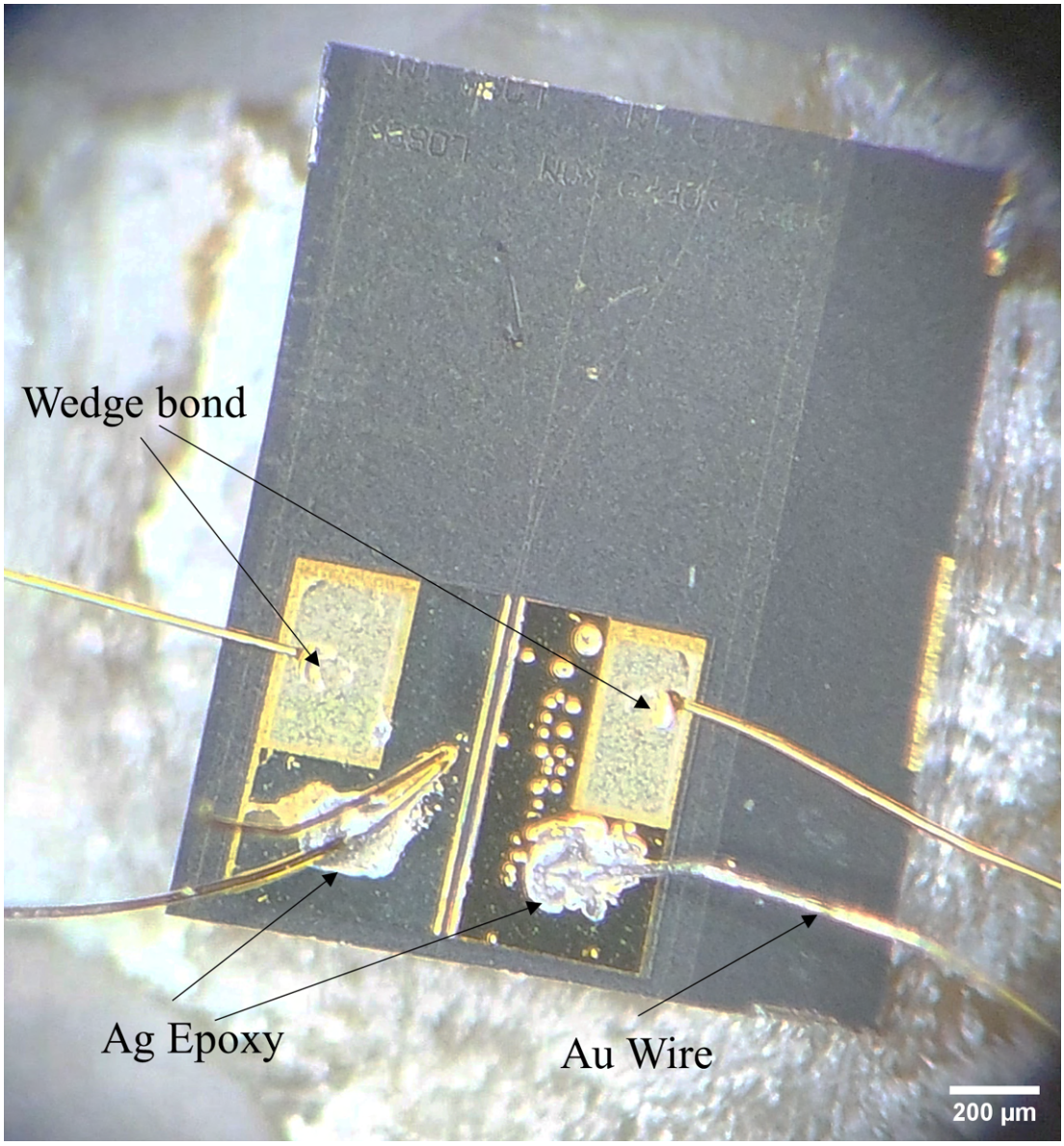


Figure 3.28: *Optical microscope image showing a gold wire bonded device. Bonds to the p-contacts have been reworked using silver epoxy to improve the reliability of the bond*

3.8 Summary

In this chapter, the successful fabrication of novel optical switching devices for use in NIR quantum sensing experiments has been discussed. The fabrication process involved twenty main process steps, individually optimised for repeatability and reliability. Key points included: optimisation of the photolithography steps; troubleshooting of micromasking during dry etching of the mesa, and reworking of the gold wire bonding using silver epoxy to ensure good quality electrical contacts to the PCB submount. Figure 3.29 gives a schematic summary of the entire fabrication process. In the following chapter, the design and construction of an optical and electrical test bench used to characterise these devices will be detailed.

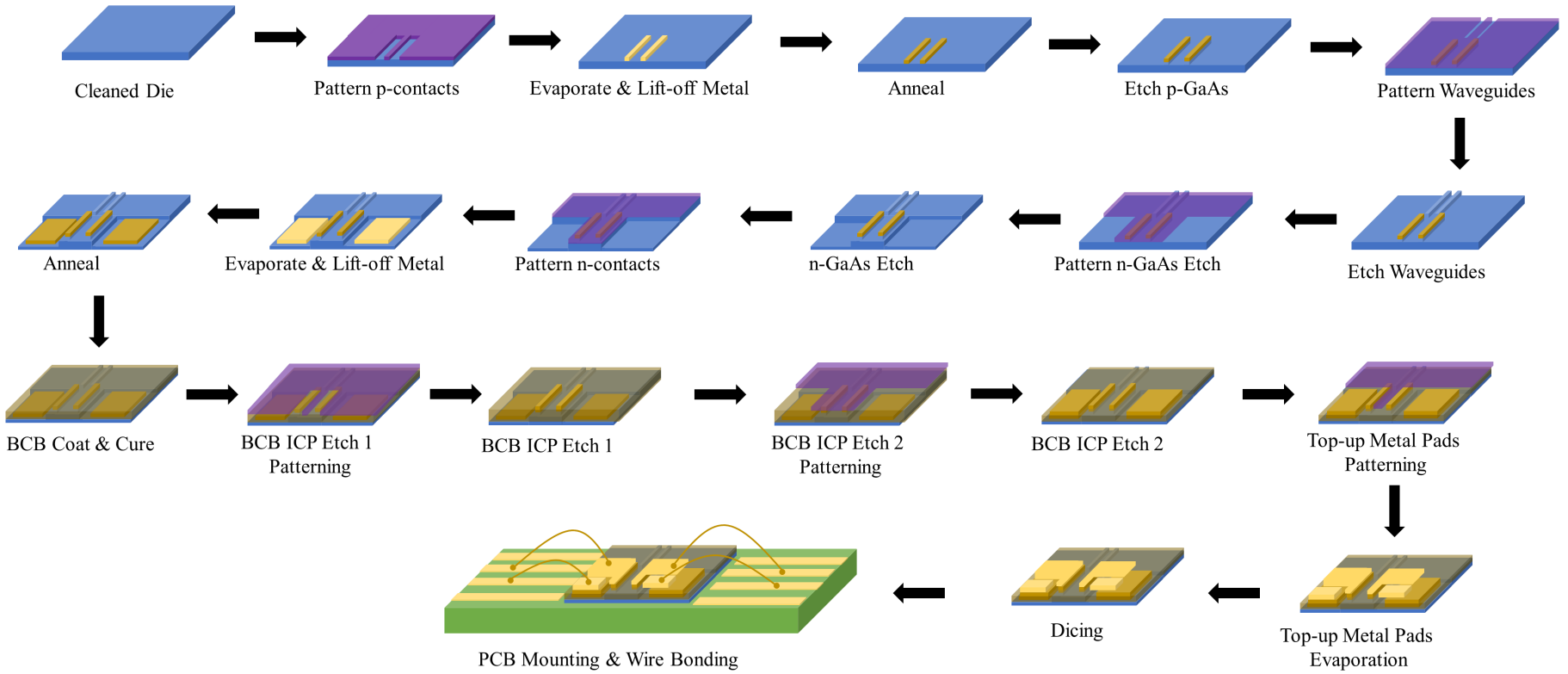


Figure 3.29: *Schematic diagram showing the main stages of the entire fabrication process for the optical switching devices. A single device is shown for clarity, however each die contains 24 devices and other various test features. BCB: Benzocyclobutene, ICP: Inductively Coupled Plasma, PCB: Printed Circuit Board.*

Chapter 4

Testing Instrumentation

4.1 Introduction

The characterisation of optoelectronic devices requires careful consideration of the alignment and coupling of light into and out of the device, as well as precise control of the electrical parameters. To perform optical measurements and electrical control of the devices fabricated in this project, a custom testing system had to be designed and constructed. In this chapter, the design considerations of this system are discussed, including a description of the hardware components of the system and Python software written to interface with this hardware. Finally, limitations of the system are discussed and suggestions for future improvements are given.

4.2 Requirements of the Test System

The major components of the testing system required to test the basic functionality of the devices are as follows: bulk optics, used to manipulate the shape and properties of the laser beam to be coupled into the device; a precise positioning system which can scan the position of the light and/or device in increments smaller than the input waveguide dimensions; imaging systems to help with alignment of the laser beam into and out of the device under test (DUT); an optical

detection system, sensitive enough to detect the low optical intensity of light exiting the device and fast enough to resolve the switching speed; and finally an electrical system which can provide electrical pulses to both channels of one device simultaneously with sufficient power limitations.

4.2.1 Electrical Control & Optical Detection Speed

As discussed in Chapter 2, the switch on delay of the devices is dominated by the charge storage delay time of the device which is related to the capacitance of the P-i-N stricture. Of course, the real switching speed of the devices will depend on the time taken for the charge distribution in the core to equalise at the level required for switching. This carrier density will differ slightly depending on the wavelength of guided light used.

The switching time of the fabricated optical switching devices is similar to the turn-on time of a laser diode, or the rise time of an LED. In a double heterostructure laser, the turn-on time is determined by the delay taken for the current density to reach the threshold of lasing. Below the threshold, the delay is related to the junction capacitance. Under forward bias, the capacitance is proportional to the current and the diode transit time. To obtain an estimate for the switching time of the fabricated devices, the threshold current can be taken as the current injection which results in a current density in the core required to produce a refractive index change needed to steer a beam of a given wavelength into the 'OFF' channel.

In the ideal case, the P-i-N structure has no capacitance, and the injected carriers arrive instantaneously in the depletion region where they recombine. In this case the rise time, t_r, is governed solely by the recombination time of the carriers and is given by [116],

$$t_r = \tau_s \ln \frac{I}{I - I_{th}}, \tag{4.1}$$

where τ_s is the charge carrier spontaneous recombination time, I is the injected

current and I_{th} is the threshold current required for stimulated emission. In the real case, the junction capacitance and stray capacitances of the driving circuit cause a delay in time taken for the carriers to arrive at the recombination region. A forward biased p-i-n diode has two types of capacitance - transition (or depletion layer) capacitance and diffusion capacitance [116]. The depletion layer capacitance is analogous to the capacitance of a parallel plate capacitor, $C_T = \epsilon_R \epsilon_0 A/d$, where A is the area of the cladding layer and d is the width of the depletion region. This capacitance is much smaller than the diffusion capacitance, which dominates in the forward bias regime. When a forward bias is applied across the p-i-n diode, injected carriers replenish those that recombine, and the remaining build up as stored charges. This is equivalent to a diffusion capacitance, C_d, where the charge is equal to the stored charge.

The switch rise time is thus dependent on the forward voltage, V_d, and intrinsic properties of the material, decreasing as V_d increases. For heavily doped GaAs p/n diodes, the zero-bais capacitance, $C_0 \sim 200$ pF per unit area. Rise times for p/n junction LEDs are on the order of 10 ns [116]. The intrinsic region of the optical switching devices increases the width of the space-charge (depletion) region. A larger intrinsic region will therefore lead to more stored charge, increasing the forward voltage required to remove the charges during switching [1]. The rise time of the optical switches due to internal resistances and capacitances during DC operation can be estimated using $\tau = RC$, with the aforementioned 10-90 rise time corresponding to 2.2τ. The resistance can be estimated from the measured I-V curves ($\sim 10\Omega$) and the capacitance assumed to similar to those quoted for typical GaAs p/n diodes. Therefore, it is expected that the switch on/off delay time for these devices will be on the order of tens of nanoseconds. This is well below the required microsecond switching times required by the intended application. The chosen constant current source therefore must be capable of sub-microsecond on/off times.

[1] It will also however decrease the depletion layer capacitance, but the diffusion capacitance is much larger and thus dominates the overall capacitance

It is important to note that a distinction must be made between the intended switching operation of the fabricated devices, and the modulation of a commercial optical modulator. Often, in telecommunications applications, optical signals are modulated at very high frequencies (GHz), but with a lower requirement on the extinction ratio between the 'ON' and the 'OFF' state, or logical '0' and '1' state in the case of an optical transmitter. Ideally, the '0' state of the transmitter would be the case when the laser is completely off and not emitting any optical power. However, when the laser is taken below the lasing threshold, the quality of the optical signal is significantly reduced [117]. Therefore, to obtain the high modulation frequencies required to transmit large quantities of data, the '0' state is taken above the lasing threshold. In the application for the optical switching devices fabricated in this project, there is a strong emphasis on completely extinguishing the beam. As described in Chapter 1, any light which is not extinguished from the MOT beams when the interferometery sequence is carried out can detrimentally affect the precision of the final measurement of the quantum sensor. Therefore, these optical switches are intended to extinguish the beam with a high extinction ratio when an electrical signal is applied and hold it in this state until switched off, at which point the beam should propagate through the device with minimal losses. The system must therefore be capable of measuring optical signal rise times of ≤ 1 μs to conclude whether the optical switches meet the design requirements.

4.2.2 Optical Coupling

The second major aspect of the test system requirements is the coupling of light into and out of the device under test (DUT). The system must be capable of both focusing the laser light into the input waveguide of the device and collecting the light from the output waveguide. In commercial optoelelectronics packaging, this coupling is often achieved using butt coupling of bare fibre, positioned using automated nanometre precision stages. In this case the core of the optical fibre

is the same size as the waveguide of the device at the facet and the numerical aperture (NA) of the fibre is greater than or equal to the divergence of the emitted beam at the output facet [118]. This method achieves high coupling efficiency and low insertion losses, however working with bare fibre is challenging due to its fragility and low inertial properties. Care must be taken to exclude temperature fluctuations of the air around the test system which would cause vibrations and a misalignment of the bare fibre. Furthermore, when testing single mode devices, single mode optical fibres must be used which can be very lossy. Additionally, if the size of the core of the fibre cannot match the device waveguide, or the NA is insufficient then an additional lens or lensed fibre must be used.

An alternative method is to use microscope objectives to both focus the light into the device under test (DUT), and collect light from the output facet. In this case the working distance of the objective must be long enough so that the face of the objective does not impinge on the surrounding hardware, and the numerical aperture of the objective must again be greater or equal to the divergence of the emitted beam at the output of the DUT. Furthermore, the objective must be able to focus the beam down to a spot size similar to that of the waveguide, in order to achieve efficient coupling.

Regardless of the coupling method implemented, fine control of the position of the fibre or microscope is required to ensure maximum coupling through the DUT. Since the constraints on single mode behaviour dictate that the width of the waveguides must be $\sim$2 μm and the depth sub-micron, the positioning system is required to have sub-micrometre precision.

4.3 Hardware Design

A schematic plan-view illustration of the assembled test system is shown in Figure 4.1. In this section, propagation of light through the various stages of the system will be discussed, along with the considerations of the system requirements and choice of appropriate hardware to facilitate these requirements. The system will

be split into three subsections: the input side, where the properties of the laser beam are prepared before entering the input facet of the DUT; the output side where the light is collected from the DUT and analysed; and finally the illumination and imaging scheme of the input and output facet which allows inspection of the device during alignment. All components are mounted in a cage system and fixed to an optical breadboard. The breadboard is then positioned on a passive isolation support frame. This configuration ensures optical components remain fixed in place, and the system is isolated from unwanted vibrations which may disturb the beam alignment during testing.

4.3.1 Input Side

Referring to Figure 4.1, light from a custom laser system, with interchangeable continuous wave (CW) laser diodes (Thorlabs L904P010 - 904 nm, L780P010 - 780 nm, Laser2000 LAS-045227 - 760 nm, LAS-045233 - 734 nm) is first collimated using an adjustable collimation tube (Thorlabs LTN330-B) and then incident on a mirror M1 (Thorlabs ME05S-M01) mounted onto a rotatable right-angled aluminium block. This arrangement allows adjustment of the beam divergence and angle of the beam exiting the laser housing. Due to laser safety requirements, the beam exiting the laser housing must be $\leq$ 2 mW peak power, so a neutral density filter (Thorlabs NE10A-B) is used to attenuate the beam power before the light leaves the housing.

The collimation tube houses an aspheric lens with focal length, $f = 3.1$ mm. Given the divergence of major axis of the beam from the packaged diode, θ, the radius of the collimated beam is then,

$$r = f \tan\left(\frac{\theta}{2}\right). \tag{4.2}$$

Table 4.1 gives the calculated beam diameters for each laser diode.

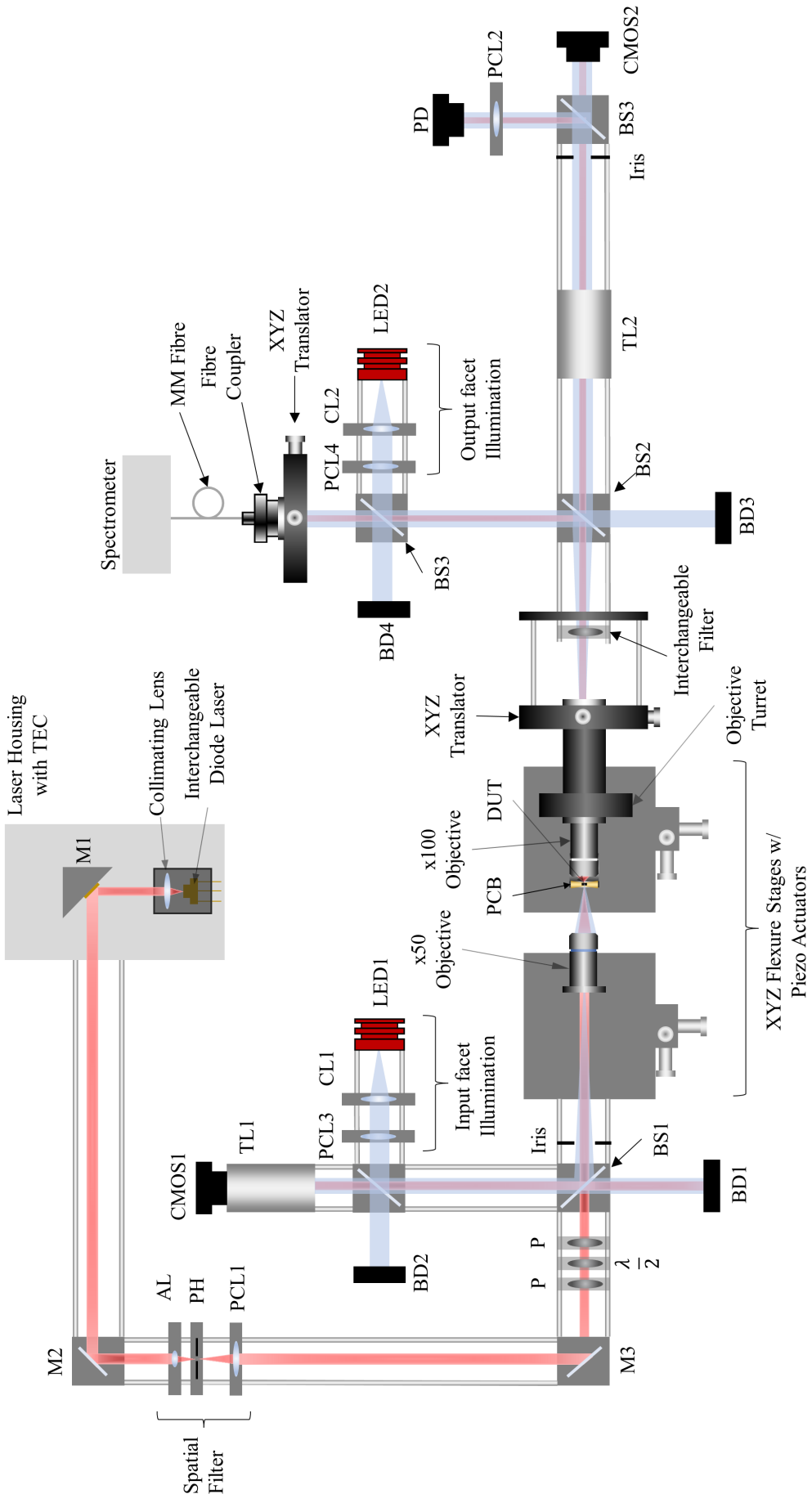


Figure 4.1: *Plan-view illustration of the assembled test system used to characterise the fabricated devices. The overhead inspection microscope assembly is not included in this illustration for clarity. M: Mirror, AL: Aspheric Lens, PH: Pinhole, PCL: Plano-convex Lens, BD: Beam Dump, TL: Tube Lens, P: Polariser, λ/2: Half Wave Plate, LED: Light Emitting Diode, CMOS: Complementary Metal Oxide Semiconductor Sensor, BS: Beamsplitter, PCB: Printed Circuit Board, DUT: Device Under Test, PD: Photodetector, MM: Multi-mode, TEC: Thermoelectric Controller.*

Laser Diode	**Centre Wavelength (nm)**	**Divergence Angle (^{o})**	**Collimated Beam Radius (mm)**
L904P010	904	30	0.83
L780P010	780	30	0.83
LAS-045227	759	35	0.98
LAS-045233	734	35	0.98

Table 4.1: Calculated beam diameters for each laser diode used for testing of the fabricated optical switches.

Spatial Filter

To ensure efficient coupling of light into the device, a clean Gaussian beam with minimal spatial intensity variations is required. Due to imperfections in the laser diode facets, heating of the diode during CW operation and unwanted feedback effects, the intensity distribution produced by the diode contains unwanted multiple-order spatial modes. Furthermore, imperfections from other optical elements may also cause undesired scattering of the beam within the optical system. Thus, a spatial filter is implemented to ensure a smooth Gaussian intensity profile before the beam enters the (DUT). The spatial filter system consists of an aspheric lens, a pinhole aperture, a positioning system and a final lens to re-collimate the beam. By centering the pinhole on the central Gaussian spot produced by the aspheric lens, the 'clean' portion of the beam passes through the system whilst the spatially varying higher order modes are filtered out. This concept is illustrated in Figure 4.2. When the beam is focused, the spatial variation at the focus becomes the Fourier transform of the beam intensity variation, so at the pinhole, the k-vectors of the beam become spatial variations.

Choosing the correct optics and pinhole for the spatial filter system requires knowledge of the input beam diameter, wavelength and desired exit beam diameter. The desired exit beam diameter depends on the chosen objective lens used to focus the light into the device. The objective lens is a long working distance Olympus LMPLFLN50x infinity-corrected objective with a numerical aperture of 0.5. The long working distance of 10.6 mm allows precise positioning of the

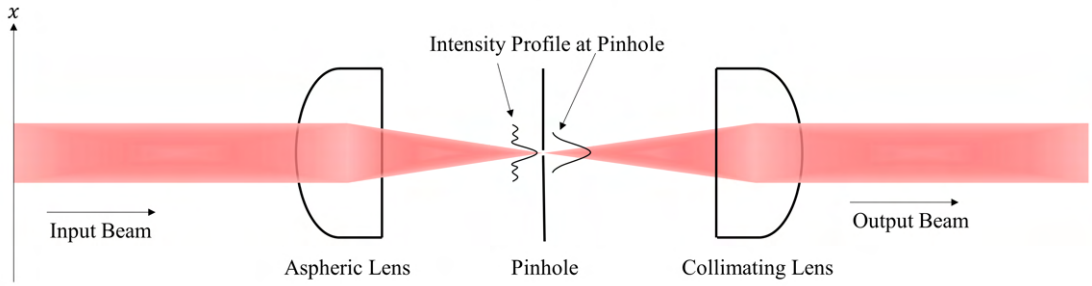


Figure 4.2: *Schematic illustration of the spatial filter system used to improve the beam quality before coupling into the DUT.*

objective with respect to the input facet of the DUT. The maximum beam diameter of a parallel beam which can enter the backside of the objective is given by the objective pupil diameter. This directly determines the exit beam diameter required from the spatial filter. The pupil diameter, ϕ, of the objective given by the manufacturer is [119],

$$\phi = 2 \times NA \times F, \tag{4.3}$$

where NA is the numerical aperture, and F is the focal length of the objective lens. The focal length of the objective is given by,

$$F = \frac{\text{Design tube lens focal length}}{\text{Magnification}}. \tag{4.4}$$

For the LMPLFLN50x objective, F = 180/50 = 3.6 mm, so $\phi = (2)(0.5)(3.6) =$ 3.6 mm. Therefore, the exit beam diameter of the spatial filter must be $\leq$ 3.6 mm. To find the appropriate sized pinhole for the spatial filter, the diffraction limited spot diameter, D, produced by the focusing aspheric lens can be used. The pinhole should then roughly be around 30% larger than D so that the smooth Gaussian beam is not significantly clipped, and not so large that the spatially varying higher order modes pass through. The expression for the diffraction-limited spot size is,

$$D = \frac{\lambda f}{r}, \tag{4.5}$$

where λ is the vacuum wavelength, f is the focal length of the aspheric lens, and r is the input beam radius at the e^{-1} point. The focal length of the chosen aspheric lens is 15.6 mm (Thorlabs C260TMD-B). The calculated spot sizes for each laser diode are summarised in Table 4.2. Given the limited availability of pinhole sizes between 10 μm and 25 μm, a 25 μm pinhole (Thorlabs P25D) was chosen. This pinhole diameter is not ideal for filtering out the lateral higher order modes at the shorter wavelengths, however, an automated positioning system helps align to the centre of the dominant fundamental mode of the beam in cases where the pinhole is significantly larger than the spot size (see Section 4.4 for more detail).

Laser Diode	**Centre Wavelength (nm)**	**Input Beam Radius (mm)**	**Spot Size (μm)**
L904P010	904	0.83	16.9
L780P010	780	0.83	14.7
LAS-045227	759	0.98	12.1
LAS-045233	734	0.98	11.7

Table 4.2: Calculated spot size diameters for each testing wavelength, using the Thorlabs C260TMD-B aspheric lens.

The pinhole is mounted in a XY translator with micrometer drives (Thorlabs ST1XY-S/M) which facilitates precise positioning of the pinhole at the focal point of the aspheric lens. The final component of the spatial filter is a plano-convex lens whose focal length results in the final required beam diameter entering the focusing objective. The required focal length can be calculated by considering the geometry of the beam expansion, as shown in Figure 4.3. Calculated values are $\leq$67.6 mm for the 904 nm and 780 nm diodes, and $\leq$ 57.4 mm for the 759 nm and 734 nm diodes. Therefore, a $f = 50$ mm plano-convex lens was chosen (Thorlabs LA1131-B-ML), resulting in an output beam radius of 2.66 mm or 3.14 mm respectively.

Polarisation Control

Before entering the focusing objective, the now spatially filtered beam is incident on another planar mirror, M3 (Thorlabs ME05S-M01) and then passes through a

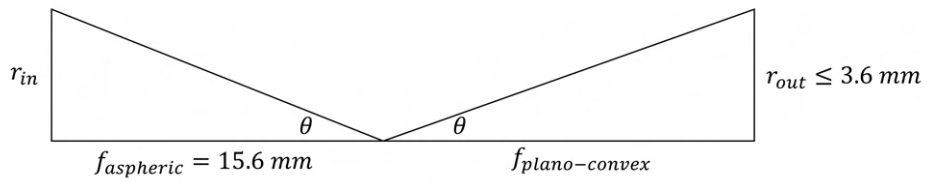


Figure 4.3: *Geometry of the focusing and expansion of the beam within the spatial filter.*

series of polarising optics: polariser (Thorlabs LPNIRE100-B), half wave-plate (Thorlabs AHWP10M-980), and another polariser (Thorlabs LPNIRE100-B). This arrangement allows control of the beam power and polarisation. The first polariser ensures the beam is linearly polarised in a given direction. The subsequent half wave plate then allows the plane of the linearly polarised light to be rotated about the optical axis, and the final polariser then allows control of the power of the final beam, by aligning its polarisation plane with or away from the fast axis of the half wave-plate.

Focusing Objective

The polarised beam then passes through a non-polarising beam splitter (Thorlabs BS014), followed by an adjustable iris (Thorlabs CP20S) which removes any light scattered by the polarising optics and beam splitter. The beam then finally enters the focusing objective, which is mounted on a flexure stage with piezo actuators (Elliot Martock MDE125). This flexure stage allows precise manual adjustment of the objective with a travel range of 2 mm in each axis, as well as 100 μm of piezo adjustment with a precision of 50 nm. This arrangement allows precise alignment of the beam spot, produced by the objective, to the input waveguide of the DUT. The theoretical beam spot diameter ($1/e^2$ width of the central Airy disc) produced by the focusing objective can be calculated using,

$$d = 0.82\frac{\lambda}{NA}. \tag{4.6}$$

The largest theoretical spot size produced by the objective is therefore 1.48 μm

with the 904 nm laser and the smallest is 1.20 μm with the 734 nm laser. This is an approximation and assumes a perfect optical system, free of aberrations, so naturally the real spot size produced by the objective will be larger. Furthermore, this approximation assumes that the rear aperture of the objective is filled with the input beam, so the slightly smaller beam diameter in this situation means that the final spot size will be larger. Nonetheless, these theoretical values are on the order of magnitude with the dimensions of the input waveguides, ensuring significant modal overlap between the waveguide modes and the laser beam.

4.3.2 Output Side

The output region of the test system is used to collect and analyse the light exiting the DUT. As mentioned in Chapter 3, the device is electrically bonded to a custom, gold-plated copper printed circuit board (PCB). This PCB is mechanically fixed to a machined aluminium stand using 2 mm diameter screws and washers. This assembly is then affixed to another flexure stage (Elliot Martock MDE123) with a Peltier module in between to control the local temperature. This stage also features piezo actuators with 25 μm of travel and 10 nm resolution, facilitating the precise adjustment of the device during alignment. 2 mm of manual coarse adjustment is also possible using the built-in micrometer drives.

As the light exits the output facet of the DUT, it is captured by a $\times$100 objective lens (Olympus MPLFLN100X). The amount of light captured by this objective depends on the numerical aperture of the output waveguide of the DUT and the numerical aperture of the objective lens. The numerical aperture of the objective lens determines its ability to gather light from a point-like source at a fixed distance. The output from the DUT can be approximated as a point-like source. Light exits the output facet of the DUT and spreads out in a cone, thus the numerical aperture of the objective lens must be sufficient to capture this light cone at the working distance. This is illustrated in Figure 4.4.

The numerical aperture of the DUT output facet (a rectangular waveguide) can

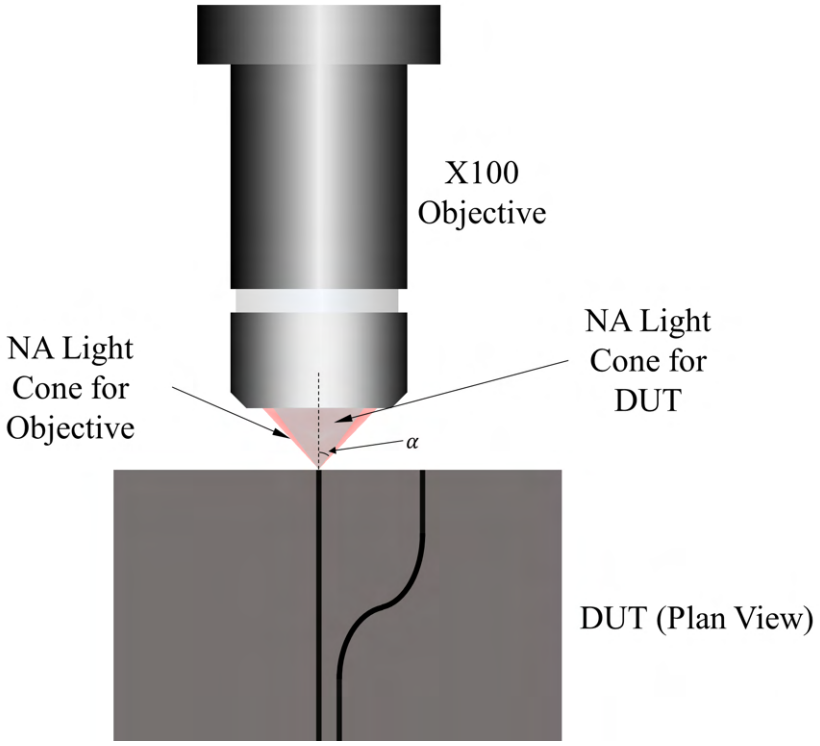


Figure 4.4: *Numerical Aperture of DUT and imaging objective.*

be approximated by [120],

$$NA \approx n_1\sqrt{2\Delta} \tag{4.7}$$

where $\Delta = \frac{n_{\text{core}}^2 - n_{\text{clad}}^2}{2n_{\text{core}}^2}$, n_1 is the refractive index of the medium at the output facet, n_{core} is the refractive index of the waveguide core, and n_{clad} is the refractive index of the waveguide cladding. The calculated numerical apertures for devices from RC101, RC184 and RC187 wafers at the relevant testing wavelengths are summarised in Table 4.3. The imaging objective chosen thus has to have a high NA to capture most of the light from the DUT. The numerical aperture of the chosen imaging objective is 0.9. Using $NA = n\sin(\alpha)$, where n is the refractive index of the medium between the objective and the DUT (air in this case), and α is the angle subtended by the edge of the light cone to the optical axis, gives $\alpha = 64.3^o$.

The imaging objective is mounted on an objective turret (Thorlabs OT1), which is affixed to a three axis translation mount (Thorlabs CXYZ1). The objective

Wafer	**Testing Wavelength**	**Numerical Aperture**
RC101	904	0.27
RC184	780	0.32
”	760	0.34
RC187	760	0.35
”	734	0.38

Table 4.3: Calculated numerical apertures (to 3 significant figures) of devices from each epitaxial design at the relevant testing wavelengths.

turret allows the imaging objective to be moved into and out of the optical axis when mounting the PCB, and also allows additional objectives to be added if required. The translation mount features ±2.5 mm of X and Y travel and ±1.5 mm of Z travel (optical axis), so that the objective can be coarsely brought into focus and alignment with the DUT. Fine adjustments are then achieved using the flexure stage which the DUT is mounted to. The input light is then coupled into the DUT via adjustment of the first flexure stage. The described optical assembly used to image the input and output facets of a DUT is shown in Figure 4.5.

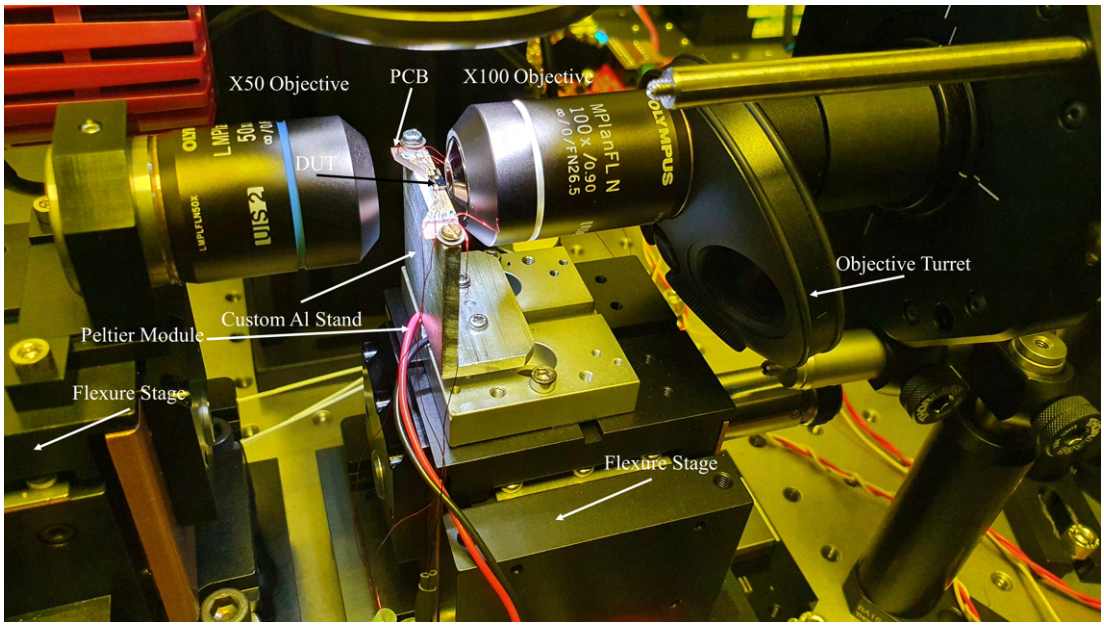


Figure 4.5: *Picture of the main central optical assembly used to image the input and output facets of a DUT.*

Filters

After the light exits the objective, it passes through a selected filter. This filter is used to extinguish most of the light generated by the DUT during operation. The DUT resembles an LED structure so naturally, electrical injection of carriers into the core of the double heterostructure produces photons with energy close to the band gap of the core, although unlike the light from a laser, the spectrum is very broad owing to the lack of optical feedback. Analysis of the electroluminescence (EL) and photoluminescence (PL) spectra (Chapter 5) facilitated the selection of appropriate filters which would extinguish most of the generated light. Further extraction of the required signal was then achieved using a lock-in detection (see Section 4.3.5 for more detail). As an example, the transmission spectrum for one of the filters (Semrock FF01-792/64-25) used for devices from the RC184 wafer (nominal core band gap 730 nm) is shown in Figure 4.6, along with the testing diode and an EL spectrum.

Optical Detection

The final stages of the test system involve components used to take measurements of the optical signals exiting the DUT. After passing through the filter, the light is incident on another non-polarising 50:50 beam splitter, BS2, Figure 4.1 (Thorlabs BSW26R). One arm of this beam then passes through another identical beam splitter, BS3, before entering a fibre coupler, which consists of an aspheric lens mounted to a fibre adapter (Thorlabs SM05SMA). This fibre coupler assembly is fixed to a XYZ translation mount (Thorlabs CXYZ1) which facilitates optimisation of the coupling of the light into a multimode fibre (Ocean Optics QP450-1-XSR). The light then passes through the fibre and into a spectrometer (Ocean Optics USB 4000+). The spectrometer allows the monitoring of the wavelength of the light as electrical parameters of the device are scanned. This assembly can also be moved to the input side of the test system to measure the wavelength of the laser beam before it enters the DUT.

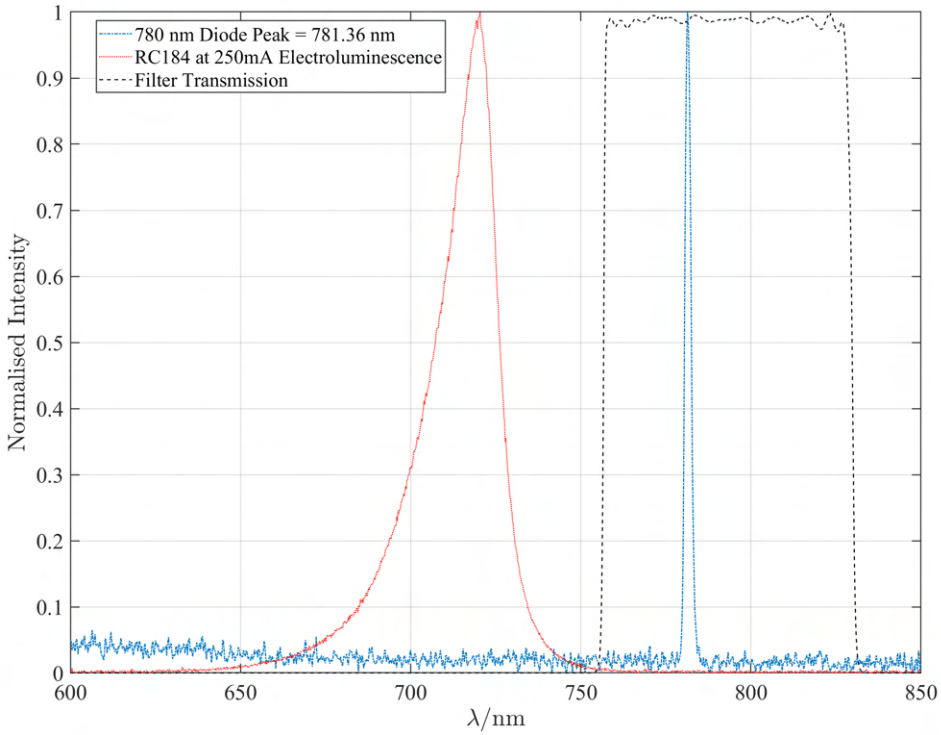


Figure 4.6: *Normalised spectrum of the 780 nm laser diode (Thorlabs L780P010) used for testing fabricated devices from the RC184 wafer, electroluminescence spectrum of a RC184 device, and an overlay of the transmission spectrum for the filter (Semrock FF01-792/64-25) used to extinguish the device emissions near the nominal band gap of* $\sim$ 730 *nm. A pulsed current of 250 mA was passed through one side of the device mesa, with a pulse width of 100 ms to reduce heating effects.*

The other arm of the beam emanating from the beam splitter, BS2, passes through an infinity-corrected tube lens, TL2 (Thorlabs TTL180-A), followed by an adjustable iris (Thorlabs SM1D12C). The tube lens is part of the widefield imaging configuration which will be discussed in the following section. The beam is then incident on another beam splitter, BS3 (Thorlabs BSW26R). One arm of this beam passes straight through and forms the image on a CMOS sensor (IDS Imaging UI-3240ML-NIR-GL), whilst the other beam is focused to a point onto a Si switchable gain photodetector (Thorlabs PDA100A2), using a plano-convex lens (Thorlabs LA1951-B-ML). The photodetector thus measures the amount of light collected by the $\times$100 objective and the iris allows the light from only the waveguide output to be isolated by cropping the light from the final image.

4.3.3 Facet Illumination & Imaging

A major aspect of the testing system is the ability to simultaneously image the input and output facets of the DUT whilst aligning the laser spot to find the optimal coupling position. This has been achieved by implementing a wide-field microscope on the input and output side, along with illumination of the facets using the Köhler principle [121]. During alignment, the input objective is used to simultaneously focus the laser spot onto the input of the DUT and image the facet, whilst the imaging objective is used to both collect this light from the output waveguide of the DUT and illuminate the output facet. During measurement, the illumination LEDs are switched off.

Appropriate optical elements had to be chosen for the wide-field imaging scheme to ensure the correct size of image formed on the sensor. To achieve this the camera must be placed at the focal plane (working distance) of the tube lens, allowing the camera to image the field of view (F.o.V). If the image is too small (i.e. the lens format does not match the camera format), vignetting can occur forming a black ring around the image of the sample. If the image is too large then cropping occurs where part of the image falls outside of the sensor area and cannot be viewed. The field of view of each imaging system (input facet and output facet) can be calculated by considering the system magnification and camera sensor format. The system magnification and field of view for the output facet must be able to distinguish the individual $\sim 6\mu$m wide tapered waveguide outputs. The system magnification is given by,

$$\text{System Mag.} = \text{Design Mag.} \times \frac{f_{\text{Tube Lens}}}{f_{\text{Design Obj. Tube Lens}}}. \tag{4.8}$$

This gives $50 \times \frac{100mm}{180mm} = 27.78\times$ for the input side and $100 \times \frac{200mm}{180mm} = 111.11\times$ for the output side. The F.o.V is then related to the camera sensor format by,

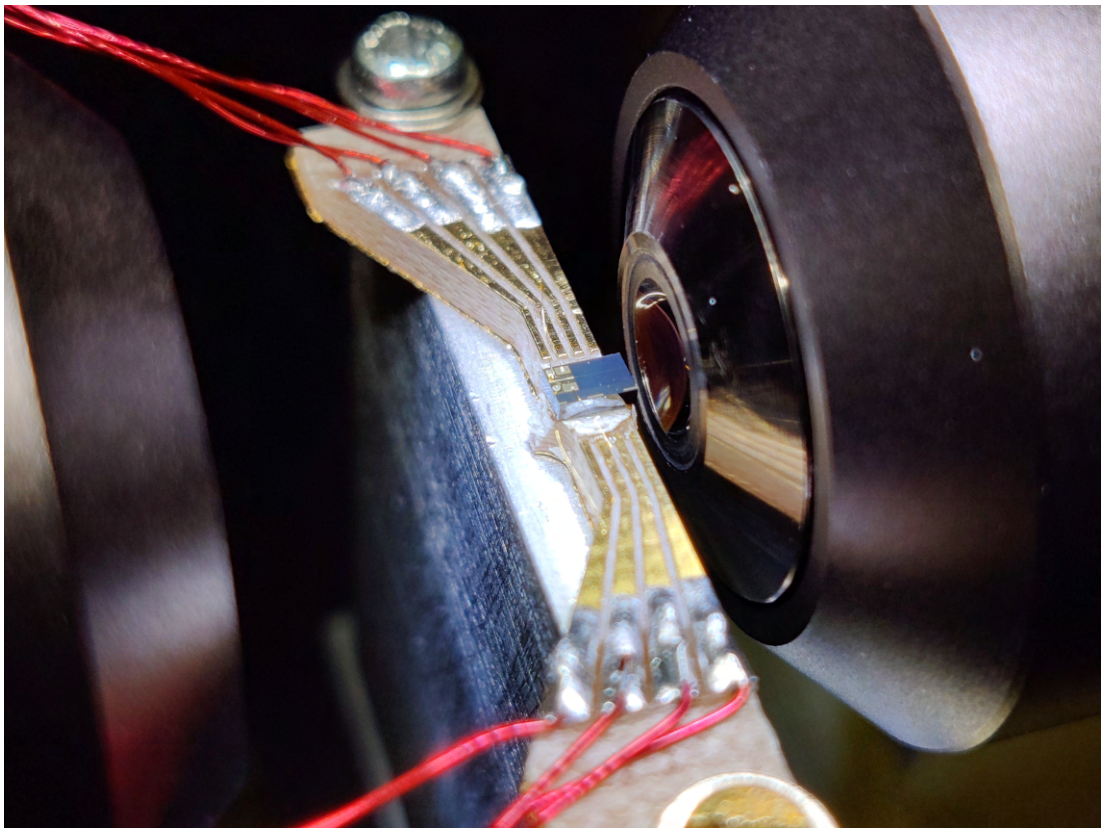
$$F.o.V = \frac{\text{Sensor Width}}{\text{System Mag.}} \times \frac{\text{Sensor Height}}{\text{System Mag.}}. \tag{4.9}$$

Using a CMOS camera (Thorlabs DCC1545M) on the input side results in a F.o.V of $\frac{6.66mm}{27.78} \times \frac{5.32mm}{27.78} = 239.7\mu m \times 191.5\mu m$, and another CMOS camera (IDS Imaging UI-3240ML-NIR-GL) on the output side results in a F.o.V of $\frac{6.78mm}{111.1} \times \frac{5.43mm}{111.1} = 61.00\mu m \times 48.9\mu m$. Figure 4.7 demonstrates the system imaging the input and output facets of a RC187 device with uniform illumination across the facet in both cases. The waveguide output of the DUT can clearly be resolved using this configuration.

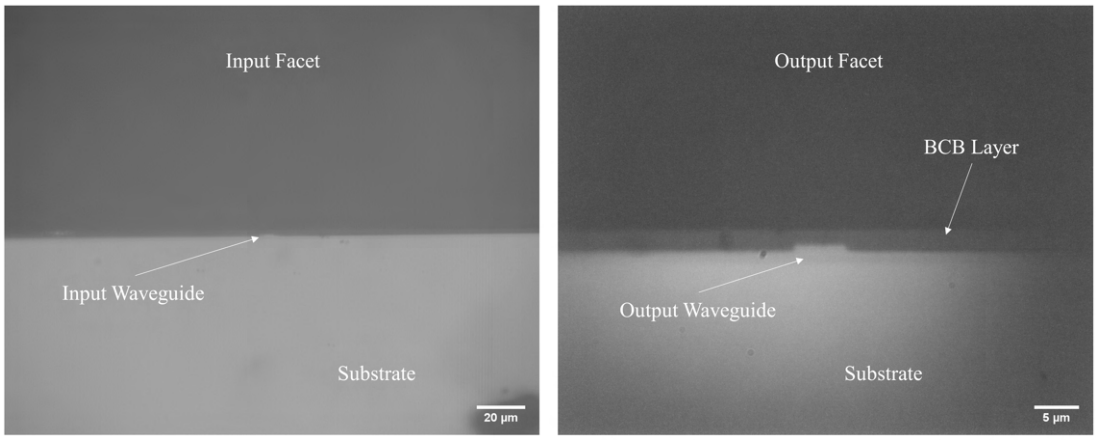
To measure the field of view of each widefield imaging system, calibrated samples were used. For the ×50 objective, a calibrated sample polymer mask was imaged in the field of view. This mask contained several different size features, including 10 μm spaced circular features. These features were analysed using Fiji imaging software to calculate the number of pixels per micron. This was then multiplied by the number of horizontal and vertical pixels in the image to calculate the field of view. For the ×100 objective, a suspension of 10 μm diameter micro particles (Sigma Aldrich 72986-5ML-F) was coated onto a glass slide and imaged by the system. The calculated field of view for the ×50 objective is 266.7 μm × 213.3 μm, and for the ×100 objective: 61.74 μm × 49.40 μm.

4.3.4 Plan-view Inspection

The final optical element of the test system is a plan view inspection microscope to aid with initial manual alignment of the DUT. A schematic illustration of the components of this system is shown in Figure 4.8. An Optem Fusion Optical Vision System is mounted to a custom assembly used to position the optical components at the correct working distances and heights. The vision system consists of a 5X objective lens, mounted to an objective adapter and clamping mount. This assembly is then connected to a 12:5:1 manual zoom module, followed by a 2X camera tube and finally a CMOS camera sensor (IDS Imaging UI-3240ML-NIR-GL). This configuration allows an adjustable magnification between 2.8× and 35×, resulting in a F.o.V between (1.9mm × 2.4mm) and (0.15mm × 0.19mm).



(a)



(b)

Figure 4.7: *(a): Picture showing the imaging of the facets of a mounted RC187 device. (b): Camera snapshots during imaging of the input (left) and output (right) facets of a RC187 device. The larger field of view on the input facet and the uniform illumination characteristics are apparent.*

The sample is illuminated using a ring LED assembly, which is clamped to the objective adapter housing.

This microscope is mounted vertically using standard Thorlabs hardware and a custom steel adapter plate. A construction rail (XT95B-250) is mounted

to a baseplate (XT95EC1) which is secured to the optical table. A compact XYZ translation stage (XRN25P-K2/M) is then mounted to an adapter plate (XT95P3) and mini breadboard (MSB1015/M). The translation stage allows the vision system assembly to be precisely moved to the correct position in X and Y and focus in Z. A custom designed steel adapter plate, made by Mr Terry Wright, is then used to mount the Optem microscope to the supports. An image taken of a mounted device from RC187 is shown in Figure 4.9.

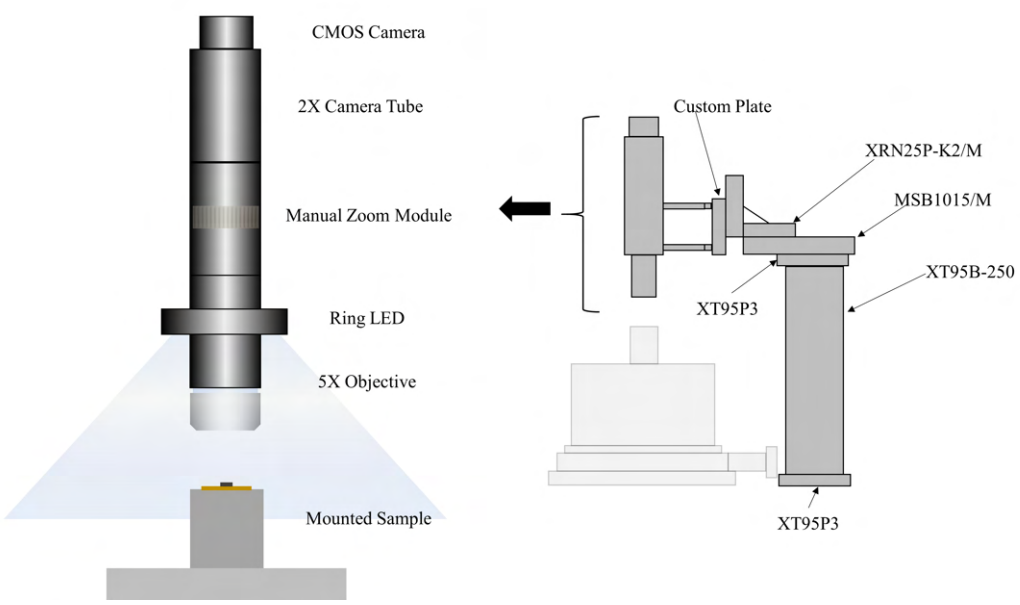


Figure 4.8: *Illustration of the overhead microscope assembly consisting of an Optem Fusion Optical Vision System and a custom configuration of Thorlabs mechanical mounting hardware.*

4.3.5 Electronics

The second aspect of the test system is the electronics used to control the function of the device, interface with hardware, and sample data to analyse device performance. A schematic diagram showing the interface between all electronic components and their corresponding optical components are shown in Figure 4.10. All components are connected to a personal computer (PC) and controlled using custom software.

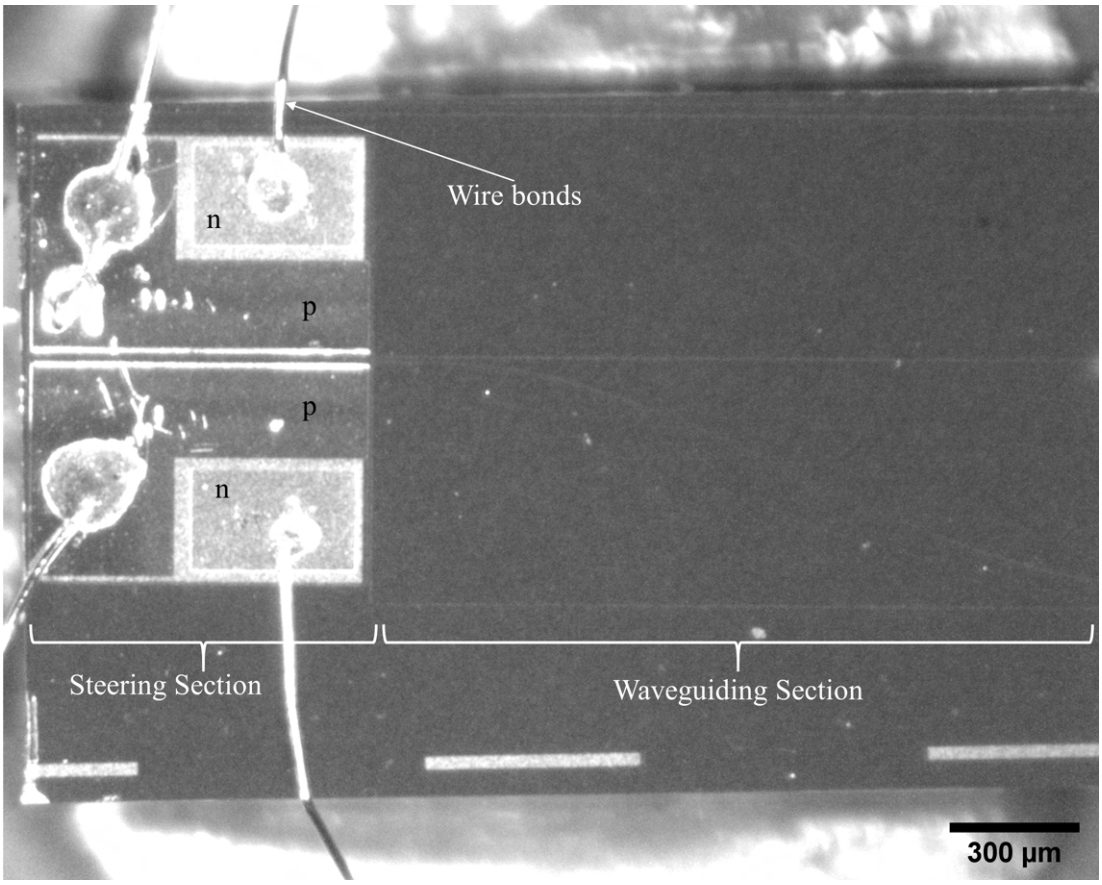


Figure 4.9: *Overhead (plan view) image of a RC187 device taken with the overhead imaging system.*

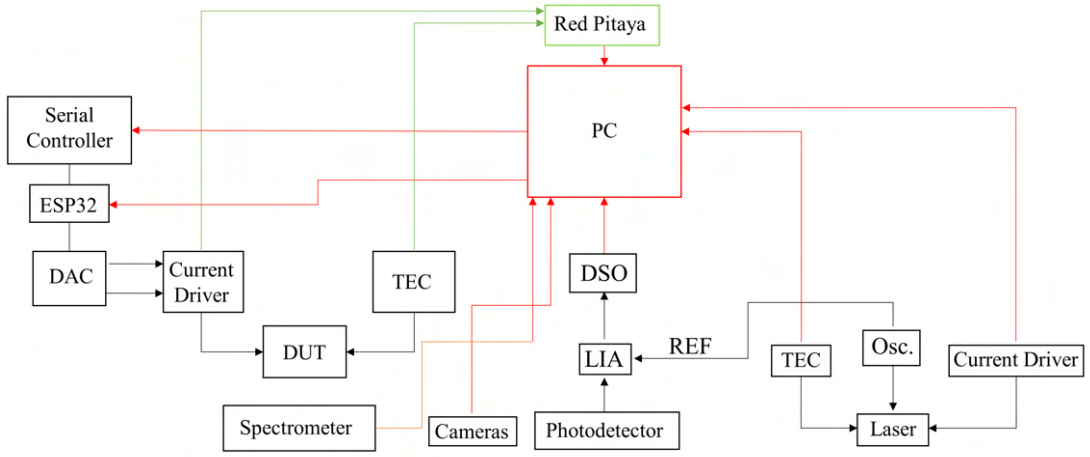


Figure 4.10: *Diagram showing the interface between electronics components used in the test system. DAC: Digital to Analogue Convertor, DUT: Device Under Test, TEC: Thermoelectric Controller, PC: Personal Computer, LIA: Lock-in Amplifier, DSO: Digital Storage Oscilloscope. The red arrows show interfacing with the PC and green arrows with the Red Pitaya FPGA.*

Device Control

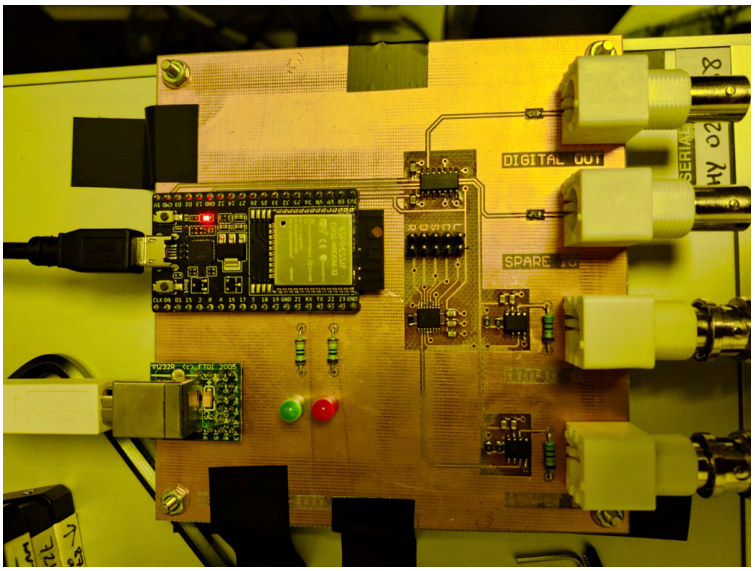
Precise electrical control of the device during testing is paramount for reliability and repeatability in the obtained results. The aim of the test system is to observe

the characteristics of a guided optical mode through the device, as the amount of current passing through each side of the mesa structure changes. Since the device resembles two diode structures, a standard two channel laser diode driver can be used to provide a constant current to pass through each side of the mesa separately. This configuration allows the amount of current passing through either side to be balanced or unbalanced, and the predicted beam steering properties of the device measured.

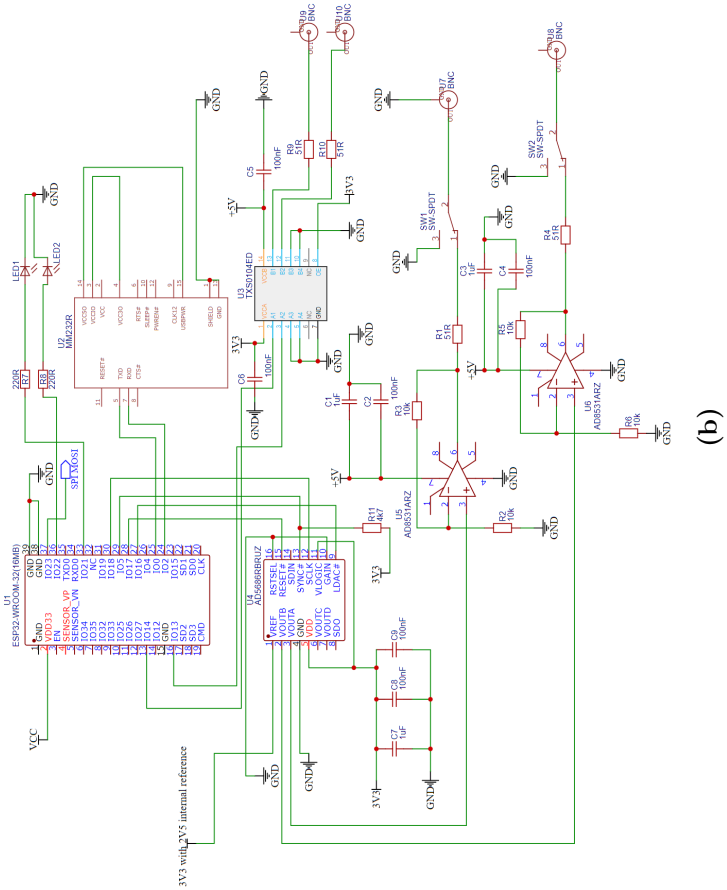
The laser diode driver (Wavelength Electronics FL591) used in the test system features two separate output channels, capable of delivering 1W per channel, with a maximum current of 250 mA on each channel simultaneously. The compliance is set using two separate external set points via 50 Ω BNC connectors. A signal (0-2V) is provided to the set point connector, with the voltage level corresponding to the current limit. To monitor the current passing through the DUT, a voltage is measured at a test point on the FL591 and converted to a current value through a transfer function, 0.125 A/V.

The set point voltages are generated using a custom analogue voltage level toggle circuit, designed and fabricated by Mr Andrew Stuart. Since the intended operation of the switches, i.e. guiding an optical wave, relies on an injection of carriers, the 'OFF' configuration of the switch may not correspond to the case where there is no current passing through the device. Furthermore, to investigate the effects of heating on the device, the system must have the capability of providing pulsed currents to the device, with an adjustable duty cycle. Therefore, the external set point signals must consist of a square wave with adjustable V_{low}/V_{high} points, with an adjustable frequency and duty cycle. A schematic and image of the custom circuit designed and fabricated with these requirements are shown in Figure 4.11.

To generate the required signals, a serial command is sent from a PC to the ESP32 microcontroller, via a USB to Serial FTDI board (Future Technology Devices MM232R). This command contains information defining the signal high



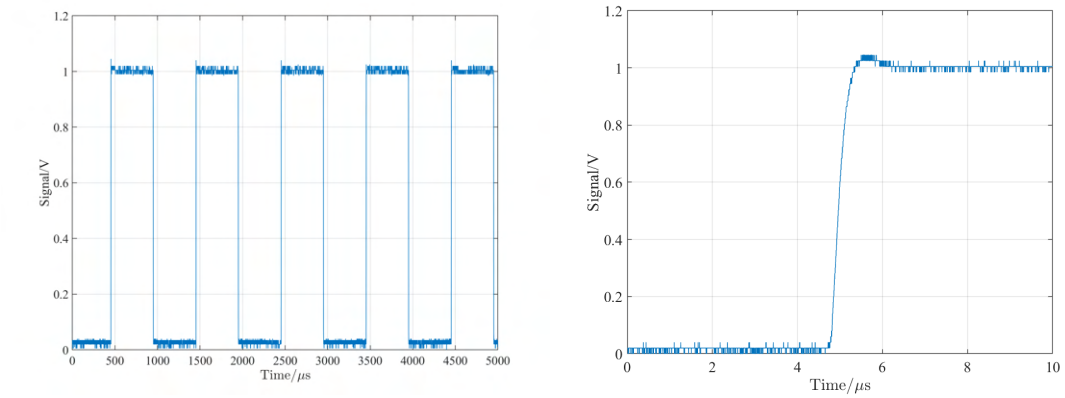
(a)



(b)

Figure 4.11: *Custom designed analogue voltage level toggle circuit for controlling device current set points. (a): Image of the populated PCB and (b): Corresponding circuit diagram. Circuit designed and fabricated by Mr Andrew Stuart.*

point, low point, frequency and duty cycle. The microcontroller generates the required clock, sync and serial data and sends this over to a 16-bit, quad-channel DAC (Texas Instruments AD5686R) through a Serial Peripheral Interface (SPI). These generated analogue signals are sent to two amplifiers (Analog Devices AD8531AR) to amplify the signal levels to the required level. The signals then pass through a 50 Ω resistor and are connected to the modulation inputs of the FL591 current driver. These control signals were then characterised using an oscilloscope (Agilent Technologies DSO-X 2002A). Figure 4.12 shows an example of a generated control signal and a measurement of the signal rise and fall times.



(a) **(b)**

Figure 4.12: *Measured signal from one of the two outputs of the custom analogue toggle circuit. In this instance, a 1kHz signal was used with 50% duty cycle. Set points were $V_{low} = 0V$, $V_{high} = 1V$ (a) shows 5ms of the signal and (b) a rising edge. The measured 10-90 rise time of the signal (time taken for the signal to transit from 10% to 90% of the final voltage) is 386.3±0.1 ns.*

Red Pitaya

A Red Pitaya (RP) computer (STEMLab 125-10) is used as the hub of the test system. Electrical signals are sampled and processed using the on-board CPU and FPGA system-on-chip (SoC) (Xilinx ZYNQ XC7Z010), and the data is accessed through the custom software via a built-in Standard Commands for Programmable Instruments (SCPI) server. The RP provides enable/disable signals to the stage TEC and current driver using the digital input/output (I/O) pins.

The RP features two radio frequency (RF) analogue inputs, controlled using

the FPGA, with a 16 bit analogue to digital converter (ADC) resolution and 40MHz bandwidth. These inputs are used to sample the monitor voltages on the FL591 current driver, and convert them to a current value using the transfer function given in the FL591 data sheet. The slower analogue inputs are used to sample voltages from the WC3243 TEC to obtain the temperature of the stage. Analogue outputs are used to define the set temperature of the stage, and digital outputs are used to enable/disable the TEC and current driver. A schematic of this setup is shown in Figure 4.13.

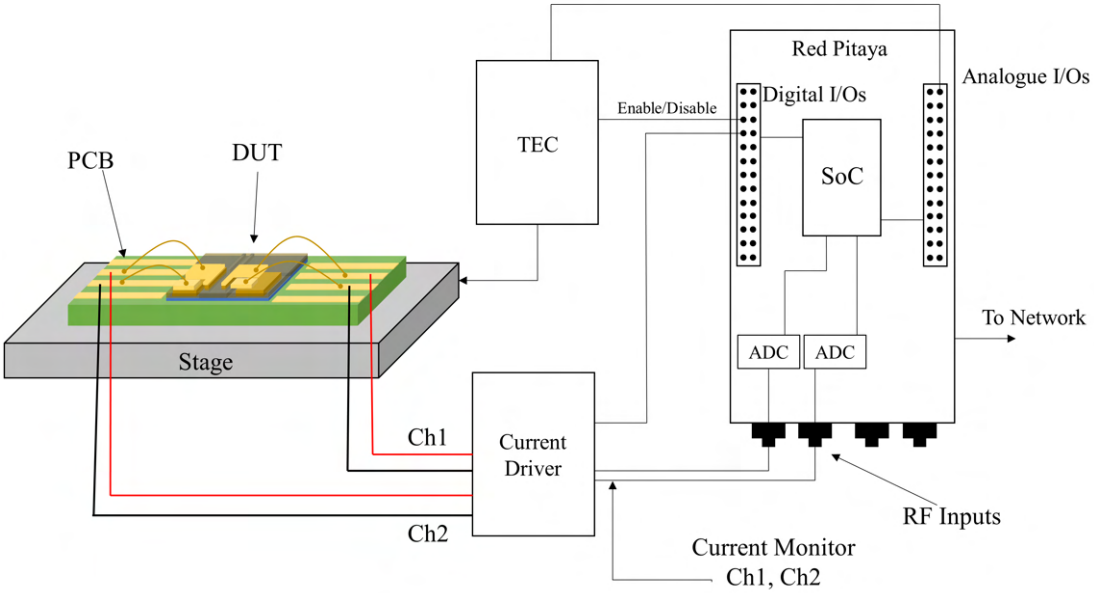


Figure 4.13: *Schematic diagram showing the interfacing between the Red Pitaya and other electronics. PCB: Printed circuit board, SoC: System on chip, I/O: Input/Output, RF: Radiofrequency, ADC: Analogue to digital converter, TEC: Thermoelectric Controller, DUT: Device under test.*

Stage Control

Fine control of the flexure stages is achieved using piezo actuators with 50 nm resolution and 100μm travel range. The piezo actuators are controlled using a piezo controller (Elliot Martock E1100) which provides an independent 0-150V DC signal for each axis. These voltage levels can be controlled using either the potentiometers on the front panel of the device, or using the USB interface which features a 16 bit DAC for converting the serial commands to a given voltage.

The potientiometers are used for manual alignment and USB commands for the automatic alignment procedure (more detail given in Section 4.4). Two E1100 provide fine control of the two XYZ flexure stages.

Lock-in Amplifier

Laser safety requirements for the clean room environment meant that the maximum optical power available from each diode was around 2 mW. Furthermore, the need for a spatial filter to improve the beam quality of the laser diodes used resulted in a significant reduction in the beam power to around 100 μW. Due to these limitations on the availability of optical power at the input facet of the DUT, a lock-in detection technique is applied in this system to detect the small optical signals exiting the DUT.

Lock-in detection employs a homodyne detection technique and low-pass filter to extract the amplitude of a signal and phase from a noisy signal, relative to a well defined reference [122]. A sine-wave reference signal is first generated using a signal generator and used as the external reference for the lock-in amplifier (EG&G 7260). The LIA then uses a phase-locked loop to track the dominant frequency of the reference and lock the internal reference to the external signal. The laser is modulated using the same reference signal, using the modulation input on the laser diode driver (Thorlabs LDC 8002). Any light guided through the DUT and collected from the output facet will then be modulated by this signal. The collected light is detected by a photodetector (Thorlabs PDA 100A2) and the output of this photodetector connected to the input of the LIA. This noisy signal is then multiplied by the internal reference as well as a $\pi/2$ phase-shifted copy before passing through a configurable low-pass filter. The output of the LIA is then a DC signal which is proportional to the amplitude of the signal, R and to the cosine of the phase shift, θ between the reference and the signal. This is known as a dual-phase demodulation and describes the basic idea behind the lock-in detection. In reality the situation is more complex due to

digital signal processing techniques of the modern LIA. The output of the LIA is set as the amplitude, R, and then sampled by a digital oscilloscope (Agilent Technologies DSO-X 2002A), which can be accessed by the computer running the custom Python software.

The power spectral density of the noise from the photodetector determines the external modulation frequency. A frequency must be chosen where the power spectral density of noise influences is lower. Figure 4.14 shows the dark power spectrum of the photodetector output. The spectrum was taken using a digital oscilloscope at a sampling rate of 250 kHz. The peak noise power for this configuration is located at frequencies $\leq$4 kHz, thus a modulation frequency of 9.6 kHz was chosen to minimise the influences of the various noise components at these lower frequencies.

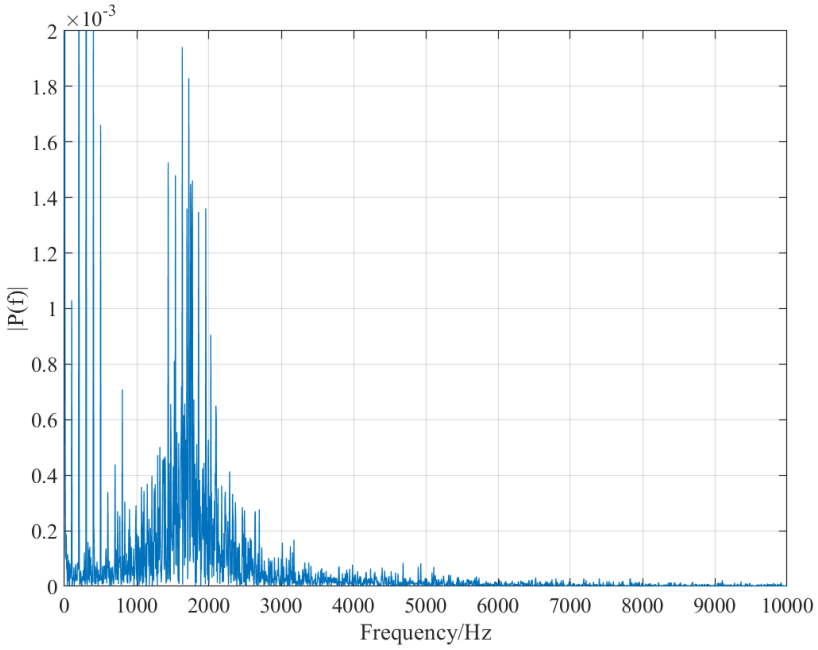


Figure 4.14: *Dark power spectrum of the Thorlabs PDA100A2.*

4.4 Software Design

A fundamental component of the test system is to be able to remotely control hardware components and automate the data collection processes. This has been

achieved using a custom built Python routine with a graphical user interface (GUI). A screenshot of the main GUI window is shown in Figure 4.15. This software was designed to allow various sub-routines to run concurrently with the GUI, which displays key information such as temperature and voltage monitoring, and facilitates fine control of the stage movement and control of the DUT voltage levels. The GUI was designed using a combination of the PyQT5 libraries [123] and QTWidgets [124] packages.

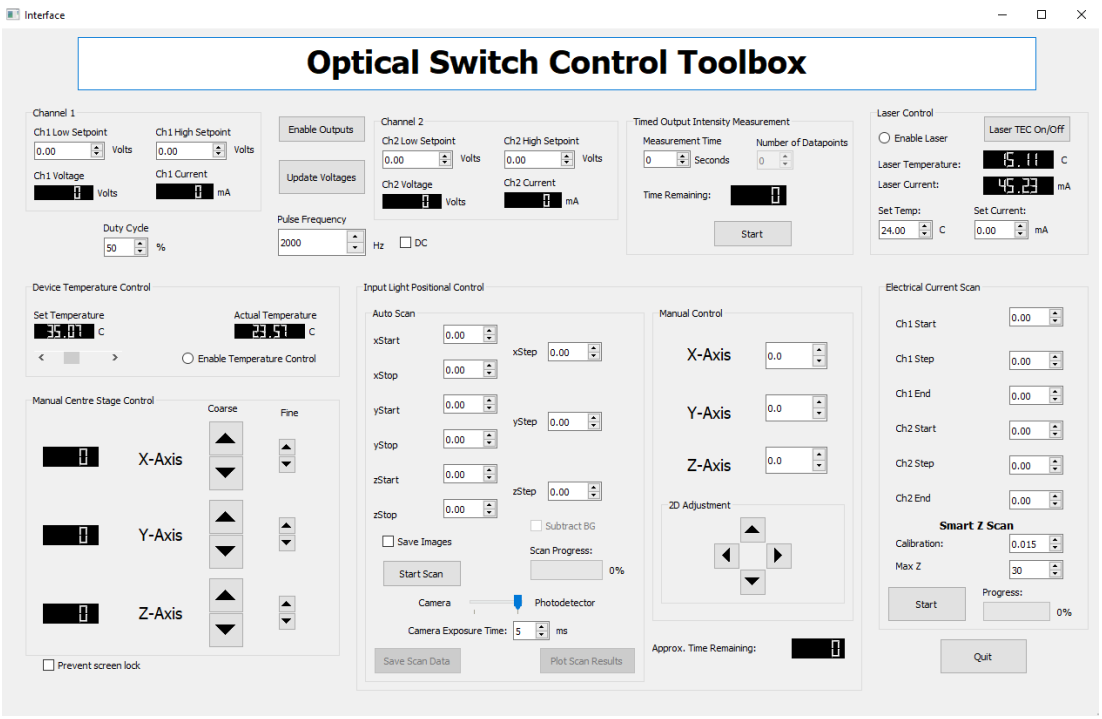


Figure 4.15: *Screenshot showing the GUI of the custom Python program built for controlling the test system.*

4.4.1 Hardware Communication

Various communication protocols and Python packages are used for communicating with the hardware components of the test system. Table 4.4 gives an overview of the packages and hardware interfaces used for each component. Hardware communication is initiated in the first instance when the program is started and before the GUI is displayed.

Component	Interface	Python Package
Laser Driver	RS-232	pySerial
Laser TEC	RS-232	pySerial
Oscilloscope	USB-2.0	pyVISA
Red Pitaya	TCP/IP	pySerial, socket
CMOS Cameras	USB-3.0	PyuEye
Piezo Drivers	USB-2.0	ctypes
Spectrometer	USB-2.0	python-seabreeze

Table 4.4: Overview of the various packages and interfaces used to communicate with the test system hardware.

4.4.2 Sub-Routines

To facilitate continuous running of the GUI whilst interacting with the system hardware and running automated measurements, the program was developed with multi-threading capabilities. In this sense, multiple aspects of the program can be executed simultaneously, without one blocking another or queuing commands which may cause the application to hang. The GUI is therefore executed in a loop in the main thread and the separate subroutines are initiated in external 'worker' threads.

A challenge involved with this implementation is accessing the GUI elements within separate threads - setting and accessing properties of GUI elements from the external worker threads is not recommended since this can cause crashes as the main thread tries to access locations in memory which have been changed by the worker thread. The solution to this is to use Signals and Slots within the PyQt framework. This allows the worker threads to send data to the main thread, which can then be used to set GUI properties. For example, one of the worker threads implemented in this program is used to scan the piezo voltage from a start point to an end point with a given step size. Each time the piezo voltage is changed, a signal is used to send this float value from the worker thread to the main thread. The main thread then sets one of the GUI elements to display this value.

Input Coupling

A major advantage of implementing remote hardware control for the testing of the fabricated optical switches is the ability to perform an optimisation of the coupling of the laser beam to the input facet of the DUT. Since the optical switch design relies on beam steering, the position and efficiency of the beam coupled into the device will affect the measured performance. For example, if the beam is coupled into the device slightly off the optical axis, a stronger current injection will be required to steer the beam into the desired position of the output waveguide. Furthermore, matching the optical modes of the microscope objective to those of the input waveguide of the DUT will affect the efficiency of the coupling and thus the intensity of light measured at the output facet. This optimisation was achieved by implementing a sub-routine which performs a raster scan of the position of the input objective, by scanning the piezo voltage of the stage in two axes. Coarse manual alignment of the light is first carried out in each axis using the micrometer drives on the stage. A scan region is then defined, along with a step size and the routine initiated. The intensity of the light at the output facet is then recorded at each point in the scan and a map produced from this data. The stage then moves to the position at which the highest intensity of light was recorded. A smaller scan region around this hot spot is then redefined, along with a finer step size and the scan repeated, producing another map. This process is then repeated until the scan region is smaller than the size of the coupling region. Figure 4.16 shows an example of the first and final scan maps produced using this method of alignment. The map is produced by taking the recorded light intensity at each point in the 2D scan and performing an interpolation over a rectangular set of data to produce a finer grid of points, using bivariate spline functions. This function is built into the Python 'scipy' package and constructs smooth interpolants for nodes of a rectangular grid [125].

Due to piezo hysteresis, the scan shows some drifting of the 'hot spot' from one scan to the next. Since the hysteresis of the piezos is given in their specifications

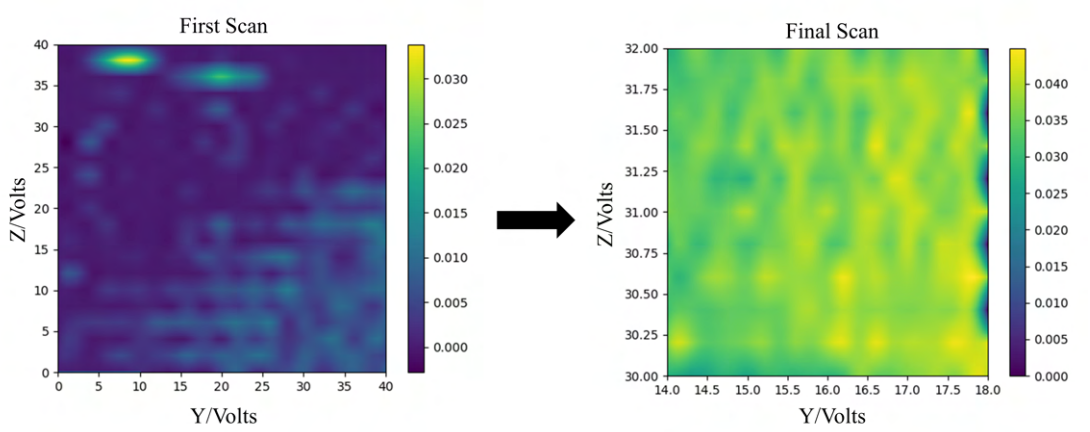


Figure 4.16: *Example of the results from semi-automated optimisation of the input coupling of light into the DUT. The hot spot in the final scan appears to be at a different piezo voltage to the first. This is due to hysteresis in the position of piezo actuator. The colour map represents the intensity of the light output as measured from the magnitude of the lock-in detection signal in Volts.*

as 12-15%, the solution to this issue implemented here was to simply manually redefine the scan region after each raster scan, with a 15% buffer around the located hot-spot. Since this solution is not ideal if the located hot-pot is near the edge of the travel range of the piezo, a more robust implementation would be to use a closed-loop system, whereby the exact position of the stage is monitored using a capacitive sensor, for example. Such a hardware upgrade would facilitate a fully automated version of this coupling routine.

Current Maps

To measure the extinction ratio of the optical switch, the intensity of light at the output facet at both the 'ON' state and 'OFF' state must be known. Since the switch design relies on continuous steering of the coupled optical beam, dependent on the injection current, the output intensity must be measured at as many combinations of the injection current across each side of the mesa as possible, to obtain the most accurate measurement. Since it is not practical nor reliable to do this manually, a separate sub-routine was incorporated into the test system to automate this measurement.

The algorithm for this sub-routine consists of first defining a start and end

point for the control voltage on each side of the mesa, and a step size. The intensity of the light at one of the output waveguides is then measured at each point in the scan, after setting the control voltages. A challenge associated with this measurement arose due to local heating of the DUT - at higher injection currents the device begins to expand in the axis perpendicular to the optical axis by small amounts, which is enough to move the DUT out of the coupled position of the input light. This issue manifests itself as a reduced intensity of the light at the output facet, leading to a false measurement of the extinction ratio. To overcome this issue, another algorithm was incorporated, featuring a 'smart' scan in the axis perpendicular to the optical axis (z), i.e in the direction of expansion. At each point in the current scan, the position of the input light is scanned in the z-axis and the intensity difference, ΔI at the output facet for each point calculated. If ΔI is less than some pre-defined tolerance, δ, the z-scan is halted and the maximum recorded intensity stored. This is repeated for every point in the current scan to ensure that the input light is coupled into the DUT before taking a measurement. Figure 4.17 gives an overview of the logic for this algorithm.

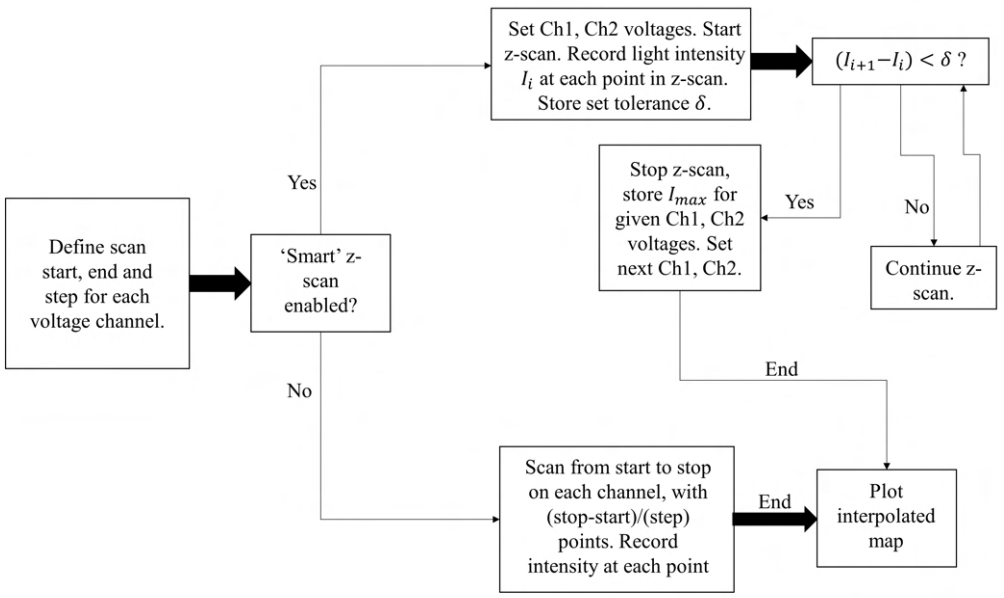


Figure 4.17: *Flow diagram showing the conditional steps of the 'smart' z-scan algorithm used to mitigate expansion of the DUT at higher injection currents.*

Timed Measurements

In some measurements, the coupled output light intensity needs to be recorded as a function of time. Two examples are, when measuring the wavelength stability of the laser, or when recording Fabry-Pérot resonances of passive waveguides (more detail in Chapter 5). Therefore, a sub-routine has been included in the software which measures the intensity of the output light of the DUT every 250 ms. This is achieved by averaging 1000 samples from the oscilloscope which continuously measures the output of the photodetector.

4.5 Limitations & Concluding Remarks

In this chapter, the design and construction of an optical and electrical test system used to characterise fabricated optical switching devices was detailed. This has included a description of the requirements of the system, the hardware components, a description of the Python software and some example of measurement outputs. Analysis of the test system has shown that it meets the minimum requirements for determining whether the fabricated optical switches meet their design requirements, however naturally there are some drawbacks of the system which would require attention to ensure that the limits of the testing are due to limits of the devices and not the measurement system. For example, although the test system is capable of switching the devices on with a limit of $\sim$400 ns, from previously presented arguments it is possible that the inherent switching speed of the devices is faster. To measure this would require an upgrade of the current driver and associated control voltage toggle circuit. Furthermore, the use of open-loop piezo controllers is not ideal in the context of a fully automated system, due to hysteresis associated with the piezo positioning. The system would therefore benefit from an upgrade which facilitates readout of the position of the flexure stages to within 50 nm, which could then be incorporated into a positioning system with feedback. This would allow more efficient testing of batches

of devices, facilitating evaluation of the yield of devices on a die and even cross wafer uniformity measurements when testing large quantities of devices.

In the next chapter, results will be presented from the initial testing of the fabricated switching devices from all three epitaxial wafers, and a discussion given on their implications and suggestions for improving the design to obtain increased performance.

Chapter 5

Device Characterisation

5.1 Introduction

Electrical and optical characterisation of the optical switching devices fabricated in this project is the final stage in the prototyping process. In this chapter, results from initial characterisation of several fabricated devices will be presented along with a discussion on the findings and their implications. Towards the end of the chapter, the carrier spreading model described in Chapter 2 will be re-evaluated according to the results from these experiments.

5.2 Current-Voltage Characteristics

The performance of optoelectronic devices is dependent on numerous factors related to the fundamental device design and quality of the fabrication process. Typically, the degradation over time of these devices is dominated by the series resistance, R_s, of the device which depends on the semiconductor material resistivity due to doping growth defects, underlying contact resistance due to the quality of the contact between metal film and underlying semiconductor layer, and geometrical factors caused by the quality of etching processes [97]. The series resistance of a given device and other important performance metrics can be obtained by measuring the current-voltage (I-V) characteristics of the device.

The equivalent circuit diagram of a forward-biased semiconductor p-i-n diode is shown in Figure 5.1, where L is the inductance, R_c is the contact resistance, and R_s the series resistance. The series resistance is a function of the forward bias current, whereas the inductance depends on the device/package geometry. This inductance is small and thus has a negligible effect on the I/V characteristics of the bare fabricated devices at low frequency and DC. The performance characteristics of the diode depends on the geometry of the device as well as the quality of the intrinsic region. When the diode is forward biased, electrons and holes are injected into the intrinsic region, where they combine after some finite lifetime, τ.

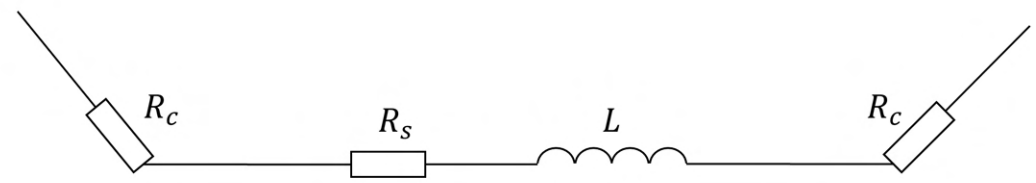


Figure 5.1: *Equivalent circuit of a forward-biased p-i-n diode, where L is the parasitic inductance, R_c is the contact resistance, and R_s the series resistance.*

For low frequency and DC, the p-i-n diode obeys the standard diode equation,

$$I = I_0 \left[\exp\left(\frac{qV}{n_f k_B T} \right) \right], \tag{5.1}$$

where I_0 is the saturation current, V is the voltage across the space-charge region, and n_f is the diode ideality factor. A theoretically perfect diode will obey Equation 5.1 with a constant ideality factor of 1. If both n_f and I_0 are constant, a plot of $\ln(I)$ vs. V will yield a straight line above the threshold voltage, with the slope given by $q/n_f k_B T$. The ideality factor of the diode can then be extracted from this plot. Due to the series resistance, the characteristics in reality are due to two components: space charge region (scr) recombination/generation and quasi-neutral region (qnr) recombination/generation. This results in the $\ln(I)$ vs V graph presenting four distinct regions [126], as shown in Figure 5.2. The I-V relationship resulting from scr and qnr recombination/generation is given by,

$$I = I_{o,scr}(e^{q(V-IR_s)/nk_BT} - 1) + I_{o,qnr}(e^{q(V-IR_s)/nk_BT} - 1), \tag{5.2}$$

For $IR_s \ll V \ll nk_BT/q$ (between 0 and 0.05V in this example), the current changes linearly with voltage resulting in a non-linear shape in the semi-log plot. The next stages ($V \gg nk_BT/q$) are dominated by scr recombination/generation at lower voltages (0.05V to 0.3V here) and qnr for larger voltages. At higher currents, the curve tails off as a result of the series resistance r_s.

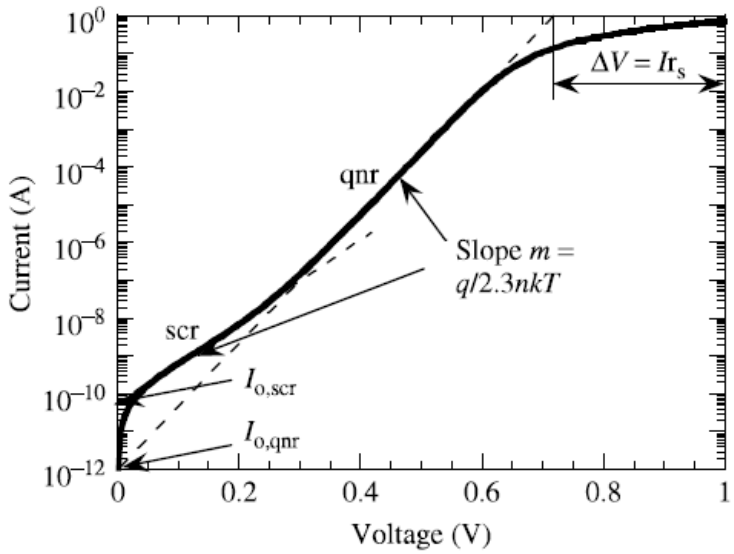


Figure 5.2: *log(I)-V characteristics for a diode with series resistance [97].*

The I-V characteristics of the fabricated devices were used as an evaluation indicator to determine whether they would be suitable for later optical characterisation. During fabrication, after deposition of the n-type contacts on the n-GaAs layer, a series of I-V measurements were taken using the p-i-n test structures on the die. These measurements were used to determine the quality of the fabrication process at this point and used as an indicator for the quality of the on-die devices, which were not able to be characterised at that point due to the small size of the p-contact pads. Figure 5.3 shows an optical microscope image of the on-die p-i-n test structures from a RC184 die, used for these measurements.

The ln(I)-V characteristics of the six p-i-n diode structures as shown in Figure 5.4b

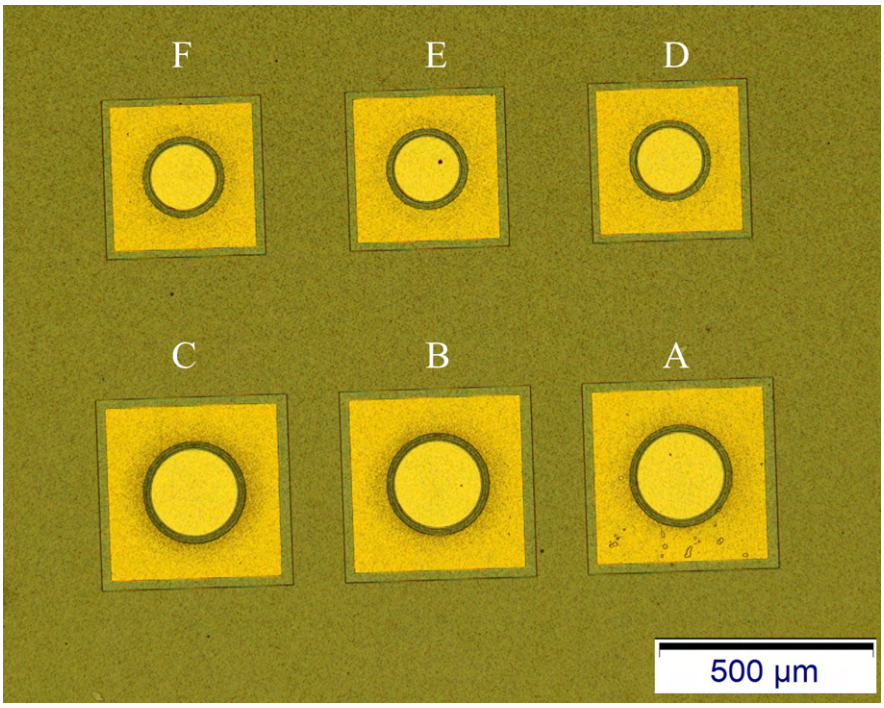


Figure 5.3: *Optical microscope image showing the on-die p-i-n test structures for RC184.*

for RC184-AC were measured. For consistency, the ideality factor of the diode was extracted from only the linear region of the $\ln(I)$ vs V graph. The calculated ideality factors are listed in Table 5.1. All but one of the diode structures exhibit an ideality factor of < 2 indicating good quality structures. As can be seen, the behaviour of RC184-D deviates from the other p-i-ns. In this case, the diode begins to conduct current at a much lower voltage, indicative of the behaviour of a resistor, perhaps due to imperfections and defects in the material causing recombination in the depletion region, or due to surface recombination as a result of imperfections in the etched sidewalls of the mesas [126]. Rather simply, this could also just be caused by a poor quality ohmic contact to the underlying semiconductor. It is also noted that all other diode structures display strong qnr recombination/generation characteristics. This indicates a good quality intrinsic region, and that carrier recombination occurs outside the space-charge region [127].

After depositing the top-up metal contacts, the I-V characteristics of each beam-steering device on-die (i.e. before dicing) were measured and the ideality

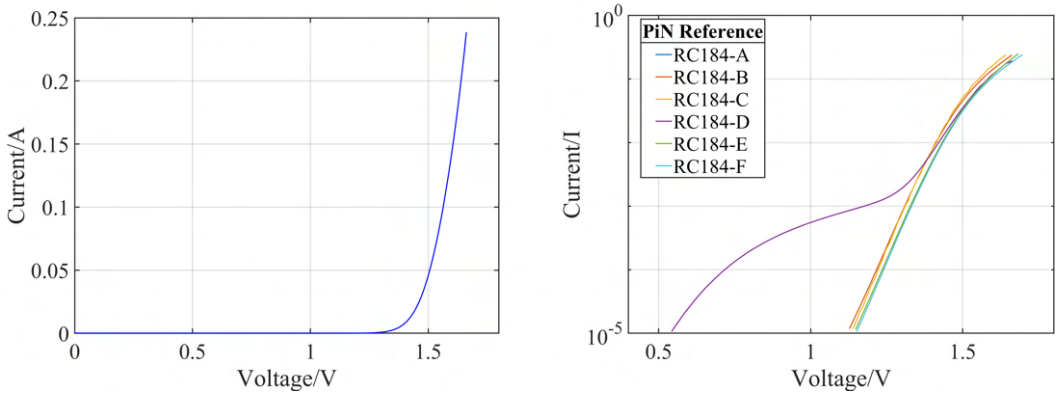


Figure 5.4: *(a): I-V characteristics from RC184-A p-i-n test structure and (b): log(I)-V characteristics of all test devices from RC184 above the threshold voltage. p-i-n structures A-F refer to those shown in the optical microscope image of Figure 5.3.*

Die Reference	p-i-n Reference	Ideality factor
	B	1.72±0.02
	C	1.64±0.01
	D	-
	E	1.74±0.06
	F	1.68±0.03

Table 5.1: Summary of the ideality factors obtained from the p-i-n I/V measurements. Structure D did not display diode-like I/V behaviour so the ideality factor could not be calculated using the same method in this instance. p-i-n test structures were not patterned onto the RC187 die due to its smaller size after half of the sample was damaged early in the fabrication process.

factors calculated using the same method as described above for the test structures. Since each device contains two pairs of p and n-contacts, there are two ideality factors associated with each device, using a 'L' and 'R' identifier. Figure 5.5 shows a map of the RC184 and RC187 die and their associated test labels. Measurements were carried out using a probe station and source-measure unit (Keysight B9202A SMU) with a four-probe technique to eliminate parasitic resistances from the cables which would adversely affect the calculation of the ideality factor.

The log(I)-V characteristics of each diode for the active region of each device was measured on-die and the ideality factor calculated as per the aforementioned method. Figure 5.6 shows a summary of the calculated ideality factors for each p-i-n structure, starting with 'A1L' and ending with 'F4R' for RC184 and 'D4R'

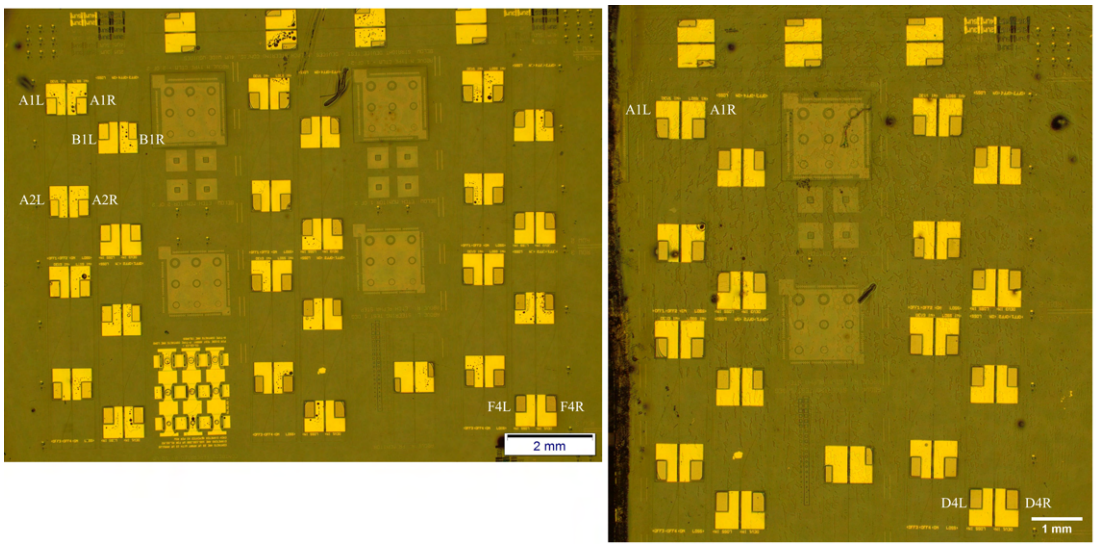


Figure 5.5: *Identifier labels for each p-i-n diode structure of fabricated devices for RC184 (left) and RC187 (right).*

for RC187. All but two diodes (one device) from the RC184 die exhibit low ideality factors indicating a high yield of devices ($\sim$ 95.6%) for this particular wafer. However, only two whole devices from the RC187 die show acceptable diode characteristics indicating a much lower yield (12.5%). The lower yield of devices for the RC187 wafer is attributed to the smaller sized sample which was a result of an accidental breakage near the beginning of the fabrication process. Those devices which do not exhibit low ideality factors are not expected to offer significant refractive index changing characteristics for a given injection current, since the density of carriers confined in the intrinsic (core) layer will be much lower, resulting in a weaker refractive index change effect in the region of the guided optical wave.

Figure 5.7 shows the raw $\log(I)$-V data for each tested diode on the RC184 die. The two diode failures can be clearly seen here as the behaviour in the qnr region deviates significantly from the other tested diodes. The successfully fabricated devices have slightly higher (worse) measured ideality factors than those measured for the p-i-n test structures. This is attributed to the reliability of the top-up metal contacts to the underlying annealed contacts on the semiconductor. As described in Chapter 3, the top-up metal pads make contact with the underlying

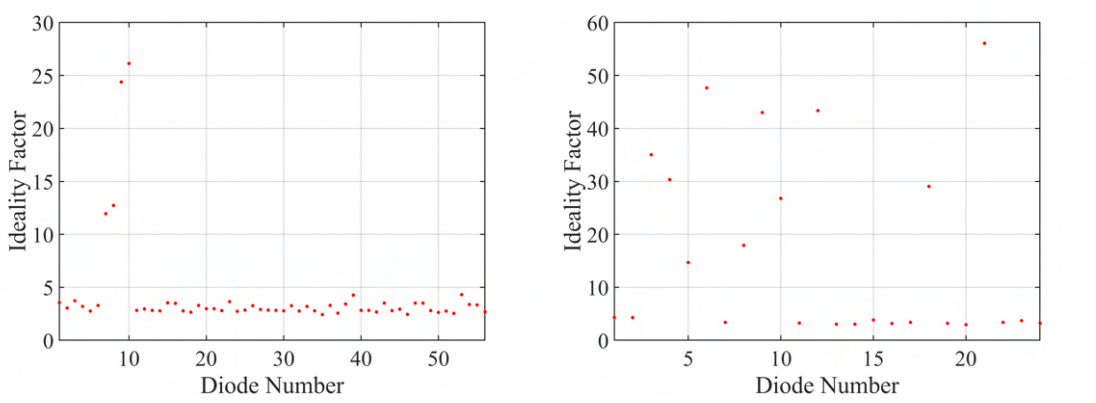


Figure 5.6: *A summary of the calculated ideality factors for RC184 (left) and RC187 (right).*

contacts through windows in the BCB layer. Since this metal is not annealed with the contacting metal, this can add a significant series resistance component to the diode depending on the area of metal in contact with the underlying metal, which manifests itself in a larger ΔV as illustrated in Figure 5.2. In contrast, the p-i-n test diodes were characterised before the BCB passivation step and were thus probed from the annealed metal contacts. This could not be achieved with the device contacts since the p-contact has a smaller dimension than the probe tip diameter and the high current density at this point caused these contacts to burn out at the contact point between the probe and metal, when one device was tested.

The extra resistance due to the thin layer of gold in contact with the metal contacts through the window in the BCB can be estimated using $R = \rho l/A$ where ρ is the electrical resistivity of the gold in the BCB window, l is its length and A its cross-sectional area, as illustrated in Figure 5.8. Using the dimensions, $w = 5$ μm, $t = 0.50$ μm, $l = 740$ μm, and the resistivity of gold $\rho = 0.024$ $\mu\Omega m$ results in $R = 7.22$ Ω. This added series resistance would cause a higher voltage drop across the device for a given current through it. The resistance would also be expected to increase due to fabrication tolerances.

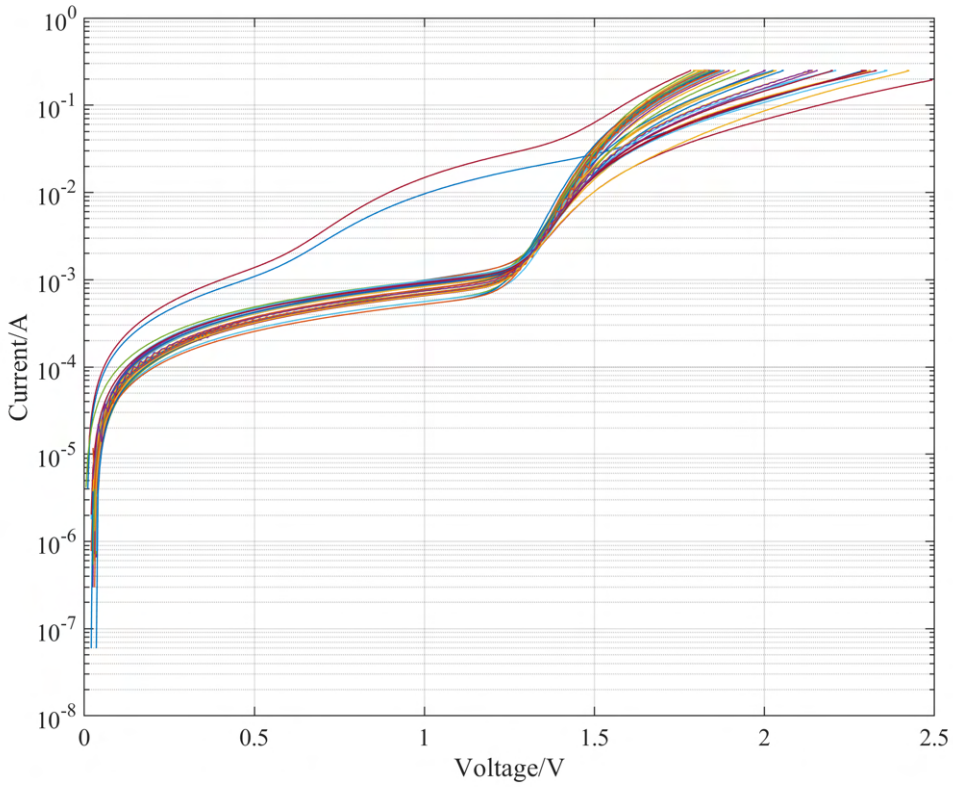


Figure 5.7: *Measured* $\log(I)$*-V data for diodes from the RC184 die.*

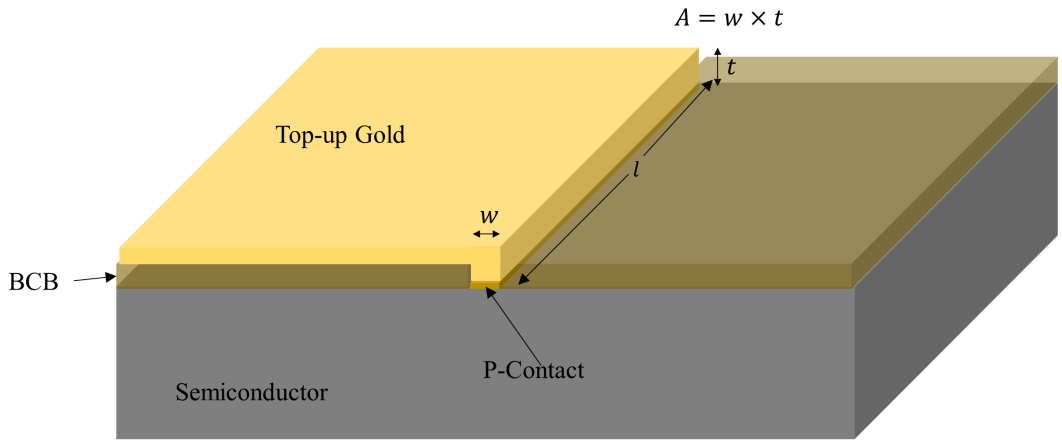


Figure 5.8: *Illustration of the extra contact resistance involved with the fabricated devices due to the interface between a thin layer of the top-up metal and the underlying annealed contact metal.*

5.2.1 Summary

Analysis of the I/V characterisation of the fabricated double heterostructure devices has shown that a good yield of devices has been achieved which resemble close to ideal diode behaviour, indicating the quality of the grown epitaxy and

fabrication process. These devices are sufficiently low powered enough to be able to be controlled using commercially available integrated electronics circuits for optoelectronics packaging, and powered using standard battery technology. Those devices which did not display ideal diode behaviour feature extra series resistances, due to fabrication imperfections.

5.3 Luminescence Spectra

Analysis of the luminescence spectra of semiconductor devices is one of the most important ways to characterise material structure and carrier recombination mechanisms. Photoluminescence and electroluminescence spectra were used in this project to study the effect of carrier injection on the apparent band-gap of the core of the double heterostructure devices. Since these devices rely on a change in the absorption spectra of the core of these double heterostructures in their intended operation, it was important to study how this effect varies with the operating characteristics to better understand the operating limits of these devices.

5.3.1 Photoluminescence Measurements

Photoluminescence (PL) of semiconductor materials is the process by which photons of energy greater than the energy band-gap of the material are absorbed, generating excited carriers. At 300 K the thermal energy, $k_BT \approx 26$ meV, is much greater than the excitonic binding energy, so the excited carries exist as free carriers within their respective energy bands. These photo-generated carriers then exist for a short time (the carrier lifetime), before recombining radiatively. In direct band-gap semiconductors, this radiative recombination results in the emission of a photon with energy near to the band-gap energy, due to conservation of momentum. Thus, excitation of the semiconductor with photons of energy greater than the band gap energy will result in an emission spectrum with

a peak near the band-gap energy. The position of the peak may shift due to local heating, doping concentration and the presence of impurities and traps within the semiconductor crystal lattice [128]. The layer structure of each of the epitxial wafers, first presented in Chapter 2, are included again here in Table 5.2 to aid in the explanation of the luminescence measurements.

Wafer ID	**Layer**	**Thickness (μm)**	**Doping (cm^{-3})**
RC101	SI GaAs	625	-
	Buffer layers	~ 0.3	-
	n-GaAs	1	2.5×10^{18}
	n-$Al_{0.2}Ga_{0.8}As$	**1**	$\mathbf{2 \times 10^{18}}$
	GaAs	**0.2**	-
	p-$Al_{0.2}Ga_{0.8}As$	**1**	$\mathbf{2 \times 10^{18}}$
	p-GaAs	1	2.5×10^{18}
	p-GaAs	0.2	2×10^{19}
RC184	SI GaAs Substrate	625	-
	Buffer layers	~ 0.3	-
	n-GaAs	1.2	4×10^{18}
	n-$Al_{0.45}Ga_{0.55}As$	**0.1**	$\mathbf{4 \times 10^{18}}$
	$Al_{0.22}Ga_{0.78}As$	**0.39**	-
	p-$Al_{0.45}Ga_{0.55}As$	**1**	$\mathbf{4 \times 10^{18}}$
	p-GaAs	0.4	2×10^{19}
RC187	SI GaAs Substrate	625	-
	Buffer layers	~ 0.2	-
	n-GaAs	1	4×10^{18}
	n-$Al_{0.55}Ga_{0.45}As$	**0.8**	$\mathbf{4 \times 10^{18}}$
	$Al_{0.25}Ga_{0.75}As$	**0.3**	-
	p-$Al_{0.55}Ga_{0.45}As$	**0.85**	$\mathbf{4 \times 10^{18}}$
	p-GaAs	0.4	2×10^{19}

Table 5.2: Layer compositions of semi-insulating (SI) GaAs epitaxial wafers, grown by Dr Richard Campion, for optical switching devices. The p-i-n region is highlighted in bold.

PL measurements were carried out by Mr James Felton on a sample of each epitaxial wafer, at three locations on each sample separately using a green (532 nm) and red (632 nm) excitation laser. These measurements are presented in Figures 5.9-5.11. For the RC101 wafer (Figure 5.9) we observe two distinct peaks with the red laser excitation and a single peak with the green excitation. Both excitation wavelengths are higher energy than both the cladding and core nominal band-gap energies and thus these photons will be absorbed. The most intense

peak is observed at $\sim$ 729 nm which is near the nominal cladding band-gap of $\sim$ 742 nm. The apparent blue shift of the cladding excitation compared to the expected nominal band-gap energy is most likely due to the uncertainty in the fractional aluminium concentration of each epitaxial layer. The high doping density (10^{18}cm^{-3}) may also cause an apparent blue shift of the band gap due to the Moss-Burstein effect, however at the excitation wavelengths of 632 nm and 532 nm, the change in absorption caused by the high density of dopant atoms in these layers is negligible since they are far ($>$ 100 nm) from the nominal band gap wavelength of the cladding. The observed $\sim$15 nm discrepancy between the nominal band gap and observed emission peak would only correspond to a $\sim$2.5% difference in the fractional aluminium concentration. A small proportion of photons from the red laser emission make it through to the core material where they are absorbed, resulting in an emission peak at $\sim$ 855 nm, near the expected nominal core band-gap of 872 nm.

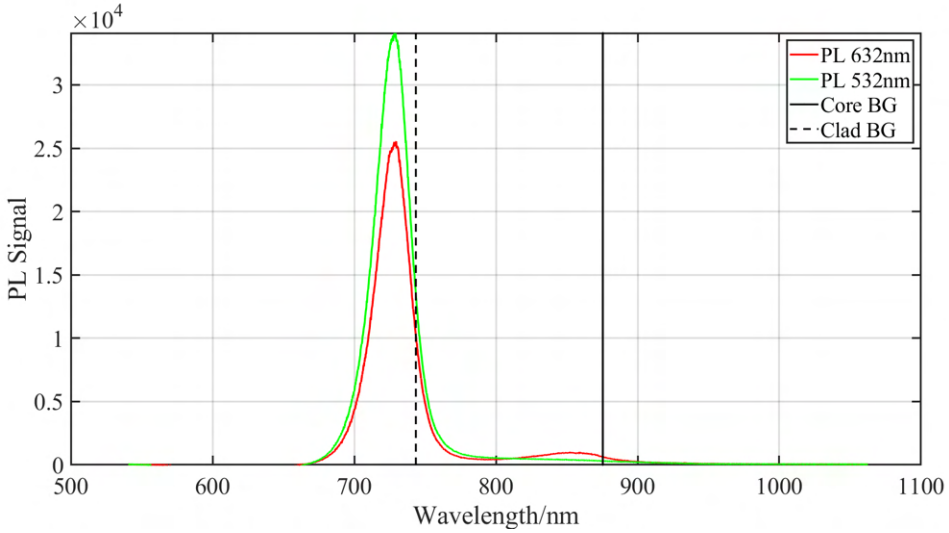


Figure 5.9: *Measured photoluminescence spectrum at two different excitation wavelengths for a sample of RC101 with the top p-GaAs cap removed. Measurements were carried out by Mr James Felton.*

PL spectra for the RC184 and RC187 wafers differ significantly from the RC101 wafer. For the red excitation of the RC184 wafer, we observe two distinct peaks: an intense broad peak centred around 842 nm and a smaller peak centred around 723 nm. The red excitation is transparent to the $Al_{0.45}Ga_{0.55}As$ cladding but

absorbing to the $Al_{0.22}Ga_{0.78}As$ core. These peaks are therefore attributed to luminescence of the core layer and the n-GaAs buffer layer - excitation photons pass through the upper cladding into the core where they cause luminescence. The core is thin (390 nm) so a large majority of these photons pass through the core and lower cladding into the heavily doped n-GaAs layer. Furthermore, given that the diffusion length of free photo-generated carriers is much longer than the core thickness, these carriers may have diffused into the n-GaAs layer causing a secondary luminescence. The same observation and explanation also applies to the red excitation of the RC187 wafer.

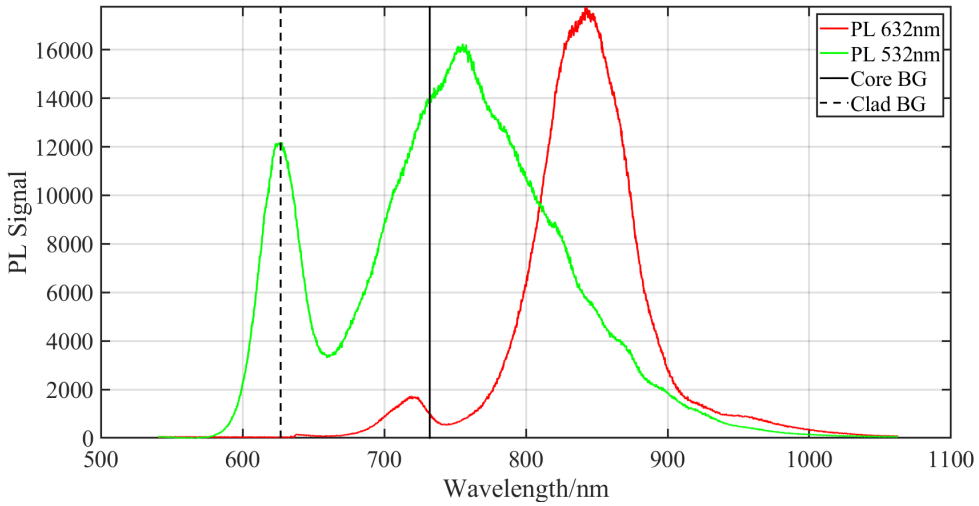


Figure 5.10: *Measured photoluminescence spectrum at two different excitation wavelengths for a sample of RC184 with the top p-GaAs cap removed. Measurements carried out by Mr James Felton.*

The green excitation for both the RC184 and RC187 wafer show some interesting behaviour. In this case the excitation is absorbed by both the cladding and core layers. Both spectra involve a large broad peak with the emergence of several repeated satellite peaks at lower energy. The broadening mechanism is complex, however it may be generally accounted for by considering the spread in the energy states, thermal broadening of the hole distribution, impurity-assisted broadening, and interface roughness [129]. Interface roughness assisted broadening manifests as broadening of the high energy side of the PL spectral features whilst electrons from substitutional impurities within the semiconductor crystal

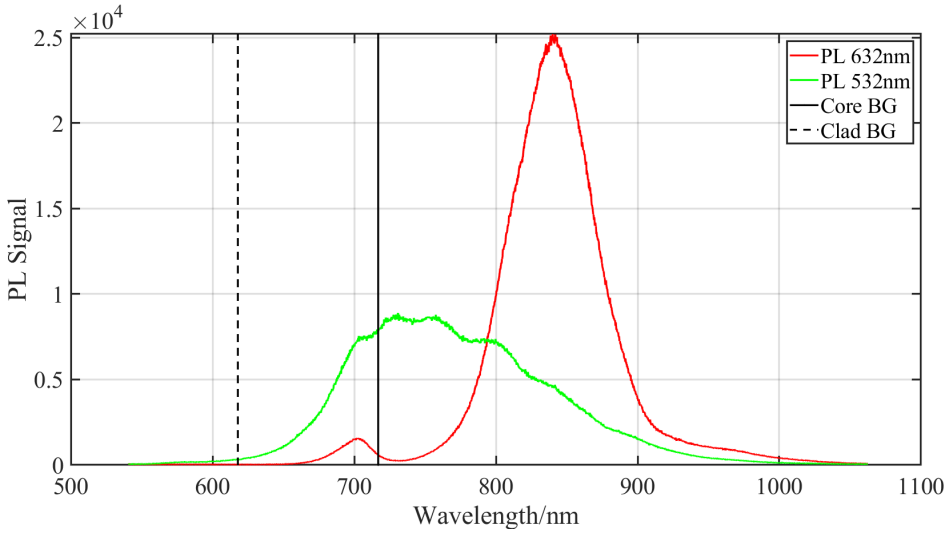


Figure 5.11: *Measured photoluminescence spectrum at two different excitation wavelengths for a sample of RC187 with the top p-GaAs cap removed. Measurements carried out by Mr James Felton.*

may lie closer to the conduction band than the valence band, leading to absorption and emission of photons with energies less than the band gap energy [130]. The series of repeated smaller satellite peaks within the larger peak may be attributed to 'phonon replicas' and may be a consequence of phonons coupling to free excitons [131]. This may be investigated further by plotting the normalised PL intensity as a function of the emission energy (Figure and 5.12). The spectrum for RC184 consists of a higher energy sharper peak which may be generally referred to as the bound-exciton (BE, or zero-phonon) peak, and a broader peak at lower energies as a result of conduction band to acceptor, free to bound (F–B) and donor to acceptor (B–B) transitions [132]. No phonons are released during the emission at the zero-phonon energy, hence its name. The higher energy peak in the RC187 spectrum has a very low intensity and can no longer be resolved. This may be explained due to the higher fractional concentration of aluminium in layers of this wafer. The replica peaks in the lower energy broad peak are a repetition of the main (highest intensity) peak at lower energies due to the phonon emission [133]. By approximating this broad structured luminescence spectrum as a superposition of Gaussian functions, the energy position of their peaks, E_{max} may be extracted. The values obtained for E_{max} from this approximation follow

a linear relationship with the peak number, and the slope determines the phonon energy $\hbar\omega_{LO}$ [128]. The extracted parameters from this analysis are compared with theoretical values and given in Table 5.3.

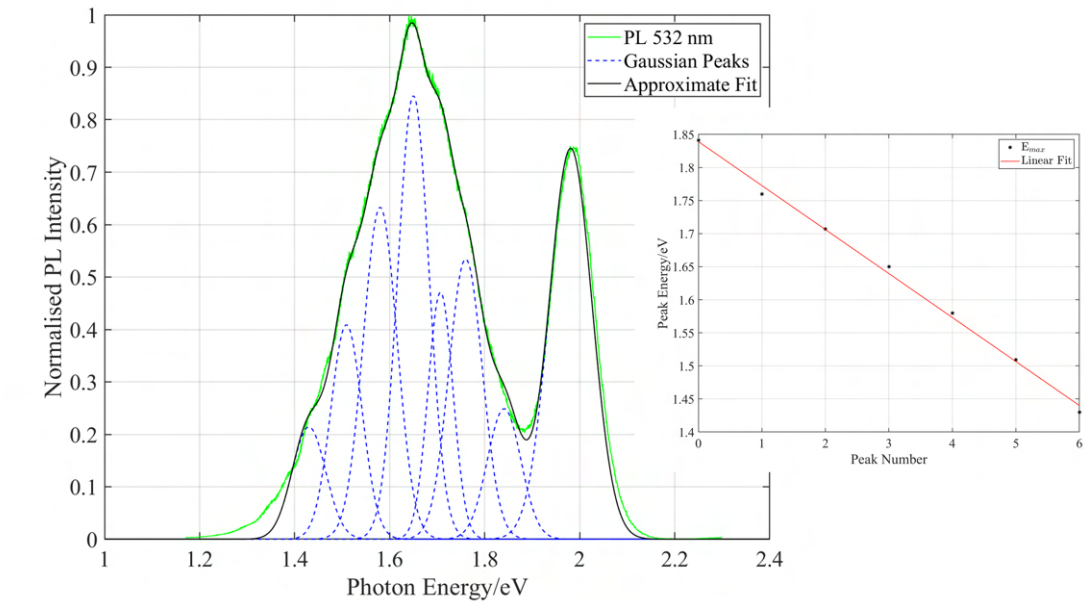
Wafer	**Clad Effective Phonon Energy (meV)**	**Core Effective Phonon Energy (meV)**	**Measured Phonon Energy (meV)**
RC184	40.1 (LO), 38.2 (TO)	37.4 (LO), 35.6 (TO)	66.5±4.5
RC187	41.6 (LO), 39.3 (TO)	37.7 (LO), 36.0 (TO)	80.2±2.5

Table 5.3: Empirical effective phonon energies due to the GaAs and AlAs-like longitudinal optical (LO) and transverse optical (TO) phonon modes [134], compared with the measured phonon energies from fitting the phonon replica peaks to Gaussian functions. Uncertainties on the measured values have been determined by the 95% confidence bounds on the linear fit.

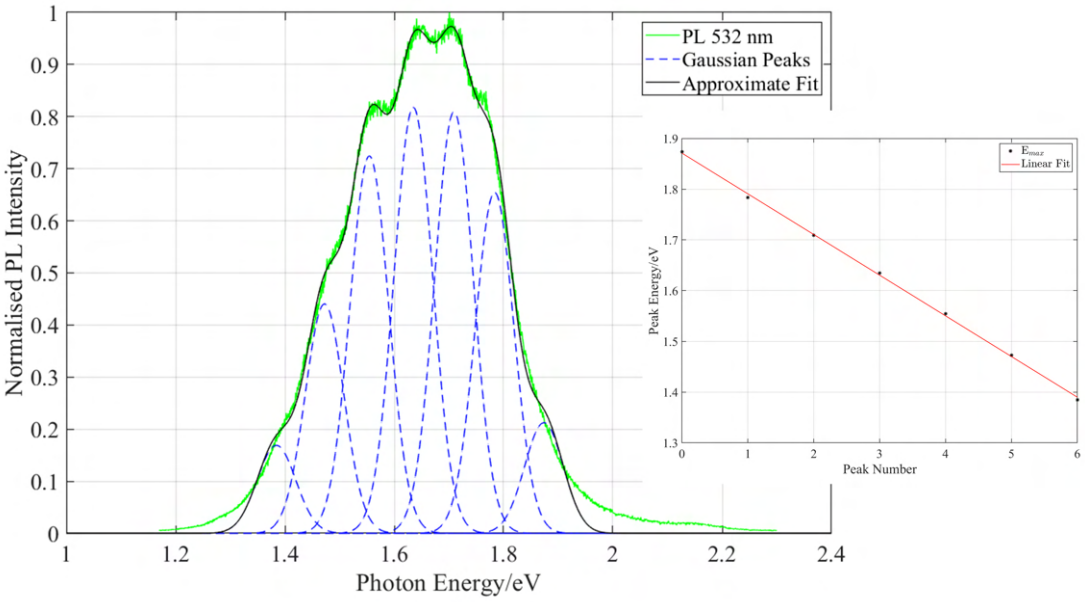
The exciton-phonon coupling strength may be determined by considering the Huang-Rhys factor, S. This parameter represents the mean number of phonons emitted as the F-B or B-B transitions occur. The larger the value of S, the stronger the interaction. At 0 K, the shape of the emission spectrum is determined by a series of narrow lines, spaced equidistantly by the phonon energy, and whose intensities are determined by a certain probability distribution for the transitions involved. At T>0 K, these lines broaden. The intensity distribution of these lines follow Poisson statistics,

$$I(n) = \frac{S^n \exp\left(-S^n\right)}{n!}, \tag{5.3}$$

where $n = 0, 1, 2, ...$, is the vibrational level of the excited electronic state. For very weak coupling (S=0), the spectrum will consist of a single line corresponding to the zero-phonon transition. The intensities of the phonon peaks have been plotted as a function of n for the RC184 and RC187 wafers and are shown in Figure 5.13. We find Huang-Rhys factors of 3.60±0.01 and 3.90±0.02 respectively for these structures, indicating medium exciton-phonon coupling [128]. Interestingly, the measured phonon energy from the fitting process is much larger than



(a)

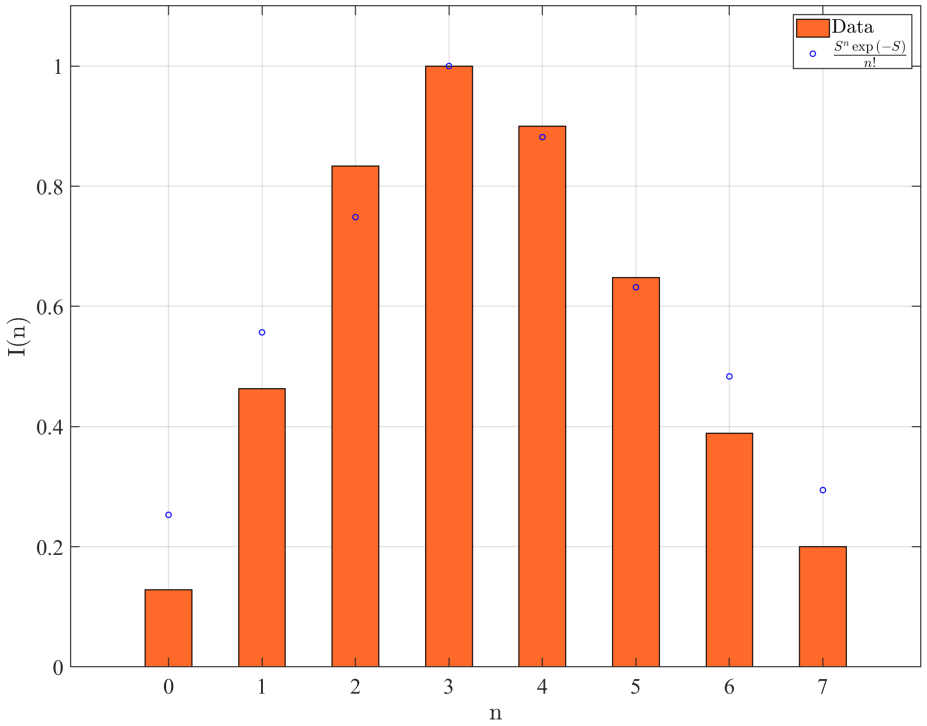


(b)

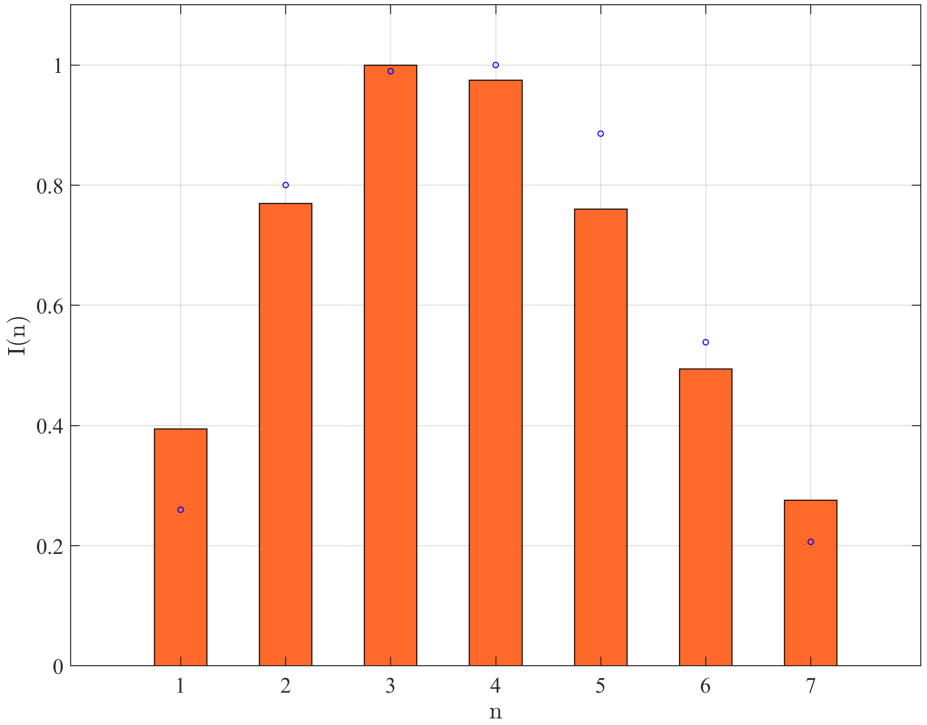
Figure 5.12: *Photoluminescence spectrum as a function of photon emission energy for 532 nm excitation of (a): RC184 and (b): RC187 wafers. Positions of the phonon replica peaks within the overall spectrum have been estimated by fitting a series of Gaussian functions with fixed width of 50 meV to the spectrum. The insets show the least squares linear fitting of the maximum energy of these peaks as a function of the peak number - $R^2 = 0.996$ and $R^2 = 0.997$ respectively. The extracted slope determines the phonon energy, $\hbar\omega_{LO}$.*

the theoretical predicted effective phonon longitudinal optical (LO) and transverse optical (TO) energies due to GaAs and AlGaAs-like modes which have been empirically determined from experimental data [134]. The measured phonon en-

ergies do not match the expected phonon energies (or multiples of them) for neither clad nor core layers in each wafer, and furthermore the measured Huang-Rhys factors are much too large than those typically reported for $Al_xGa_{(1-x)}As$ - < 0.6 for $Al_{0.35}Ga_{0.65}As$ [135]. It is not immediately clear why the measured phonon energies are much larger than the theoretically predicted phonon energies. One possible explanation is that these peaks observed in the PL spectra are not phonon replicas, but are rather simply interference fringes caused by multiple reflections from the epitaxial layers.



(a)



(b)

Figure 5.13: *Graphs showing the dependence of the normalised peak intensities, $I(n)$, which make up the PL spectra, as a function of the vibrational level of the excited state, n, for (a): RC184 and (b): RC187 respectively. The Huang-Rhys factors have been determined by fitting Equation 5.3 to the data and determining the factor S. In this case $S = 3.6$ for (a) and $S = 3.9$ for (b) respectively.*

5.3.2 Electroluminescence Measurements

Electroluminescence (EL) of semiconductor material is similar to photoluminescence except that the luminescence is stimulated by an electric current, rather than by light. Electroluminescence in this context refers to injection electroluminescence, which is characterised by the radiative interband recombination of majority and minority carriers injected into a semiconductor p-n or p-i-n junction [128]. In a p-i-n junction, the minimum wavelength of the emitted radiation is determined by the bandgap of the core region, $\lambda_m = hc/E_g$. In most cases however, the peak of the emission band is shifted to longer wavelengths compared to λ_m as the injected carriers do not combine radiatively via bimolecular recombination, but rather through extrinsic luminescence of donor-acceptor pairs, or excitons bound to impurities. The emission spectra may therefore also be influenced by light absorption and scattering due to impurities in the cladding material surrounding the core region, or by polymer-based encapsulation layers, such as the BCB layer used in the fabrication of the devices fabricated in this project.

During testing of the devices, light generated by the electrical injection of carriers was observed emanating from the region between the two p-contacts of the device due to the thinned cladding layer in this region. This was unintentional in the design, however these emissions were used to investigate the electrical injection or recombination properties of the core region of the devices. The bonded devices were mounted on a probe station and the probes positioned on the relevant metal contacts of the PCB. A multimode fibre was mounted to a micropositioner and carefully positioned to collect the light from above the device, as shown in Figure 5.14. The fibre was connected to a spectrometer (Ocean Optics USB 4000+) and the data processed using a computer.

To reduce effects due to heating, the EL spectra were recorded for a series of current peaks from 200 mA to 700 mA using 1 ms square wave pulses, with a repetition rate of 200 ms. Figure 5.15 shows the results of this experiment for an RC101 device. We observe that the peak of the spectrum begins to red shift

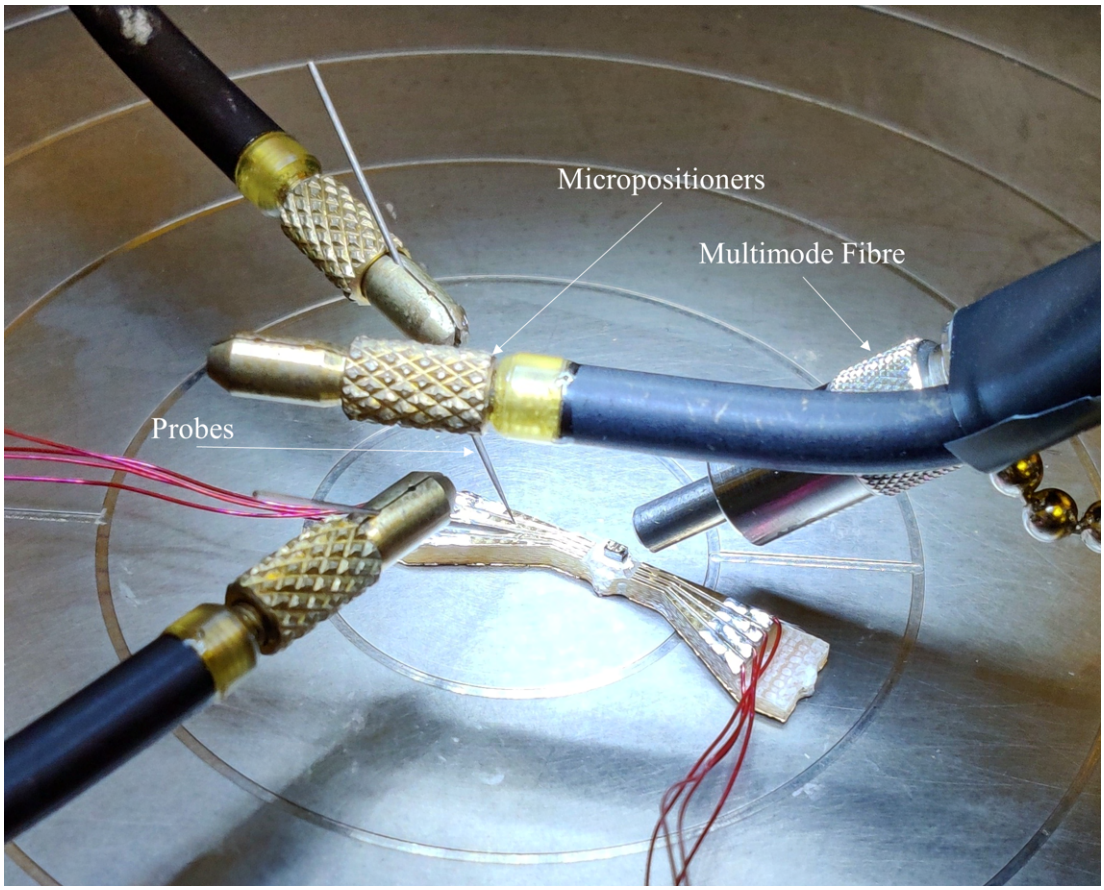


Figure 5.14: *Experimental arrangement for characterisation of the electroluminescence emitted from the top of the device.*

with increasing current due to local heating caused by the high current density. At 700 mA the device failed, as the edge of the top up metal contact into the BCB window melted, which can be seen in the microscope image of Figure 5.16.

As a result of the damage caused to the RC101 device due to excessive heating from high current injection, the EL of RC184 and RC187 devices were characterised using a longer pulse width of 100 ms and lower current peaks. The same behaviour was observed with devices from both wafers. Figure 5.17 shows the EL spectrum peak position as a function of the input current for both wafers. In all cases we observe that the low current emission peaks at ∼15 nm below the expected nominal core band gaps of 872 nm, 731 nm and 715 nm for RC101, RC184 and RC187 respectively. The EL spectra at low currents has also shown that luminescence occurs when the voltage across the heterojunction is less than the band gap energy of the core. Electroluminescence may occur in a forward bi-

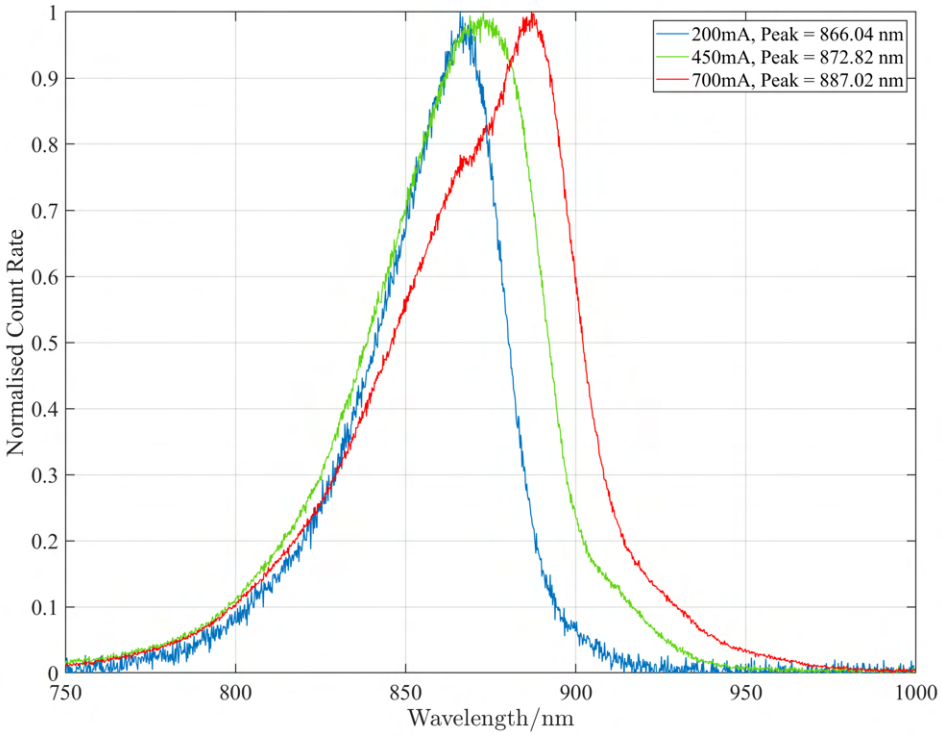


Figure 5.15: *Electroluminescence spectra from the top of an RC101 device, using square wave current pulses with a width of 1 ms and a repetition rate of 200 ms.*

ased p-i-n junction at even very low currents below the threshold voltage (E_g/e), resulting in the emission of photons with energy greater than the applied voltage, $h\nu > eV$. The reason for this is that the barrier of the junction is overcome by a small fraction of electrons or holes with energy high above the bottom of the conduction band or below the top of the valence band respectively. This energy is gained from the lattice and leads to cooling of the area in the close vicinity if the quantum efficiency is greater than 0.97 [136]. Since the band-gap of semiconductors can shift with temperature [137], this phenomena may contribute to the red shifting at higher injection currents and blue shifting at very low currents. It must also be noted that an apparent shift in the band gap of the core corresponds to only a 3% fractional aluminium content difference compared to the expected value. These two phenomena, coupled with apparent blue shifting of the band gap due to band-filling may explain the origin of the observed spectral peaks in these devices. However, the blue shifting due to band-filling at very low currents

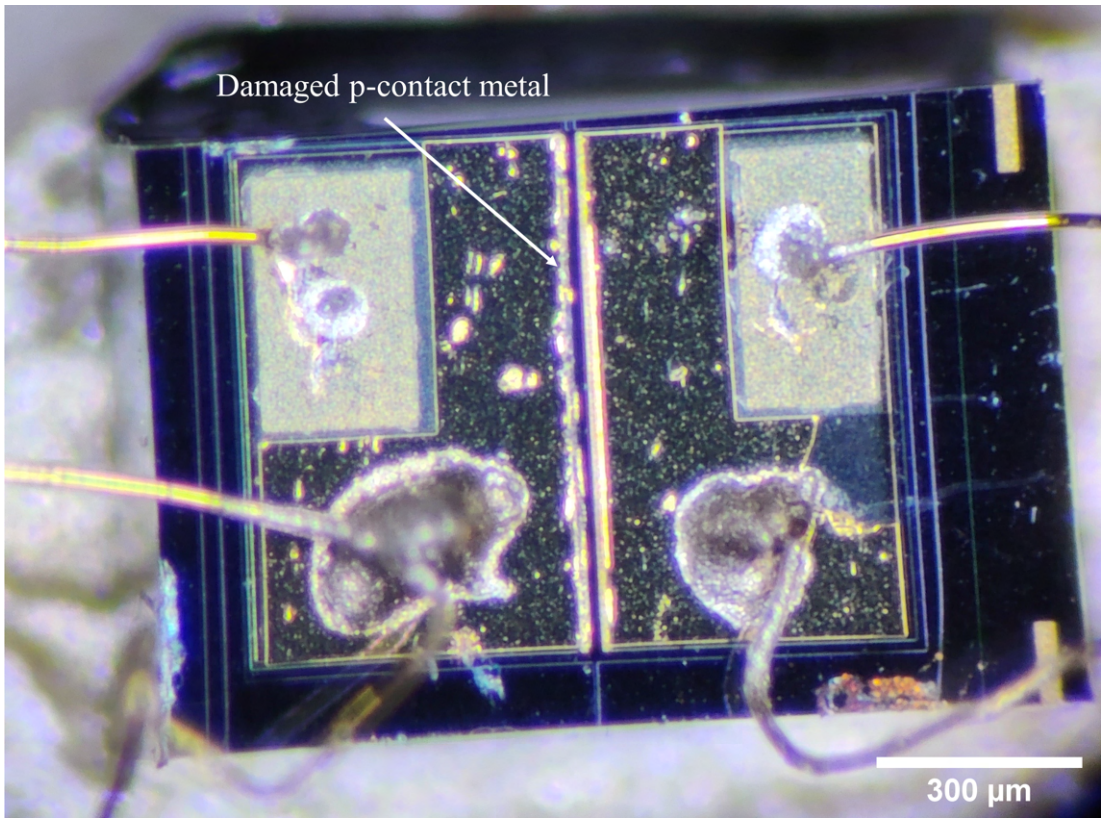


Figure 5.16: *Optical microscope image showing a failed top-up p-contact due to excessive heating from current injection.*

is expected to be negligible, as per the theory discussed in Chapter 2. The blue shifting due to the band-filling effect is expected to be identified at higher injection currents, and in this case would manifest as a shift in the EL spectrum at a threshold current density, followed by red shifting as the current is increased. This blue shifting at higher currents is not observed in these data and this may be attributed to the red shifting due to hot carriers masking the effect.

It is also apparent from Figure 5.15 that, at higher currents, there is a second emerging peak at shorter wavelengths. Imaging of the facet of this RC101 device during testing revealed that there was significant luminescence emanating from the facet, as shown in Figure 5.18. This was more apparent with this device than others since the waveguides had been cleaved off to test the optical steering properties (more detail given in Section 5.5). A possible explanation for the emergence of this peak only at higher currents when collecting EL from the top of the device is that some of the light emitted from the facet is being collected by

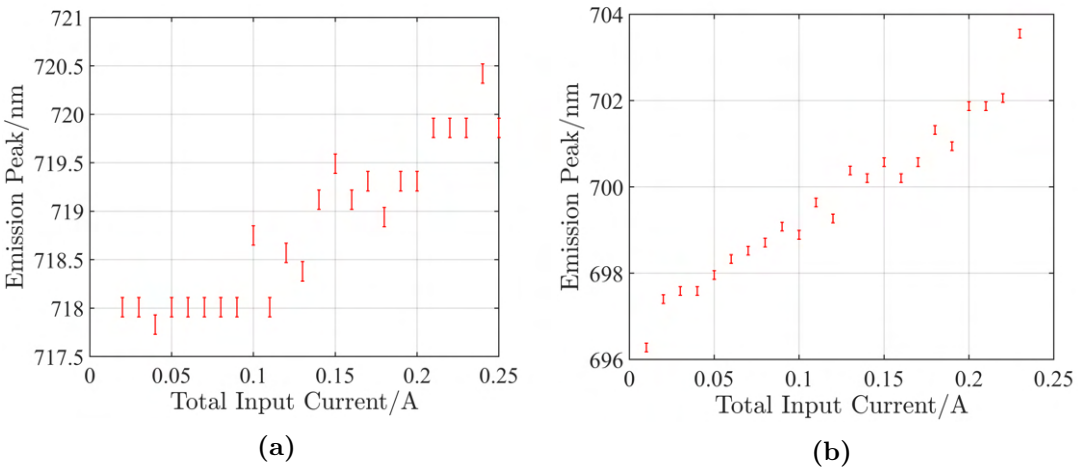


Figure 5.17: *Electroluminescence peaks of (a): RC184 and (b): RC187 devices as a function of injection current. Emission peaks determined by curve fitting to spectra, and uncertainties associated with fitting.*

the fibre in this configuration. To investigate this further, a separate experiment was carried out to characterise this EL from the facet of the device and compare it to the EL emitted from the top thinned cladding. In this case, to ensure only the facet EL was analysed, the device was mounted onto the test system described in Chapter 5 and the EL collected by the ×100 objective before being focused by a lens and collected by the multimode fibre.

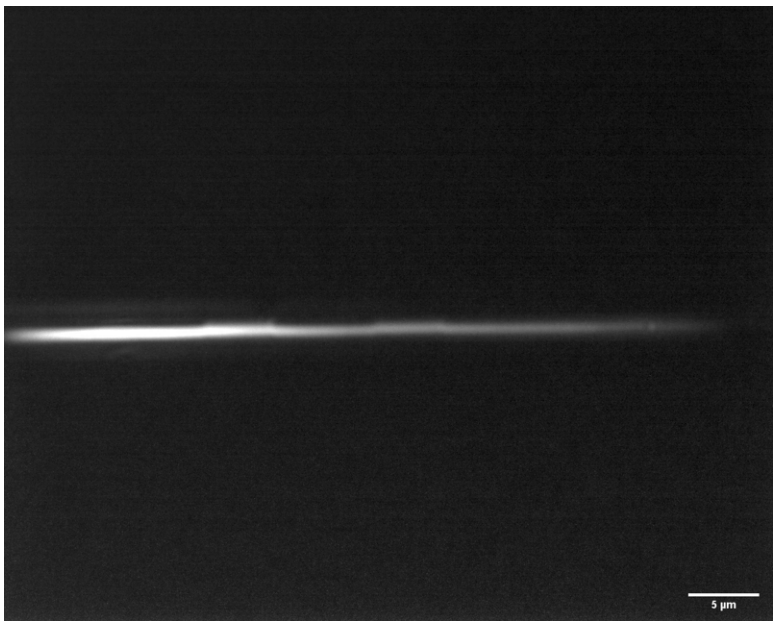


Figure 5.18: *Optical microscope image of the facet of a RC101 device with waveguides removed. Electroluminescence can be seen exiting the facet. A square wave signal was applied to each p-i-n region with a current peak of 150 mA, at 2 kHz with 5% duty cycle.*

Figure 5.19 shows the EL spectrum of the RC101 device at the facet, under the same electrical conditions as the previous experiment. Here we observe two distinct peaks in the spectrum. Fitting of this spectrum to two Gaussian functions reveals that the shorter wavelength peak occurs at 876.2±1.2 nm and the larger peak at 905.0±0.5 nm. The shorter wavelength peak was observed even at low current injection, which is further evidence that the short wavelength peak observed in the spectrum taken above the device was due to light from the facet being collected by the fibre. Once again, both of these peaks are observed to red shift with increasing current. The emergence of the shorter wavelength peak appearing at the facet may be explained by considering the optical confinement in a direction perpendicular to the propagation axis: carriers are electrically pumped into the core region where they recombine, producing photons. The wavelength of these photons will depend on the potential landscape of the double heterostructure, which changes depending on the applied voltage and the lattice temperature. The propagation direction of the generated photons will be random, however the refractive index contrast between the cladding and the core will confine photons to the core in an axis perpendicular to the layer growth, meaning that most of the photons will travel parallel to the cladding layers and exit at the facet. Longer wavelength photons may not be confined as strongly, resulting in a greater emission of these photons from the top window where the cladding has been thinned.

5.3.3 Summary of Luminescence Data & Implications

Analysis of the luminescence spectra of the fabricated devices has revealed some interesting results which have direct implications for the intended beam-steering properties. From the luminescence data we can infer the actual epitaxial structure of the p-i-n region for each wafer and how this affects the strength of the beam-steering due to carrier induced refractive index change effects at the design wavelengths.

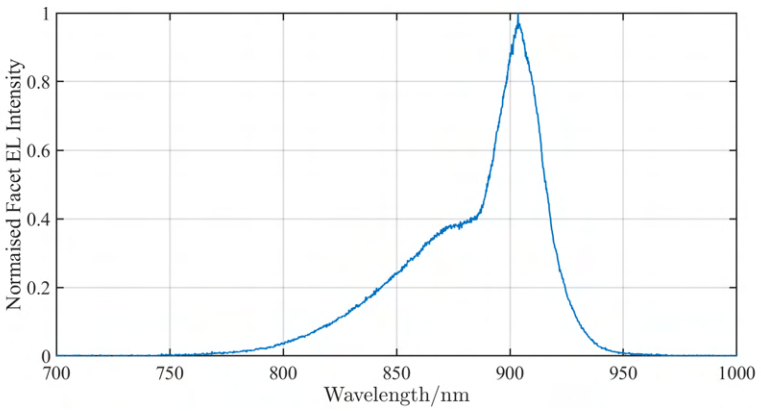


Figure 5.19: *EL spectrum for a device from the RC101 wafer with the waveguides removed, measured at the facet. Total current injection was 150 mA.*

For RC101 we found photoluminescence peaks at ∼729 nm and ∼855 nm, corresponding to the cladding and core layers respectively. The expected nominal band gap of the core was 872 nm, corresponding to the GaAs layer, however an uncertainty of 2% on the aluminium concentration in the core layer would place the band gap around 856 nm, closer to the observed value. The expected nominal bandgap of the cladding was 742 nm for 20% aluminium concentration. However, once again an uncertainty of 2% on this aluminium concentration results in a band gap of 731 nm, much closer to the observed value. The EL spectra showed emission at ∼866 nm at low currents, due to radiative recombination of carriers in the core. This would correspond to an $Al_{0.01}Ga_{0.99}As$ core, however, we have seen that the peak of the EL curve can shift to longer wavelengths due to the injection of hot carriers, and also blue shift due to the Moss-Burstein effect in cases where this effect is stronger than the band-edge shifting due to lattice heating and/or hot carrier injection. We can therefore conclude that the aluminium concentration of the core is between 0-2%. Referring back to the theory in Chapter 2, it was shown that the strength of the refractive index change effects are strongly wavelength dependent close to the band-gap. Therefore, if the uncertainty in the aluminium concentration acts to bring the band gap of the core layer closer to the design wavelength, this will ultimately increase the strength of the beam steering. Of course, the opposite is also true if the band

gap is shifted away from the design wavelength. We can calculate the difference in Δn produced by the carrier-induced refractive index change effects, between a GaAs and $Al_{0.02}Ga_{0.98}As$ core, as a function of carrier concentration, at the design wavelength of 894.5 nm. The results from these calculations are shown in Figure 5.20. From this simulation, the average difference in Δn between the GaAs and $Al_{0.02}Ga_{0.98}As$ curves is approximately 37% for carrier concentrations above 5×10^{17} cm^{-3}. This is quite a large difference, given the small change in aluminium concentration and indicates that the dimensions of the device must facilitate these tolerances, if the device design wavelength is closer to the band gap of the core layer. The strength of the beam steering effects due to these carrier-induced refractive index change effects determines how long the device must be and the exact positioning of the output waveguides to enable high extinction ratio switching. Furthermore, the observation of the unintended electroluminescence from the facet and top window of the devices would have to be addressed in the packaging since these peaks are close to the design wavelength. This could be achieved by using a narrow band filter in the optoelectronic package, centred at the design wavelength.

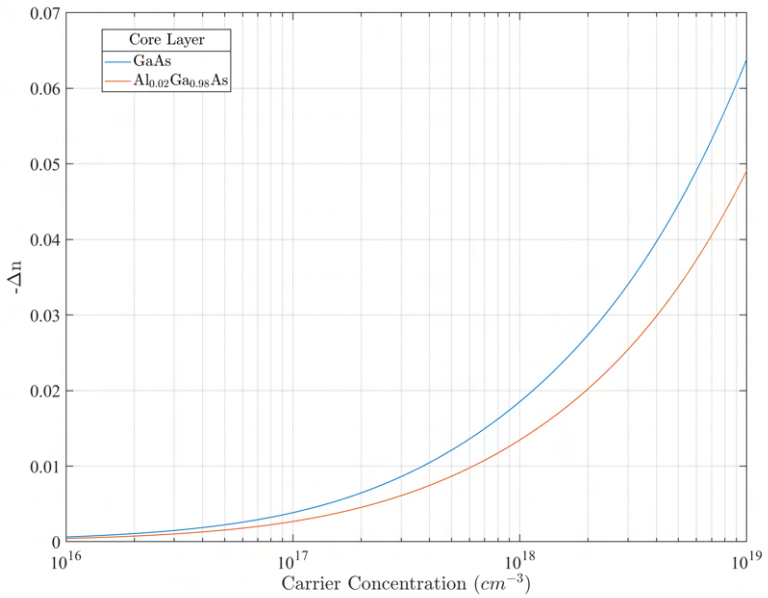


Figure 5.20: *Change in refractive index due to the Moss-Burstein effect for GaAs and $Al_{0.02}Ga_{0.98}As$, at the design wavelength for RC101 of 894.5 nm.*

For RC184, PL measurements revealed an emission peak around 723 nm, and EL showed a peak around 718 nm at low current injection. The expected band gap of the core is 731 nm, however the observed 723 nm peak only corresponds to a 1.5% difference in the aluminium concentration. In this case, the shorter wavelength peak observed in the EL spectra may be due to the aforementioned blue shifting due to the Moss-Burstein effect. We can repeat the calculation outlined above for RC101 to determine the difference in Δn due to this uncertainty in the aluminium concentration at the design wavelength of 780 nm. In this case, since the design wavelength for RC184 is further away from the core band gap, the difference in Δn between $Al_{0.20}Ga_{0.80}As$ and $Al_{0.22}Ga_{0.78}As$ is less than for RC101, at around 20%. Figure 5.21 shows the results of this simulation.

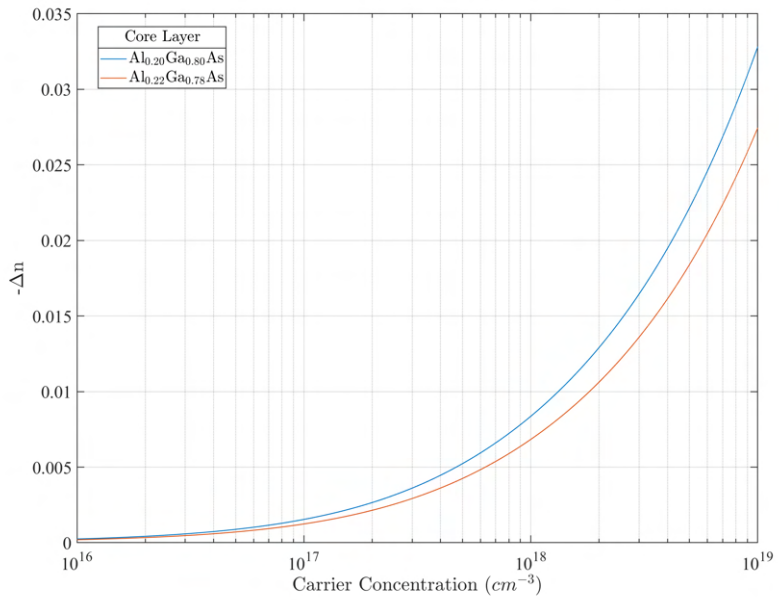


Figure 5.21: *Change in refractive index due to the Moss-Burstein effect for $Al_{0.20}Ga_{0.80}As$ and $Al_{0.22}Ga_{0.78}As$, at the design wavelength for RC184 of 780 nm.*

Finally, PL measurements on the RC187 material revealed an emission peak around 702 nm, and the EL spectrum an emission peak at $\sim$ 697 nm. The expected band gap of the core corresponds to 715 nm. These measurements represent the largest difference between the expected core band gap and the measured emission. Again, the EL measurements show evidence of blue shifting from the PL measurements. The observed peak at 702 nm corresponds to an

AlGaAs core with approximately 27.6% aluminium content. The larger difference between the expected core band gap and the observed one here may originate from the growth of an indirect bandgap $Al_{0.55}Ga_{0.45}As$ layer before the core was grown. Concerning the effect this has on the strength of the beam steering, we find similar differences as calculated for the RC184 wafer.

5.4 Passive Waveguide Testing

An important characteristic of any integrated photonic device is the attenuation or propagation loss that an optical wave experiences as it passes through. This attenuation is usually attributed to three main loss mechanisms: absorption, scattering loss and radiation loss [17]. For an active device, these losses can depend on the operating conditions and thus it is difficult to obtain a generalised figure under these conditions. However, propagation losses are largely dependent on the device and material design, thus an estimate of the overall propagation loss of the device may be obtained by measuring the properties of the passive waveguides.

Absorption losses are intrinsic to the semiconductor materials used and can be minimised by fine tuning epitaxial design for the intended guiding wavelength. This is easily achievable for passive devices as the design wavelength of the device can be far from the absorption peak of the semiconductor material. However, when combining active and passive components which exploit the carrier-induced refractive index change effects as discussed in Chapter 2, the epitaxial structure had to be designed to both incorporate a significant refractive index change for a given carrier injection which occurs near the band edge, whilst still minimising absorption losses.

Scattering losses are caused by imperfections within the volume of the waveguide due to fabrication defects, causing scattering 'centres'. The size and number of these imperfections per unit volume determine the extent of the scattering loss due to this mechanism. Scattering losses can also be caused by surface rough-

ness, which is more pronounced for higher order guided modes [138]. These losses can be largely overcome by optimisation of the material growth and fabrication process.

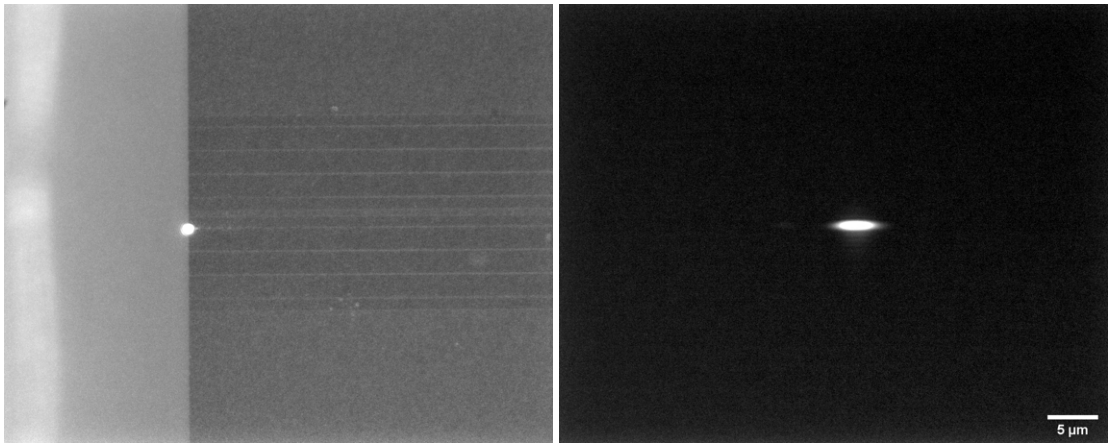
Radiation losses are related to leakage of the evanescent field of the guided optical mode in a waveguiding structure. This becomes significant when considering bent or curved waveguides, which are implemented in the devices designed in this project.

5.4.1 Propagation Loss Measurements

The fundamental aspect of measuring the propagation loss of a passive waveguide involves coupling a known optical power into one end of the waveguiding structure and measuring the optical power at the output. However, there are several major flaws with this simplified method, the main being that there may be significant coupling losses at the input and output of the waveguide which are not accounted for. Thus, several, more complex, well defined methodologies have been developed over the past few decades for measuring the overall loss of a waveguiding structure, such as the cut-back method [17], measurement of scattered light [139], and the Fabry-Pérot cavity method [140] to name just a few of many.

As a first attempt to measure the propagation loss of the passive waveguides, a 15x15mm^2 die was cleaved from each RC184 and RC187 parent wafer. The waveguides were patterned onto the die and etched using the process described in Chapter 3. The 12mm long waveguide structures were cleaved from the die, rinsed with deionised water and blow dried with nitrogen to remove any GaAs dust resulting from the cleave. The waveguides were then mounted to the test system and the relevant optical wavelength coupled into the input facet using the automated coupling routine described in Chapter 4. The optical power at the output facet was then measured using a lock-in detection method. The waveguides were then shortened by half and the process repeated. Figure 5.22 shows an image of light aligned to one of these waveguides. Unfortunately, this cut-back

method relies on both the propagation loss and the Fabry-Pérot etalon effect due to the reflectivity of the cleaved facets. This means that the quality of the cleaved facet must be identical with each measurement which is not possible to attain without the use of an anti-reflection coating. This method therefore resulted in very high propagation losses which were not indicative of the intrinsic propagation loss of the waveguide.



(a) **(b)**

Figure 5.22: *Plan-view (a) and output facet (b) microscope images of light aligned to one of the waveguides during measurement of the propagation loss.*

As an alternative, a simplified, non-destructive approach was used to measure the strip-loaded waveguide propagation losses, which involved heating the waveguiding structures and measuring the Fabry-Pérot resonances due to expansion of the material [140, 141]. The reflectivity of the cleaved facets causes the waveguide chip to act as a Fabry-Pérot cavity with loss. As light travels through the waveguide, some light is reflected from the facet and interferes with the propagating light producing resonance peaks. Heating of the device causes a change in the propagation length changing the phase difference between the interfering waves. This results in resonant and anti-resonant peaks in the recorded transmission intensity. Calculation of the propagation loss relies on the measurement of the contrast, K, between these peaks,

$$K = \frac{I_{max} - I_{min}}{I_{max} + I_{min}}, \tag{5.4}$$

where I_{max} is the maximum intensity of the resonance, I_{min} is the minimum. The contrast is independent of the input laser beam intensity at the facet, and a function of the combined loss-reflection factor, $\tilde{R} = R\exp(-\alpha L)$, where α is the propagation loss coefficient of the waveguide, R is the mode reflectivity of the end facet, L is the waveguide length. Namely,

$$K = \frac{2\tilde{R}}{1+\tilde{R}^2}. \tag{5.5}$$

Therefore, the the combined loss-reflection factor, $\tilde{R}$, is given by the measured contrast K,

$$\tilde{R} = \frac{1}{K}(1-\sqrt{1-K^2}), \tag{5.6}$$

The mode reflectivity can be estimated by calculating the effective refractive index, n_{eff} of the strip-loaded waveguide, and applying the following expression,

$$R = \left(\frac{n_{eff}-1}{n_{eff}+1}\right)^2. \tag{5.7}$$

Finally, the waveguide propagation loss (in dB/cm) can be obtained by,

$$\alpha = \frac{4.34}{L}\ln\left(\frac{R}{\tilde{R}}\right). \tag{5.8}$$

Waveguides were placed on the optical test system and light coupled at the input facet using the semi-automated scanning routine as described in Chapter 4. The transmitted optical power at the output facet was then measured using a lock-in detection as the waveguide structure was heated from above using a resistive heater. This was repeated for various operating wavelengths for each epitaxy, and the propagation loss calculated as per the aforementioned method. Figure 5.23 shows an example of the data recorded for RC184 waveguides at 790 nm, and Table 5.4 gives a summary of all measurements. To correct for alignment drift, light was coupled into the same waveguide and the output intensity measured

over the same time period, at a fixed temperature. The decrease in intensity over this time period was recorded and the measurements from the waveguide heating were adjusted according to this drift value. The variance on the recorded data corresponds to an uncertainty on the calculated loss, which has been calculated and included in the results.

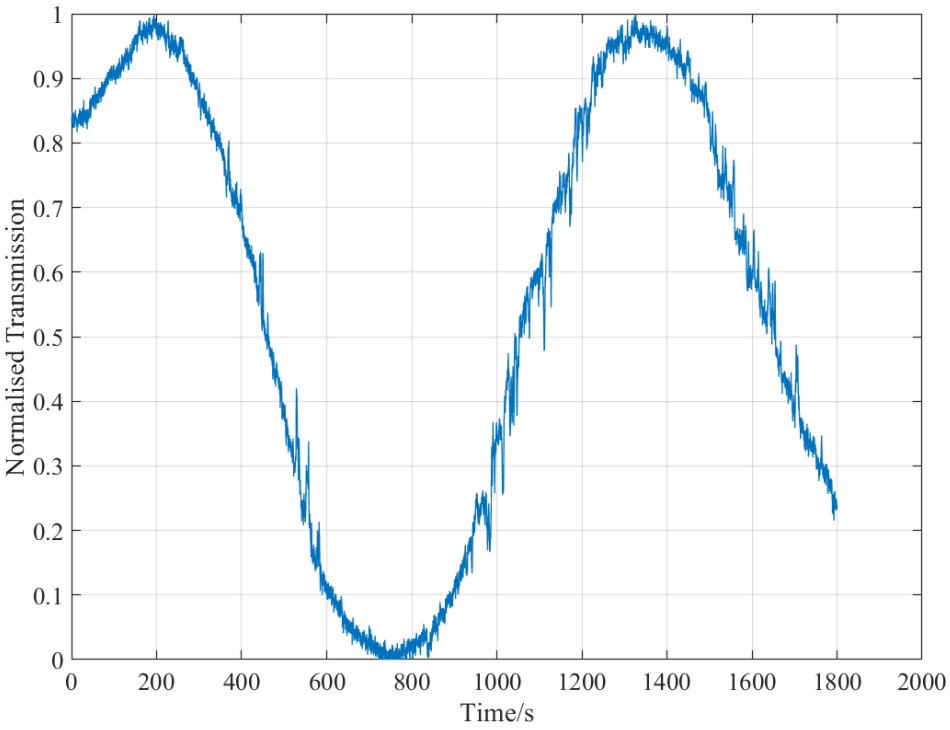


Figure 5.23: *Measured normalised transmitted optical power at the output facet of the RC184 sample, as a function of time whilst radiatively heating the sample from above using a resistive heater. Optical power input into the device was ∼300 μW and the collected optical power was ∼100 nW.*

Die Reference	**Test Wavelength (nm)**	**Propagation Loss (dB/cm)**
RC184	790	4.27±0.64
RC184	760	4.34±0.62
RC187	790	5.61±0.12

Table 5.4: Summary of the measured propagation losses of the test waveguides.

5.4.2 Discussion

Comparing these measured propagation loss measurements with the relevant literature [92], where $Al_xGa_{(1-x)}As$ strip-loaded single mode waveguides were fabricated for propagation of 1.3 μm and 1.55 μm wavelengths, we note that the waveguides fabricated here show propagation losses around five times higher than similar waveguiding structures. However, it must be noted that in this case the fabricated strip-loaded waveguides have been fabricated as part of an optical switching device which exploits a mechanism that relies on the propagation wavelength being near the band gap of the core of the waveguide. Therefore, there will be higher absorption losses in the waveguides fabricated here than for waveguides designed for wavelengths far from the band edge of the core region. In the design of these optical switches, a trade off was made between acceptable propagation loss due to absorption at the design wavelength, and operating near the band edge of the core to obtain a sufficient carrier-induced refractive index change for beam steering [64].

Furthermore, by considering the total length of the device, the measured material propagation losses can be used to calculate an estimate of the insertion loss experienced by an optical beam coupled into the device. With a packaged device, the facet can be coated with an anti-reflection coating so that the loss due to reflection is negligible. Using the largest of the calculated loss values, we find that one single RC187 device of length 1.9 mm at 790 nm experiences an insertion loss of $\sim$1 dB. Comparing this value to a $\sim$1 dB/cm Mach-Zender interferometer switch which requires a length of $> 1cm$ to achieve comparable switching extinction, it is now clear that the beam steering devices fabricated from this material in fact offer comparable or lower insertion losses than those reported the literature, due to their smaller dimensions.

5.5 Switching Characteristics

Characterisation of the switching characteristics of the devices is the most important aspect of the project and determines the suitability of this optical switch design for use in quantum sensing experiments. The test system described in Chapter 4 has been used to investigate the switching ability of the fabricated devices, namely the ability of the device to redirect an optical signal from one position to another. This section describes the methodology used to perform this testing and the results obtained. These results will be discussed and allow us to evaluate the performance of these devices in the context of integration into a quantum sensing experiment.

5.5.1 Extinction Ratio

As described in Chapter 1, the extinction ratio is measure of the intensity of light at an output of the device in the 'ON' state to the 'OFF' state. To measure the extinction ratio of the fabricated devices, the appropriate wavelength of light to the epitaxy was coupled into the input facet of the device. A small current was allowed to flow through each p-i-n junction of the device and the optical power at the output of the straight waveguide was monitored whilst the semi-automated coupling procedure was carried out. Once the light was successfully aligned to the device, the optical power output at the straight waveguide was measured whilst scanning through a series of electrical current values for each p-i-n junction. This was achieved using an automated procedure, where the start, end and step values for each channel were defined using the software GUI. The optical power at the output facet was then measured for each of these current values and a 'heat' map produced from this data. The extinction ratio was then calculated using the highest and lowest measured output optical power levels. It was not possible to repeat this procedure for the normally 'OFF' curved waveguide since the amount of optical power coupled into this waveguide was very low and the measurements were limited by the noise floor of the equipment. This is most likely due to

a combination of radiation losses due to the curvature of the waveguide, and imperfections due to fabrication tolerances. Figure 5.25 shows an example of a map obtained for a device from the RC187 wafer at 755 nm. This map contains interpolated data to give an indication of the performance at current levels not measured, however the extinction ratio of 18.71±0.03 dB was calculated with respect to the equally spaced measured data. Figure 5.25 shows an image of the illuminated output facet of the straight waveguide of the same RC184 device, at the current values corresponding to the maximum measured output intensity. The expected single-mode behaviour of the waveguide is apparent here. This process was repeated for devices from each wafer at various optical wavelengths. The results are summarised in Table 5.5.

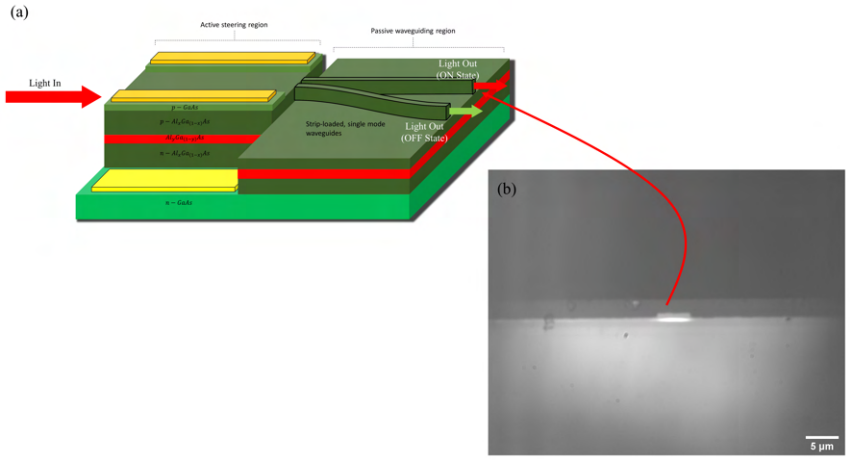


Figure 5.24: *(a): Schematic representation of the device and (b): Image of the facet of an RC184 device at the end of the taper for the straight waveguide, with 760 nm light coupled into the device and 10 mA through each p-i-n channel.*

Die Reference	**Test Wavelength (nm)**	**Extinction Ratio (dB)**
RC101	904	13.40±0.03 [142]
RC184	783	2.39±0.03
”	755	18.71±0.03
RC187	760	6.69±0.03
”	734	21.42±0.03

Table 5.5: Summary of the measured extinction ratios for optical switching devices from each wafer at various operating wavelengths.

What is immediately clear from these results is the strong wavelength depen-

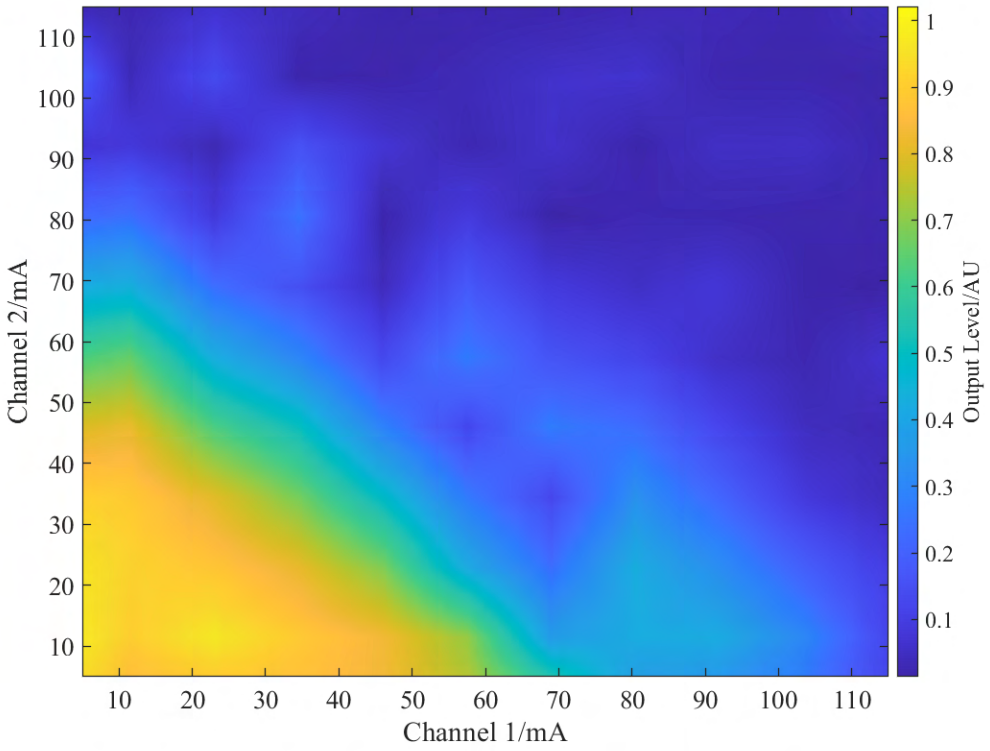


Figure 5.25: *Interpolated map showing the output intensity at the output facet of the straight waveguide for a device from the RC184 wafer, as a function of the current through each p-i-n region. The wavelength of the light used was 755 nm. The calculated extinction ratio for this device was 18.71±0.03. The extinction ratio is calculated with respect to the measured data. The current through each p-i-n junction was scanned from 5 mA to 115 mA in steps of 5 mA.*

dence of the extinction ratio on the operating wavelength, as predicted by the theory in Chapter 2. At currents < 50 mA we observe that the maximum intensity occurs when the current through channel 2 is greater than the current through channel 1. This is expected, since the waveguides which are delineated at the end of the steering section are offset from the centre of the propagation axis. Therefore, to fully couple into the straight waveguide requires some slight beam steering towards the channel 1 region, which would be achieved by increasing the current through channel one and decreasing the current through channel 2. This offset is shown in the microscope image of Figure 5.26. Due to limitations of the control circuit defining the voltage set points, the output of the current driver can never fall below 5 mA unless the power is switched off. Therefore, the map begins at 5 mA through each channel, rather than 0 mA.

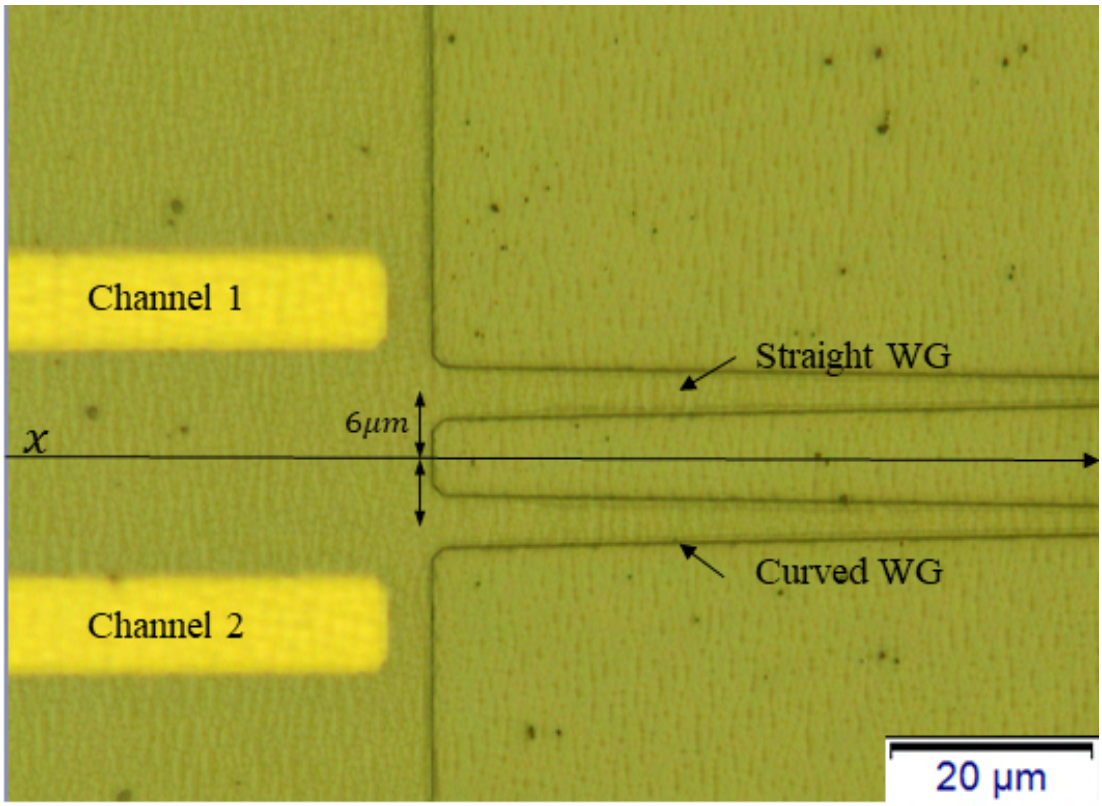


Figure 5.26: *Microscope image showing the tapered waveguide inputs delineated at the end of the steering region. Each waveguide input is offset by 6μm meaning that a slight current imbalance is required to steer the beam into either channel. The single mode behaviour of the waveguide is clearly apparent here.*

We also observe, that in all cases, the point at which the optical output power is the lowest occurs at the higher current injection values. This is not the behaviour that is expected with this design, since at higher injection currents the refractive index contrast in the steering region caused by carrier injection is expected to be higher, meaning that the guided beam will be more strongly confined in a direction perpendicular to the propagation. In the best case, this would mean the beam is essentially squeezed and focused in a region in between the input region of the tapered waveguides, as illustrated by the simulation in Figure 5.27.

To further investigate the beam steering capabilities of these devices, the wave guiding section was removed from another set of fabricated devices before the bonding step (refer to Chapter 2 for detailed diagrams of each section of the device). These devices were then mounted to a PCB and bonded using the same process described in Chapter 3. This resulted in a device with only the

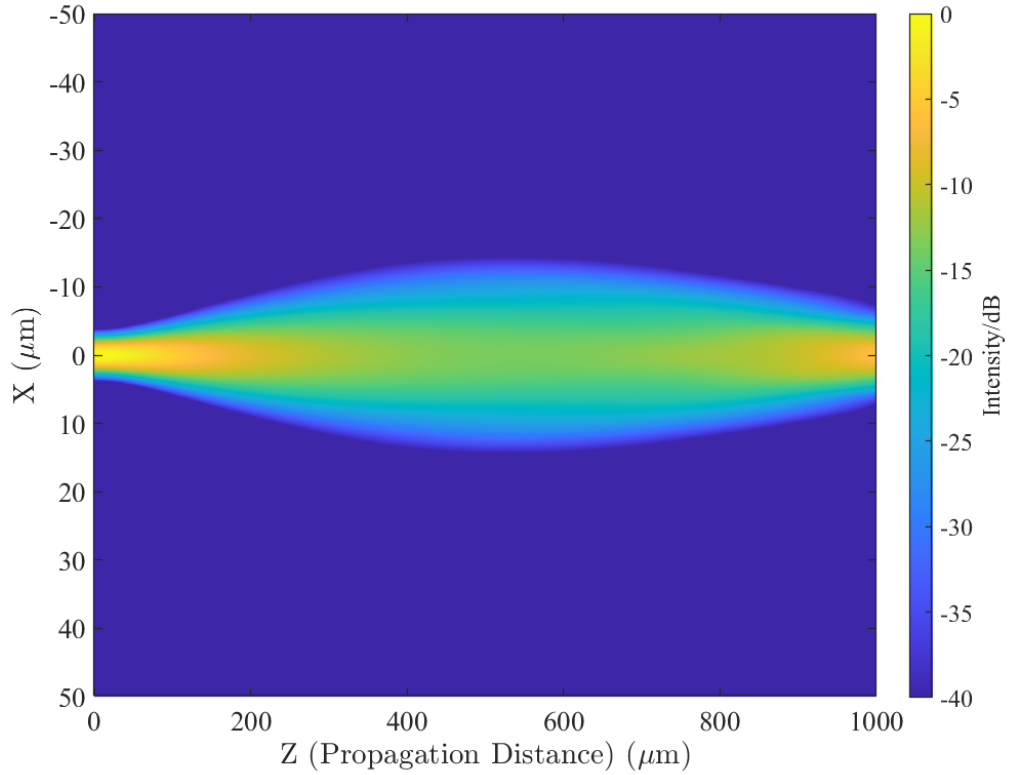
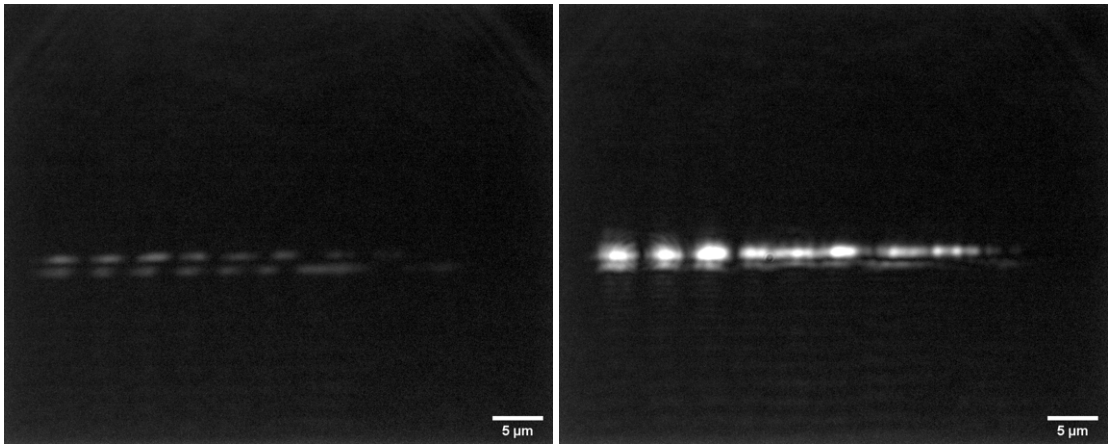


Figure 5.27: *Beam propagation simulation showing the effect of a current injection of 115 mA through both p-i-n channels for RC101 at 904 nm.*

beam steering section, allowing the beam profile before entering the wave guiding section to be examined. One of these devices was also used for the EL testing and can be seen in Figure 5.16. In this series of experiments, the facets of these devices were imaged whilst the injection current through each p-i-n section was altered. When light is coupled in and the device is off, i.e. no current through either p-i-n section, we observe light at the output facet which had been weakly guided and reflected off the sidewalls of the device, causing an interference pattern. The explanation for this is that, when the device is off, there is no confinement of the guided wave in the direction perpendicular to propagation, so the beam is free to spread out in the core until it reaches the sidewall. When the device is switched on with a small amount of current (10 mA passing through each p-i-n section) we immediately observe the brightness of the output increase due to the stronger confinement caused by carrier injection. These situations are shown in Figure 5.28. A band-pass filter (Semrock FF01-900/32-25) was used to remove

electroluminescence produced by the device from the current injection, and a 2 kHz square wave with 5% duty cycle used to reduce local heating effects.



(a) **(b)**

Figure 5.28: *Images of the output facet of an RC101 device with the waveguides removed and 904 nm light coupled in, with (a): electrical signals off and (b): 10 mA, 2kHz square wave with 5% duty cycle through each p-i-n section. A band-pass filter (Semrock FF01-900/32-25) was used to remove electroluminescence produced by the device from the current injection. When light is coupled in and the device is off, i.e. no current through either p-i-n section, weakly guided light is observed at the output facet which has reflected off the sidewalls of the device, causing an interference pattern. When the device is off, there is very little confinement of the guided wave in the direction perpendicular to propagation, so the beam is free to spread out in the core until it reaches the sidewall. When the device is switched on with a small amount of current (10 mA passing through each p-i-n section) we immediately observe the brightness of the output increase due to the stronger confinement caused by carrier injection.*

When the injection current is increased through each p-i-n region, we observe unexpected behaviour. As was shown with the current map in Figure 5.25, when the current through the device is gradually increased, the guided light at the output facet gradually reduces in intensity. Unbalancing the currents through the two channels does not appear to change the intensity as we expect, but rather the output intensity reduces depending on the total electrical power through the device. Apart from the discussed observations at low currents, we do not observe the expected beam steering properties in any of the devices at higher currents.

These results may be explained by considering the local heating of the device due to hot carriers, i.e. carriers with a significant amount of kinetic energy, accelerated by a strong electric field. As we have seen from the analysis of the electroluminescence spectra, the peak emission wavelength of the devices is sensitive to

the amount of electrical current supplied to the device, red shifting with increasing current due to contraction of the band gap due to various thermodynamic effects [137]. Even if the sample is cooled using the temperature controlled stage, the local temperature of the lattice may differ significantly due to the proportion of electrically injected carriers with high kinetic energy. This was attempted during testing with no observed differences in the measured data. It is therefore possible that, at higher injection currents, the band structure of the device changes enough to negate the weak beam steering effects and instead shifts the energy bandgap of the core far away from the intended operating region. When an optical wave of the design wavelength is the coupled into the device, there is less confinement due to this change and the amount of light guided by the device to the output facet decreases. Therefore, the higher measured extinction ratios reported in Table 5.5, may not be a result of the intended operating mechanism, but rather due to local heating of the device caused by high current densities. This would thus explain why we observe some beam steering properties at lower injection currents, but at higher injection currents the beam is not manipulated as expected, but is simply no longer guided in the device. The devices therefore still act as an optical switch due to this heating mechanism, but the time taken for the lattice to heat up to a level where the beam is extinguished to an appropriate level is on the order of hundreds of milliseconds, thus would not be suitable for the intended application.

5.5.2 Current Crowding

Despite the observation of switching effects at lower currents, the fabricated devices did not achieve the intended beam squeezing and steering properties predicted by the theory and demonstrated in previous work [19]. One hypothesis is that the distribution of carriers in the core layer of the double heterostructure devices, does not follow the theory described in Chapter 2 due to the geometry of the mesa design.

The effect of current crowding in mesa geometry double heterostructures has been studied in previous literature [143, 144, 145]. By incorporating a relevant model from the literature with the BPM simulations presented in Chapter 2, we can gain a more quantitative insight into how the mesa geometry affects the beam steering properties of the fabricated devices. Figure 5.29 shows a schematic of the model used by [144] for the theoretical calculation of the current crowding effect.

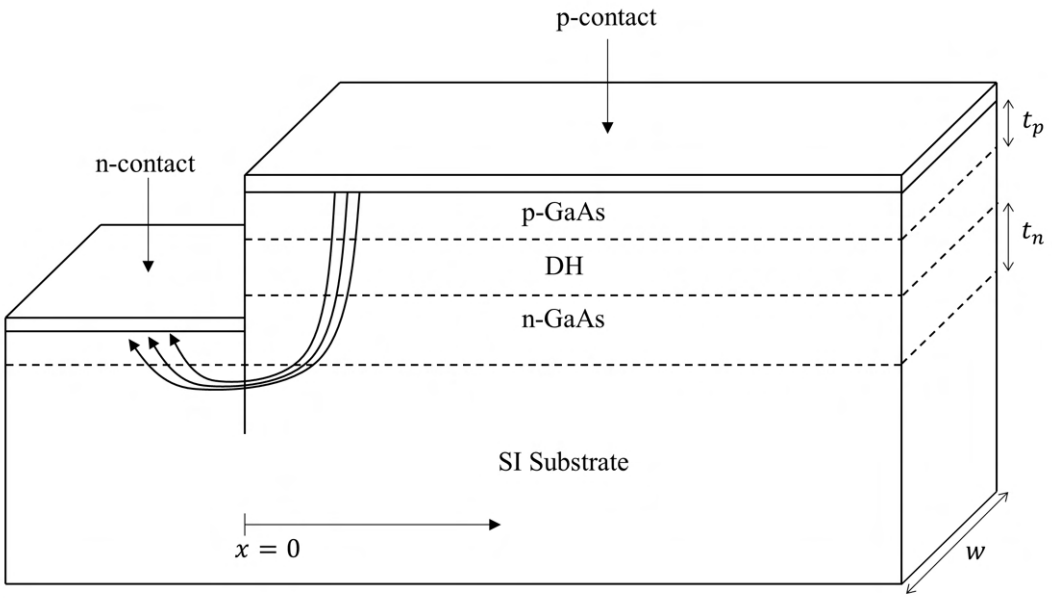


Figure 5.29: *Schematic illustration of the model used by [144] for the calculation of the current crowding effects in a mesa geometry, double heterostructure (DH) device on a semi insulating substrate. The arrows show the direction of the current path. The thickness of the p-GaAs layer is given by t_p and the n-GaAs layer by t_n. The width of the simulated region is given by w.*

By considering the resistance of the layers on both sides of the p-i-n junction, an expression can be obtained providing the current density profile as a function of x, the lateral distance from the edge of the p-contact,

$$J(x) = J(0) \exp\left(-\sqrt{\frac{\rho_n}{t_n(\rho_c + \rho_p t_p)}}x\right), \tag{5.9}$$

where ρ_n and t_n are the resistivity and thickness of the n-type layer respectively, ρ_c is the specific p-type contact resistance, and ρ_p and t_p are the resistivity and thickness of the p-type layer respectively. A useful parameter to define is the

current spreading length, L_s which defines the length where the current density falls to $1/e$ of J_0, and is given by,

$$L_s = \sqrt{\frac{(\rho_c + \rho_p t_p) t_n}{\rho_n}}. \tag{5.10}$$

Equation 5.10 demonstrates that, to minimise current spreading (maximise L_s), the resistivity of the n-type layer should be as low as possible and the p-type resistivity should be as large as possible. In the devices fabricated for this project, the n-type resistivity is low due to the high doping but so is the p-type layer. The geometry of the fabricated devices can be applied to this model by applying Equation 5.9 for each p-type contact and combining the results by taking the centre of the mesa as the $x = 0$ point, with J_0 at the edges of the p-contacts nearest the mesa sidewall ($x = -20\mu m$ and $x = 20\mu m$ respectively). The results of this simulation for a RC101 device with a current injection of 10 mA through each contact are shown in Figure 5.30. Here we immediately observe the current crowding effect near the sidewalls of the mesa. The current spreading length is calculated to be 1.16 μm which is approximately 3% of the mesa width. Table 5.6 gives a summary of the calculated current spreading lengths for each epitaxy. These calculations show that, due to the electrical properties of the semiconductor layers in each epitaxial design, the current spreading length due to the mesa geometry is less than 3% of the mesa width in all cases. This would significantly reduce the beam steering properties of the devices since the areas of high current density would be confined to the sidewalls of the mesa. To confine a waveguide mode, the carrier distribution must have a sufficiently sharp gradient in the region of the guided optical mode, which is not possible with this configuration.

Die Reference	**Current Spreading Length,** L_s (μm)
RC101	1.16
RC184	0.86
RC187	0.97

Table 5.6: Summary of the theoretically calculated current spreading lengths due to the mesa geometry, according to [144].

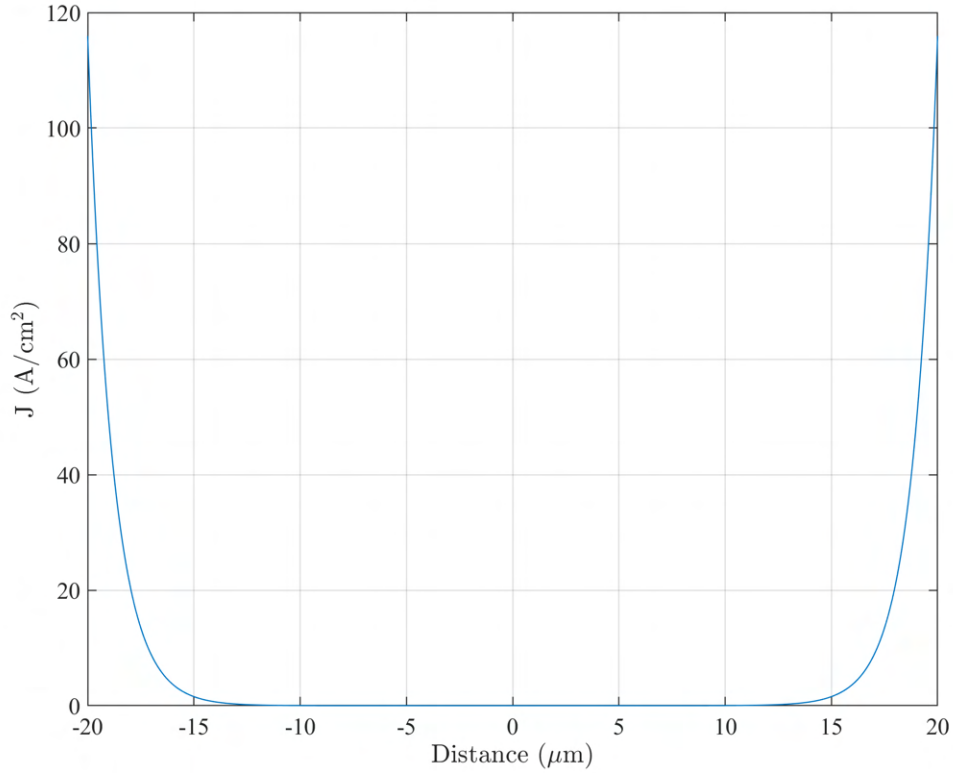


Figure 5.30: *Current density as a function of the lateral distance across the mesa for parameter from the RC101 wafer, with 10 mA applied though each p-contact. The point 0 μm marks the centre point of the mesa and the left and right hand edges are located at -20 μm and 20 μm respectively.*

Finally, this carrier profile can be re-incorporated in to the BPM model to determine the beam profile at the output of the steering region for a given input current. Figure 5.31 shows the propagation of a 904 nm fundamental TE mode through the steering section of RC101, with input currents of 115 mA through each side of the mesa, as a direct comparison with the old model in Figure 5.27. A key point to note here is that the areas of high current density are too far confined to the edges of the propagation region, so the propagating beam is not strongly confined. This also shows the origin of the interference pattern effects observed at the output facet - the beam is reflected from the regions of high current density at the edges of the mesa. In this situation the accuracy of the BPM algorithm is reduced due to these reflections so it is difficult infer any quantitative measurements with confidence from these simulations. Nonetheless, this has allowed us

to better qualitatively understand how a beam may be propagating through the fabricated devices, and explains why the intended beam steering properties were not observed during testing.

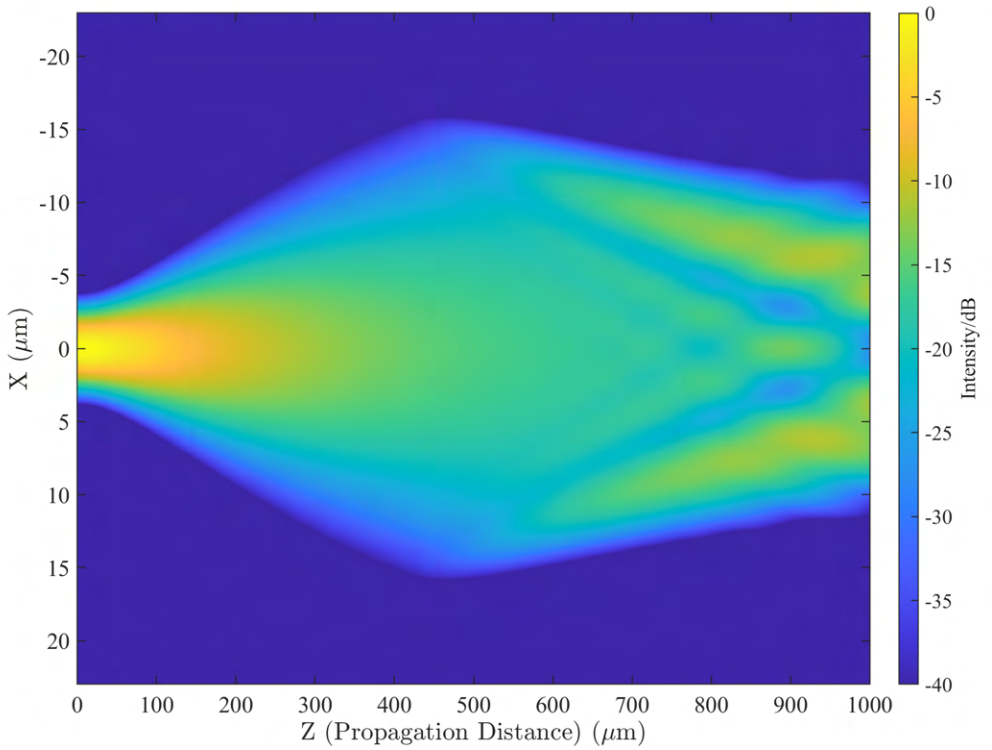


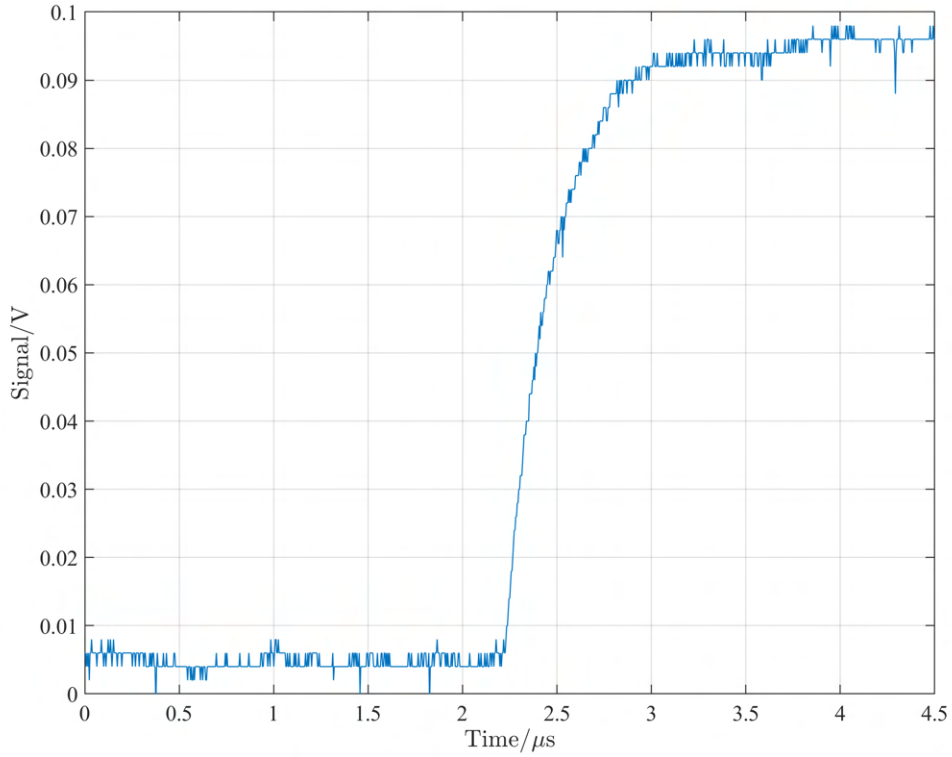
Figure 5.31: *Updated beam propagation simulation of a 904 nm, fundamental TE mode through the steering section of an RC101 device, with 115 mA applied through each contact, as a result of current crowding due to the mesa geometry.*

5.5.3 Switching Speed

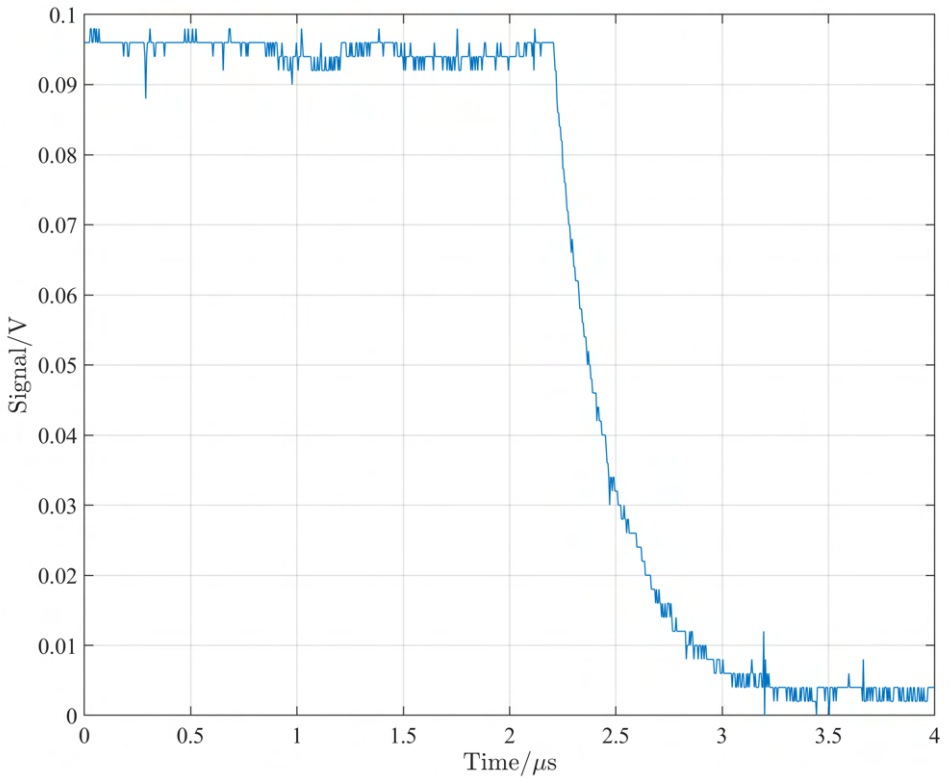
Despite the fact that beam steering from the straight waveguide to the curved waveguide was not observed, an estimate of the switching speed of the devices can be obtained by analysing the observed beam steering effects at low currents. As previously mentioned, there was a significant increase in the observed light intensity at the output of the straight waveguide when the current through the device was switched from 0 mA to 10 mA. Taking the light intensity at the output at 0 mA as the 'OFF' state and at 10 mA as the 'ON' state, the switching speed due to the beam steering mechanism may be determined.

To make this measurement, 904 nm light was coupled into an optical switch from the RC101 wafer, using the aforementioned semi-automated coupling routine whilst the current through the switch was held at 20 mA through each p-i-n channel. Once coupled, the output of the photodetector was recorded on the oscilloscope and set to trigger on a falling edge. Power to the current driver was then switched off, and the falling edge was detected on the oscilloscope. This data was exported and analysed in MATLAB to determine the switch off time for the device. This procedure was repeated for the rising edge of a switch on sequence. Figure 5.32 shows plots of these measurements. The measured rise time is 670±5 ns, and the measured fall time is 675± 5 ns.

The measured rise and fall times are on the order of magnitude of the predictions made in Chapter 4, however they are slower than what is theoretically possible due to the intrinsic switching mechanism exploited in their design. There are a number of factors that may contribute to this. One possibility is the added parasitic capacitances due to the wire bonds and top-up metal contacts which are not annealed with the device metal contact. Another major point to note is that the measurements were made at relatively low current injections compared to those predicted to be sufficient from the theory in Chapter 2, due to heating issues at the higher current values. At higher currents, the carrier concentration would be much larger, resulting in a larger refractive index change effect which in turn would result in a more pronounced switching effect. Finally, it must be noted that the limits of the test system do not allow rise and fall times shorter than 300 ns to be measured, due to the limitations of the current driver. Nonetheless, the measured switching times, even in the non-ideal conditions measured, show that the intrinsic switch mechanism is suited for the sub-millisecond switching times required for use in an quantum gravimeter, according to the requirements discussed in Chapter 1.



(a)



(b)

Figure 5.32: *Graphs showing the measured (a): rise time of a switch on sequence, and (b): fall time of a switch off sequence, using 904 nm lgiht coupled into a fabricated device from RC101. The measured rise time is 670±5 ns, and the measured fall time is 675± 5 ns respectively.*

5.6 Heating Effects

Throughout Chapter 2, the models used to explain the operation of the optical switches fabricated in this study assumed that the temperature of the device remained constant during operation. However, as we have observed in this chapter, the intended operation of the switch was hampered by excessive heating due to injection of carriers, resulting in regions of high current density. Similar devices reported in the literature have shown similar heating characteristics [146]. These devices were bonded to large copper heat sinks to dissipate the heat generated by current injection, and were only capable of operating in pulsed mode. Further developments [147] lead to devices being able to operate in DC mode, with five times less current injection. This was achieved by diffusing a layer of zinc into the structure to aid with current guiding into the core. It must be noted however, that the intended switching operation of these devices was for a telecomms application, whereby it is sufficient to perform the switch on, switch off action momentarily to produce a pulse of light, as discussed in Chapter 1. The devices designed and fabricated in this study must perform the switch off sequence with high extinction, and hold this state indefinitely. This requires an injection of significant amount of carriers as has been discussed, and therefore the device will have a tendency to heat up more than if they were operated in a pulsed regime. Further to these arguments, to guide the beam into the normally 'ON' state (the straight waveguide), requires a small injection of carriers. When the device is not connected to a power supply, light will not be sufficiently guided within the steering section to be able to be coupled into the straight waveguide. When the power supply is connected and a small current is passed through the device, the carriers are weakly guided, and light is observed at the facet of the straight waveguide. This was shown in the previous section and used to measure the switching speed of the device. Once the device is in this 'normally on' state, carriers are therefore being injected into the device, and some of this energy will be dissipated as heat through inter-valley phonon scattering.

The electroluminescence results have shown high carrier temperatures - observed as significant red shifting the the EL peak with temperature. The injected carriers can have much higher temperature than the lattice, and ultimately, the dissipated energy from these high temperature carriers will heat the bulk material. Whilst the current is applied to the device, the carriers will be out of equilibrium with the lattice, which is often referred to as hot electron effects. Hot electron effects arise from so-called hot-carrier injection whereby an electron or a hole gains sufficient kinetic energy to overcome a potential barrier necessary to break an interface state - in this case the barrier is the width of the band gap of the core material of the device. These hot electrons are described by their effective temperature, T_e, coming from the Fermi-Dirac distribution of a gas of carriers excited by an electric field,

$$f_e = \frac{1}{1 + \exp\left[(\epsilon - \mu_0)/k_B T_e\right]}, \tag{5.11}$$

where μ_0 is the chemical potential. The effective electron temperature can be examined by considering balance between the net power (per unit area), P_e emitted by the electronic system as inter-valley phonons, P_e, and the power (per unit area) given to the electronic system by the electric field, P_f [148]. In the steady state, the electronic system absorbs and emits energy at the same rate, thus $P_e = P_f$.

The magnitude of these heating effects in a given time scale may be estimated by considering the heat capacity of the device, its dimensions and the operating electrical power, as well as considering the thermal conductance of the generated heat away from the device. The heat capacity of GaAs is given as c =0.33 J/g ^{o}C [149]. The dimensions of the steering section of a single device are 750 μm length, 1 mm width and ~630 μm thickness, giving a total volume of 4.725×10^{-4} cm^3. The density of GaAs is 5.32 g/cm^3, giving a mass for a single device of 2.5 mg. The electrical power applied during a switching sequence of 200 mA $\times$ 1.6 V = 0.32 W. Therefore, the temperature increase per second is given by, $\Delta T = E/mc = 0.32/((2.5 \times 10^{-3})(0.33) \approx 388K$. Of course the device does not

continue to heat - the thermal conductance of this heat generation away from the device then occurs through the wire bonded contacts on the top of the device to the wire bonded contacts on the gold-plated copper PCB at ambient temperature. The device will then eventually reach a steady state temperature, at which point the effective carrier temperature will be equal to the lattice temperature. The key point here is that, although the bulk material takes time to heat up, the injected hot carriers will have an effect on the optical properties of the devices in a much shorter timescale (as soon as free carriers reach the core of the double heterostructure) which is what was observed during testing.

The heat generated at the metal contact by the injection of current causes a temperature increase which is then conducted across the surface of the metal and through the semiconductor bulk material. The thermal conductivity of GaAs is given by 0.55 W cm^{-1} K^{-1}. For a slab of GaAs 1 mm thick (approximate device dimensions), for every 1 K rise in temperature, the rate of heat transfer is 0.055 W. Without significant heat sinking, the bulk temperature of the device will rise. It must be noted however that these assumptions assume that the device heats evenly across its volume which is not necessarily the case due to the mesa geometry. This will lead to regions of the device structure with higher current densities than others as has been seen in the previous section, resulting in localised heating. If these localised heated regions are in areas where the beam steering occurs, the strength of the carrier induced effects which lead to beam steering will be further reduced, affecting the function of the device.

Further arguments to this relate to the change in band structure from the generated heat dissipated in the lattice. As the temperature of the lattice increases, the energy of the direct band gap of the core begins to shrink, which works against the Moss-Burstein effect contributing to the beam steering effects. Considering the direct band gap of the core of RC101, GaAs, the temperature dependence of the band gap is given by [150],

$$E_g = 1.522 - \frac{5.8 \times 10^{-4} T^2}{(T + 300)} eV, \tag{5.12}$$

where T is the absolute temperature. An as example the change in band gap energy for a temperature increase of, say, 10 K from room temperature (300 K) is approximately 4 meV, corresponding to a wavelength change of 2.5 nm. This may seem a small quantity but as has been shown in Chapter 2, a small change in the photon energy can lead to a significant change in the magnitude of the refractive index change effects caused by carrier injection.

5.7 Discussion of Results

The characterisation of the fabricated optical switching devices has revealed some interesting behaviour. In some aspects, the optical switches match or better the required design specifications discussed in Chapter 1. Namely, the device I/V characteristics show near ideal diode behaviour and high device yield per die, and waveguide propagation loss measurements revealed that the insertion loss of a packaged device is sufficiently low and would compare well with the relevant literature. However, the intended switching mechanism has proven to be much more sensitive to the device geometry and semi-insulating substrates than was initially predicted. We have observed the switching mechanism through low injection currents, but this is suppressed at the higher current densities due to crowding of carriers at the mesa sidewalls, causing excessive heating. Optimisation of the device geometry, metal contact dimensions and choice of an appropriate n^+-doped substrate are the next recommended step to improve the performance of the devices and match all of the stipulated design requirements discussed at the start of this thesis. A recommended redesign of the 780 nm optical switch will be discussed in more detail in the following chapter.

5.8 Conclusion

In this chapter, the major performance characteristics of the fabricated optical switches have been evaluated. We have shown, through I/V measurements, that the fabricated devices operate electrically as expected and the power requirements for operation are sufficiently low to be incorporated into standard photonics packages and powered by commercially available electronics. The extinction ratio of the fabricated switches at various wavelengths were measured, which was shown to be strongly wavelength dependent as predicted by the theory in Chapter 2. Evidence of beam steering was shown at low operating currents (< 20 mA), however, analysis of the steering section of the devices showed limited beam steering effects at higher currents which was most likely due to localised heating from hot carriers. The effect of the mesa geometry on the carrier distribution in the device was investigated, and it was shown that this had a detrimental effect on the desired manipulation of the carrier distribution from unbalancing the currents through each p-i-n section. These predictions were compared with the simplified case of an optical switch with a 10^{18}cm^{-3} n^{+}-doped substrate with backside n-contact, which was shown to have the desired beam steering effects in the simulations presented in Chapter 2. The electroluminescence and photoluminescence spectra of the devices was also investigated, which revealed some interesting behaviour, namely the observation of high energy phonons which did not correspond to the expected LO and TO phonon energies for the given epitaxial layers. Further investigation is required to determine the exact cause of these high energy phonons. In the next and final chapter, a summary of the project will be given and some suggestions made for improving future iterations of the presented optical switch design. Finally, future prospects for integrated photonics for quantum sensors will be discussed.

Chapter 6

Conclusions and Outlook

6.1 Summary of Work

In this thesis, the requirement for developing underpinning technologies for the next generation of quantum sensors has been discussed. Specifically, this project has focused on the need for a compact, integrated optical switch, which would offer long term stability and reduced bulk manufacturing costs. In Chapter 1, current technologies, used in lab-based quantum sensing experiments, have been evaluated in terms of their suitability for miniaturisation and adaptation into portable, low power, sensing devices. We have argued that some components, such as bulk and free space optical components, will need to be replaced with more compact integrated photonics to transition from lab-based and semi portable units into handheld, low cost commercial products.

As a contribution to this problem, this project has detailed the design, fabrication, and testing of near-infrared semiconductor optical switching devices on semi-insulating gallium arsenide substrates, for use in a quantum gravimeter. These optical switches are intended to replace the use of AOMs and mechanical fibre switches for switching off MOT beams in the experiment, and for controlling the pulses used for the measurement of gravity, during the interferometry sequence. The switch design is a mesa geometry, double heterostructure p-i-n device based on the carrier-induced refractive index change effects, and relies on

the manipulation of the carrier distribution in the core layer to guide and 'steer' a guided beam into one of two output waveguides. This carrier distribution is designed to be controlled by changing the balance of currents through either side of the mesa. In Chapter 2, the relevant theory and operating principles of the device design were discussed, and some models adapted from relevant literature on double heterostructure devices were used to predict the strength of the beam steering effects for the epitaxial structures designed by Dr James Moss [64], at the start of the project. These models were incorporated into a custom FFT-BPM simulation to demonstrate the ideal and intended switching characteristics of the devices, and to quantitatively evaluate some starting points for testing the fabricated devices.

In Chapter 3, details on the fabrication process were presented, which included twenty major processing steps, from substrate to final devices, bonded and mounted to a custom PCB. Devices from the RC101 wafer had already been fabricated by Dr James Moss, so this chapter detailed the fabrication process for the RC184 and RC187 wafers. Devices were fabricated on 15×15 mm^2 die, which included 24 full devices. The fabrication process is directly scalable to a 625 μm thick, 3-inch diameter wafer, and the mask design incorporates 9 die on one wafer, for a total of 216 devices. The process is therefore suitable for most production lines, which typically use 3 or 4-inch diameter wafers.

In Chapter 4, the design and construction of an optical test bench and associated software was presented, including the implementation of a semi-automated alignment procedure for efficient coupling of an optical mode in and out of a DUT. This system consisted of bulk optical components on a stabilised optical bench and facilitated the careful alignment and characterisation of the fabricated devices, to ensure reliability and repeatability of the obtained results. Python programming language was used to develop the software which included a graphical user interface for ease of testing and monitoring of various parameters.

In Chapter 5, the characterisation of devices from all wafers was detailed,

including I/V measurements, evaluation of the switching extinction ratio, propagation loss measurements, photo and electroluminescence spectra, and switching speed. I/V measurements confirmed that the devices performed electrically as expected, and that the power requirements of the devices were suitable for commercial photonics packaging circuitry. The luminescence spectra revealed some interesting results, namely the observation of high energy phonons for RC184 and RC187 wafers which did not match up with the theoretically predicted LO and TO phonon energies. These high energy phonons, we suspect, are associated with deep trap centres in the indirect band-gap cladding layers of the RC184 and RC187 wafers, but further investigation is needed to confirm this. Measurements of the extinction ratio showed strong wavelength dependence, as was predicted by the theory in Chapter 2, and extinction ratios near 20 dB for wavelengths near the band-edges. However, when investigating the beam steering capabilities of the devices, the predicted beam steering capabilities were not observed at high injection currents, indicating that the high extinction ratios measured may have been due to band-edge shifting from local heating of the devices due to the high current densities. Evidence of beam steering at low currents was confirmed however, as the output of the device was seen to significantly increase when a small current was injected into the device. This was used as the basis for testing the intrinsic switching speed of the beam steering mechanism, which was evaluated to be on the sub-microsecond timescale. This confirmed the suitability of the switching mechanism in terms of the switching speed required for the intended application. Finally, spreading of injected carriers was re-investigated due to the geometry of the mesa and subsequent simulations revealed that carriers are confined to the mesa sidewall. This effect reduces the strength of the beam steering since the carrier distribution can no longer be well controlled by unbalancing the currents on either side of the mesa. The carrier spreading length from the edge of the mesa sidewall was calculated to be less than 3% of the mesa width for all epitaxial designs.

In this final chapter, limitations and suggested improvements of the optical switch design will be discussed, along with a brief consideration of possible optoelectronic packaging designs for future iterations. Finally, an outlook on integrated photonics for quantum technologies will be given.

6.2 Design Limitations and Future Work

Results from testing fabricated devices, and subsequent investigation into their mode of operation revealed several possible limitations inhibiting their intended performance. This section explores several approaches to reduce these limitations and improve the performance of the devices to the point where they could be subsequently packaged and incorporated into a quantum gravimeter experiment.

6.2.1 Carrier Spreading

As discussed in the previous chapter, one of the main issues experienced with the fabricated devices was local heating due to high carrier densities. Theoretical investigations into current spreading in double heterostructure, mesa geometry lasers revealed that injected carriers can bunch near the mesa sidewall, due to the resistivity of the confining layers in the heterostructure. In the best case scenario, the injected carriers at the p-contacts should have a straight, direct path to the n-contact to reduce areas of very high current density which can lead to heating. This would entail using a n^+-doped substrate with a backside n-contact. In fact, this configuration was used successfully in previous work with a $10^{18}cm^{-3}$ n^+-doped substrate, exploiting the same carrier-induced refractive index change effects for telecomms switches first at 900 nm [19] and subsequently at 1550 nm [151]. In this project, semi-insulating GaAs substrates were used, since this allows integration of optical and electrical devices on a single chip, which would significantly reduce the SWaP of future quantum sensors. This design however, significantly increases the complexity of the fabrication process due to the re-

quirement of the mesa geometry and separate electrical access to the underlying metal contacts which was achieved using vias in a BCB encapsulation layer. If the devices were to be fabricated on doped substrates, this would significantly reduce the complexity of the fabrication process, however this would increase the complexity of integration of other components on the same wafer. This suggests that perhaps heterogeneous integration may be the preferred approach to take. Simulations carried out here have shown that a doped substrate thickness of 100μm gives the desired carrier profile and similar devices fabricated in the literature have used doped substrate thicknesses of <125μm [146]. This would require the addition of substrate thinning and polishing processes into the fabrication steps before evaporation of the n-type contact metal.

An alternative solution would be to modify the epitaxial design to increase the tendency of the carriers to spread out through the heterostructure. As per Equation 5.10, to maximise the spreading length of the carriers from the edge of the mesa sidewall, the resistivity of the n-type layer should be as low as possible, the p-type layer as high as possible and the thicknesses of the respective layers as large as possible. Since increasing the thickness and resistivity of a layer would subsequently increase the Joule heating of the device, the most appropriate way to approach this would be to increase the doping of the n-type layer as high as the epitaxial growth allows, whilst finding a balance between the other three parameters. Ideally, the current distribution should have a sharp cutoff near the edges of the guided mode, so the current spreading length would need to be significantly larger than in the current situation.

One other way to control carrier spreading is to selectively diffuse zinc into an n-type cladding layer [147]. This is achieved using a n-i-n double heterostructure, and selectively diffusing zinc into the top n-type cladding layer to form a low conductive channel for the carriers to pass through into the core region. Carriers then tend to follow this low resistive path and the spreading effects are reduced. This would require a slight redesign of the epitaxy, but could be incorporated

with the mesa geometry design to maintain the use of a semi-insulating substrate. Figure 6.1 shows a schematic illustration of this proposed design.



Figure 6.1: *Schematic illustration of the p-dopant diffusion in a n-i-n double heterostructure device.*

To perform the Zn in-diffusion or in-diffusion of any other p-dopant atoms, the same photolithography mask which was used to pattern the p-contacts could be used by the following suggested process, based on previous literature [147]. First a layer of silicon nitride (Si_3N_4) is deposited on the sample, and the p-contacts pattern transferred to the sample using the AZ5214E photoresist. A dry or wet etch is then used to remove the Si_3N_4 in the regions where the p-contacts will be later deposited, resulting in windows in the Si_3N_4 layer. The sample is then placed in a quartz tube furnace, in a graphite container with the zinc source, and the furnace heated to around 500^oC in an atmosphere of nitrogen. The time spent at this elevated temperature controls the diffusion depth of the Zn atoms. The Si_3N_4 layer is then entirely removed using a dry etch and the p-contact metals patterned and evaporated as per the standard process. This results in a region of high p-dopant density under the metal contacts, acting as a low resistance channel for injected carriers. An issue with this process is that the diffusion process is challenging to control accurately without in-situ monitoring and furthermore, diffused dopant atoms can diffuse through the semiconductor during other high-temperature processing steps. If the zinc diffuses too far into the structure it may spike into the intrinsic region which would destroy the diode characteristics of the device.

In a similar way to the p-dopant diffusion, carrier spreading in the original

p-i-n structure could be controlled via the formation of an oxide aperture. Oxide apertures are used extensively in the fabrication of vertical cavity surface emitting lasers (VCSELs) to reduce the threshold current and to encourage single-mode operation [152]. In these situations, an $Al_xGa_{(1-x)}As$ layer with a high fractional aluminium content ($x > 0.9$) is grown near the active region. Once the device structure has been formed, the wafer is placed in an oxidation furnace at around 400^oC in an inert atmosphere of nitrogen. Water vapour is then pumped into the chamber and the $Al_xGa_{(1-x)}As$ layers with a high aluminium content begin to oxidise laterally from the edge of the mesa, forming a stable, insulating oxide. The time spent in the wet furnace at the elevated temperature determines the rate of growth of the oxide. Layers with higher aluminium content oxidise at a faster rate. The process is halted when the desired length of oxide has grown and the final result is an oxide aperture buried in the VCSEL structure which helps increase the current density in the active region. This is known as a hydrolisation (or wet) oxidation process [153]. This process could be used in the optical switching devices to reduce carrier spreading and guide injected carriers into the intrinsic region. The oxide layer also has a low refractive index so this, along with the high carrier densities, will ensure guiding of the coupled optical mode. Figure 6.2 shows a schematic illustration of the proposed design, which would require regrowth of the epitaxy to include a thin $Al_{0.95}Ga_{0.05}As$ layer near the active region. Layers with $< 80\%$ aluminium content would oxidise very slowly in this process so their unintended oxidation during this process would not be of concern.

6.2.2 Metal Contacts

A major challenge in the fabrication of the optical switching devices, was forming the top-up metal contact pads to the underlying device contacts. This processing step was required since the device p-contacts could not be bonded to or even probed due to their small dimensions. Therefore, a BCB planarisation and encapsulation layer was used as an intermediary for forming larger top-up contacts on

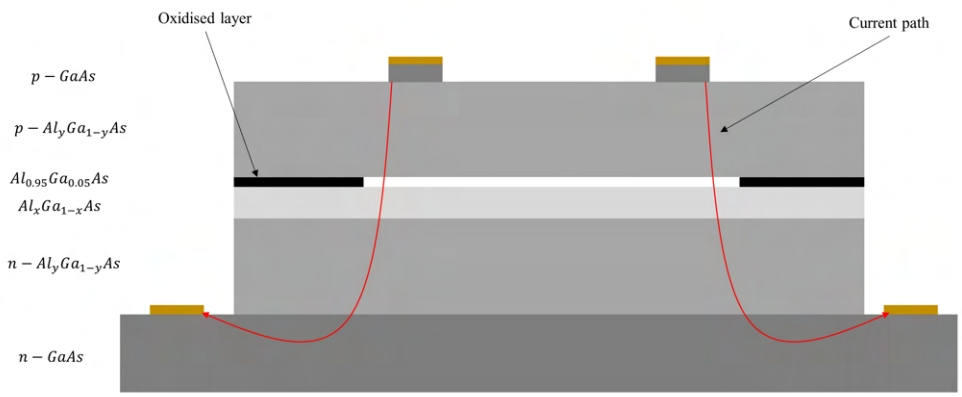


Figure 6.2: *Schematic illustration showing the proposed epitaxial design for inclusion of an oxide aperture to limit carrier spreading effects.*

the same level. However, this process proved to be challenging. After forming the planarisation layer, windows were etched into the BCB to reveal the underlying contacts. The BCB was then ion-milled and a seed layer of Ti sputtered to improve the adhesion of the evaporated gold in the subsequent step. The challenges associated with this process were ensuring the correct etch depth into the BCB, since the contacts were located at different heights; adhesion of the evaporated gold layer to the BCB; clean lift-off of the evaporated metal film; and ensuring good contact between the top-up metal and the underlying contacts into the BCB window. As was shown in Chapter 5, the areas where the top-up metal flowed into the BCB windows acted as weak-points during high current operation, and furthermore the adhesion of the gold to the BCB was not quite strong enough to facilitate a consistent ball-bonding process.

A solution to these difficulties would be a redesign of the photolithography mask defining the p-contacts, to incorporate larger pads. This would negate the need for the BCB process entirely and instead the packaged devices could be passivated with a thinner layer of silicon nitride, for example. Figure 6.3 shows an illustration of a suggested redesign of the p-contact metals. In this case, the

pads are large enough to allow direct ball bonding. If a thin (∼100 nm) silicon nitride passivation layer was to be used, the same mask could be used to form windows into the metal contacts. Ball bonding from the device contacts could then be carried out.

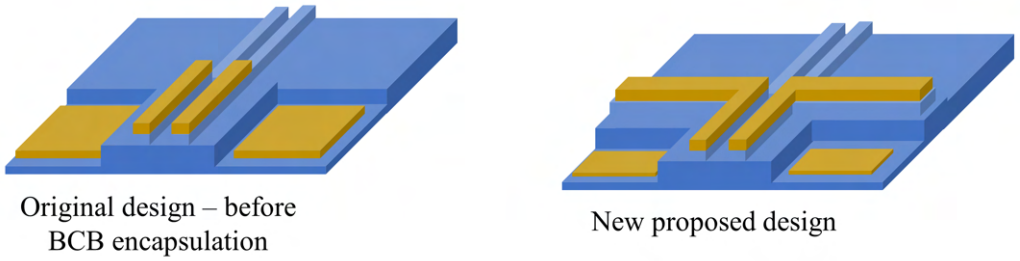


Figure 6.3: *Schematic illustration demonstrating the original and new proposed design for larger p-contacts, which would facilitate direct ball bonding.*

6.2.3 Packaging

Packaging processes for optoelectronic devices forms a large part of their development and is perhaps the most costly process for a manufacturer in the development of new devices. Packaging and assembly processes for optoelectronics can be significantly more complex than for traditional microelectronics, due to the requirements on accurate placement of components which ensure efficient coupling of light in/out of the device. Furthermore, appropriate materials must be selected which ensure dissipation of any generated heat to maintain device performance during operation, and adhesives which hold aligned components in place throughout the lifetime of the device [154]. To enable efficient operation of the fabricated devices in a real quantum sensing experiment, an optoelectronic package would be required which is capable of efficiently coupling light into and out of the device with minimum insertion losses. To aid packaging design, the devices have been fabricated with several optoelectronic packaging standards. Firstly, waveguide tapers have been implemented at the input and outputs of the device. The waveguide taper helps to adjust the mode fields of the semiconductor waveguide to those of the coupling fibre and can increase the coupling efficiency up to

7 dB over standard butt fibre coupling [154]. Secondly, the output waveguides have been separated by a standardised 250 μm, to allow for integration into a optoelectronic packaging assembly line. This reduces the complexity and cost of packaging since a bespoke system would not need to be constructed for packaging of these devices. Finally, the contact electrodes are located at directions perpendicular to the optical propagation axis. This allows the ball bonding process to take place without interfering with the aligned optical components. Figure 6.4 shows a schematic illustration of a proposed inner packaging design, incorporating the aforementioned features. The facets of the chip would need to be coated in an anti-reflection coating the reduce Fresnel reflections and a microlens incorporated between the fibre and facet to facilitate precise alignment of the optical modes of the fibre with the integrated waveguides. This inner package would then be hermetically sealed in an outer packaging which would feature standard SMA fibre connectors and insulated ribbon cable for electrical interfacing. Future iterations could also incorporate the relevant driving electronics and thus would only require a power supply and control signal input.

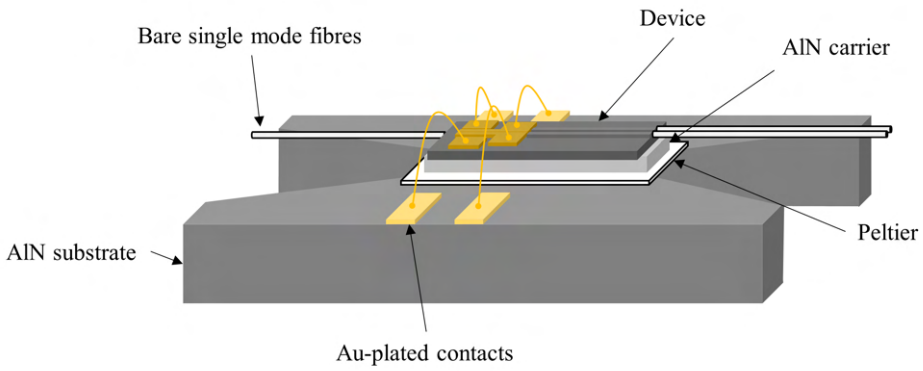


Figure 6.4: *Schematic illustration of a proposed inner packaging design for the fabricated optical switches. AlN: aluminium nitride*

6.2.4 780 nm Switch Redesign

Following the findings from the characterisation and investigation of the results from testing the fabricated devices in Chapter 5, simulations have been carried out to redesign the RC184 wafer which was intended for optical switches operating at 780 nm. Table 6.1 summarises the main epitaxial layers for this wafer redesign.

Wafer ID	**Layer**	**Thickness (μm)**	**Doping Conc. (cm^{-3})**
NewEpi	n^+-GaAs	100	1.0×10^{18}
	n-GaAs	1.00	2.0×10^{18}
	n-$Al_{0.55}Ga_{0.45}As$	**1.00**	$\mathbf{2.0 \times 10^{18}}$
	$Al_{0.15}Ga_{0.85}As$	**0.33**	-
	p-$Al_{0.55}Ga_{0.45}As$	**1.00**	$\mathbf{2.0 \times 10^{18}}$
	p-GaAs	1.00	2.5×10^{18}

Table 6.1: Layer compositions for the new proposed epitaxial design, for optical switching devices at 780 nm. The p-i-n region is highlighted in bold.

Firstly, the thickness of the core and cladding layers have been optimised to ensure mode matching of the effective index of the slab mode in the steering section to the effective index of the strip-loaded waveguides in the wave-guiding section. Figure 6.5 shows the results of the simulation carried out to perform this mode matching. From this we can see that the effective index of the steering section can be very sensitive to the core thickness in some configurations. Therefore, a core thickness has been selected which results in an effective index which is close to that of the strip-loaded waveguides, but which is away from these regions where the structure may experience mode-hopping. In this scenario, the mode matching becomes less sensitive to the uncertainties associated with the MBE-grown core thickness.

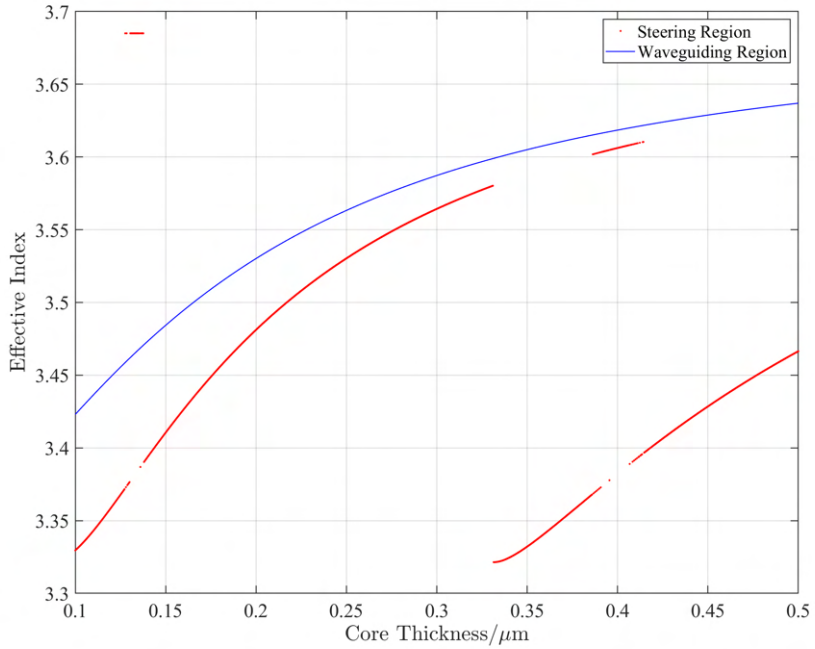


Figure 6.5: *Simulation of the effective indices of the slab of the steering region and the strip-loaded waveguides of the waveguiding section, as a function of the core thickness for an optical wavelength of 780 nm and parameters shown in Table 6.1*

The second major change is the use of a 100 μm thick n^+-doped substrate to ensure that the carrier distribution in the core layer can be well controlled by changing the current through each p-i-n channel. The intention here is to begin with a 300 μm wafer and then thin the backside of the wafer by a lapping process before depositing the n-contact metals. Figure 6.6 shows a simulation of the carrier distribution under the metal contacts for this configuration, due to a current injection of 100 mA through each contact.

Finally, the aluminium concentrations have been changed so that the operating wavelength is closer to the nominal bandgap of the core, which will increase the strength of the carrier-induced refractive index change effects. This will ensure less electrical current is needed to steer the beam into the desired output channel. Figure 6.7 shows the results of the simulation carried out to calculate the strength of the refractive index change effects for the proposed new epitaxy at 780 nm. This shows that the new design changes Δn twice as much for the same carrier concentration.

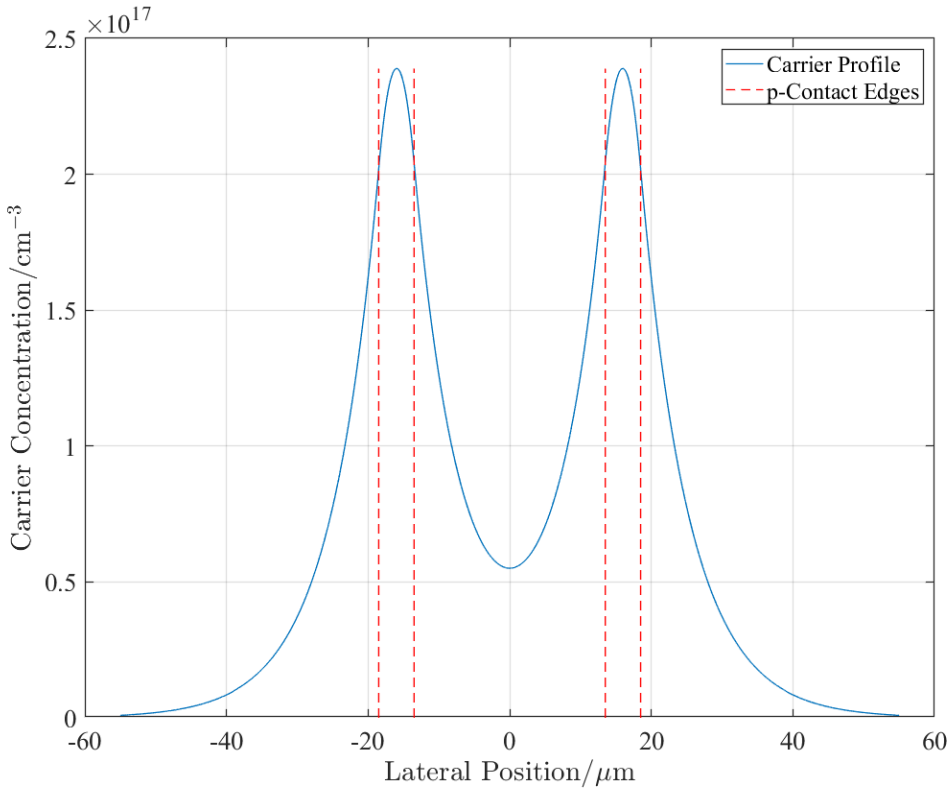


Figure 6.6: *Simulation of the concentration of carriers in the core region of the new epitaxial design, as a function of the lateral distance across the layer, for a current injection of 100 mA through each contact.*

6.3 Recent Developments & Future Trends

Over the past decade, there has been significant development in the field of integrated optics for quantum sensing applications. In an effort to reduce the SWaP of future quantum sensors, researchers have focused on the optimisation of optoelectronics in wavelength ranges suitable for cold atom quantum sensing. In particular, much attention has been given to the development of narrow linewidth lasers. Stable, high power, narrow linewidth, and tunable laser sources are crucial for a wide range of applications, in particular for the development of quantum technologies based on cold atoms with transitions at specific optical frequencies [155], as was discussed in Chapter 1. A key step forward in the development of photonic integrated circuits for quantum technologies will be the integration of passive and active components on a heterogeneous platform, compatible with the high yield and tolerances of current silicon foundry tool-sets, which have been

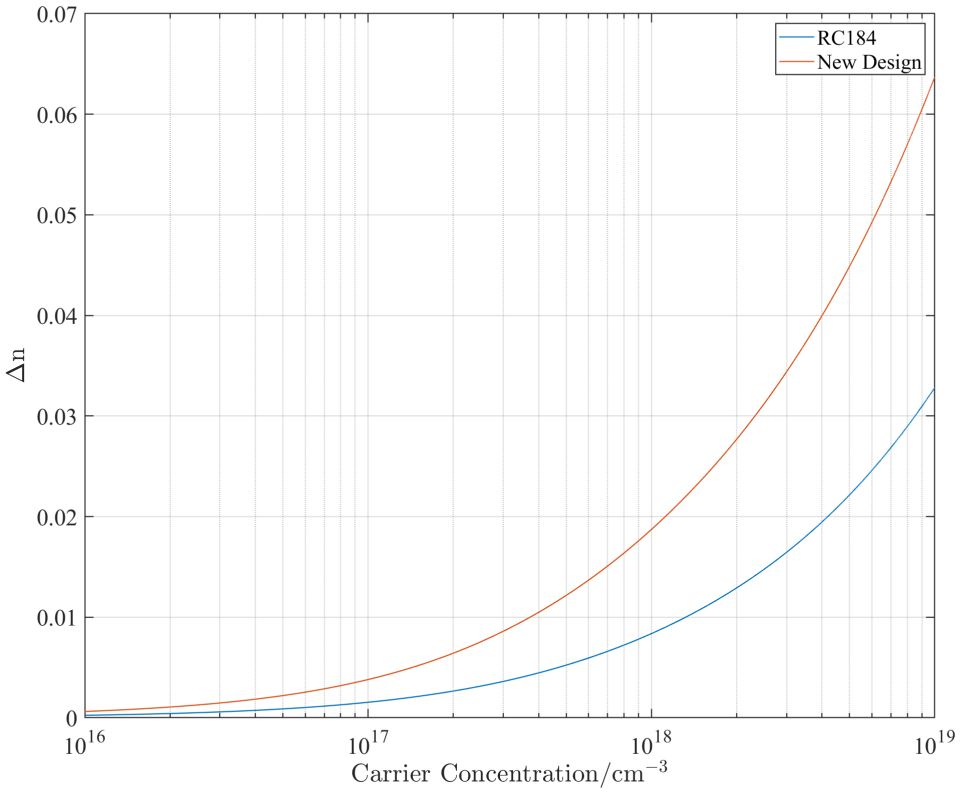


Figure 6.7: *Simulation of the change in refractive index as a function of carrier concentration for the new epitaxial design at 780 nm, and a comparison with the original RC184 design.*

operating seamlessly for decades on end [156]. For example, the ideal scenario is one where the base platform consists of a multi-layer dielectric which is capable of forming the passive components of the PIC such as low loss waveguides and resonators, whilst the active components may then be finely placed onto these structures using optical couplers [157] and bonded in place. Such a platform would facilitate the full realisation of high density, high performance fully integrated PICs for quantum processing, sensing and communication applications.

6.3.1 Silicon Nitride Technologies

In recent years, silicon nitride (SiN) has gained serious attention due to its CMOS compatibility and flexible optical properties [158]. SiN has a wide optical band-gap that can be varied from 2.7 to 5.0 eV by increasing the N/Si ratio of the material, thus enabling tunability of its optical properties (band gap and re-

fractive index) during fabrication to fulfil specific requirements of the intended application. Furthermore, SiN has a lower thermal conductivity than silicon and a negligible two photon absorption at the communications wavelength of 1550 nm. SiN integrated circuits can thus be designed to operate efficiently from the low end of the visible spectrum all the way to mid infrared. Key to this development is the reliable and efficient growth of thick films of SiN on SiO_2 which can be prone to cracking due to internal stresses.

Relevant to this work, there has been promising research into various passive photonic components in SiN, such as the demonstration of SiN microring resonators for use at 780.24 nm with propagation losses of $\sim$0.2 dB/cm [159]. These micro resonators have potential applications as references for laser frequency stabilisation, facilitating chip-scale atomic systems. The demonstrated microrings require a temperature stability of $\pm$15 mK for laser frequency locking applications. This represents a major step forward in developing bespoke photonic systems for quantum sensing wavelengths, by adapting technologies from more mature telecommunications applications.

6.3.2 Final Remarks

Looking ahead, the promising performance and continued development of the aforementioned photonic components for future quantum sensing applications will eventually lead to the goal of a photonic integrated circuit or platform, capable of implementing multiple different photonic components on a single chip. This will significantly reduce optical propagation losses and other current challenges faced by integrating standalone photonic components into a system comprising of other bulk optical sub-systems. The work carried out in this project thus makes a small step forward towards this goal and adds to the growing list of bespoke photonic components available at this moment in time, aiming to drive forward the miniaturisation of quantum sensors and subsequent accessibility of their many exciting applications.

Appendix A

Device Fabrication Process Flow

This appendix contains a step-by-step guide for fabrication of the optical switching devices designed in this project. This guide details the specific processing steps and conditions carried out in the cleanrooms of The University of Nottingham to fabricate the optical switching devices from a three-inch semi-insulating GaAs wafer, grown using molecular beam epitaxy (MBE) by Dr Richard Campion.

A.1 Wafer Dicing

A.1.1 Standard Solvent Clean

The first step is to cleave out a die from the 3-inch wafer so that a 15 mm^2 cell from the photolithography masks can be patterned. Before cleaving, the wafer must be cleaned of any organic residue using a standard solvent clean. Place the wafer in a beaker of acetone, ensuring the whole wafer is submerged. Cover the beaker with a watch glass and place on an orbital stirrer for ten minutes at 140 rpm to gently agitate the solvent. After ten minutes has elapsed, carefully remove the wafer from the beaker using appropriate tweezers, rinse with methanol and place in another beaker of methanol. Repeat the agitation process for another ten minutes. Once again, remove the wafer from the beaker, rinse with methanol

and place in a beaker of isopropyl alcohol (IPA). Repeat the agitation process for another ten minutes. Finally, remove the wafer from the beaker of IPA, rinse thoroughly with IPA and blow dry using a nitrogen gun. Place the wafer on a preheated hotplate at 120^{o}C for ten minutes to evaporate off any remaining solvents. This process defines the standard solvent clean and will be referred to as such from this point onwards.

A.1.2 Tape & Wafer Mounting

The wafer must now be prepared for cleaving by mounting onto a tape ring. This is achieved using the Loadpoint Presspoint Tape Ring Applicator. Take a pair of tape rings and place the larger ring on the base of the Presspoint with the smooth edge pointing upwards and the smaller ring on the upper disk with the hard edge pointing down. Pull the tape over the bottom ring so it is smooth and lower the upper arm. Lock the arm and pull down the handle with some force several times to ensure the two rings lock together with the tape in between. Unlock and raise the arm. The rings should now be securely fixed together. If not, repeat the process. The excess tape can now be carefully trimmed using a scalpel and the tape ring removed.

The next step is to mount the wafer onto the tape in the correct place so that all areas of the wafer can be accessed by the movement of the JFP Microtechnic S100 motorised stages. Switch on the S100 and open the software. Select the program 'JamesMay2019' and select 'unload wafer'. The motorised stage will move outwards and the tape ring can then be loaded. Secure the tape ring and, using a marker pen, mark where the edge of the cleaving blade is on the tape. Remove the tape ring and place the major flat of the 3 inch wafer approximately 1 cm from the marked line. Rub the backside of the tape to ensure the tape is in good contact with the wafer. Re-load the tape ring onto the S100 and select 'Return's wafer' [sic].

A.1.3 Scribing & Breaking

Die must now be cleaved from the parent wafer with minimal wastage. To achieve this, a die-per-wafer (DPW) estimate can be calculated to workout the best method of cleaving. The DPW can be estimated using the following equation,

$$DPW = d\pi \left(\frac{d}{4S} - \frac{1}{\sqrt{2S}} \right), \tag{A.1}$$

where d is the wafer diameter and S is the die area. Since the die size needs to be at least 15 mm × 15 mm, there should be a small buffer around the edge to allow for die handling. Therefore, a die size of 16.5 mm × 18 mm (W×H), which works out as $S = 297$ mm^2, is chosen. The three-inch wafer has a standard diameter of 76 mm, however a 3 mm exclusion zone is used on the outer edge since devices fabricated at the edge of the wafer may be defective. Using these values, DPW = 4.68, so approximately 5 full die per 3-in wafer is expected. Figure shows how the 3-inch wafer is to be cleaved.

Before making the first scribe, the angle of the wafer must be manipulated to ensure it aligns with the on-screen crosshair. To do this, align the horizontal crosshair with the major flat of the wafer and use the joystick to move the stage in the horizontal direction across the major flat. If the horizontal crosshair moves away from the major flat during this movement, the angle of the wafer must be adjusted. Coarse movements can be achieved by simple rotating the tape ring and finer rotations by using the manual micrometer drive on the stage.

Once the wafer has been straightened, to make the first scribe, use the joystick to manipulate the stage and the measurement tool on the JFP software to move the desired horizontal distance from the edge of the wafer. Once the on-screen crosshair is located in the correct position horizontally, move the centre of the crosshair to the bottom of the wafer. Select ‘scribe’ mode and ‘auto’ using the buttons on the front panel of the JFP. The scribe length should already be set to 1 mm in the program. If not, it can be changed using the panel on the right hand side of the screen. Press the enter button on the front panel to begin the scribe.

Once the scribe is complete, move the centre of the crosshair to the bottom edge of the scribe line. Use the front panel buttons to select 'break', and press enter to begin the break. A blade should emerge from below the stage and an arm pressed against the top of the wafer. An audible click should be heard when the wafer breaks. If not, inspect and repeat the break process. If a break is not possible, re-run the scribe with a longer scribe length.

Remove the wafer ring from the JFP by first pressing 'unload wafer' and removing the tape ring. Carefully separate the cleaved sections of wafer using tweezers and by stretching the tape from below. Remove the wafer from the tape ring and rinse the cleaved edges of the wafer using deionised water, and dry using the nitrogen gun. Repeat this entire process for the other cleave lines until the desire die size has been achieved. Perform a standard solvent clean on the resulting die.

A.2 p-Type Contacts

A.2.1 Patterning

To pattern the p-type contacts, first preheat a hotplate to 110^{o}C and another to 120^{o}C. Place the cleaned die onto an appropriate vacuum chuck on the Laurell WS650 spin coater. Clamp down using the vacuum enable button. Using a pipette, dispense a sufficient quantity of AZ5214E photoresist onto the top of the die. This should be enough to flood coat the die. Close the lid of the spin coater and ensure there are no bubbles present in the dispensed resist before proceeding. Select the AZ5214 process on the spin coater and press start. The die will be spun for 30 seconds at 4000 rpm, resulting in a film thickness of $\sim$1.5 μm . Once the process is complete, open the lid of the spin coater and wait 3 minutes. Cure the resist film by placing the die on the 110^{o}C hotplate for 90 seconds. Allow the die to cool for 5 minutes before proceeding to the next step.

Switch on the Süss MA/BA6 Gen 3 mask aligner and wait for system to initialise. Load program 'JLM_IMAGE_EXP' and note down required mask and

chuck holders. Ensure correct mask holder is loaded and change if necessary. Place the p-type contacts mask, chrome side up, on the mask holder and clamp using the vacuum. Return the mask holder to the aligner and clamp. The microscope assembly will move down after an audible warning tone. Use the joystick to manipulate the microscope head and focus on one of the edges of the centre die of the mask. Slide out the substrate chuck and load the coated die into the machine. Press 'next' on the software to bring the chuck up towards the mask. Switch the joystick control to the substrate chuck and manipulate until the whole centre pattern of the mask fits within the area of the die. Alignment is not crucial in this step but try to ensure the mask pattern is straightened with respect to the die. Once alignment is complete, expose the die using 'OLD20/20/20' light source for a dose of 22 mJ/cm^2, as defined by the recipe. Wait three minutes before proceeding to the next step to allow any nitrogen produced by UV exposure of the photoresist to out-gas.

Place the exposed die on the 120^{o}C hotplate for 2 minutes for the post-exposure bake. Allow the die to cool for 3 minutes. Return the die to the mask aligner and select recipe 'JLM_FLOOD_EXP', for the flood exposure. This step does not require a mask, nor alignment. Perform the flood exposure as defined by the recipe: '20/0/0' light source for a 250 mJ/cm^2 dose. Wait 5 minutes after this before proceeding to the next step. This defines the standard flood exposure step.

Prepare a beaker of concentrated AZ726 MIF developer and a separate beaker of deionised water. Immerse the exposed die into the developer and agitate for 45 seconds. Immediately place int he deionised water bath and agitate for 30 seconds. Thoroughly rinse with deionised water and blow dry with nitrogen. This defines the process for patterning the p-type contacts.

A.2.2 Thermal Evaporation

The next step is to deposit the p-type contact metals onto the patterned sample. Start by cleaning the gold and zinc metals in a beaker of IPA, placed in an

ultrasonic bath for 5 minutes. Blow dry the metals and load into the appropriate boats of the Edwards Auto 206 Thermal evaporator. Prepare a beaker of diluted hydrochloric acid (HCl) (1 part HCl to 1 part water by volume), and agitate the patterned samples for 30 seconds to remove any surface oxides. Load the sample into the thermal evaporator, close the chamber and pump down the vacuum. Add liquid nitrogen to the cold trap to increase the pump down rate. Wait until the vacuum level has reached 10^{-7} mbar before proceeding.

Rotate the carousel so that the gold boat is in contact with the electrode. Switch on the current source and slowly increase the current until the film thickness monitor shows a significant deposition rate. Check the log book for recommended deposition rates and currents. Continue deposition until the film thickness monitor reads 5 nm, then slowly decrease the current and switch off the current source. Repeat this process for the zinc boat, to deposit a film of 20 nm, and finally return to the gold boat for a thickness of 200 nm. Allow the chamber to cool for 30 minutes, then release the vacuum and unload the coated sample.

A.2.3 Metal Lift-off

To remove the unwanted metal film and isolate the p-contact metal areas, a lift-off process is carried out. Prepare a beaker of dimethylsulfoxide (DMSO), cover with a watch glass and heat on a hotplate to 80^{o}C. Place the coated sample in the DMSO and leave for around 45 minutes to an hour or until the metal film is almost completely removed, occasionally agitating. Remove the die from the hot DMSO and thoroughly rinse with fresh DMSO. Place in another beaker of room temperature DMSO. Place on the orbital stirrer and agitate for 15 minutes. Remove the sample from the DMSO and again thoroughly rinse with DMSO until all the unwanted metal film is removed. Immediately place in a beaker of IPA and agitate on the orbital stirrer for 10 minutes. Rinse with IPA and finally blow dry with nitrogen. This defines the standard metal lift-off process. It is important that the sample is not dried until the end of this process, else liberated metal film

can be redeposited and adhered onto the surface in unwanted areas.

A.2.4 Metal Anneal

The final step in defining the p-type contacts is to anneal the deposited meals into an alloy with the semiconductor. Switch on the Annealsys AS-One Rapid Thermal Annealer and the nitrogen gas supply. Unlock the chamber and remove the lid of the susceptor. Place the sample face down onto the graphite susceptor plate and cover with the lid. Close the chamber and lock the door using the software. Load recipe 'BSM_420_30s'. Run the anneal program, allow the chamber to cool and finally remove the sample from the chamber. If there is any baked on photoresist remaining after this step then it can be removed using a gentle oxygen plasma process, using the plasma asher. At this point, the specific contact resistivity ρ_c can be evaluated, using the CTLM method detailed in Chapter 3. A value of $\sim 10^{-6}\ \Omega cm^2$ is expected for this recipe.

A.3 p-GaAs Etch

In this step, the top p-GaAs layer is removed using a dry etch recipe. No patterning is needed in this step, as the p-type metal contacts can be used as a hard mask to protect the p-GaAs layer below. This step electrically isolates the p-contacts. Only a small amount, $\sim$ 10 nm of the metal will be etched during this process.

Load the sample into the Corial 200IL RIE/ICP dry etcher and tile the sample around the perimeter with blank GaAs pieces which have been coated with a small amount of Y-VAC grease on the backside. This prevents the sample from moving around during the etch. First clean any organic residues using an O_2 plasma etch if this was not done in the previous step. Load the recipe 'GaAs_Etch' and run the process. The end point detection signal should oscillate as the p-GaAs layer is thinned and eventually removed. The etch will self-terminate when the

p-AlGaAs layer is reached and the EPD signal will stop oscillating. End the etch process when this is observed and unload the sample from the etcher.

A.4 Waveguide Etch

A.4.1 Waveguide Patterning

Give the sample a standard solvent clean before loading into the spin coater. Preheat a hotplate to 115^{o}C. Dispense an appropriate quantity of AZ5214E photoresist onto the sample - enough to flood coat the surface. Run the AZ5214 process on the spin coater which will spin the sample at 4000 rpm for 30 seconds, resulting in a film thickness of $\sim$ 1.55 μm. Open the lid of the spin coater and leave the sample to rest for 3 mins. Remove the sample and place on the hotplate for 50 seconds. Remove the sample from the hotplate and allow to rest for 3 minutes to cooldown.

Prepare a beaker with a small amount of acetone. Re-load the cured sample onto the spin coater. Soak the tip of a cotton swab with the acetone and carefully brush along each edge of the sample to remove the edge bead. This defines the standard edge bead removal process.

Switch on the mask aligner and load the program 'JLM_WGUIDES' noting the required mask holder and substrate chuck. Load the waveguides photo mask into the ask aligner and, as before, locate one of the edges of the central die of the mask. Load the substrate into the mask aligner and carefully align the mask to the first pattern on the die. Start with the edges of the pattern, then use the alignment marks to ensure precise alignment in all axes. Expose the die using the 15/15/15 light source, for a dose of 10 mJ/cm^2 as per the recipe. Allow the die to rest for three minutes before proceeding to the next step.

Unload the die from the mask aligner and place on the preheated hotplate at 115^{o}C for 3 minutes. Remove from the hotplate and allow to cool for 5 minutes.

Re-load the sample into the mask aligner and, as before, perform the standard

flood exposure.

Prepare a beaker of concentrated AZ726 MIF developer and a separate beaker of deionised water. Place the sample carefully into the developer and agitate for 22 seconds. Immediately place the die into the deionised water and agitate for 30 seconds. Rinse thoroughly with deionsed water and blow dry with nitrogen. This process defines the waveguide patterning recipe.

A.4.2 Etching

This etching step removes a portion of the top p-AlGaAs cladding to form the strip-loaded waveguides. Load the sample into the Corial etcher and tile with blank GaAs pieces, stuck down with Y-VAC grease. Load recipe 'CJM-BCL3_RIE_NOV_2018' and run the etching process. The required etch depth here will depend on the design wavelength of the single-mode waveguides. Refer to Chapter 3 for more details on how to determine the required etch depth. Use the simulated EPD signal to determine when the required etch depth has been achieved by observing the EPD signal from the etcher. Remove the sample from the etcher and use the stylus profiler to determine the etch depth. Reload into the etcher and repeat if a deeper etch is required. Once the waveguide etch is complete, use an oxygen plasma to remove the photoresist and perform a standard solvent clean to complete the process.

A.5 n-GaAs Reveal Etch

A.5.1 Patterning

Follow the procedure detailed in step A.4.1, but using the n-GaAs etch photolithography mask, to form the pattern for the n-GaAs reveal etch. Again, ensure the mask pattern is carefully aligned in all axes to the previous pattern by initially using the corners of the die and then using the alignment marks on each side.

A.5.2 Etching

This etching step removes the epitaxial layers above the n-GaAs layer to form the mesa and allow access to the n-GaAs layer for the n-type contacts in the next step. Before the etch, dip the sample in a diluted solution of HCl for 1 nminute (1 part HCl to 1 part deionised water) to remove any redeposited metal which may be present on the surface from previous steps, as this can cause micromasking. Load the sample into the Corial 200IL etcher and select process 'CJM_BCL3_RIE_NOV_2018'. The etch depth required depends on the epitaxy. The etch depths required are 2050 nm, 2490 nm, and 2300 nm for RC107, RC184 and RC101 respectively. The etch time is around 45-55 minutes.

Unload the sample from the etcher and used the stylus profiler to check the etch depth. If the required etch depth has been achieved, reload the sample into the etcher and use an oxygen plasma to strip off the photoresist. Perform a standard solvent clean to complete this processing step.

A.6 n-Type Contacts

A.6.1 Patterning

Follow the procedure detailed in step A.2.1, but using the n-type contacts photolithography mask, to apply the pattern onto the die for the n-type contacts. Again, ensure careful alignment of the pattern to the previous one.

A.6.2 Thermal Evaporation

The next step is to deposit the n-type contact metals onto the patterned sample. Start by cleaning the gold, nickel and germanium metals in a beaker of IPA, placed in an ultrasonic bath for 5 minutes. Blow dry the metals and load into the appropriate boats of the Edwards 306 Turbo evaporator. Prepare a beaker of diluted hydrochloric acid (HCl) (1 part HCl to 1 part water by volume), and

agitate the patterned samples for 30 seconds to remove any surface oxides. Load the sample into the thermal evaporator, close the chamber and pump down the vacuum. Add liquid nitrogen to the cold trap to increase the pump down rate. Wait until the vacuum level has reached 10^{-7} mbar before proceeding.

Rotate the carousel so that the gold boat is in contact with the electrode. Switch on the current source and slowly increase the current until the film thickness monitor shows a significant deposition rate. Check the log book for recommended deposition rates and currents. Continue deposition until the film thickness monitor reads 5 nm, then slowly decrease the current and switch off the current source. Repeat this process for the germanium boat, to deposit a film of 5 nm, followed by the gold boat for a film of 20 nm, then the nickel boat for a film of 15 nm and finally return to the gold boat for a thickness of 200 nm. Allow the chamber to cool for 30 minutes, then release the vacuum and unload the coated sample.

A.6.3 Metal Lift-off

Perform the standard metal lift-off process at detailed in step A.2.3 to isolate the n-type metal contacts.

A.6.4 Metal Anneal

Switch on the Annealsys AS-One Rapid Thermal Annealer and the nitrogen gas supply. Unlock the chamber and remove the lid of the susceptor. Place the sample face down onto the graphite susceptor plate and cover with the lid. Close the chamber and lock the door using the software. Load recipe 'JAS_380C_30sDWELL'. Run the anneal program, allow the chamber to cool and finally remove the sample from the chamber. If there is any baked on photoresist remaining after this step then it can be removed using a gentle oxygen plasma process, using the plasma asher.

A.7 BCB Encapsulation

A.7.1 Si_3N_4 Deposition

Before coating the sample with BCB, an intermediate layer of silicon nitride needs to be introduced to improve adhesion. Load sample into the Corial D250 PECVD and tile with quartz cover-slips around the perimeter to ensure the sample does not move around during chamber evacuation. Pump down the chamber and deposit a ∼50 nm thick layer of Si_3N_4 at 280^{o}C using a timed deposition. The deposition time will depend on the deposition rate. Check the log book for details. A blank GaAs sample can be used to check the deposition rate by loading into the chamber as described above and running the deposition process for a fixed time. The thickness of the Si_3N_4 layer can then be confirmed using the J.A. Woollam M-2000 Ellipsometer.

A.7.2 Adhesion Promoter

A layer of adhesion promoter is required to further improve the adhesion of the cured BCB layer to the semiconductor. Place the sample in a beaker of deionised water and agitate on the orbital stirrer for 5 minutes. Remove from the beaker and blow dry with nitrogen. Preheat a hotplate to 120^{o}C.

Load sample onto an appropriate chuck on the Laurell spin coater and clamp down by activating the vacuum. Using a pipette, dispense 12 drops of AP3000 adhesion promoter onto the sample and leave to rest for 30 seconds. Select program 6 on the spin coater which will spread the AP3000 at 3000 rpm for 20 seconds. Allow to rest for 30 seconds once the program has finished. Place the sample on the 120^{o}C hotplate for 1 minute to cure. Remove from the hotplate and allow to rest for 1 minute.

A.7.3 BCB Coating

Re-load sample back into the spin coater and clamp down with the vacuum. Using a pipette, dispense 20 drops of Cyclotene 3022-46 (BCB) onto the sample, radially from the outer edge inward. Allow to rest for 30 seconds. Select program 7 on the spin coater with will bread the BCB at 3000 rpm for 60 seconds, resulting in a film thickness of $\sim$3 μm. Allow to rest for 30 seconds before unloading sample. Place on the 120^{o}C hotplate to cure for 1 minute. Remove from the hotplate and allow to rest for 1 minute.

To hard cure the BCB, the sample must be slowly heated in a plane-levelled hot plate in an atmosphere of nitrogen. Open the hot plate door using the lever arms and place a spirit level in the centre to check the base is levelled. If the hot plate is not levelled, alter the four individual height adjustable feet. Place the sample carefully in the centre of the hot plate and close the lid. Turn on the nitrogen valve and adjust the flow rate to 85 sccm. Switch on the hot plate. The temperature will ramp to 100^{o}C at a rate of 10^{o}C/min, and remain at 100^{o}C for 30 minutes. The temperature will then ramp to 250^{o}C at a rate of 10^{o}C/min and remain at this temperature for 1 hour. The temperature will then cool down to 22^{o}C over the course of 2 hours. Once the process is complete, turn off the nitrogen and remove the sample from the hot plate.

A.8 BCB Etching

A.8.1 Patterning: Part 1

Windows now need to be etched into the cured BCB to access the underlying metal contact pads. Follow the procedure in step A.2.1, but using the top-up pads mask, to pattern the top-up pads onto the BCB-coated sample.

A.8.2 Etch 1

Since the underlying contacts exist at differing heights under the BCB, the windows into the BCB must be formed using two separate etches. This first etch opens up the window into the p-type contacts.

Due to the high power of the ICP etch, the sample must be mounted onto a carrier silicon wafer to dissipate heat. Place the carrier wafer on a hotplate at 65^{o}C. Melt a small amount of CRIE BLOC wax onto the centre of the carrier wafer and place the sample on top. Remove the carrier wafer from the hotplate and allow to cool.

Mount the silicon wafer to the graphite chuck of the Corial 200IL dry etcher using YVAC grease. Load recipe 'CJM_BCB_PR'. This recipe etches the BCB at approximately 200 nm/min. Run the etch to remove at least 1 μm of BCB. This should clear the BCB into the p-type contact windows, and remove 1/3 of the BCB into the n-type contact windows.

Remove the carrier wafer form the etcher and place back onto the hotplate to melt the wax and remove the sample from the carrier wafer. Carefully clean the backside of the sample using an acetone-soaked cotton bud. Perform a standard solvent clean on the sample to remove the remaining AZ5214E photoresist. The presence of BCB into the p-type contact window can be checked using AFM and SEM EDX, as described in Chapter 3.

A.8.3 Patterning: Part 2

Follow the same patterning procedure in step A.2.1, but using the second top-up pads mask, to pattern the n-type top-up pad window into the BCB-coated sample. This will cover the previously etched p-type contact window in the BCB with AZ5214E resist, but leave the window into the n-type contact open so that the etch can be completed.

A.8.4 Etch 2

Follow the same procedure as detailed in step A.8.2 to complete the etch into the n-type contact under the BCB. Run the etch to remove at least 2 μm of BCB. Perform a standard solvent clean on the sample to remove the remaining AZ5214E photoresist. This completes the BCB window etching step.

A.9 Top-up Metal Contacts

A.9.1 Ion Milling & Ti Sputter

Before depositing the top-up gold pads onto the sample, the BCB surface must first be ion milled and a seed layer of titanium sputtered into the roughened surface, to improve the adhesion of the final gold film.

Tape sample to ion miller holder using copper tape at two opposing corners. Load sample into the Mantis Deposition dual ion milling and sputter system. Mill sample under a vacuum of 0.5 mTorr for 3 minutes 20 seconds at 300V and an ion flux of 41 mA. Sputter 10 nm of titanium onto the roughened surface, using a forward current of 100 μA and a pressure of 5 mTorr. Set power to 28.6W and an argon flow rate of 25 sccm. This completes the ion milling and Ti sputter process.

A.9.2 Patterning

Follow the same patterning procedure in step A.2.1, but using first top-up pads mask, to pattern the top-up pads onto the sample.

A.9.3 Thermal Evaporation

Start by cleaning the zinc metal and a sufficient quantity of gold in a beaker of IPA, placed in an ultrasonic bath for 5 minutes. This process requires a 500 nm film of gold. Blow dry the metals and load into the appropriate boats of

the Edwards Auto 306 thermal evaporator. Load the sample into the thermal evaporator, close the chamber and pump down the vacuum. Add liquid nitrogen to the cold trap to increase the pump down rate. Wait until the vacuum level has reached 10^{-7} mbar before proceeding.

Rotate the carousel slowly so that the gold boat is in contact with the electrode. Switch on the current source and slowly increase the boat begins to glow. Keep the shutter closed as this step is solely to melt the large quantity of gold into the boat so it does not fall out during rotation of the carousel. Slowly ramp down the current and switch off the source. Rotate the carousel to the titanium position and switch on the current source. Slowly increase the current to an appropriate level, until the film thickness monitor shows a deposition rate. Check the log book for recommended deposition rates and currents. Continue until 20 nm of titanium has been deposited. Repeat this process for the gold metal, for a film thickness of 500 nm. This process should take approximately one hour. Leave the chamber to cool for 30 minutes before pumping down and unloading the sample. This completes the deposition of the top-up metal pads.

A.9.4 Lift-off

Perform the standard metal lift-off process at detailed in step A.2.3 to isolate the top-up metal pads. This process may cause the BCB to swell which appears as bubble formation under the BCB layer when viewed under a microscope. To rectify this, place the sample on a hot plate at 200^{o}C for 5 minutes after the lift-off process has been completed. Allow to cool for 5minutes before proceeding.

A.9.5 Isolation Etch

The final step is to electrically isolate the top-up metal pads by removing the titanium seed layer in regions in between the metal pads. To do this, load the sample into the Corial 200IL dry etcher and select recipe 'A_Ge_RIE_Fixed'. Run the etch for approximately 30 seconds to blanket etch the sample and remove the

∼10 nm of Ti. This completes the entire top-up metal contacts processing step. Devices are now complete on-die and I/V characterisation can be carried out to ensure the devices function as expected before cleaving.

A.10 Dicing & PCB Mounting

A.10.1 Preparation

To prepare the die for dicing, follow the procedure outlined in step A.1.2 to mount the die to a tape ring. In this case, since the sample is small, extra tension is required on the tape. To achieve this, set the sample die aside and mount the tape ring back onto the upper arm of the Loadpoint PressPoint by pressing the inner ring into the mounting points. The tape should now be facing down towards the lower plate.

Place another large ring on the bottom plate with the smooth edge facing upwards towards the ring. Pull down the upper arm using the lever which should slide the new ring onto the mounted tape ring and push the original one off. This will tighten the tape. Follow the steps outlined in A.1.2 to mount the die back onto the now more taught tape ring, in the correct position ready for scribing.

A.10.2 Dicing

The sequence of cleaving in this step is very important to be able to isolate single devices. This is because it is much more challenging to achieve a clean break, and subsequently smooth optical facets, for smaller samples than for larger ones. The mask layout is designed such that devices are arranged in bars. Each bar contains four devices. These instructions are for separating a single device from one bar, cleaved from a die.

The first step is to remove the waveguide test features from the die. Rotate the die on the tape so that the waveguides run vertically from the perspective of the camera on the JFP Microtechnic scriber. Load recipe ‘JamesMay2019’ and

change the scribe length to 500 μm. Follow the procedure in step A.1.2 to align the die with the cross-hairs so that the vertical line is perfectly level with the edge of the die. Move the centre of the crosshair to the start of the waveguide test features on the die and perform the scribe. Check the scribe line, realign the crosshairs to the starting edge of the scribe line and perform the break. Unload the tape ring and carefully remove the cleaved section, leaving the die with only the devices remaining.

Re-load the tape ring into the JFP Microtechnic and rotate the die so that the device bars now run vertically from the perspective of the camera. Straighten the die in all axes as before and then align the centre of the crosshairs in between the first two bars of devices. Move the stage vertically up the die to check that the scribe and break line will not pass through a device. Realign the crosshairs to the original point and perform the scribe and break as before. Unload the tape ring from the scriber and isolate the cleaved bar carefully, ensuring the facets do not rub together. Dust all facets with the nitrogen gun and re-load the separated bar of four devices horizontally onto the tape ring.

The next step is to open the first facet of the first device by breaking off the edge of the bar. To do this, re-load the tape ring into the scriber and align the bar in all axes. The long edge of the bar should be placed on the right-hand side of the break arm. This will make the break easier to perform. Change the scribe length to 100 μm to ensure the scribe does not run through a device. Align the edge of the first device on the left had side of the bar using the vertical crosshair. Move the centre of the crosshair to the bottom edge of the bar to perform the scribe. Double check the scribe direction before proceeding. Move the bar to the top of the field of view of the camera on the scriber before performing the break sequence. This is to ensure the break arm makes contact with the top of the bar. If the sample does not break easily, as the break blade raises from the stage bed, a light upwards force can be applied to the end of the break bar so that more pressure is exerted on the top of the sample, pushing it into the break blade. If

the sample still does not break, re-run the scribing procedure. Once the break has been successfully performed, unload the tape ring and very carefully separate the end piece of the bar. Re-load the bar into the scriber to make the final break which will separate the first device from the bar. TO make this break, follow the same procedure outlined above, aligning to the starting edge of the first device. When separating the diced device from the bar, handle with fine tipped tweezers only from the sides of the device, taking extra care not to touch the facets under any circumstances. This completes the dicing procedure.

A.10.3 PCB Mounting

Before mounting the device to the PCB, the PCB must be gold-plated and a sufficient length of enamelled copper wire soldered to the ends of the PCB wings. The final thickness of the gold plating should be approximately 2 μm to aid adhesion of the gold ball bonds in the final step.

The device should be mounted to the centre of the PCB using EPO-TEK H20E silver epoxy. Preheat a hot plate to 150^{o}C. Mix a small amount of parts A and B of the epoxy in a container. Using the end of a cocktail stick, dot a very small quantity of the mixed epoxy onto the centre of the PCB. This quantity must be small enough so that it does not seep from under the device onto the facets or other edges which would cause a short-circuit of the epitaxial layers. Using fine tipped tweezers, carefully place the device onto the epoxy on the PCB, ensuring the epoxy contacts the bottom of the device. If any epoxy seeps onto the device edges, immediately wipe clean with an acetone-soaked Q-tip. However, this step should be avoided if at all possible as this can damage the device facets. Place the PCB onto the hotplate, ensuring the bottom of the PCB makes contact with the hotplate. Leave to cure for 1 hour. Remove PCB from the hotplate and leave to cool down for 30 minutes. This completes the PCB mounting procedure.

A.11 Wire Bonding

A.11.1 Ball & Wedge Bonding

The final step in the fabrication process is to make electrical connection between the gold PCB tracks and the device contacts. This is achieved using a TPT HB10 Wire Bonder. To prepare the bonder, switch on using the rocker switch at the back of the machine. Set the stage temperature to 80^{o}C and allow to heat up for 15 minutes. Whilst the stage is heating, the gold wire can be prepared for bonding. Unclamp the wire using the settings in the 'Bond' menu and rotate the clamp arm to move away from the wire. Change the capillary if required and ensure it is secured using 27 cNm of torque, using the torque driver. Carefully feed a small length of wire through the capillary and trim a few millimetres below the tip of the capillary using fine-tipped scissors. If the the wire does not feed through the capillary it may be blocked and needs to be cleaned by soaking in a concentrated solution of potassium iodide for 5 hours. When feeding the wire through the capillary, use fine tipped tweezers and ensure that no kinks form in the wire. If this happens, trim the wire above the kink and start again.

Once the wire has been fed through the capillary, move the clamp arm back into position and clamp the wire. Next, manually move the flame-off wand in and out of the working area to check the height. Adjust the height using the screw if needed. Mount the PCB onto the work holder stage and ensure it is clamped securely using the spring-actuated lever. Form a ball on the end of the wire by activating the flame-off. Select 'Ball & Wedge' as the bond type in the bond menu.

Move the work holder into position under the bonder. Set the height parameters by using the 'auto setup' function in the menu. Using the puck, move the work holder into position so that the PCB track sits directly under the capillary. Use the laser spot for alignment. Press the bond button on the puck to set the first height. Move the work holder again using the puck so that the laser spot is on

the device contact. Press the bond button to set the second height. The bonder is now configured for the bonding process.

The bonding process relies on finding the appropriate conditions and parameters for a consistent bond. During trials, consistent ball bonds were formed to the PCB but wedge bonding to the device was more challenging. The parameters given here resulted in the most consistent bonds but these may need to be adjusted according to the sample and conditions at the time of the bonding process. Enter the bonding menu and set the following parameters: Bond 1: Power = 450 mW, Time = 200 ms, Force = 290 mN; Bond 2: Power = 300 mW, Time = 320 ms, Force: 350 mN. Loop height = 1000 μm, Up CO = 470 μm.

Move the work holder to the first bond position on the PCB track. Press and hold the bond button, the capillary will move down to a set height above the bonding position. If the positioning at this point is not correct, use the puck to move the work holder so that the capillary hovers above the desired bonding position (all the time holding down the bond button). Release the bond button to make the first ball bond. Use the puck to slowly drag the wire and capillary over to the second bond position - above the device contact. Repeat the same process to make the second bond which will be a wedge bond. When the bond button is released at this point, the capillary will move up and the flame off wand will trim the wire and form a ball for the next bond. Repeat this process to make bonds to all four contacts on the device. This completes the ball bonding process. If any bonds fail, follow the procedure outlined in the next step.

A.11.2 Bond Reworking

If any bonds made in the previous step should fail, they may be re-worked using the EPO-TEK H20E silver epoxy by the following process. Mount the PCB onto the probe station and use the microscope to locate the failed bond. Mix equal parts of A and B of the epoxy in a separate container and allow to partially set for an hour. This will make the epoxy more viscous and easier to manipulate in

the next step. Transfer a small amount of the mixed epoxy to a piece of electrical tape, placed in the vicinity of the PCB on the probe station stage. Mount a probe needle onto a micropositioner and wet the end of the probe by moving it into the epoxy on the tape. Position the wetted probe over the location of the failed bond, and use the micropositioner to lightly wet the surface where the bond has failed, as well as the end of the detached wire. Using a clean probe needle and a separate micropositioner, press the wire onto the wetted surface of the contact pad. The surface tension and viscosity of the epoxy should temporarily hold the wire to the contact pad surface. This is a delicate process and may take several attempts to succeed. Once the wire is in sufficient contact with the surface, carefully transfer the PCB onto a hotplate at 150^{o}C and leave the epoxy to set for an hour. Once cured, leave to cool for 30 minutes and check electrical continuity of the bond using the probe station and multi-meter. This completes the bond rework process and the prototype devices are now complete and ready for optical characterisation.

Bibliography

[1] Louis de Broglie. "Research on the theory of quanta". *Annales de Physique*. Vol. **10**. (3). 1925, pp. 22–128.

[2] A. Hinton et al. "A portable magneto-optical trap with prospects for atom interferometry in civil engineering". *Philosophical Transactions of the Royal Society A: Mathematical, Physical and Engineering Sciences* **375**.(2099) (2017), p. 20160238.

[3] V. Ménoret et al. "Gravity measurements below 10^{-9} g with a transportable absolute quantum gravimeter". *Scientific Reports* **8**.(1) (2018), pp. 1–11.

[4] L. Zhou et al. "Test of equivalence principle at 10^{-8} level by a dual-species double-diffraction Raman atom interferometer". *Physical Review Letters* **115**.(1) (2015), p. 013004.

[5] A. Wicht et al. "A preliminary measurement of the fine structure constant based on atom interferometry". *Physica Scripta* **2002**.(T102) (2002), p. 82.

[6] G. Rosi et al. "Precision measurement of the Newtonian gravitational constant using cold atoms". *Nature* **510**.(7506) (2014), pp. 518–521.

[7] J. M. Hogan and M. A. Kasevich. "Atom-interferometric gravitational-wave detection using heterodyne laser links". *Physical Review A* **94**.(3) (2016), p. 033632.

[8] M. Hauth et al. "First gravity measurements using the mobile atom interferometer GAIN". *Applied Physics B* **113**.(1) (2013), pp. 49–55.

[9] K. Bongs et al. "isense: A technology platform for cold atom based quantum technologies". *Quantum Information and Measurement*. Optical Society of America. 2014, QTu3B–1.

[10] J. I. Malcolm. "Construction of a portable platform for cold atom interferometry". PhD thesis. University of Birmingham, 2016.

[11] J. Bouman et al. "Antarctic outlet glacier mass change resolved at basin scale from satellite gravity gradiometry". *Geophysical Research Letters* **41**.(16) (2014), pp. 5919–5926.

[12] I. Marson and J. E. Faller. "g - The acceleration of gravity: Its measurement and its importance". *Journal of Physics E: Scientific Instruments* **19**.(1) (1986), p. 22.

[13] R. Karcher et al. "Improving the accuracy of atom interferometers with ultracold sources". *New Journal of Physics* **20**.(11) (2018), p. 113041.

[14] A. Louchet-Chauvet et al. "The influence of transverse motion within an atomic gravimeter". *New Journal of Physics* **13**.(6) (2011), p. 065025.

[15] R. Soref. "Tutorial: Integrated-photonic switching structures". *APL Photonics* **3**.(2) (2018), p. 021101.

[16] K. Shimomura and S. Arai. "Semiconductor waveguide optical switches and modulators". *Fiber & Integrated Optics* **13**.(1) (1994), pp. 65–100.

[17] R. Hunsperger. *Integrated Optics: Theory and Technology*. 6th ed. Springer-Verlag New York, 2009. ISBN: 978-0-387-89774-5.

[18] S. Ravindran et al. "GaAs based long-wavelength microring resonator optical switches utilising bias assisted carrier-injection induced refractive index change". *Optics Express* **20**.(14) (2012), pp. 15610–15627.

[19] P. Dong X.and LiKamWa, J. Loehr, and R. Kaspi. "Current-induced guiding and beam steering in active semiconductor planar waveguide". *IEEE Photonics Technology Letters* **11**.(7) (1999), pp. 809–811.

[20] C. J. Foot et al. *Atomic physics*. Vol. **7**. Oxford University Press, 2005.

[21] Zhou Lin et al. "Measurement of local gravity via a cold atom interferometer". *Chinese Physics Letters* **28**.(1) (2011), p. 013701.

[22] A. L. Migdall et al. "First observation of magnetically trapped neutral atoms". *Physical Review Letters* **54**.(24) (1985), p. 2596.

[23] AM Steane, M Chowdhury, and CJ Foot. "Radiation force in the magneto-optical trap". *JOSA B* **9**.(12((1992), pp. 2142–2158.

[24] J. Ye et al. "Hyperfine structure and absolute frequency of the ^{87}Rb $5P_{3/2}$ state". *Optics Letters* **21**.(16) (1996), pp. 1280–1282.

[25] S. Bize et al. "High-accuracy measurement of the ^{87}Rb ground-state hyperfine splitting in an atomic fountain". *EPL (Europhysics Letters)* **45**.(5) (1999), p. 558.

[26] Aidan Arnold. "Preparation and Manipulation of a ^{87}Rb Bose-Einstein Condensate". PhD thesis. University of Sussex, 1999.

[27] S. Chu et al. "Three-dimensional viscous confinement and cooling of atoms by resonance radiation pressure". *Physical Review Letters* **55**.(1) (1985), p. 48.

[28] A. L. Migdall et al. "First observation of magnetically trapped neutral atoms". *Physical Review Letters* **54**.(24) (1985), p. 2596.

[29] M. Kasevich and S. Chu. "Measurement of the gravitational acceleration of an atom with a light-pulse atom interferometer". *Applied Physics B* **54**.(5) (1992), pp. 321–332.

[30] A. D. Ferguson et al. "Low-loss, single-mode GaAs/AlGaAs waveguides with large core thickness". *IEE Proceedings-Optoelectronics* **153**.(2) (2006), pp. 51–56.

[31] *Rise Time, Frequency Response, and 3 dB Bandwidth*. Tech. rep. Thorlabs, Apr. 2009.

[32] Yang Yang et al. "Crosstalk reduction of integrated optical waveguides with nonuniform subwavelength silicon strips". *Scientific Reports* **10**.(1) (2020), pp. 1–8.

[33] D. Pinnow. "Guidelines for the selection of acoustooptic materials". *IEEE Journal of Quantum Electronics* **6**.(4) (1970), pp. 223–238.

[34] J. M. Hammer. "Modulation and switching of light in dielectric waveguides". *Integrated Optics*. Springer, 1975, pp. 139–200.

[35] L. Kuhn et al. "Deflection of an optical guided wave by a surface acoustic wave". *Applied Physics Letters* **17**.(6) (1970), pp. 265–267.

[36] D. A. Wille and M. C. Hamilton. "Acousto-optic deflection in Ta_2O_5 waveguides". *Applied Physics Letters* **24**.(4) (1974), pp. 159–160.

[37] Y. Ohmachi. "Acousto-optical light diffraction in thin films". *Journal of Applied Physics* **44**.(9) (1973), pp. 3928–3933.

[38] N. Chubachi, J. Kushibiki, and Y. Kikuchi. "Monolithically integrated Bragg deflector for an optical guided wave made of zinc-oxide film". *Electronics Letters* **9**.(10) (1973), pp. 193–194.

[39] J. Kerr. "A new relation between electricity and light: Dielectrified media birefringence". *The London, Edinburgh, and Dublin Philosophical Magazine and Journal of Science* **50**.(333) (1875), pp. 446–458.

[40] C. L. Manganelli, P. Pintus, and C. Bonati. "Modeling of strain-induced Pockels effect in Silicon". *Optics express* **23**.(22) (2015), pp. 28649–28666.

[41] A. Yariv. *Quantum electronics*. 3rd ed. New York: New York : Wiley, 1989. ISBN: 0471609978.

[42] S. Akiyama et al. "Low-chirp 10 Gbit/s InP-based Mach-Zehnder modulator driven by 1.2 V single electrical signal". *Electronics Letters* **41**.(1) (2005), pp. 40–41.

[43] K. Tsuzuki et al. "40 Gbit/s nin InP Mach-Zehnder modulator with a/spl pi/voltage of 2.2 V". *Electronics Letters* **39**.(20) (2003), pp. 1464–1466.

[44] L. V. Keldysh. "The effect of a strong electric field on the optical properties of insulating crystals". *Sov. Phys. JETP* **7**.(5) (1958), pp. 788–790.

[45] David AB Miller et al. "Band-edge electroabsorption in quantum well structures: The quantum-confined Stark effect". *Physical Review Letters* **53**.(22) (1984), p. 2173.

[46] F. K. Reinhart. "Electroabsorption in $Al_yGa_{1-y}As/Al_xGa_{1-x}As$ double heterostructures". *Applied Physics Letters* **22**.(8) (1973), pp. 372–374.

[47] H. Soda et al. "High-speed and low-chirp GaInAsP/InP optical intensity modulator". *Integrated and Guided Wave Optics* (1988), p. 28.

[48] Daniel May-Arrioja. "Integrated InP Photonic Switches". PhD thesis. University of Central Florida, 2006.

[49] M. Harjanne et al. "Sub-μs switching time in silicon-on-insulator Mach-Zehnder thermooptic switch". *IEEE Photonics Technology Letters* **16**.(9) (2004), pp. 2039–2041.

[50] D. A May-Arrioja and P. LiKamWa. "Integrated electro-optic Mach-Zehnder switch realized by Zinc in-diffusion". *5th Iberoamerican Meeting on Optics and 8th Latin American Meeting on Optics, Lasers, and Their Applications*. Vol. **5622**. International Society for Optics and Photonics. 2004, pp. 833–837.

[51] R. A. Becker. "Comparison of guided-wave interferometric modulators fabricated on $LiNbO_3$ via Ti indiffusion and proton exchange". *Applied Physics Letters* **43**.(2) (1983), pp. 131–133.

[52] S. Cao, L. Sun, and M. Savoie. "2× 2 MMI-MZI GaAs-GaAlAs carrier-injection optical switch". *IEEE Photonics Society Summer Topicals 2010*. IEEE. 2010, pp. 207–208.

[53] Rabeya Khatun et al. "Optimization of 2× 2 MZI electro-optic switch and its application as logic gate". *2015 18th International Conference on Computer and Information Technology (ICCIT)*. IEEE. 2015, pp. 294–299.

[54] EAJ Marcatili. "Bends in optical dielectric guides". *Bell System Technical Journal* **48**.(7) (1969), pp. 2103–2132.

[55] Vien Van. *Optical microring resonators: theory, techniques, and applications*. CRC Press, 2016.

[56] Ali Shahidinejad, Iraj Sadegh Amiri, and Toni Anwar. "Enhancement of indoor wavelength division multiplexing-based optical wireless communication using microring resonator". *Reviews in Theoretical Science* **2**.(3) (2014), pp. 201–210.

[57] V Van et al. "Optical signal processing using nonlinear semiconductor microring resonators". *IEEE Journal of Selected Topics in Quantum Electronics* **8**.(3) (2002), pp. 705–713.

[58] Bipin Bhola and William H Steier. "A novel optical microring resonator accelerometer". *IEEE Sensors Journal* **7**.(12) (2007), pp. 1759–1766.

[59] Ioannis Chremmos, Otto Schwelb, and Nikolaos Uzunoglu. *Photonic microresonator research and applications*. Vol. **156**. Springer, 2010.

[60] Kishore Padmaraju and Keren Bergman. "Resolving the thermal challenges for silicon microring resonator devices". *Nanophotonics* **3**.(4-5) (2014), pp. 269–281.

[61] Xiaohua Ma and Geng-Sheng Kuo. "Optical switching technology comparison: optical MEMS vs. other technologies". *IEEE communications Magazine* **41**.(11) (2003), S16–S23.

[62] Rubab Amin, Jacob B Khurgin, and Volker J Sorger. "Waveguide-based electro-absorption modulator performance: comparative analysis". *Optics express* **26**.(12) (2018), pp. 15445–15470.

[63] Shih-Jung Chang et al. "A compact and low power consumption optical switch based on microrings". *IEEE Photonics Technology Letters* **20**.(12) (2008), pp. 1021–1023.

[64] James L. Moss. "Beam Steering Optical Switches in AlGaAs via the Burstein-Moss Effect". PhD thesis. University of Nottingham, 2020. Chap. 4.

[65] R de L Kronig. "On the theory of dispersion of x-rays". *Josa* 12.6 (1926), pp. 547–557.

[66] K. Ishida et al. "InGaAsP/InP optical switches using carrier induced refractive index change". *Applied Physics Letters* **50**.(3) (1987), pp. 141–142.

[67] X. Dong et al. "Current-induced guiding and beam steering in active semiconductor planar waveguide". *IEEE Photonics Technology Letters* **11**.(7) (1999), pp. 809–811.

[68] D. A. May-Arrioja and P. LiKamWa. "An Integrated 1x3 InP Photonic Switch". *LEOS 2006-19th Annual Meeting of the IEEE Lasers and Electro-Optics Society*. IEEE. 2006, pp. 532–533.

[69] E. Burstein. "Anomalous optical absorption limit in InSb". *Physical Review* **93**.(3) (1954), p. 632.

[70] T. S. Moss. *Semiconductor opto-electronics*. London: New York: Wiley, 1973. ISBN: 0408703261.

[71] B. R. Bennett, R. A. Soref, and J. A. Del Alamo. "Carrier-induced change in refractive index of InP, GaAs and InGaAsP". *IEEE Journal of Quantum Electronics* **26**.(1) (1990), pp. 113–22.

[72] K. A. Whittaker et al. "Hilbert transform: Applications to atomic spectra". *Physical Review A* **91**.(3) (2015), p. 032513.

[73] J. D. Dow and D. Redfield. "Toward a unified theory of Urbach's rule and exponential absorption edges". *Physical Review B* **5**.(2) (1972), pp. 594–610.

[74] P. A. Wolff. "Theory of the band structure of very degenerate semiconductors". *Physical Review* **126**.(2) (1962), p. 405.

[75] K. F. Berggren and B. E. Sernelius. "Band-gap narrowing in heavily doped many-valley semiconductors". *Physical Review B* **24**.(4) (1981), p. 1971.

[76] C. H. Henry, R. A. Logan, and K. A. Bertness. "Spectral dependence of the change in refractive index due to carrier injection in GaAs lasers". *Journal of Applied Physics* **52**.(7) (1981), pp. 4457–4461.

[77] HC Casey Jr, DD Sell, and KW Wecht. "Concentration dependence of the absorption coefficient for n- and p- type GaAs between 1.3 and 1.6 eV". *Journal of Applied Physics* **46**.(1) (1975), pp. 250–257.

[78] Sadao Adachi. *GaAs and related materials: bulk semiconducting and superlattice properties*. World Scientific, 1994.

[79] David Wells Winston. "Physical simulation of optoelectronic semiconductor devices." PhD thesis. University of Colorado, 1997.

[80] A. R. Goodwin et al. "Threshold temperature characteristics of double heterostructure $Ga_{(1-x)}Al_xAs$ lasers". *Journal of Applied Physics* **46**.(7) (1975), pp. 3126–3131.

[81] C. M. Wu and E. S. Yang. "Physical mechanisms of carrier leakage in DH injection lasers". *Journal of Applied Physics* **49**.(6) (1978), pp. 3114–3117.

[82] N. G. Nilsson. "Empirical approximations for the Fermi energy in a semiconductor with parabolic bands". *Applied Physics Letters* **33**.(7) (1978), pp. 653–654.

[83] C. B. Su and R. Olshansky. "Carrier lifetime measurement for determination of recombination rates and doping levels of III-V semiconductor light sources". *Applied Physics Letters* **41**.(9) (1982), pp. 833–835.

[84] Y. A. Goldberg. "Aluminium Gallium Arsenide". *Handbook Series On Semiconductor Parameters, Vol. 2: Ternary And Quaternary III-V Compounds* **43**.(F43m) (1996), p. 26.

[85] Peter W Epperlein. *Semiconductor laser engineering, reliability and diagnostics: a practical approach to high power and single mode devices*. John Wiley & Sons, 2013.

[86] D. L. Rode. "How much Al in the AlGaAs/GaAs laser?" *Journal of Applied Physics* **45**.(9) (1974), pp. 3887–3891.

[87] H Page et al. "Carrier Leakage Effects in GaAsP/AlGaAs Single-Quantum-Well Lasers Determined by Hydrostatic Pressure Measurements". *Solid State Physics B* **211**.(1) (1999), pp. 533–538.

[88] B. W. Hakki. "Carrier and gain spatial profiles in GaAs stripe geometry lasers". *Journal of Applied Physics* **44**.(11) (1973), pp. 5021–5028.

[89] AD Ferguson et al. "Low-loss, single-mode GaAs/AlGaAs waveguides with large core thickness". *IEEE Proceedings Optoelectronics.* **153**.2 ((2006)), pp. 51–6.

[90] V Ramaswamy. "Strip-loaded film waveguide". *The Bell System Technical Journal* **53**.(4) (1974), pp. 697–704.

[91] Hirosuke Furuta, Hideki Noda, and Akira Ihaya. "Novel optical waveguide for integrated optics". *Applied optics* **13**.(2) (1974), pp. 322–326.

[92] Hiroaki Takeuchi and Kunishige Oe. "Low-loss single-mode GaAs/AlGaAs miniature optical waveguides with straight and bending structures". *Journal of lightwave technology* **7**.(7) (1989), pp. 1044–1054.

[93] Simon M Sze, Yiming Li, and Kwok K Ng. *Physics of semiconductor devices*. John Wiley & Sons, 2021.

[94] MD Feit and JA Fleck. "Light propagation in graded-index optical fibers". *Applied Optics* 17.24 (1978), pp. 3990–3998.

[95] Dietrich Marcuse. *Theory of dielectric optical waveguides*. Elsevier, 2013.

[96] *AZ5214E Technical Datasheet*. Merck Performance Materials GmbH.

[97] D. K. Schroder. *Semiconductor material and device characterization*. John Wiley & Sons, 2015.

[98] Tatsuyuki Sanada and Osamu Wada. "Ohmic contacts to p-GaAs with Au/Zn/Au structure". *Japanese Journal of Applied Physics* **19**.(8) (1980), pp. L491–L494.

[99] A. G. Baca and C. I. H. Ashby. *Fabrication of GaAs devices*. (6). Institute of Engineering and Technology, 2005.

[100] J. H. Klootwijk and C. E. Timmering. "Merits and limitations of circular TLM structures for contact resistance determination for novel III-V HBTs". *Proceedings of the 2004 International Conference on Microelectronic Test Structures (IEEE Cat. No. 04CH37516)*. IEEE. 2004, pp. 247–252.

[101] MCJCM Kramer. "Fabrication and characterization of metal-semiconductor contacts for application in AlGaN/GaN HEMTs". PhD thesis. 2000.

[102] Tatsuyuki Sanada and Osamu Wada. "Ohmic contacts to p-GaAs with Au/Zn/Au structure". *Japanese Journal of Applied Physics* **19**.(8) (1980), p. L491.

[103] Kazuo Nojiri. *Dry etching technology for semiconductors*. Springer, 2015.

[104] Dale E Ibbotson, Daniel L Flamm, and Vincent M Donnelly. "Crystallographic etching of GaAs with bromine and chlorine plasmas". *Journal of Applied Physics* **54**.(10) (1983), pp. 5974–5981.

[105] YZ Juang et al. "Comparing reactive ion etching of III–V compounds in $Cl_2/BCl_3/Ar$ and $CCl_2F_2/BCl_3/Ar$ discharges". *Journal of Vacuum Science & Technology A: Vacuum, Surfaces, and Films* **12**.(1) (1994), pp. 75–82.

[106] S Salimian and CB Cooper III. "Selective dry etching of GaAs over AlGaAs in $SF_6/SiCl_4$ mixtures". *Journal of Vacuum Science & Technology B: Microelectronics Processing and Phenomena* **6**.(6) (1988), pp. 1641–1644.

[107] P. B. Vigneron et al. "Advanced and reliable GaAs/AlGaAs ICP-DRIE etching for optoelectronic, microelectronic and microsystem applications". *Microelectronic Engineering* **202** (2018), pp. 42–50.

[108] X. Sun et al. "Selective wet etching of $Al_{0.7}Ga_{0.3}As$ layer in concentrated HCl solution for peeling off GaAs microtips". *Solid-state Electronics* **53**.(9) (2009), pp. 1032–1035.

[109] R. Tummala, E. J. Rymaszewski, and A. G. Klopfenstein. *Microelectronics Packaging Handbook: Subsystem Packaging*. Springer Science & Business Media, 1997.

[110] *Processing Procedures for BCB Adhesion*. Dow Chemical Company. 2007.

[111] *Rework Procedures for CYCLOTENE 3000 Series and 4000 Series Resins*. Dow Chemical Company. 2005.

[112] George G. Harman. "Reliability and yield problems of wire bonding in microelectronics: The application of materials and interface Science, International Society for Hybrid Microelectronics (ISHM) Monograph" (1989).

[113] Yu Hin Chan et al. "Comparative performance of gold wire bonding on rigid and flexible substrates". *Journal of Materials Science: Materials in Electronics* **17**.(8) (2006), pp. 597–606.

[114] Han Zongjie et al. "High reliable wire bonding consistency control in MMCM". *2017 18th International Conference on Electronic Packaging Technology (ICEPT)*. IEEE. 2017, pp. 1520–1524.

[115] C Marsan-Loyer and T Dequivre. "Effective Method for Wire Bonds Rework Using Conductive Epoxy". *IEEE Transactions on Components, Packaging and Manufacturing Technology* **9**.(3) (2018), pp. 557–561.

[116] Tien Pei Lee. "Effect of Junction Capacitance on the Rise Time of LEDs and on the Turn-on Delay of Injection Lasers". *Bell System Technical Journal* **54**.(1) (1975), pp. 53–68.

[117] *Measuring Extinction Ratio of Optical Transmitters: Application Note 1550-8*. Agilent Technologies. 2001.

[118] Mark Shaw, Robert Galeotti, and Giacomo Coppo. "Method of fixing an optical fibre in a laser package". *2001 Proceedings. 51st Electronic Components and Technology Conference (Cat. No. 01CH37220)*. IEEE. 2001, pp. 1441–1446.

[119] *Pupil Diameter and Beam Spot Diameter of Objective Lens*. Olympus. 2021. URL: https://www.olympus-ims.com/en/microscope/terms/luminous_flux/.

[120] Katsunari Okamoto. *Fundamentals of optical waveguides*. Academic Press, 2006.

[121] August Köhler. "New method of illumination for photomicrographical purposes". *Journal of the Royal Microscopical Society* **14** (1894), pp. 261–262.

[122] Gerhard Kloos. "Applications of lock-in amplifiers in optics". SPIE. 2018.

[123] *PyQt5*. Riverbank Computing Limited, The Qt Company. 2021. URL: https://pypi.org/project/PyQt5/.

[124] Martin Fitzpatrick. *QtWidgets*. MIT. 2021. URL: https://pypi.org/project/qtwidgets/.

[125] Cristian Constantin Lalescu. "Two hierarchies of spline interpolations. Practical algorithms for multivariate higher order splines". *arXiv preprint arXiv:0905.3564* (2009).

[126] B. Corbett and W. M. Kelly. "Surface recombination in dry etched AlGaAs/GaAs double heterostructure p-i-n mesa diodes". *Applied Physics Letters* **62**.(1) (1993), pp. 87–89.

[127] V. K. Dixit et al. "Effect of high dose γ-ray irradiation on GaAs pin photodetectors". *Nuclear Instruments and Methods in Physics Research Section A: Accelerators, Spectrometers, Detectors and Associated Equipment* **785** (2015), pp. 93–98.

[128] Ivan Pelant and Jan Valenta. *Luminescence spectroscopy of semiconductors*. Oxford University Press, 2012.

[129] M Wojtowicz et al. "Photoluminescence characterization of MBE grown AlGaAs/InGaAs/GaAs pseudomorphic HEMTs". *Journal of Crystal Growth* **175** (1997), pp. 930–934.

[130] Sidney Perkowitz. *Optical characterization of semiconductors: infrared, Raman, and photoluminescence spectroscopy*. Elsevier, 2012.

[131] AWR Leitch and HL Ehlers. "The characterization of GaAs AND AlGaAs by photoluminescence". *Infrared Physics* 28.6 (1988), pp. 433–440.

[132] DC Reynolds et al. "Phonon replicas in the photoluminescence emission of Al x Ga1- x As alloys". *Applied Physics Letters* **66**.(25) (1995), pp. 3447–3449.

[133] Do G Thomas, M Gershenzon, and FA Trumbore. "Pair Spectra and" Edge" Emission in Gallium Phosphide". *Physical Review* **133**.(1A) (1964), A269.

[134] Sadao Adachi. "GaAs, AlAs, and $Al_xGa_{(1-x)}As$: Material parameters for use in research and device applications". *Journal of Applied Physics* **58**.(3) (1985), R1–R29.

[135] K Takarabe et al. "Plausible evidence of existence of deep acceptors in Si δ-doped AlGaAs". *ICDS*. 1997, p. 1299.

[136] GC Dousmanis et al. "Evidence of refrigerating action by means of photon emission in semiconductor diodes". *Physical Review* **133**.(1A) (1964), A316.

[137] KP O'donnell and X Chen. "Temperature dependence of semiconductor band gaps". *Applied physics letters* **58**.(25) (1991), pp. 2924–2926.

[138] PK v Tien. "Light waves in thin films and integrated optics". *Applied Optics* **10**.(11) (1971), pp. 2395–2413.

[139] Yasuyuki Okamura, Atsushi Miki, and Sadahiko Yamamoto. "Observation of wave propagation in integrated optical circuits". *Applied optics* **25**.(19) (1986), pp. 3405–3408.

[140] R Regener and W Sohler. "Loss in low-finesse Ti: $LiNbO_3$ optical waveguide resonators". *Applied Physics B* **36**.(3) (1985), pp. 143–147.

[141] KH Park et al. "Nondestructive propagation loss and facet reflectance measurements of GaAs/AlGaAs strip-loaded waveguides". *Journal of Applied Physics* **78**.(10) (1995), pp. 6318–6320.

[142] Bruce Saleeb-Mousa et al. "Near infrared integrated photonic switches for portable quantum sensors". *Journal of Physics: Conference Series*. Vol. **1919**. (1). IOP Publishing. 2021, p. 012007.

[143] CP Lee, S Margalit, and A Yariv. "Double-heterostructure GaAs-GaAlAs injection lasers on semi-insulating substrates using carrier crowding". *Applied Physics Letters* **31**.(4) (1977), pp. 281–282.

[144] X Guo and EF Schubert. "Current crowding in GaN/InGaN light emitting diodes on insulating substrates". *Journal of applied Physics* **90**.(8) (2001), pp. 4191–4195.

[145] Chien-Ping Lee, S Margalit, and A Yariv. "GaAs-GaAlAs heterostructure lasers on semi-insulating substrates". *IEEE Transactions on Electron Devices* **25**.(10) (1978), pp. 1250–1256.

[146] Xuesong Dong. "Electrically-controlled optical beam steering and switching in semiconductor slab waveguide". PhD thesis. University of Central Florida, 2000.

[147] D. May-Arrioja. "Integrated InP Photonic Switches". PhD thesis. University of Central Florida, 2006.

[148] Anders Blom. "Resonant states in modulation-doped heterostructures". PhD thesis. Lund University, 2003.

[149] JS Blakemore. "Semiconducting and other major properties of gallium arsenide". *Journal of Applied Physics* **53**.(10) (1982), R123–R181.

[150] MB Panish and HC Casey Jr. "Temperature dependence of the energy gap in GaAs and GaP". *Journal of Applied Physics* **40**.(1) (1969), pp. 163–167.

[151] Daniel A May-Arrioja, Nathan P Bickel, and Patrick L LiKamWa. "Integrated beam-steered optical switch". *Enabling Photonic Technologies for Aerospace Applications VI*. Vol. **5435**. International Society for Optics and Photonics. 2004, pp. 91–96.

[152] Kent D Choquette et al. "Selective oxidation of buried AlGaAs versus AlAs layers". *Applied Physics Letters* **69**.(10) (1996), pp. 1385–1387.

[153] John Michael Dallesasse et al. "Hydrolyzation oxidation of Al x Ga1- x As-AlAs-GaAs quantum well heterostructures and superlattices". *Applied Physics Letters* **57**.(26) (1990), pp. 2844–2846.

[154] Ulrich Fischer-Hirchert. *Photonic Packaging Sourcebook: Fiber-Chip Coupling for Optical Components, Basic Calculations, Modules*. Springer, 2015.

[155] Leonardo Fallani and Anders Kastberg. "Cold atoms: A field enabled by light". *Europhysics Letters* **110**.(5) (2015), p. 53001.

[156] Galan Moody et al. "Roadmap on Integrated Quantum Photonics". *ArXiv Preprint ArXiv:2102.03323* (2021).

[157] Min Liu et al. "Efficient Silicon Nitride Grating Coupler with Silicon Reflector at Near-Infrared Wavelengths". *Asia Communications and Photonics Conference*. Optical Society of America. 2020, M4A–166.

[158] Hyundai Park et al. "Heterogeneous silicon nitride photonics". *Optica* **7**.(4) (2020), pp. 336–337.

[159] Martin Sinclair et al. "1.4 Million Q-Factor 780 nm Wavelength Si3N4 Micro-rings for Chip-Scale Atomic Systems". *CLEO: Science and Innovations*. Optical Society of America. 2020, STu4O–8.